



UNIL | Université de Lausanne

Unicentre

CH-1015 Lausanne

<http://serval.unil.ch>

Year : 2021

Constraints on the generation of petit-spot volcanoes: numerical studies on oceanic plate subduction and melt migration

Bessat Annelore

Bessat Annelore, 2021, Constraints on the generation of petit-spot volcanoes: numerical studies on oceanic plate subduction and melt migration

Originally published at : Thesis, University of Lausanne

Posted at the University of Lausanne Open Archive <http://serval.unil.ch>

Document URN : urn:nbn:ch:serval-BIB_B630DB56BEB13

Droits d'auteur

L'Université de Lausanne attire expressément l'attention des utilisateurs sur le fait que tous les documents publiés dans l'Archive SERVAL sont protégés par le droit d'auteur, conformément à la loi fédérale sur le droit d'auteur et les droits voisins (LDA). A ce titre, il est indispensable d'obtenir le consentement préalable de l'auteur et/ou de l'éditeur avant toute utilisation d'une oeuvre ou d'une partie d'une oeuvre ne relevant pas d'une utilisation à des fins personnelles au sens de la LDA (art. 19, al. 1 lettre a). A défaut, tout contrevenant s'expose aux sanctions prévues par cette loi. Nous déclinons toute responsabilité en la matière.

Copyright

The University of Lausanne expressly draws the attention of users to the fact that all documents published in the SERVAL Archive are protected by copyright in accordance with federal law on copyright and similar rights (LDA). Accordingly it is indispensable to obtain prior consent from the author and/or publisher before any use of a work or part of a work for purposes other than personal use within the meaning of LDA (art. 19, para. 1 letter a). Failure to do so will expose offenders to the sanctions laid down by this law. We accept no liability in this respect.

Faculté des géosciences et de l'environnement

Institut des sciences de la Terre

CONSTRAINTS ON THE GENERATION OF PETIT-SPOT
VOLCANOES: NUMERICAL STUDIES ON OCEANIC PLATE
SUBDUCTION AND MELT MIGRATION

THÈSE DE DOCTORAT

présentée à la Faculté des géosciences et de l'environnement de l'Université de Lausanne par

ANNELORE BESSAT

Maîtrise ès Sciences en géosciences de l'environnement de l'Université de Lausanne

Jury

Prof. Dr. Sébastien Pilet	Université de Lausanne	Directeur de thèse
Prof. Dr. Stefan M. Schmalholz	Université de Lausanne	Co-directeur de thèse
Prof. Dr. Yury Y. Podladchikov	Université de Lausanne	Expert interne
Dr. Thibault Duretz	Université de Rennes 1	Expert externe
Prof. Dr. Jolante van Wijk	New Mexico Tech	Expert externe
Prof. Dr. Christian Kull	Université de Lausanne	Président du jury

Lausanne, 2021

IMPRIMATUR

Vu le rapport présenté par le jury d'examen, composé de

Président de la séance publique :	M. le Professeur Christian Kull
Président du colloque :	M. le Professeur Christian Kull
Directeur de thèse :	M. le Professeur Sébastien Pilet
Co-directeur de thèse :	M. le Professeur Stefan Schmalholz
Expert interne :	M. le Professeur Yury Podladchikov
Experte externe :	Mme la Professeure Jolane van Wijk
Expert externe :	M. le Docteur Thibault Duretz

Le Doyen de la Faculté des géosciences et de l'environnement autorise l'impression de la thèse de

Madame Annelore Bessat

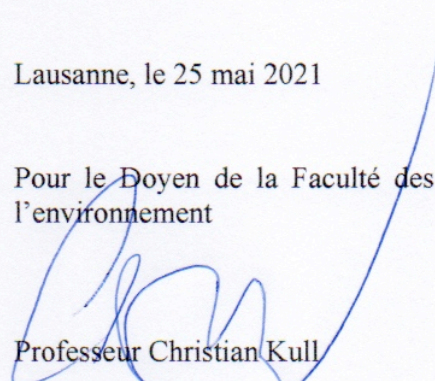
*Titulaire d'un
Master ès Sciences en géologie
de l'Université de Lausanne*

intitulée

**Constraints on the generation of petit-spot volcanoes:
numerical studies on oceanic plate subduction and melt migration**

Lausanne, le 25 mai 2021

Pour le Doyen de la Faculté des géosciences et de
l'environnement


Professeur Christian Kull

Contents

1	General Introduction	1
1.1	Outline of the thesis	2
1.2	Motivation	3
1.3	Objectives and approach	11
1.3.1	Chapter 2: thermo-mechanical numerical simulation of plate flexure . .	11
1.3.2	Chapter 3: Melt migration by reactive porosity waves	16
2	Stress and deformation mechanisms at a subduction zone: insights from 2-D thermomechanical numerical modelling	27
2.1	Introduction	29
2.2	Mathematical model	31
2.2.1	Governing equations for numerical simulations	31
2.2.2	Calculation of slab pull and gravitational potential energy	37
2.3	Model configuration	39
2.3.1	Configuration of the thermo-mechanical models	39
2.3.2	Configuration for the gravity anomaly calculations	42
2.4	Results	42
2.4.1	Quantification of slab pull force and gravitational potential energy . .	43
2.4.2	Analyses of strain rate, deformation mechanisms, effective viscosity and horizontal deviatoric stress	47
2.5	Discussion	61
2.6	Conclusions	67
2.7	Acknowledgements	69

3	Melt migration and chemical differentiation by reactive porosity waves	79
3.1	Introduction	81
3.2	Mathematical model	85
3.2.1	Thermodynamic model	85
3.2.2	Thermo-Hydro-Mechanical-Chemical model	93
3.2.3	Coupled THMC and thermodynamic model and numerical method . .	96
3.2.4	Model configuration and characteristic values	97
3.3	Results	99
3.3.1	Linearization of thermodynamic results	99
3.3.2	THMC model results: comparison of initial profiles, maximum melt velocity and evolution over time	102
3.4	Discussion	110
3.4.1	Mobility and mass transport	110
3.4.2	Magnesium in melt	111
3.4.3	2D reactive porosity wave model, channelization and melt-rock interaction	111
3.4.4	Estimates of melt velocity	116
3.5	Conclusions	117
	Appendix A. THMC model equations, additional explanation	126
	Appendix B. Additional figures and tables	130
	Appendix C. Thermodynamic part, additional explanation	137
4	General conclusion and perspectives	141
A	Code for gravimetry calculations	159
B	Code for thermodynamic	167
C	Code for THMC transport	181

Abstract

The discovery by Japanese researchers in 1997 of small volcanoes on the ocean floor of the Pacific plate that is subducting beneath Japan, was a great scientific surprise. The presence of volcanoes in this region close to the subduction zone where no deep mantle plumes are observed, has prompted questions concerning the formation of intra-plate volcanism. The hypothesis for the formation of these volcanoes, known as petit-spot volcanoes, is that they are linked to the flexure of the lithosphere at the subduction front. This flexure results in extension at the base of the lithosphere allowing for the extraction of small quantities of pre-existing melts at the base of the lithosphere. Nevertheless, this model remains a hypothesis based only on general observations. Extraction of these melts would be associated with the development of lithospheric-scale fractures, needed to allow melts to be transported and form volcanoes at the surface. However, no physical model has been developed to test these hypotheses.

The aim of this thesis is to understand the formation of petit-spot volcanoes by providing mechanical constraints on the flexure of a lithospheric plate in a subduction zone and the extraction of melts in a viscous medium. The first part of my thesis focuses on the resulting stress and deformation within an oceanic lithosphere that is flexing due to subduction. Here I aim to identify the key parameters that affect the mechanics of a subduction zone using the 2D thermo-mechanical (TM) code, MDoodz. This numerical code utilises finite difference (FD) and marker-in-cell methods. We test two subduction scenarios: (1) “forced subduction” where horizontal velocities are applied to the lateral boundaries of the plates during the entire simulation, and (2) “free subduction” where horizontal velocities are stopped when the subducting slab is long enough to continue subducting without far-field horizontal velocity. We have determined that a slab pull of $1.8 \text{ TN}\cdot\text{m}^{-1}$ is required to continue free subduction. The major results of this study show that elasto-plastic deformation is the dominant deformation mechanism in the upper part of the lithosphere and within the slab, and that viscous deformation dominates the lower part of the lithosphere. The magnitude and distribution of the deviatoric stresses, which illustrate the regions of compression and extension, shows

that maximum values are in the upper lithosphere and in the region of flexure. Values are close to zero at the base of the lithosphere and there is no significant extension at the base of the lithosphere. We also tested the impact of elasticity and reduction of the internal angle of friction in our simulations. The results show that elasticity has a large impact on the magnitude and distribution of deviatoric stresses and if the internal angle of friction is too small, it results in the detachment of the slab and slab pull can no longer be transmitted to the plate. Comparisons of the topography and gravity anomaly of our model with natural bathymetry and free-air gravity anomalies across the Mariana trench, demonstrates that the chosen density fields and the modelled flexural behaviour is compatible with natural data.

The second part of this thesis examines, on the one hand, the mechanisms linked to the percolation and extraction of melts at the base of the lithosphere, in an environment where viscous deformation dominates, and on the other hand the physico-chemical interaction between the solid and the melt. In order to study this percolation process and to investigate the impact of chemical differentiation on melt migration, we have developed a 1D thermo-hydro-mechanical-chemical transport (THMC) code with two phases (melt and solid). Our code is based on modelling porosity waves coupled to a thermodynamic database for Gibbs free energy minimisation. Our chemical system is simple and composed of the ternary system forsterite-fayalite-silica. All variables, such as density, MgO or SiO₂ concentrations for melt and solid are functions of pressure (P), temperature (T) and total silica concentration. We use pressure and temperature conditions applicable to the base of the lithosphere and we use two geothermal gradients, one adiabatic and one conductive, to evaluate the impact of temperature on melt migration. The results show that both the total SiO₂ concentrations and the variable geotherms have a strong impact on the velocity of melt migration. The results of our preliminary 2D model demonstrates that the melt velocity transported by the porosity wave mechanism varies between 1 and a few hundred metres per year, depending on the viscosity of the melt. These values are comparable to transport velocities of melt estimated at mid-ocean ridges.

The results presented in this thesis demonstrate that the formation of petit-spot volcanoes is more complex than once thought. The first study highlighted the lack of extension and the

dominance of viscous deformation mechanisms in regions at the base of the lithosphere. It therefore seems impossible to extract melts from the base of the lithosphere via the development of fractures at the lithospheric scale. Our observations are, on the contrary, compatible with an alternative model for the formation of petit-spot melts. Our model proposes that small quantities of melts first percolate and interact with the base of the lithosphere. This process will then produce a so-called "metasomatic" enrichment of the region. A dynamic view of this process shows that small quantities of melts, after interacting with the base of the metasomatized lithosphere, will subsequently reach brittle portions of the lithosphere and thus allow for the development of hydrous fractures allowing melts to rise up and reach the surface. The second study enabled a better constraint on the mechanisms of melt percolation in ductile regions, and investigated the processes needed to extract and percolate melt under conditions associated with the base of the lithosphere. During this percolation, the melt will interact with the solid resulting in compositional changes. This highlights the link between the processes of metasomatism that are observed in petrological studies of petit-spot volcano rocks and the physical mechanisms that control the extraction of melt.

Résumé

La découverte par des chercheurs japonais en 1997 de petits volcans sur le plancher océanique de la plaque pacifique qui plonge sous le Japon a été une grande surprise scientifique. En effet, la présence de volcans dans cette région, proche de la zone de subduction mais où aucun plume mantellique profond n'est connu, remet en question l'hypothèse de formation du volcanisme intra-plaque. L'hypothèse de formation de ces volcans, dits de type petit-spot, est qu'ils sont liés à la flexure de la lithosphère en front de subduction. Cette flexure produirait une extension à la base de la lithosphère permettant l'extraction de petites quantités de magmas préexistants à la base de la lithosphère. Néanmoins, ce modèle de formation reste une hypothèse ne reposant que sur des observations générales. Par exemple, l'extraction de ces magmas serait associée au développement de fractures à l'échelle lithosphérique permettant à ces magmas de remonter et de former les volcans à la surface, mais aucun modèle physique n'a été développé pour tester ces hypothèses.

Le but de cette thèse est de comprendre la formation des volcans petit-spot en fournissant des contraintes mécaniques sur la flexure d'une plaque lithosphérique dans une zone de subduction et l'extraction de magma dans un milieu visqueux. La première partie de ma thèse étudie les contraintes et les déformations d'une lithosphère océanique fléchie dans une zone de subduction. Elle a pour but d'identifier les paramètres clés qui impactent la mécanique d'une zone de subduction en utilisant le code 2D thermo-mécanique (TM) MDoodz. Ce code numérique est basé sur la méthode des différences finies (FD) et des « marker-in-cell ». Nous avons testé deux scénarii de subduction : (1) une subduction forcée où une vitesse horizontale est appliquée aux bordures des plaques durant l'entier de la simulation et (2) une subduction libre où nous stoppons la vitesse horizontale lorsque le panneau plongeant (c.-à-d. slab) est assez long pour continuer à subduire sans aide. Nous avons déterminé qu'une force de traction (slab pull) de $1.8 \text{ TN}\cdot\text{m}^{-1}$ est nécessaire pour continuer une subduction libre. Les résultats majeurs de cette étude ont montré que la déformation élasto-plastique est le mécanisme de déformation dominant dans la partie supérieure de la lithosphère et le panneau plongeant et que la déformation visqueuse domine la partie inférieure de la lithosphère. La magnitude

et la distribution des contraintes déviatoriques, qui illustrent les régions en compression ou en extension, montrent que les valeurs maximales se situent dans la partie supérieure de la lithosphère et dans la région de la flexure. Les valeurs sont proches de zéro à la base de la lithosphère et il n'y a pas d'extension significative à la base de la lithosphère. Nous avons également testé l'impact de l'élasticité et de la réduction de l'angle de friction interne dans nos simulations. Les résultats montrent que l'élasticité a un grand impact sur la magnitude et la distribution des contraintes déviatoriques et que si l'angle de friction interne est trop faible, il cause le détachement du panneau plongeant et la force traction (slab pull) ne peut plus être transmise à la plaque. La comparaison entre la topographie et l'anomalie de gravité de notre modèle avec des données naturelles de bathymétrie et d'anomalie à l'air libre dans la région de la fosse des Mariannes nous montre que les champs de densités choisis et le comportement de la flexure modélisée sont compatibles avec des données naturelles.

La deuxième partie de cette thèse s'interroge d'une part aux mécanismes liés à la percolation et à l'extraction de magmas à la base de la lithosphère, dans un milieu où la déformation visqueuse domine, et d'autre part à l'interaction physico-chimique entre le solide et le magma. Dans le but d'étudier ce processus de percolation et d'investiguer l'impact de la différenciation chimique dans la migration du magma, nous avons développé un code de transport thermo-hydro-mécanico-chimique (THMC) en 1D avec deux phases, une partie magma et une partie solide. Notre code est basé sur la modélisation des vagues de porosité « porosity waves » et est couplé à une base thermodynamique obtenue par la minimisation de l'énergie de Gibbs. Notre système chimique est simple, composé du système ternaire forstérite-fayalite-silice. Toutes les variables, comme la densité ou les concentrations en MgO ou SiO₂ pour le magma et le solide sont des fonctions de la pression (P), de la température (T) et de la concentration totale de silice. Nous utilisons des conditions de pression et de température applicable à la base de la lithosphère et nous utilisons deux gradients géothermiques, un adiabatique et un conductif, pour voir quel impact a la température sur la migration du magma. Les résultats montrent que la concentration totale en SiO₂ et les différents géothermes ont un impact fort sur la vitesse de migration du magma. Les résultats d'un modèle préliminaire en 2D mettent en évidence que la vitesse des magmas transportés par le mécanisme de « porosity waves » varie

entre 1 et quelques centaines de mètres par an, en fonction de la viscosité du magma. Ces valeurs sont comparables aux vitesses de transport des magmas estimées au niveau des rides médio-océaniques.

Les résultats présentés dans cette thèse montrent que la formation des volcans petit-spot est plus complexe qu'il n'y paraît. La première étude a permis de mettre en évidence le manque d'extension à la base de la lithosphère et que la déformation visqueuse est le mécanisme dominant dans cette région. Il semble donc impossible d'extraire des magmas de la base de la lithosphère via le développement de fracture à l'échelle lithosphère. Nos observations sont, au contraire, compatibles avec un modèle alternatif pour la formation des magmas de type petit-spot. Ce modèle propose que de faibles quantités de magmas commencent par percoler et interagir avec la base de la lithosphère. Ce processus va produire un enrichissement dit « métasomatique » de cette région. Dans une vision dynamique de ce processus, de petites quantités de magmas, après avoir interagi avec la base de la lithosphère métasomatisée, vont atteindre la partie cassante de la lithosphère permettant le développement de fracture jusqu'à la surface. La deuxième étude a permis de mieux contraindre le mécanisme de percolation des magmas dans le domaine ductile et a permis d'investiguer comment il est possible d'extraire et faire percoler un magma dans des conditions relatives à la base de la lithosphère. Durant cette percolation, le magma va interagir avec le solide et changer sa composition. Ceci permet de mettre en lumière le lien entre les processus de métasomatisme qui sont observés par l'étude pétrologique des roches des volcans petit-spot et les mécanismes physiques qui contrôlent l'extraction des magmas.

CHAPTER 1

General Introduction

1.1 Outline of the thesis

This thesis is structured as four chapters with an appendix section. Chapters 2 and 3 are written as article format. They are supported by a general introduction in this first chapter, which will give an overall view of the study context and the questions that we will develop afterwards. In chapter 4, a general conclusion will provide a summary of major results obtained during the thesis and a discussion on the perspectives of this study.

- *Chapter 2: Stress and deformation mechanisms at a subduction zone: insights from 2D thermomechanical numerical modelling.*

This chapter consists of an article published in *Geophysical Journal International*. Co-authors are Thibault Duretz, György Hetényi, Sébastien Pilet and Stefan M. Schmalholz.

Here, we present a 2D thermo-mechanical (TM) numerical model to simulate deformation in subduction zone. We investigate which mechanical parameters are important in this geological environment, and quantify stresses. This allows to determine the distribution of stress and dominant deformation mechanism around flexural regions, which is important for the formation of petit-spot volcanoes and the potential Earthquake location within the subducting plate.

- *Chapter 3: Melt migration and chemical differentiation by reactive porosity waves.*

This chapter is an article to be submitted. Co-authors are Sébastien Pilet, Yuri Y. Podladchikov and Stefan M. Schmalholz.

This chapter aims to understand the percolation of magma in a porous viscous medium at pressure and temperature conditions relevant for the base of the lithosphere. We present a 1D thermo-hydro-mechanical-chemical (THMC) numerical model of porosity waves coupled with thermodynamic data obtained from numerical Gibbs energy minimisation calculations. This model allows to evaluate the chemical aspect of melt-peridotite reaction in a simplified system MgO-FeO-SiO_2 for magma rising into the ductile litho-

spheric mantle. We will present implications for magma extraction in intraplate setting and for the metasomatism enrichment of the lithospheric mantle.

1.2 Motivation

The motivation of this PhD thesis is to provide new constraints on the formation of petit-spot volcanoes observed first in the oceanic plate east of Japan. The publication in Science in 2006 of the Hirano et al. paper entitled *Volcanism in Response to Plate Flexure* have create a polemic in the scientific community (McNutt, 2006) as the discovery of the so-call petit-spot volcanoes have questioned the general idea that intraplate magmas are associated to deep mantle plumes. In the next paragraphs, I will present the context of the petit-spot discovery and the implication for intraplate magma formation. Then I will explain the goal of this PhD thesis, and how this study will help to constrain the mechanism of petit-spot formation.

The discovery of petit-spot volcanoes was a big scientific surprise. In 1997, during a cruise off the coast of Japan led by JAMSTEC (Japan Marine Science and Technology Center) to test their new KAIKO submarine, Japanese researchers observed fresh young alkaline basalts on the ocean slope of the Japan trench (Site A on Figure 1.1) (Hirano et al., 2001, 2006). The presence of these basalts dated from 6 to 8 Ma on the top of a 135 Ma old Pacific plate was unexpected as most seamounts in this area has been formed during Cretaceous age and no hot-spot are known in this region close to the subduction zone.

After this discovery, in 2004, Japanese researchers made extensive surveys in the same region where they found the first samples (Site A), and the assumed position of emission, “Site B”, 600 km to the southeast (Figure 1.1). The estimated position of emission was determined by calculating the distance travelled of basalts from their emission point to the trench by knowing the speed of the Pacific plate ($10 \text{ cm}\cdot\text{yr}^{-1}$; Gripp and Gordon, 1990) and their ages at “Site A” ($\sim 6 \text{ Ma}$; Hirano et al., 2001) and the current direction of the Pacific plate motion. The age of the basalts found in “Site B” were dated from 0.05 to 1 Ma and that’s how Hirano and coworkers found where these basalts were initially emitted. Another place close to the Japan trench was identified and named “Site C” (Sato et al., 2017).

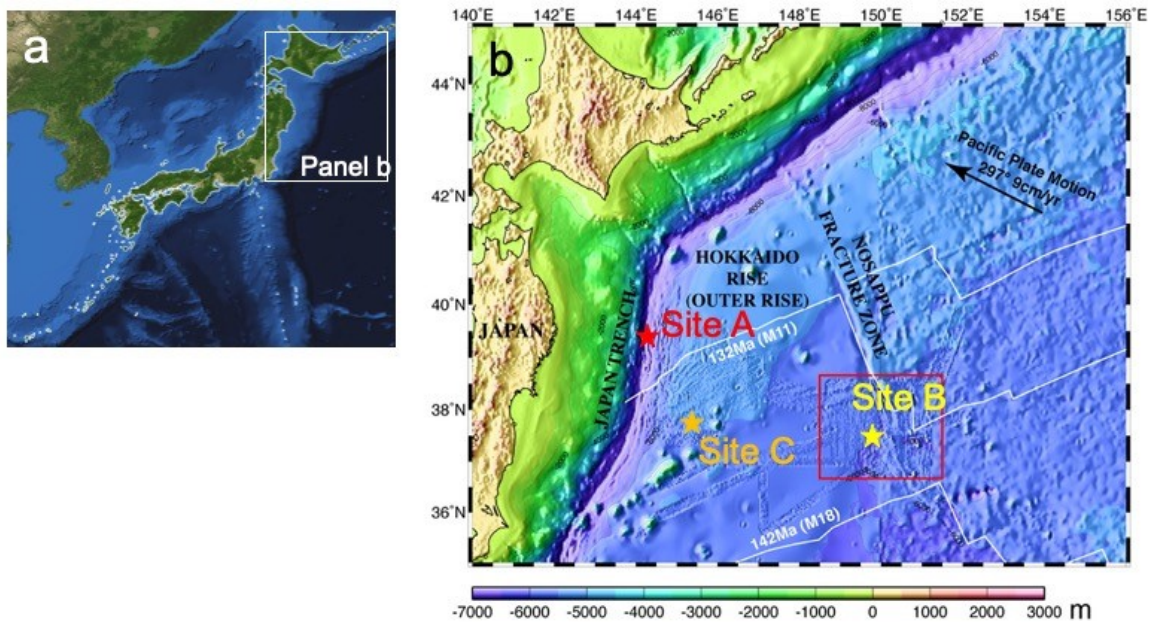


Figure 1.1: Location of petit-spot volcanoes observed in front of Japan. a) general location of the area investigated by JAMSTEC researchers. b) Location of the different sites where petit-spot volcanoes has been described (Site A: Hirano et al., 2001; site B: Hirano et al., 2006; Site C: Sato et al., 2017)

To understand why it is extraordinary to find these basalts, we must first describe what is happening in a subduction zone. In plate tectonic theory, a subduction zone is the place where two tectonic plates converge and the location of oceanic plate recycling process (Molnar, 2015). Several major geological processes take place in this subduction environment as arc volcanism, earthquakes and metamorphism of high and ultra-high pressure. Subduction zones are characterized by an arc volcanism on the overriding plate, a deep trench and a bulge (or swell, outrise) on the subducting plate.

The case of petit-spot volcanoes is different as they were found in the subduction plate, close to the trench and seaward after the bulge where normally no volcanism is expected. The emission's position of petit-spot volcanoes at 600 km from the trench suggests a connection between the flexure of the subducting plate and the formation of these volcanoes. Hirano and co-workers (2006) have interpreted petit-spot as small intraplate volcanoes produced by extraction of low degree melts from the base of the lithosphere in response to the flexure of the plate (Figure 1.2). In addition to Japan, several petit-spot localities have been identified

from the Tonga (Hirano et al., 2008), Chile (Hirano et al., 2013), and Sunda trenches (Taneja et al., 2015), or as an accreted petit-spot in Costa Rica (Buchs et al., 2013), suggesting that petit-spot volcanism is a global process in subduction zones.

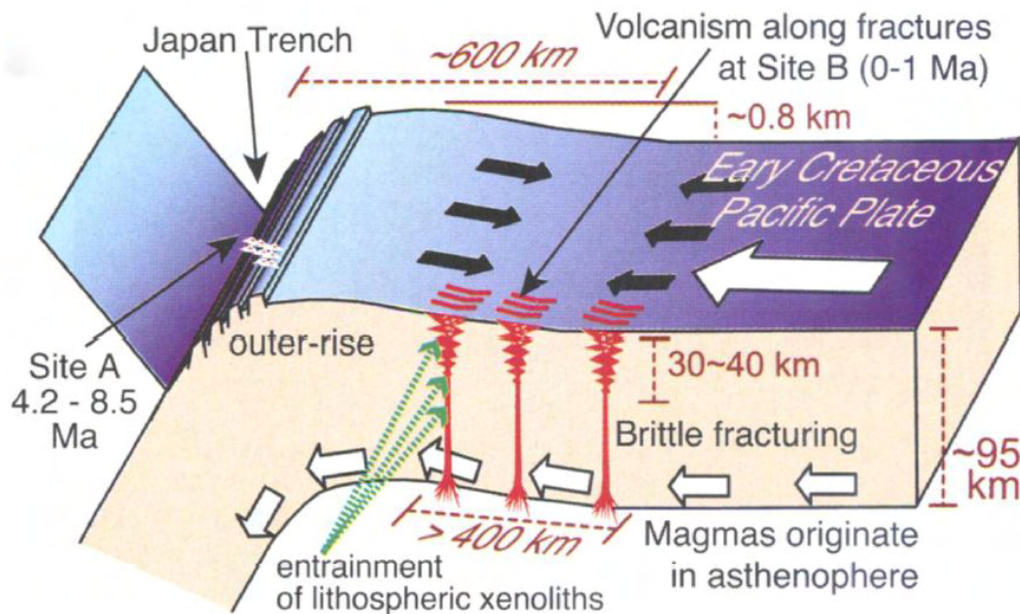


Figure 1.2: Schematic figure from Hirano et al. (2006, Fig. 3c of their paper), illustrating the conceptual model for the formation of petit-spot volcanism. Asthenospheric magmas escape to the surface due to extension at the base of the lithosphere made by the flexure of the subduction plate.

The formation of petit-spot volcanoes differs from typical volcanism observed at mid-ocean ridges, associate to mantle upwelling, in arc setting, dehydration of the subducting plate and hydrous melting of the mantle wedge, or in oceanic islands, volcanism interpreted as the activity of deep mantle plumes. As illustrated by the schematic figure of Yamamoto et al. (2014), (see Figure 1.3) the proposed model for the formation of petit-spot volcanoes suggests the presence of small melt fraction at the base of the lithosphere and the propagation of brittle fractures in response to plate flexure until the base of the lithosphere. This later process is postulated in order to explain the extraction of melts from the LAB to the surface.

The presence of low degree melts has been documented by various geophysical studies. Seismic studies of the Pacific plate subducting below Japan have shown a large shear wave velocity reduction at the lithosphere asthenosphere boundary (Kawakatsu et al., 2009). Kawakatsu

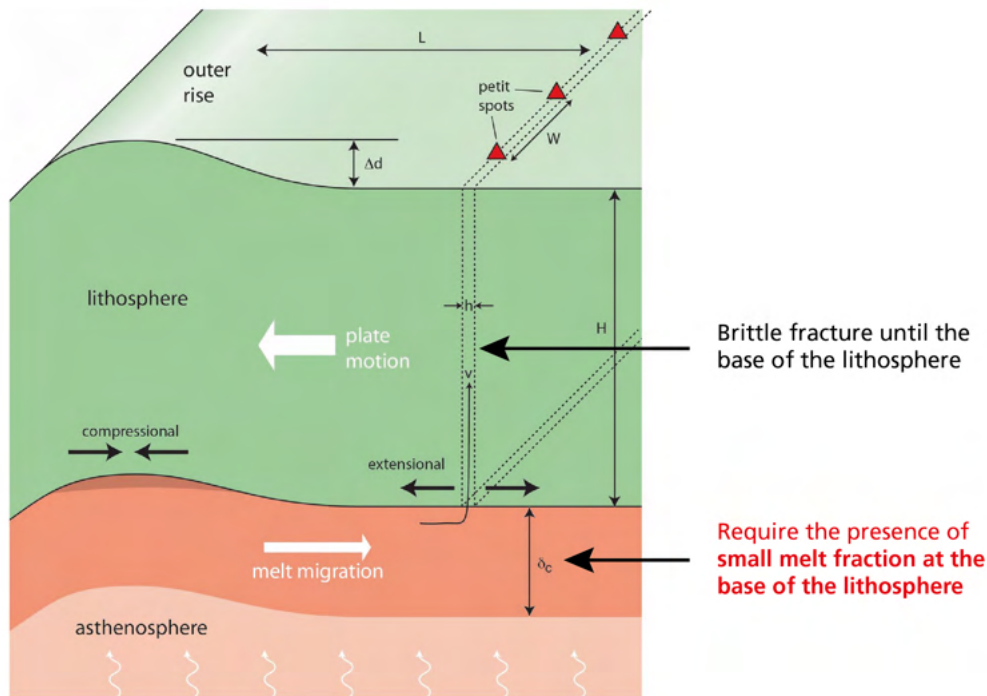


Figure 1.3: Schematic figure modified from Yamamoto et al. (2014, Fig. 2 of their paper) illustrating the extraction of low degree melt from the base of the lithosphere in order to explain the formation of petit-spot volcanoes at the surface.

and co-authors interpret this anomaly as partially molten asthenosphere consisting of horizontal melt-rich layers embedded in meltless mantle (Figure 1.4). Similar seismic observation has been made for the Pacific plate subducting below New Zealand (Stern et al., 2015) with a reduction of seismic velocity at the base of the lithosphere (Figure 1.5). This 10 km thick layer illustrated in figure 1.5b, was also interpreted as the presence of small melt fraction. This presence of small degree melts at the top of the asthenosphere was also documented by magnetotelluric study for the Coco plate subducting below American plate (Naif et al., 2013) (Fig.1.6).

An important question related to the conclusion of these different geophysical studies is how to explain the presence of low degree melts at the base of the lithosphere. The figure 1.7 shows a pressure-temperature diagram, modified from Dasgupta et al. (2013), where the solidus for dry-peridotite or in presence of various amount of CO_2 are plotted. In addition, conductive (lithospheric) and convective (asthenospheric) mantle geotherms are reported for the case of

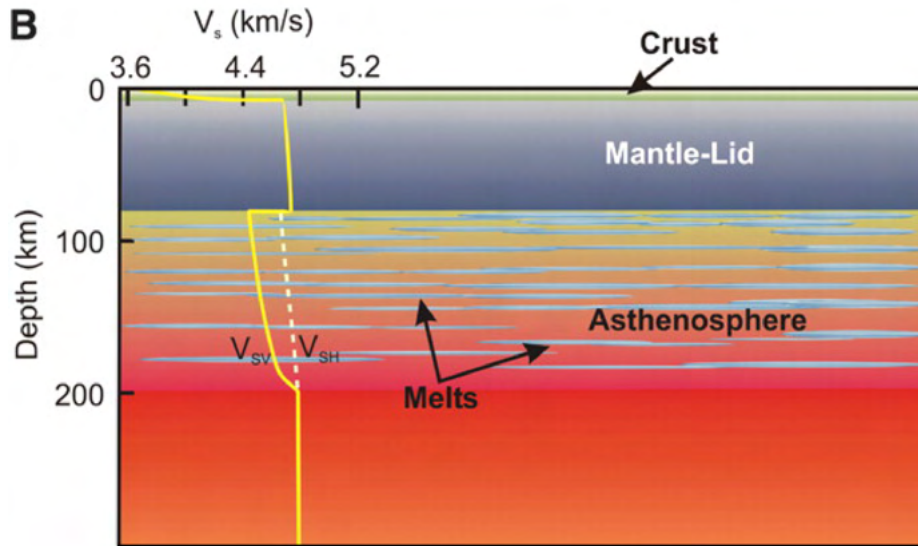


Figure 1.4: Schematic figure of upper mantle with the lithosphere-asthenosphere transition from Kawakatsu et al. (2009, Fig. 4B of their paper). Yellow line shows the velocity profile of a seismic S-wave, with a reduced region at the LAB.

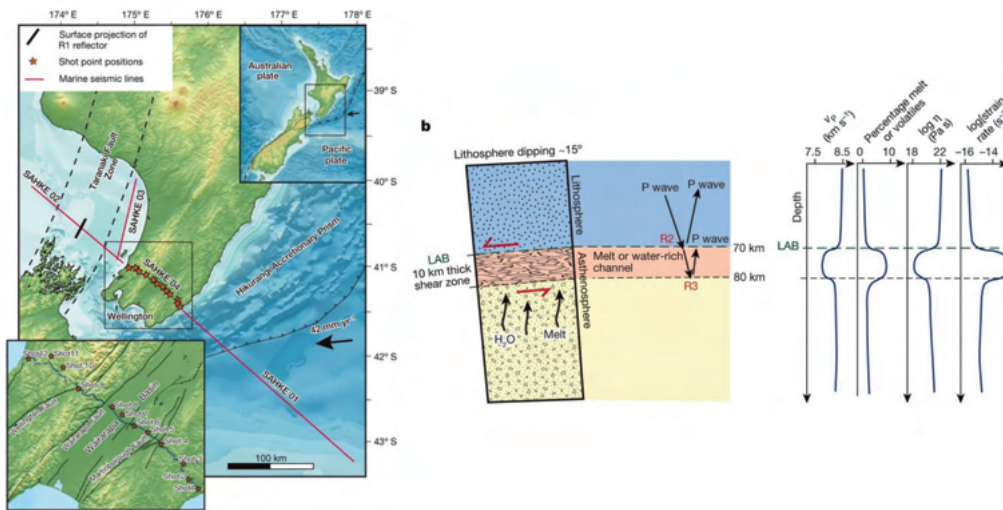


Figure 1.5: a) Location of the seismic study for the Pacific plate subducting below continental New Zealand. b) schematic interpretation of physical properties at the base of the Pacific plate lithosphere. Stern and co-authors interpret a channel about 10 km thick at the LAB due to the pooling of melt. This presence of melts deduced from the v_p reduction implying changes in the percentage melt, in viscosity and strain rate. (Figures 1 and 4b modified from Stern et al. 2015)

a mature oceanic lithosphere. This P-T diagram illustrates that no melt is expected at the base of the lithosphere for the case of mantle containing no-volatile, because the dry solidus of peridotite doesn't intercept the oceanic geotherm for oceanic lithosphere characterized by

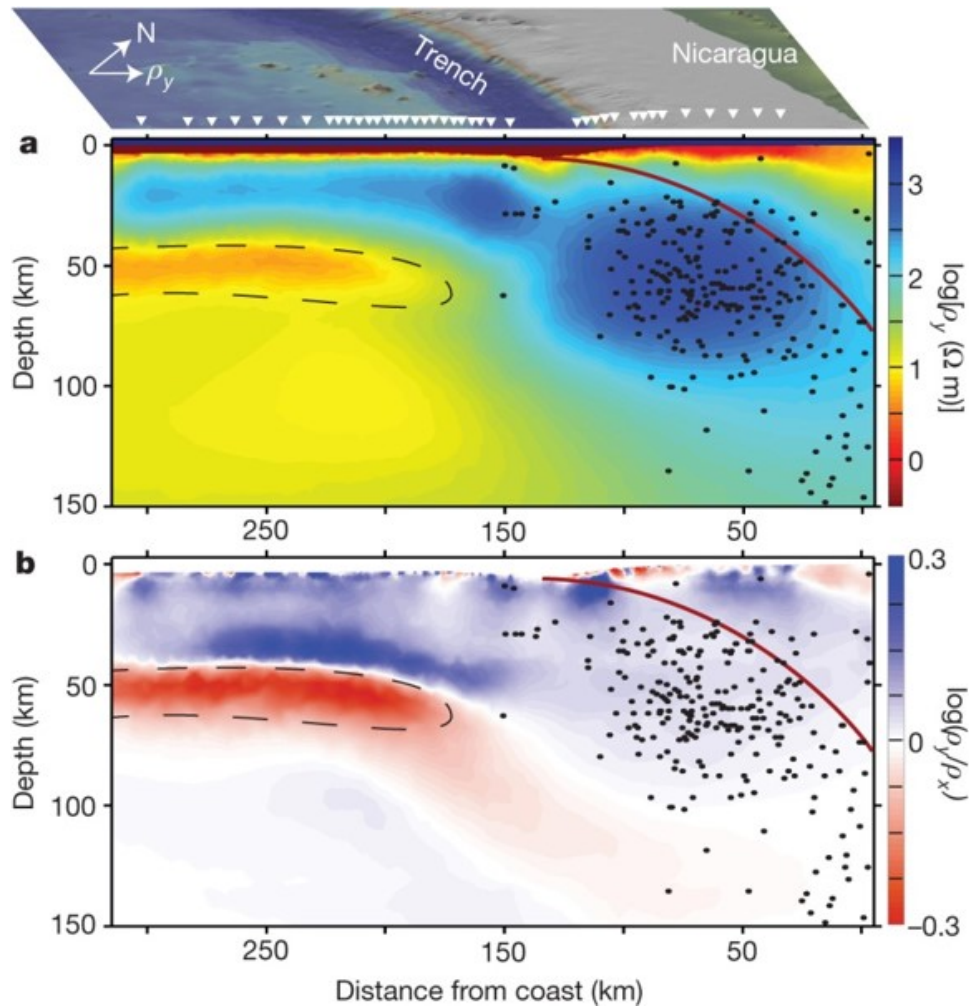


Figure 1.6: Presence of a conductive layer, area surrounded by dotted lines, at the base of the Coco plate subducting below American plate. Colour codes in panels a) and b) show the resistivity and the anisotropy respectively revealed by magnetotelluric data. Figure from Naif et al. (2013, Fig. 2 of their paper).

a $55 \text{ mW}\cdot\text{m}^{-2}$ heat flow. However, the addition of volatiles, illustrated in figure 1.7 by the addition of CO_2 , depress the solidus temperature of peridotite. As the mantle contains small amount of CO_2 , this figure predicts the formation of small degree volatile rich melts at the base of the lithosphere, while the composition of this melt, carbonatitic or CO_2 rich silicate melts, will depend on the geotherm and the depth of interest. In the current example, small volume of carbonatic melts and CO_2 -rich silicate melts coexist at the base of the lithosphere and in the top of the asthenosphere. Carbonatic melts (blue area in Figure 1.7) are present at $\sim 70\text{-}80$ km depth in the lithosphere where temperatures exceed $\sim 1'000^\circ\text{C}$. As the temperature

increase close to lithosphere-asthenosphere boundary, small volume of CO_2 -rich silicate melts are formed (red area), as carbonatic to CO_2 rich silicate melt transition is fixed at 25 wt.% of CO_2 in the melt (Dasgupta et al., 2013). The relative slopes of the geotherm regarding mantle solidus changes in the asthenosphere according the convective mechanism of heat transfer. This explains the presence of melts of CO_2 rich silicate at the top of the asthenosphere, while the composition of melts evolves to carbonatic as the depth/pressure increase (Figure 1.7).

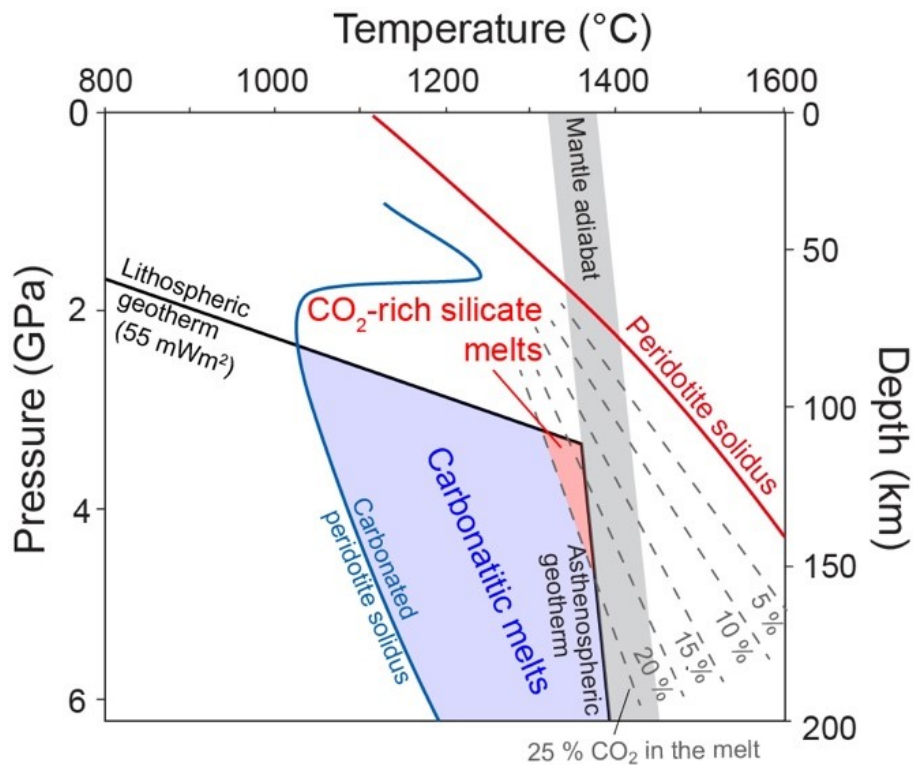


Figure 1.7: Modified figure from Dasgupta et al. (2013) including geotherm location for a mature oceanic lithosphere (>80 Ma old). The red and blue lines correspond to the peridotite solidus dry or in presence of carbonates. Dash grey lines reports the stability of melts with various CO_2 contents (5 to 25 wt.%). The 25 wt.% CO_2 content line corresponds to the transition from carbonatic to silicate composition (Dasgupta et al., 2013). The blue and red zones indicates the P-T condition where small degree of carbonatic and silicate melts could exist below mature oceanic plate.

These different constraints on the solidus of peridotite and on the geotherm support the presence of small degree melts at depth and provide a potential explanation for the low seismic velocity zone observed at the base of the lithosphere. However, this interpretation is based on a static view, which assume a homogeneous distribution of volatiles in the mantle and do not take into account the amount of melt potentially present at depth. Considering

that the convecting mantle contains only 60 ppm CO_2 , the amount of silicate melt that one could produce at the base of the lithosphere is extremely low, below 0.1% (Hirschmann, 2010). Such low degree melts seem insufficient to explain the seismic anomaly observed in the low-velocity zone, even this melts is concentrated in lenses as proposed by Kawakatsu et al. (2009). To solve this problem, Marc Hirschmann (2010) suggests that seismic discontinuity observed at the lithosphere-asthenosphere-boundary correspond to the accumulation of melts at the base of the lithosphere that have migrated from greater depths in the periphery of mid-ocean ridges or by upwelling processes as illustrated in figure 1.8. These accumulated melts are considered as the source of magma emitted in petit-spot volcanoes.

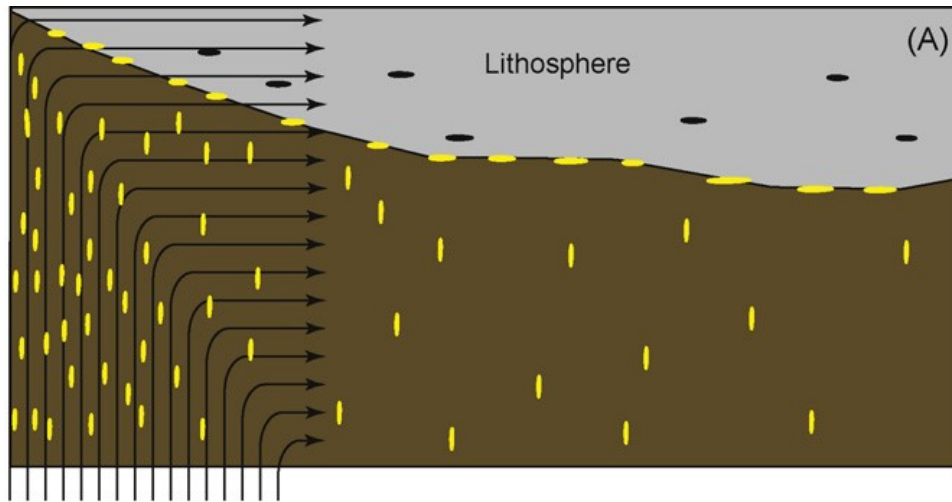


Figure 1.8: Schematic figure illustrating the addition of melts to the LAB, either in periphery of mid-ocean ridges or by melt migration. Figure from Hirschmann (2010, Fig. 11a of his paper).

If this idea seems mostly accepted in the literature, this model has some important implication, in particular for the thermal state of the upwelling melts and on the mechanical aspect of the melt rising in the asthenosphere or in the base of the lithosphere. The question related to the migration of low degree melts within the mantle will be the main subject of the second part of this PhD (chapter 3).

1.3 Objectives and approach

The hypothesis proposed by Hirano and co-authors for the formation of petit-spot lavas, i.e. extraction of low degree melt from the base of the lithosphere in response to plate flexure, seems therefore in agreement with current geophysical and petrological knowledge on the presence of melt at the lithosphere asthenosphere boundary. However, the mechanical aspect of melt extraction from ~ 80 km depth to the surface is mostly unconstrained. The schematic figure from Yamamoto et al. (2014, Figure 1.3) illustrates the hypothesis of a direct extraction of melts to the surface by the opening of deep fracture in response to plate flexure. Nevertheless, no model has tried to quantify the extension at the base of the lithosphere. In addition, the propagation of fracture is expected only in the brittle domains. But it remains unclear if such brittle domain extends until the base of the lithosphere. These questions are the motivation of the first part of this thesis (chapter 2).

1.3.1 Chapter 2: thermo-mechanical numerical simulation of plate flexure

The chapter 2 is designed as a scientific article with the motivation and the general context of this numerical study introduced in the first sections. In the following paragraphs, I will introduce additional general rheological concept used in this chapter.

Numerical models to study large-scale geodynamic process include some constitutive equations, flow laws or combinations of flow laws, with rheological parameters corresponding to rocks that best represent our study area, for our purposes mantle lithologies. The definition of rheology is the study of the material deformation and its flow in response to an applied stress. Each rock has its own proper rheological properties, which could be determined using rock deformation experiments. One can fit these experimental results with so-called power-law flow law that we use in geodynamic models (e.g. Hirth and Kohlstedt, 2003; Karato, 2008; Mei et al., 2010). Several critical parameters such as the dependence of strain rate on stress, grain size, temperature dependence (activation energy), and pressure dependence (activation volume) must be determined carefully.

When we apply a force to the surface of an object, we deform this object through stress, σ . The result is a change in size or volume called strain, ε . This force can be normal or tangential to the surface, corresponding to normal stress or shear stress respectively. When the applied force is released, if the object returns to its original shape, the deformation is non-permanent (i.e. non-dissipative, reversible or recoverable). This is the case of elastic deformation. The mathematical relation for an elastic deformation, known as Hooke's law, between stress and strain is linear, $\sigma = E\varepsilon$, with a constant E named Young's modulus. E depends on the nature of the material, and time has no impact on the deformation. By contrast, when the applied force is released but the object keeps its change of shape, the deformation is permanent. This is the case of frictional-plastic (i.e. brittle-plastic or Mohr-Coulomb criterion) or viscous deformation (i.e. creep). The frictional-plastic deformation follows the Mohr-Coulomb theory. The Coulomb failure criterion is the mathematical relation between shear and normal stress. The frictional-plastic deformation is done by sliding and it is the normal stress that resists to the sliding. For the viscous deformation, the mathematical relation between the stress and the strain implies to take the time into account; $\sigma = \mu\dot{\varepsilon}$, where $\dot{\varepsilon}$ is the strain rate and μ the viscosity. If the deformation is slow, the stresses will be low and if the deformation is fast, the stresses will be high. There are several types of viscous deformation as diffusion creep, dislocation creep and Peierls creep.

Diffusion creep (i.e. linear creep) deformation (Figure 1.9) involves the movement of atoms, ions or vacancy through a mineral by diffusion and implies punctual defects in the crystal structure of the mineral (Kohlstedt, 2007). Diffusional creep occurs at relatively low stress, high temperature and small grain size. The diffusion of these defects can occur along the edge of the mineral grain; this deformation is called the Coble creep (e.g. Passchier and Trouw, 2005; Turcotte and Schubert, 2014). If the diffusion takes place through the interior of grain, we speak rather of Nabarro-Herring creep (e.g. Passchier and Trouw, 2005) (Figure 1.9). When the crystal is more compressed in one direction (black arrows in Figure 1.9), the defects migrate in the direction with the lowest compression, which tends to shorten the crystal in the compression direction. In order to move a vacancy through a crystal, chemical bonds must be broken, which is why a certain amount of activation energy is required. If

Diffusion creep: diffusion of vacancies

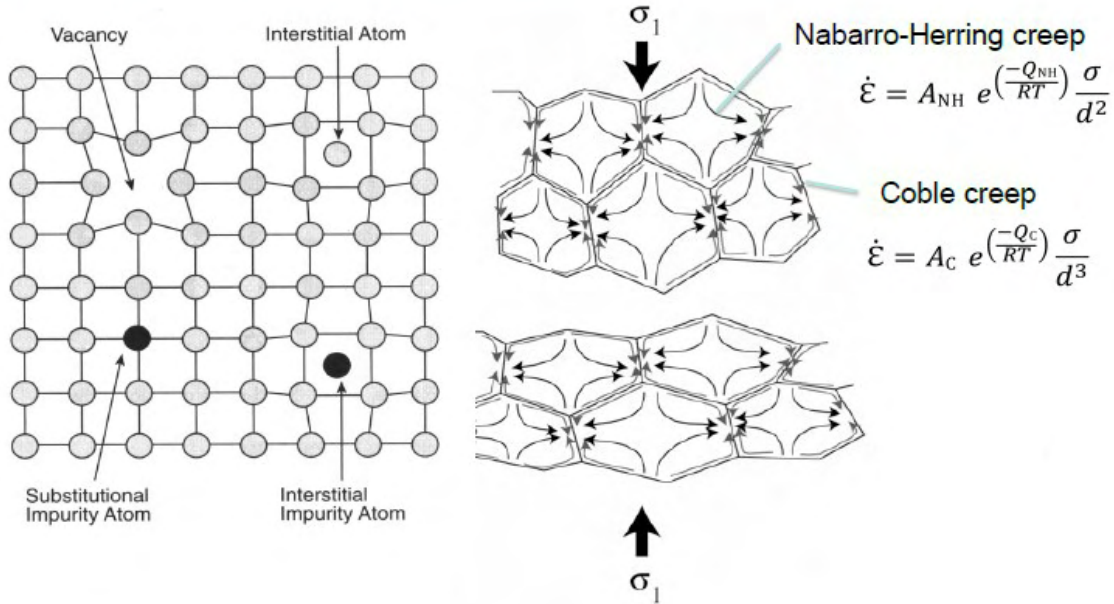


Figure 1.9: Schematic view of diffusion creep (Passchier and Trouw, 2005).

the temperature is higher, it will be easier to move the vacancy through the crystal. The mathematical relation between stress σ and strain rate $\dot{\epsilon}$ is linear, stress exponent n is equal to 1 (eq. 2.11 and Table 2.1 in chapter 2):

$$\dot{\epsilon}_{ij}^{dif} = F_{dif} A_{dif} \tau_{ij}^{n_{dif}} d^{-m_{dif}} \exp\left(-\frac{E_{dif}^* + PV_{dif}^*}{RT}\right)$$

Dislocation creep (i.e. power law creep) is a deformation mechanism involving a collective motion of atoms as crystal dislocations that will move and propagate in a crystal (Figure 1.10). Dislocations in the crystal are caused by their slippage and the rise of line defects (Kohlstedt, 2007), such as the movement of caterpillars. The rate of deformation is proportional to the density and velocity of dislocation. In general, they increase with an applied stress. A variety of resistance forces controls the velocity of glide motion as intrinsic resistance due to the crystal lattice or lattice impurity. The diffusion of atoms control also the movement of dislocation, which implies that dislocation creep is sensitive to the temperature and the

Dislocation creep

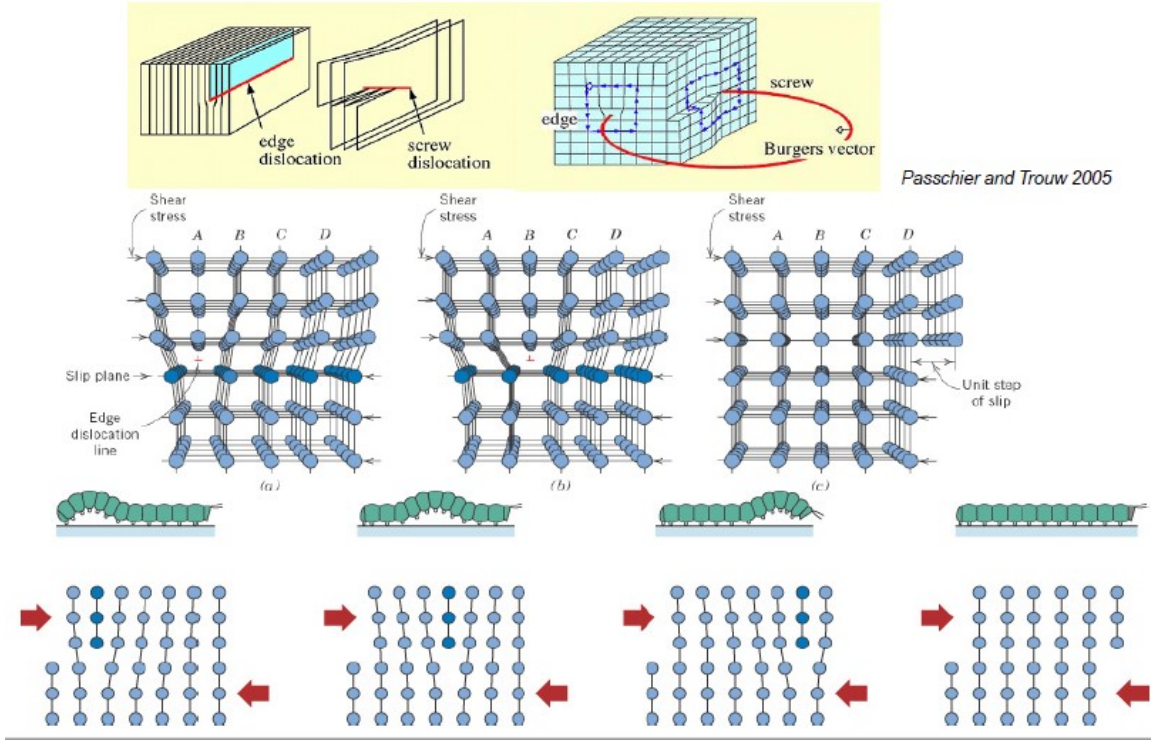


Figure 1.10: Schematic view of dislocation creep (Passchier and Trouw, 2005).

chemistry (Karato, 2008). The mathematical relation between stress σ and strain rate $\dot{\epsilon}$ is a power law, stress exponent n is more than 3 (eq. 2.12 and Table 2.1 in chapter 2):

$$\dot{\epsilon}_{ij}^{\text{dis}} = F_{\text{dis}} A_{\text{dis}} \tau_{ij}^{n_{\text{dis}}} d^{-m_{\text{dis}}} \exp\left(-\frac{E_{\text{dis}}^* + PV_{\text{dis}}^*}{RT}\right)$$

Peierls creep (i.e. low-temperature plasticity or exponential creep) mechanism is important for low temperature and high stress deformation (Kameyama et al., 1999). The Peierls stress is the stress needed to move a dislocation in a crystal without the help of thermal activation. It is determined by the crystal structure and chemical bonding and hence is intrinsic to a given material. The mathematical relation between stress σ and strain rate $\dot{\epsilon}$ is exponential (eq. 2.13 in chapter 2):

$$\dot{\epsilon}_{ij}^{\text{pei}} = F_{\text{pei}} A_{\text{pei}} \exp\left[-\frac{E_{\text{pei}}}{RT}(1 - \gamma)^{n_{\text{pei}}}\right] \left(\frac{\tau_{ij}}{\gamma\sigma_{\text{pei}}}\right)^S$$

During rock deformation, several types of deformation can occur, depending on the type of material and the force applied on. For that, it is important to consider not only one deformation mechanism in a geodynamic model (Kohlstedt, 2007). In our model, we consider five deformation mechanisms: elastic and frictional-plastic deformation, and for the viscous deformation a combination of diffusion creep, dislocation creep and Peierls creep. Equations combining these different rheologies and deformation mechanisms are described in the "Mathematical Model" section in chapter 2, (equations 2.6 to 2.15).

Numerous processes occur at a subducting zone such as metamorphic reactions, fluid and melt transfer and earthquakes. They are all influenced by deformation and stress distribution. Hence, it is important to quantify stresses and deformation mechanisms to understand what is happening mechanically in a subduction zone, more precisely in the flexure of the subducting plate. We use the 2D thermo-mechanical code MDoodz, which is based on the finite difference and marker-in-cell method developed by Duretz et al. (2011b), to model a subduction zone (see chapter 2 for more details). We consider two subduction scenarios: a forced subduction where horizontal velocities are applied to the lateral boundaries of the plates during the entire simulation and a free subduction where we stop the horizontal velocities when the slab is long enough to continue the subduction itself without far-field horizontal velocities. We found that we need a slab pull of at least $1.8 \text{ TN}\cdot\text{m}^{-1}$ to continue the subduction in the free scenario. The major results of the study showed that firstly elasto-plastic deformation is the dominant mechanism in the upper region of the lithosphere and subducting slab (from ca. 5 to 60 km depth from the top of the slab) and viscous deformation dominates in the lower region of the lithosphere and in the asthenosphere. Secondly, elasticity has an important impact on the magnitude and distribution of deviatoric stress. Simulations with increased shear modulus, in order to reduce elasticity, exhibit considerably different stress fields. Thirdly, limiting absolute stress magnitudes by decreasing the internal friction angle causes slab detachment and the slab pull cannot be transmitted anymore to the plates. Using a combined visco-elasto-plastic deformation behaviour is therefore important to take into account in numerical model studies. The comparison between our modelled topography and gravity anomaly with natural data of seafloor bathymetry and free-air gravity anomalies across the Mariana trench, showed that

elasticity and deviatoric stress magnitudes of several hundreds of MPa are required to best fit the natural data. This agreement suggests that the modelled flexural behaviour and density field are compatible with natural data. In the "Discussion" section in chapter 2, we discuss potential applications of our results to the depth of faulting in a subducting plate and to the generation of petit-spot volcanoes.

1.3.2 Chapter 3: Melt migration by reactive porosity waves

The thermo-mechanical numerical model for the flexure of the oceanic plate shown in chapter 2 indicates that the transition from brittle to ductile domains happened at middle lithosphere depth (around 60 km). This conclusion calls into question the mechanism of melts extraction from the base of the lithosphere located at 80 km depth in order to explain the formation of petit-spot volcanoes, as fracture is unlikely to propagate within the ductile (i.e. viscous) domain. Various arguments suggest that magma observed in petit-spot volcanoes does not originate directly from the low-velocity zone, but first interact with the lithosphere, potentially producing metasomatic enrichment of the base of the lithosphere. The first argument comes from multiple saturation experiments from Machida et al. (2017). The figure 1.11, redrawn from Machida et al. (2017) study, shows mineral assemblages obtained for experiments performed between 1'200 to 1'320°C and pressure between 1.5 to 2.5 GPa using two distinct primitive petit-spot compositions as starting material. Multiple saturation experiments target the condition where basaltic magma is saturated in all major peridotitic phases. These experiments show that petit-spot melts are in equilibrium with olivine, orthopyroxene and clinopyroxene at relatively low temperature ($< 1'290^{\circ}\text{C}$) and pressure (< 2.1 GPa). Such P-T conditions are unlikely to represent asthenospheric conditions, but point out a last equilibration of petit-spot melt with peridotitic assemblage at 60 km deep, i.e. within the lithosphere. Machida et al. (2017) conclude that low degree melts from the base of the lithosphere rise, first, within the base of the lithosphere before to be extracted to the surface from a depth close to brittle-ductile transition zone.

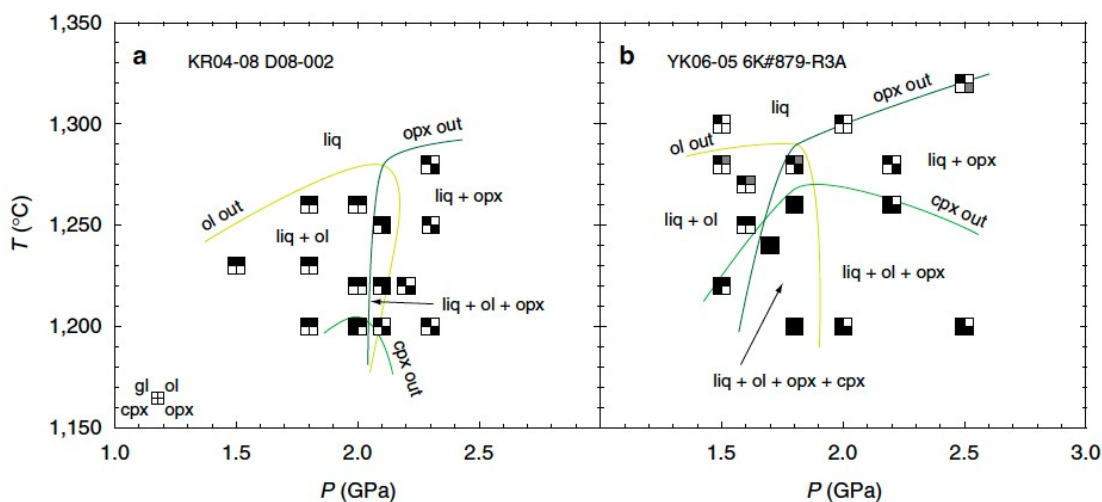


Figure 1.11: Melting phase relations of the primary petit-spot basalts determined for two estimated primitive petit-spot magma composition. Stable phases are shown by the filled squares. Figure redrawn from Machida et al. (2017).

The second arguments supporting the interaction of petit-spot melt with the lithosphere is provided by the study of mantle xenoliths sampled by petit-spot magmas (Pilet et al., 2016). Pilet et al. (2016) indicate that, if these xenoliths show mineral assemblages typical of abyssal peridotite (Figure 1.12a), element patterns of their clinopyroxene, indicated in red in figure 1.12b, are similar to the one from melt-metasomatized garnet peridotites sample by kimberlite in Kaapval craton (grey lines, Figure 1.12). As trace element patterns of clinopyroxene from Kaapval peridotites are interpreted as the percolation and interaction of low degree melt across the base of the cratonic lithosphere, similar interpretation is proposed, by Pilet et al. (2016), for the petit-spot xenoliths. The composition of petit-spot xenolith supports, therefore, a metasomatic enrichment of the pacific lithosphere before the emission of petit-spot lavas.

These different arguments suggest that petit-spot magmas are not directly extracted from the base of the lithosphere, but first rise, percolate, cool, and metasomatize the base of the lithosphere before to be extracted to the surface from mid-lithosphere depth. The chemical consequence of melt migration across the mantle has been studied theoretically (O'Hara, 1968; Navon and Stolper, 1987), and documented by various studies on mantle xenoliths and outcrops (e.g. Kelemen et al., 1992; Nielson and Noller, 1987; Wilshire, 1987; Nielson and Wilshire, 1993; Harte et al., 1993). These studies indicate that melt migration across peri-

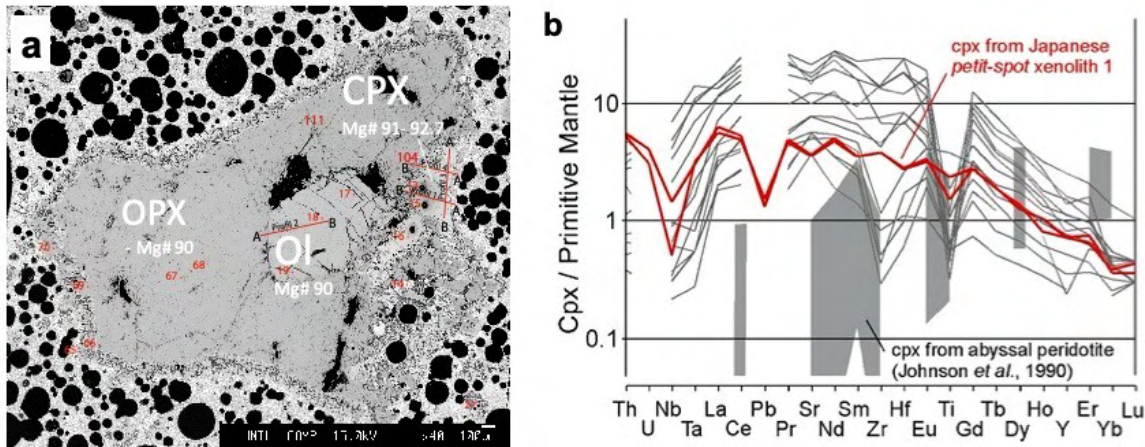


Figure 1.12: a) Backscattered electron image of xenolith from Japanese petit-spot lavas. b) Clinopyroxene composition normalized to primitive mantle for Japanese petit-spot peridotite xenolith compared to abyssal peridotite (grey areas) and melt-metasomatized garnet-peridotites from Kaapval craton (grey lines). Figure modified from Pilet et al. (2016).

dotitic matrix is partially controlled by melt-rock reaction which could modify the composition of the rising melt by dissolution or precipitation of olivine or orthopyroxene (\pm clinopyroxene) (Lambart et al., 2012; O'Hara, 1968; Pilet et al., 2008). This melt-rock reaction will depend on the composition of the rising melt and pressure and temperature condition. The implication on trace element budget of melt-rock reaction is also relatively well constrained (e.g. Lambart et al., 2012; Mallik and Dasgupta, 2012; Pilet et al., 2008). However, the mechanical aspect associated to melt percolation across the lithosphere remains mostly unconstrained. Many studies target the mechanical aspect of melt migration in the context of mid ocean ridge (e.g. Spiegelman and McKenzie, 1987; Scott and Stevenson, 1989; Aharonov et al., 1995; Kelemen et al., 1997; Katz et al., 2006), but these models neglect the thermal effect on mechanical parameters as the thermal gradient below mid ocean ridges is limited. The mechanical aspect of melt migration within the lithospheric mantle characterized by a high thermal gradient is the subject of the chapter 3 of this PhD thesis.

The generation of small volcanic edifices requires the formation of high-permeability pathways to allow the rapid extraction of low volume of melts from a deep source as low degree melt is unable to carry sufficient heat to preclude crystallization at depth (McKenzie, 1989). Melt migrations in the ductile domain is controlled by two-phase flow equations (McKenzie, 1984), while the ability of a melt to separate from the residual crystals depends on the viscosity of

the melt (e.g. McKenzie, 1985). As melt will move in the porous spaces between the grains, another important point to consider is whether our porous network is interconnected in three-dimension. A geometric relationship can be used to determine the distribution of the melt with the relative surface tension between the crystal grains and the melt. This relationship can be expressed as the dihedral angle (e.g. Watson and Brenan, 1987; Harte et al., 1993), if the angle is smaller than 60° we say that our network is connected and that the melt can disperse/propagate in our network along edge grain. Whereas if the angle is greater than 60° , the melt will remain isolated and capture in the pores. According to a compilation from Cheadle (1989) of experiments to determine this dihedral angle between melt and solid, the angles are smaller than 60° for various mantle rocks (e.g. basaltic, komatiitic or carbonatitic melts). Nevertheless, the formation of a connected network is also dependant of the homogeneity of the system and how melts are distributed.

Melt generated in heterogeneous lithological domain leads to spatial variations in melt content that may evolve into porosity waves (Jordan et al., 2018) which potentially allow melt to rise up (Connolly and Podladchikov, 1998, 2007). Melt transport by porosity waves is therefore an interesting mechanism to explain the propagation of low degree melts from the low-velocity zone across the base of the lithosphere. However, current porosity waves models do not involve the chemical effect of melt-rock reaction, neither consider the temperature effect on the viscosity of the rising melt. The development of a full thermo-hydro-mechanical-chemical (THMC) model for the extraction and the transport of melt in the ductile mantle domain is the long-term goal of the research group at Lausanne. The study presented in chapter 3 is a first step including the coupling of mechanical aspect of melt transport with thermodynamic data base allowing to calculate the chemical equilibration of basaltic magma rising into peridotitic matrix.

The motivation and the general context of this THMC numerical study is presented in the beginning of the chapter 3 designed as scientific article. We present the THMC transport model for the melt migration, which is coupled to thermodynamic results obtained from Gibbs energy minimisation, to investigate the impact of chemical differentiation on melt migration. We consider melt migration to occur by porosity waves within a deformable viscous man-

tle and use a simple ternary thermodynamic system of forsterite-fayalite-silica for the solid and melt phases. We solve the one-dimensional (1D) THMC transport model numerically with a pseudo-transient finite differenced method, a relevant and efficient method for solving nonlinear problems, and Gibbs energy minimisations with linear programming routines using MATLAB. Model variables, such as solid and melt densities or mass concentrations of MgO and SiO₂ in solid and melt, are functions of pressure (P), temperature (T) and total silica mass fraction of the system ($C_T^{\text{SiO}_2}$). These variables are pre-computed with Gibbs energy minimisation and implemented in the THMC porosity wave transport code via parameterized equations, determining the P - T - $C_T^{\text{SiO}_2}$ dependence of the model variables. We consider pressure (P) and temperature (T) conditions relevant for the base of the lithosphere and employ adiabatic and conductive geotherms. The results show that the total silica concentration and the geotherm have a strong impact on melt migration. We discuss results of a systematic series of 1D simulations to investigate the impact of the initial distribution of porosity and total silica concentration on the melt velocity and present preliminary results from a 2D reactive porosity wave model.

Bibliography

- Aharonov, E., Whitehead, J. A., Kelemen, P. B., 1995. Channeling instability of upwelling melt in the mantle. *Journal of Geophysical Research* 100 (B10), 20,433–20,450.
- Buchs, D. M., Pilet, S., Cosca, M., Flores, K. E., Bandini, A. N., Baumgartner, P. O., 2013. Low-volume intraplate volcanism in the Early/Middle Jurassic Pacific basin documented by accreted sequences in Costa Rica. *Geochemistry, Geophysics, Geosystems* 14 (5), 1552–1568.
- Cheadle, M., 1989. Properties of Texturally Equilibrated Two-phase Aggregates. Ph.D. thesis, University of Cambridge.
- Connolly, J. A. D., Podladchikov, Y. Y., 1998. Compaction-driven fluid flow in viscoelastic rock. *Geodinamica Acta* 11 (2-3), 55–84.
- Connolly, J. A. D., Podladchikov, Y. Y., 2007. Decompaction weakening and channeling instability in ductile porous media: Implications for asthenospheric melt segregation. *Journal of Geophysical Research* 112 (B10).
- Dasgupta, R., Mallik, A., Tsuno, K., Withers, A. C., Hirth, G., Hirschmann, M. M., 2013. Carbon-dioxide-rich silicate melt in the Earth's upper mantle. *Nature* 493, 211–215.
- Duretz, T., May, D. A., Gerya, T. V., Tackley, P. J., 2011b. Discretization errors and free surface stabilization in the finite difference and marker-in-cell method for applied geodynamics: A numerical study. *Geochemistry, Geophysics, Geosystems* 12 (7).
- Gripp, A. E., Gordon, R. G., 1990. Current plate velocities relative to the hotspots incorporating the NUVEL-1 global plate motion model. *Geophysical Research Letters* 17 (8), 1109–1112.
- Harte, B., Hunter, R., Kinny, P., 1993. Melt geometry, movement and crystallization, in relation to mantle dykes, veins and metasomatism. *Philosophical Transactions of the Royal Society of London. Series A: Physical and Engineering Sciences* 342 (1663), 1–21.

- Hirano, N., Kawamura, K., Hattori, M., Saito, K., Ogawa, Y., 2001. A new type of intra-plate volcanism; Young alkali-basalts discovered from the subducting Pacific Plate, Northern Japan Trench. *Geophysical Research Letters* 28 (14), 2719–2722.
- Hirano, N., Koppers, A. A. P., Takahashi, A., Fujiwara, T., Nakanishi, M., 2008. Seamounts, knolls and petit-spot monogenetic volcanoes on the subducting Pacific Plate. *Basin Research* 20 (4), 543–553.
- Hirano, N., Machida, S., Abe, N., Morishita, T., Tamura, A., Arai, S., 2013. Petit-spot lava fields off the central Chile trench induced by plate flexure. *Geochemical Journal* 47 (2), 249–257.
- Hirano, N., Takahashi, E., Yamamoto, J., Abe, N., Ingle, S. P., Kaneoka, I., Hirata, T., Kimura, J.-I., Ishii, T., Ogawa, Y., Machida, S., Suyehiro, K., 2006. Volcanism in Response to Plate Flexure. *Science, New Series* 313 (5792), 1426–1428.
- Hirschmann, M. M., 2010. Partial melt in the oceanic low velocity zone. *Physics of the Earth and Planetary Interiors* 179 (1-2), 60–71.
- Hirth, G., Kohlstedt, D., 2003. Rheology of the upper mantle and the mantle wedge: A view from the experimentalists. *Washington DC American Geophysical Union Geophysical Monograph Series* 138, 83–105.
- Jordan, J. S., Hesse, M. A., Rudge, J. F., 2018. On mass transport in porosity waves. *Earth and Planetary Science Letters* 485, 65–78.
- Kameyama, M., Yuen, D. A., Karato, S.-I., 1999. Thermal-mechanical effects of low-temperature plasticity (the Peierls mechanism) on the deformation of a viscoelastic shear zone. *Earth and Planetary Science Letters* 168 (1-2), 159–172.
- Karato, S.-i., 2008. *Deformation of Earth Materials: An Introduction to the Rheology of Solid Earth*. Cambridge University Press, Cambridge.
- Katz, R. F., Spiegelman, M., Holtzman, B., 2006. The dynamics of melt and shear localization in partially molten aggregates. *Nature* 442 (7103), 676–679.

- Kawakatsu, H., Kumar, P., Takei, Y., Shinohara, M., Kanazawa, T., Araki, E., Suyehiro, K., 2009. Seismic Evidence for Sharp Lithosphere-Asthenosphere Boundaries of Oceanic Plates 324, 5.
- Kelemen, P. B., Dick, H. J. B., Quick, J. E., 1992. Formation of harzburgite by pervasive melt/rock reaction in the upper mantle. *Nature* 358 (6388), 635–641.
- Kelemen, P. B., Hirth, G., Shimizu, N., Spiegelman, M., Dick, H. J. B., 1997. A review of melt migration processes in the adiabatically upwelling mantle beneath oceanic spreading ridges. *Philosophical Transactions of the Royal Society A: Mathematical, Physical and Engineering Sciences* 355, 283–318.
- Kohlstedt, D. L., 2007. 2.14 - Properties of Rocks and Minerals – Constitutive Equations, Rheological Behavior, and Viscosity of Rocks. In: *Treatise on Geophysics*. Elsevier, Amsterdam, pp. 389–417.
- Lambart, S., Laporte, D., Provost, A., Schiano, P., 2012. Fate of Pyroxenite-derived Melts in the Peridotitic Mantle: Thermodynamic and Experimental Constraints. *Journal of Petrology* 53 (3), 451–476.
- Machida, S., Kogiso, T., Hirano, N., 2017. Petit-spot as definitive evidence for partial melting in the asthenosphere caused by CO₂. *Nature Communications* 8, 14302.
- Mallik, A., Dasgupta, R., 2012. Reaction between MORB-eclogite derived melts and fertile peridotite and generation of ocean island basalts. *Earth and Planetary Science Letters* 329-330, 97–108.
- McKenzie, D., 1984. The Generation and Compaction of Partially Molten Rock. *Journal of Petrology* 25 (3), 713–765.
- McKenzie, D., 1985. The extraction of magma from the crust and mantle. *Earth and Planetary Science Letters* 74 (1), 81–91.
- McKenzie, D., 1989. Some remarks on the movement of small melt fractions in the mantle. *Earth and Planetary Science Letters* 95 (1-2), 53–72.

- McNutt, M. K., 2006. Another Nail in the Plume Coffin? *Science* 313, 1394–1395.
- Mei, S., Suzuki, A. M., Kohlstedt, D. L., Dixon, N. A., Durham, W. B., 2010. Experimental constraints on the strength of the lithospheric mantle. *Journal of Geophysical Research* 115 (B8).
- Molnar, P., 2015. *Plate Tectonics: A Very Short Introduction*. Very Short Introductions. Oxford University Press, Oxford, New York.
- Naif, S., Key, K., Constable, S., Evans, R. L., 2013. Melt-rich channel observed at the lithosphere–asthenosphere boundary. *Nature* 495 (7441), 356–359.
- Navon, O., Stolper, E., 1987. Geochemical consequences of melt percolation: the upper mantle as a chromatographic column. *The Journal of Geology*, 23.
- Nielson, J. E., Noller, J. S., 1987. Processes of mantle metasomatism; Constraints from observations of composite peridotite xenoliths. *Geological Society of America* 215, 61–76.
- Nielson, J. E., Wilshire, H., 1993. Magma transport and metasomatism in the mantle: A critical review of current geochemical models. *American Mineralogist* 78, 1117–1134.
- O’Hara, M. J., 1968. The bearing of phase equilibria studies in synthetic and natural systems on the origin and evolution of basic and ultrabasic rocks. *Earth-Science Reviews* 4, 69–133.
- Passchier, C. W., Trouw, R. A. J., 2005. *Microtectonics*, 2nd Edition. Springer-Verlag, Berlin Heidelberg.
- Pilet, S., Abe, N., Rochat, L., Kaczmarek, M.-A., Hirano, N., Machida, S., Buchs, D. M., Baumgartner, P. O., Müntener, O., 2016. Pre-subduction metasomatic enrichment of the oceanic lithosphere induced by plate flexure. *Nature Geoscience* 9 (12), 898–903.
- Pilet, S., Baker, M. B., Stolper, E. M., 2008. Metasomatized Lithosphere and the Origin of Alkaline Lavas. *Science* 320 (5878), 916–919.

- Sato, Y., Hirano, N., Machida, S., Yamamoto, J., Nakanishi, M., Ishii, T., Taki, A., Yasukawa, K., Kato, Y., 2017. Direct ascent to the surface of asthenospheric magma in a region of convex lithospheric flexure. *International Geology Review* 60 (10), 1231–1243.
- Scott, D. R., Stevenson, D. J., 1989. A self-consistent model of melting, magma migration and buoyancy-driven circulation beneath mid-ocean ridges. *Journal of Geophysical Research: Solid Earth* 94 (B3), 2973–2988.
- Spiegelman, M., McKenzie, D., 1987. Simple 2-D models for melt extraction at mid-ocean ridges and island arcs. *Earth and Planetary Science Letters* 83 (1), 137–152.
- Stern, T. A., Henrys, S. A., Okaya, D., Louie, J. N., Savage, M. K., Lamb, S., Sato, H., Sutherland, R., Iwasaki, T., 2015. A seismic reflection image for the base of a tectonic plate. *Nature* 518 (7537), 85–88.
- Taneja, R., O'Neill, C., Lackie, M., Rushmer, T., Schmidt, P., Jourdan, F., 2015. $^{40}\text{Ar}/^{39}\text{Ar}$ geochronology and the paleoposition of Christmas Island (Australia), Northeast Indian Ocean. *Gondwana Research* 28 (1), 391–406.
- Turcotte, D., Schubert, G., 2014. *Geodynamics*, 3rd Edition. Cambridge, UK: Cambridge University Press.
- Watson, Bruce, E., Brenan, J. M., 1987. Fluids in the lithosphere, 1. Experimentally-determined wetting characteristics of $\text{CO}_2\text{H}_2\text{O}$ fluids and their implications for fluid transport, host-rock physical properties, and fluid inclusion formation. *Earth and Planetary Science Letters* 85 (4), 497–515.
- Wilshire, H., 1987. A model of mantle metasomatism. *Mantle Metasomatism and Alkaline Magmatism*. Geological Society of America, Special Papers 215, 47–60.
- Yamamoto, J., Korenaga, J., Hirano, N., Kagi, H., 2014. Melt-rich lithosphere-asthenosphere boundary inferred from petit-spot volcanoes. *Geology* 42 (11), 967–970.

CHAPTER 2

Stress and deformation mechanisms at a subduction zone: insights from
2-D thermomechanical numerical modelling

**Annelore Bessat¹, Thibault Duretz^{2,1}, György Hetényi¹, Sébastien Pilet¹ and
Stefan M. Schmalholz¹**

¹Institute of Earth Sciences, University of Lausanne, 1015 Lausanne, Switzerland.

²Univ Rennes, CNRS, Géosciences Rennes - UMR 6118, F-35000 Rennes, France.

Summary

Numerous processes such as metamorphic reactions, fluid and melt transfer and earthquakes occur at a subducting zone, but are still incompletely understood. These processes are affected, or even controlled, by the magnitude and distribution of stress and deformation mechanism. To eventually understand subduction zone processes, we quantify here stresses and deformation mechanisms in and around a subducting lithosphere, surrounded by asthenosphere and overlain by an overriding plate. We use two-dimensional thermo-mechanical numerical simulations based on the finite difference and marker-in-cell method and consider a 3200 km wide and 660 km deep numerical domain with a resolution of 1 km by 1 km. We apply a combined visco-elasto-plastic deformation behaviour using a linear combination of diffusion creep, dislocation creep and Peierls creep for the viscous deformation. We consider two end-member subduction scenarios: forced and free subduction. In the forced scenario, horizontal velocities are applied to the lateral boundaries of the plates during the entire simulation. In the free scenario, we set the horizontal boundary velocities to zero once the subducted slab is long enough to generate a slab pull force large enough to maintain subduction without horizontal boundary velocities. A slab pull of at least $1.8 \text{ TN}\cdot\text{m}^{-1}$ is required to continue subduction in the free scenario. We also quantify along-profile variations of gravitational potential energy (GPE). We evaluate the contributions of topography and density variations to GPE variations across a subduction system. The GPE variations indicate large-scale horizontal compressive forces around the trench region and extension forces on both sides of the trench region. Corresponding vertically-averaged differential stresses are between 120 and 170 MPa. Furthermore, we calculate the distribution of the dominant deformation mechanisms. Elasto-plastic deformation is the dominant mechanism in the upper region of the lithosphere and subducting slab (from ca. 5 to 60 km depth from the top of the slab). Viscous deformation dominates in the lower region of the lithosphere and in the asthenosphere. Considering elasticity in the calculations has an important impact on the magnitude and distribution of deviatoric stress; hence, simulations with increased shear modulus, in order to reduce elasticity, exhibit considerably different stress fields. Limiting absolute stress magnitudes by decreasing the internal

friction angle causes slab detachment so that slab pull cannot be transmitted anymore to the horizontal lithosphere. Applying different boundary conditions shows that forced subduction simulations are stronger affected by the applied boundary conditions than free subduction simulations. We also compare our modelled topography and gravity anomaly with natural data of seafloor bathymetry and free-air gravity anomalies across the Mariana trench. Elasticity and deviatoric stress magnitudes of several hundreds of MPa are required to best fit the natural data. This agreement suggests that the modelled flexural behaviour and density field are compatible with natural data. Moreover, we discuss potential applications of our results to the depth of faulting in a subducting plate and to the generation of petit-spot volcanoes.

Keywords

Numerical modelling; Subduction zone processes; Lithospheric flexure; Rheology: mantle; Dynamics: gravity and tectonics

2.1 Introduction

Subduction zones are critical locations on Earth where the oceanic lithosphere dives into the convecting mantle and, hence, contributes to the cooling of the Earth and to the recycling of rocks and water (e.g. Stern, 2002; Turcotte and Schubert, 2014; Cramer et al., 2019). Many geophysical and geochemical processes are related to subduction zones, such as hydration of the mantle wedge and associated melt generation related to arc magmatism (e.g. Plümper et al., 2016), major earthquakes observed at different depths in the subducting slab and at megathrusts (e.g. Youngs et al., 1997), water transport in subducting slabs along faults (e.g. Faccenda et al., 2009) or the generation of petit-spot volcanoes, which might be associated with plate flexure around subduction zones (Hirano et al., 2006; Yamamoto et al., 2014). However, many of these processes are still incompletely understood. Processes inside and around subducting plates are, to a larger or smaller extent, controlled by the magnitude and the type of stress (extensive, compressive or shear) and by the dominant deformation mechanism

(elastic, frictional-plastic or viscous). Since it is not possible to study stress and deformation mechanisms around subduction zones in situ, indirect approaches like geophysical imaging (e.g. Kearey et al., 2009) and numerical modelling in two-dimensions (2D) (e.g. Gurnis et al., 2004; Yamato et al., 2007; Schmeling et al., 2008; Gerya, 2011) and 3D (e.g. Schellart et al., 2007; Yamato et al., 2009; Duretz et al., 2014) are frequently used to study subduction systems. Numerical models are suitable to quantify the magnitude of stress and the associated distribution of deformation mechanisms for subduction systems (e.g. Čížková et al., 2007; Garel et al., 2014). A better understanding of the magnitude of stress, their distribution and their associated dominant deformation mechanisms in subduction systems might ultimately help us to understand subduction-related geophysical and geochemical processes.

The main aim of this study is to quantify stresses and to determine the distribution of stress and dominant deformation mechanism around flexural regions in a subducting plate. Although there are numerous studies of numerical subduction simulations, only few numerical models quantified the distribution of stress (e.g. Hassani et al., 1997; Funicello et al., 2003; Sobolev et al., 2006; Čížková et al., 2007; Babeyko and Sobolev, 2008; Farrington et al., 2014; Holt et al., 2015) and deformation mechanisms (e.g. Čížková et al., 2007; Garel et al., 2014). Like all models, they have limitations in their hypotheses, such as neglecting elastic deformation (e.g. Čížková et al., 2007; Chertova et al., 2012; Garel et al., 2014; Holt et al., 2015), no or only one creep deformation mechanism (e.g. Hassani et al., 1997; Funicello et al., 2003; Farrington et al., 2014), a prescribed slab geometry (e.g. Sobolev et al., 2006; Babeyko and Sobolev, 2008), no free surface boundary condition (e.g. Čížková et al., 2007; Holt et al., 2015) or a yield stress being a function of depth only (e.g. Čížková et al., 2007; Garel et al., 2014) and not a function of the total pressure (negative mean stress). Here, we build on the above mentioned models, but without the mentioned limitations with the aim to make a step further in calculating stress and dominant deformation mechanisms at subduction systems. We apply a high-resolution (1 km grid spacing) 2D thermo-mechanical numerical model of the lithosphere-asthenosphere system and we consider five deformation mechanisms: elastic, frictional-plastic (Mohr-Coulomb criterion), diffusion creep, dislocation creep and Peierls creep. We apply a local iteration strategy to correctly calculate the partitioning of the strain

rate between these five deformation mechanisms, because calculations without such iterations overestimate the calculated stress (Schmalholz and Duretz, 2017). Furthermore, we consider two subduction scenarios, which represent two end-member conditions with respect to the forces driving subduction: (1) forced subduction whereby the subducting plate is pushed by far-field horizontal velocity (e.g., by ridge push), and (2) free subduction whereby subduction is driven only by the negative buoyancy of the subducting plate itself (slab pull). We initiate free subduction by forced subduction but set the far-field velocity to zero once slab pull is large enough to drive free subduction. We quantify the required minimum slab pull force to drive free subduction for our model configuration. We also quantify along-profile variations of gravitational potential energy (e.g. Molnar and Lyon-Caen, 1988; Molnar et al., 1993; Schmalholz et al., 2014, 2019) across the subduction system, because these GPE variations cause horizontal forces and, hence, stresses. We also investigate whether differentiating criteria between forced and free subduction exist and what these criteria are. Furthermore, we evaluate the impact of elasticity and yield stress on the deformation and stress field around subduction zones. We do not configure our model to fit a particular subduction system, but in order to evaluate whether the modelled subductions are applicable to natural subduction zones, we finally compare the modelled topography and gravity anomalies with natural data from the Mariana subduction zone, which is a type-example for an ocean-ocean subduction system and has often been used for comparison with theoretical models (e.g. Funicello et al., 2003; Turcotte and Schubert, 2014).

2.2 Mathematical model

2.2.1 Governing equations for numerical simulations

We use the 2D thermo-mechanical code MDoodz, which is based on the finite difference and marker-in-cell method (e.g. Duretz et al., 2011b; Gerya, 2019). The steady-state force balance equation is

$$\frac{\partial \sigma_{ij}}{\partial x_j} + \rho g_i = 0 \quad (2.1)$$

where i and j run from 1 to 2, 1 indicates horizontal and 2 vertical dimension, σ_{ij} are the components of the total stress tensor, x_j represents the spatial coordinates, ρ is the density and $g_i = [0, -g]$ is the gravitational acceleration vector with g being the gravitational acceleration. The conservation of mass for incompressible material is

$$\frac{\partial v_i}{\partial x_j} = 0 \quad (2.2)$$

where v_i are the components of the velocity vector. The temperature evolution equation is

$$\rho c \frac{dT}{dt} = \frac{\partial}{\partial x_i} \left(k \frac{\partial T}{\partial x_i} \right) + H_D + H_R \quad (2.3)$$

where d/dt represents the total time derivative, c the specific heat, k the thermal conductivity, H_R the radiogenic heat production and H_D the heating due to viscous and plastic dissipative work (here we assume that all dissipative work is converted into heat, i.e., Taylor-Quinney coefficient is 1, since we do not model grain size reduction). The density is calculated with the following equation of state:

$$\rho = \rho_0 [1 + \beta(P - P_0)] \cdot [1 - \alpha(T - T_0)] \quad (2.4)$$

where ρ_0 is the reference density at a reference pressure P_0 and temperature T_0 , P is the pressure (negative mean stress), T is the temperature, α is the thermal expansion and β is the compressibility. The components of the total stress tensor are

$$\sigma_{ij} = -P\delta_{ij} + \tau_{ij} \quad (2.5)$$

where δ_{ij} is the Kronecker delta ($\delta_{ij} = 1$ when $i = j$ and $\delta_{ij} = 0$ when $i \neq j$) and τ_{ij} are the components of the deviatoric stress tensor. We consider a visco-elasto-plastic rheology described by a Maxwell model (Moresi et al., 2003; Popov and Sobolev, 2008):

$$\dot{\varepsilon}_{ij} = \dot{\varepsilon}_{ij}^{\text{vis}} + \dot{\varepsilon}_{ij}^{\text{el}} + \dot{\varepsilon}_{ij}^{\text{pl}} = \frac{1}{2\eta}\tau_{ij} + \frac{1}{2G}\frac{D\tau_{ij}}{Dt} + \dot{\gamma}\frac{\partial Q}{\partial\tau_{ij}} \quad (2.6)$$

where superscripts $\dot{\varepsilon}_{ij}^{\text{vis}}$, $\dot{\varepsilon}_{ij}^{\text{el}}$ and $\dot{\varepsilon}_{ij}^{\text{pl}}$ indicate viscous, elastic and plastic deviatoric strain rate tensors, respectively. The quantity η represents the effective viscosity, G is the shear modulus, t is the time, D/Dt indicates the objective time derivative (e.g. Schmalholz et al., 2001), Q is the plastic flow potential and $\dot{\gamma}$ is a plastic multiplier rate. Frictional-plastic yielding is described by a Drucker-Prager criterion with the yield stress, τ_{yield}

$$\tau_{\text{yield}} = C \cos(\Theta) + P \sin(\Theta) \quad (2.7)$$

where C is the cohesion and Θ is the angle of internal friction. The yield function, F , is expressed as $F = \tau_{\text{II}} - \tau_{\text{yield}}$ and the plastic potential is formulated as $Q = \tau_{\text{II}}$, being the square root of the second invariant of the deviatoric stress tensor. Plastic deformation occurs whenever $F \geq 0$. The plastic multiplier rate is computed as $\dot{\gamma} = 2\dot{\varepsilon}_{\text{II}} - \frac{\tau_{\text{yield}} - \tau_{\text{II}}^{\text{old}}}{Gdt} + \frac{\tau_{\text{yield}}}{\eta}$ or simply $\dot{\gamma} = \frac{F}{\eta^{\text{ve}}}$, where $\eta^{\text{ve}} = (\frac{1}{\eta} + \frac{1}{Gdt})^{-1}$, τ_{ij}^{old} are advected and rotated stress components from the previous time step and dt is the time step. Subsequently, the plastic strain rate tensor is evaluated as $\dot{\varepsilon}_{ij}^{\text{pl}} = \dot{\gamma}\frac{\partial Q}{\partial\tau_{ij}} = \dot{\gamma}\frac{\tau_{ij}}{2\tau_{\text{II}}}$. In practice, the stress state is mapped back onto the yield surface by modifying the effective viscosity as

$$\eta = \eta^{\text{pl}} = \frac{\tau_{\text{yield}}}{2\dot{\varepsilon}_{\text{II}}^{\text{eff}}} \quad (2.8)$$

where $\dot{\varepsilon}_{\text{II}}^{\text{eff}}$ is the square root of the second invariant of the effective strain rate tensor, defined as

$$\dot{\varepsilon}_{ij}^{\text{eff}} = \dot{\varepsilon}_{ij} + \frac{\tau_{ij}^{\text{old}}}{2Gdt} \quad (2.9)$$

The viscous deformation is a linear combination of flow laws for diffusion creep (Hirth and Kohlstedt, 2003), dislocation creep (Hirth and Kohlstedt, 2003) and Peierls creep (Kameyama et al., 1999):

$$\dot{\varepsilon}_{ij}^{\text{vis}} = \dot{\varepsilon}_{ij}^{\text{dif}} + \dot{\varepsilon}_{ij}^{\text{dis}} + \dot{\varepsilon}_{ij}^{\text{pei}} \quad (2.10)$$

Diffusion creep (i.e. linear creep) is given by

$$\dot{\varepsilon}_{ij}^{\text{dif}} = F_{\text{dif}} A_{\text{dif}} \tau_{ij}^{n_{\text{dif}}} d^{-m_{\text{dif}}} \exp\left(-\frac{E_{\text{dif}}^* + PV_{\text{dif}}^*}{RT}\right) \quad (2.11)$$

Dislocation creep (i.e. power law creep) is given by

$$\dot{\varepsilon}_{ij}^{\text{dis}} = F_{\text{dis}} A_{\text{dis}} \tau_{ij}^{n_{\text{dis}}} d^{-m_{\text{dis}}} \exp\left(-\frac{E_{\text{dis}}^* + PV_{\text{dis}}^*}{RT}\right) \quad (2.12)$$

Peierls creep (i.e. low-temperature plasticity or exponential creep) is given by

$$\dot{\varepsilon}_{ij}^{\text{pei}} = F_{\text{pei}} A_{\text{pei}} \exp\left[-\frac{E_{\text{pei}}}{RT}(1 - \gamma)^{n_{\text{pei}}}\right] \left(\frac{\tau_{ij}}{\gamma\sigma_{\text{pei}}}\right)^S \quad (2.13)$$

with

$$S = \frac{E_{\text{pei}}}{RT} (1 - \gamma)^{(n_{\text{pei}}-1)} n_{\text{pei}} \gamma \quad (2.14)$$

In the above flow laws, F is a transformation factor to transform flow laws fitted from rock deformation data to flow laws for tensor components (e.g. Schmalholz and Fletcher, 2011; Gerya, 2019), A is a material constant determined from laboratory measurements, n is the stress exponent, d is the grain size, m is the grain size exponent, E is the activation energy, V is the activation volume, R is the gas constant, γ is an adjustable constant (Kameyama et al., 1999) and σ_{pei} is the Peierls stress (see values in Table 2.1).

Due to the occurrence of non-Newtonian creep mechanisms, eq. 2.6 is generally non-linear. We thus employ a local iteration method (Popov and Sobolev, 2008; Schmalholz and Duretz,

Table 2.1: Parameters used in the numerical simulations for the plastic and viscous rheology, namely dislocation creep, diffusion creep and Peierls creep. Parameters used for dry dislocation and dry diffusion mechanisms are from Hirth and Kohlstedt (2003). Parameters used for Peierls creep are from Kameyama et al. (1999).

Adopted values of rheological and physical parameters					
Viscous rheology		Lithosphere, Asthenosphere and Weak zone and weak hydrated crust			
		Dislocation	Diffusion	Peierls	Units
F	invariant formulation correction factor	$1/6 \cdot 2^{(1/n) \cdot 3(n-1/2n)}$	$1/6 \cdot 2^{(1/n) \cdot 3(n-1/2n)}$	$1/6 \cdot 2^{(1/S) \cdot 3(S-1/2S)}$	-
A	pre-exponential constant	$1.1 \cdot 10^{-16}$	$1.5 \cdot 10^{-15}$	$5.7 \cdot 10^{11}$	$[\text{s}^{-1} \cdot \text{Pa}^{-n} \cdot \text{m}^m]$
n	stress exponent	3.5	1	2	-
m	grain size exponent	0	3	-	-
E	activation energy	$530 \cdot 10^3$	$375 \cdot 10^3$	$5.4 \cdot 10^5$	$[\text{J} \cdot \text{mol}^{-1}]$
V	activation volume	$11 \cdot 10^{-6}$	$4 \cdot 10^{-6}$	0	$[\text{m}^3 \cdot \text{mol}^{-1}]$
γ	adjustable constant	-	-	0.1	-
σ_{pei}	the Peierls stress	-	-	$8.5 \cdot 10^9$	$[\text{Pa}]$
Plastic rheology		Lithosphere	Asthenosphere	Weak zone / Sediments	Units
C	cohesion	$1 \cdot 10^7$	$1 \cdot 10^6$	$1 \cdot 10^6$	$[\text{Pa}]$
Θ	Angle of internal friction	30	5	0	$[\text{°}]$
Constants					Units
R	universal gas constant	8.31			$[\text{J} \cdot \text{mol}^{-1} \cdot \text{K}^{-1}]$
α	thermal expansion	$8 \cdot 10^{-6}$			$[\text{K}^{-1}]$
β	compressibility	$1 \cdot 10^{-11}$			$[\text{Pa}^{-1}]$
d	grain size	$5 \cdot 10^{-3}$			$[\text{m}]$
H_{R}	radiogenic heat production	$1 \cdot 10^{-10}$			$[\text{W} \cdot \text{m}^{-3}]$
G	shear modulus	$3 \cdot 10^{10}$			$[\text{Pa}]$
g	gravity	9.81			$[\text{m} \cdot \text{s}^{-2}]$

2017) that ensures correct additive decomposition of the strain rate tensor and computation of stress tensor. The resulting effective viscosity for dissipative deformation mechanism is equal to the pseudo-harmonic mean of the viscosities of each dissipative deformation mechanism:

$$\eta = \left(\frac{1}{\eta^{\text{dis}}} + \frac{1}{\eta^{\text{dif}}} + \frac{1}{\eta^{\text{pei}}} + \frac{1}{\eta^{\text{pl}}} \right)^{-1} \quad (2.15)$$

where η^{dis} , η^{dif} , η^{pei} and η^{pl} are the effective viscosities calculated with the corresponding second invariant of strain rate tensor for each deformation mechanism for the viscous and the plastic deformations. In the performed simulations, we apply a minimum cut-off of the viscosity at 10^{19} Pa·s and a maximum cut-off at 10^{25} Pa·s, allowing for viscosities in the models with six orders of magnitude difference.

The applied method allows to calculate iteratively the individual strain rates of each deformation mechanism at a given temperature and total strain rate. Figures 2.1a-d shows the individual strain rates of each dissipative deformation mechanism, a) dislocation, b) diffusion, c) Peierls creep and d) frictional-plasticity in a temperature versus total strain rate space. We perform these calculations for a temperature range of 300-1'800°C and a total strain rate ranging from 10^5 to 10^{-50} s⁻¹ assuming a constant pressure of 1 GPa. Several mechanisms can be active simultaneously (Fig. 2.1). For illustrative purposes, we apply here a stress of 500 MPa to indicate the limit between the frictional-plastic and viscous domains. In the 2D numerical simulations, the plastic yield stress is pressure-sensitive and varies in space and time. To visualize the dominant deformation mechanism, we compare at each point in the strain rate versus temperature domain the four individual strain rates and identify which mechanism provides the highest strain rate. The mechanism associated with the largest strain rate is the dominant mechanism, as shown in the dominant deformation mechanism map displayed in Figure 2.1e. Diffusion creep is the dominant mechanism at high temperatures for low strain rates (in orange). Dislocation creep is dominant at high temperatures and higher strain rates (in red). Peierls creep is dominant at low temperature and moderate strain rates (in dark blue) and the plastic domain is dominant at low temperature and high strain rates (in light blue).

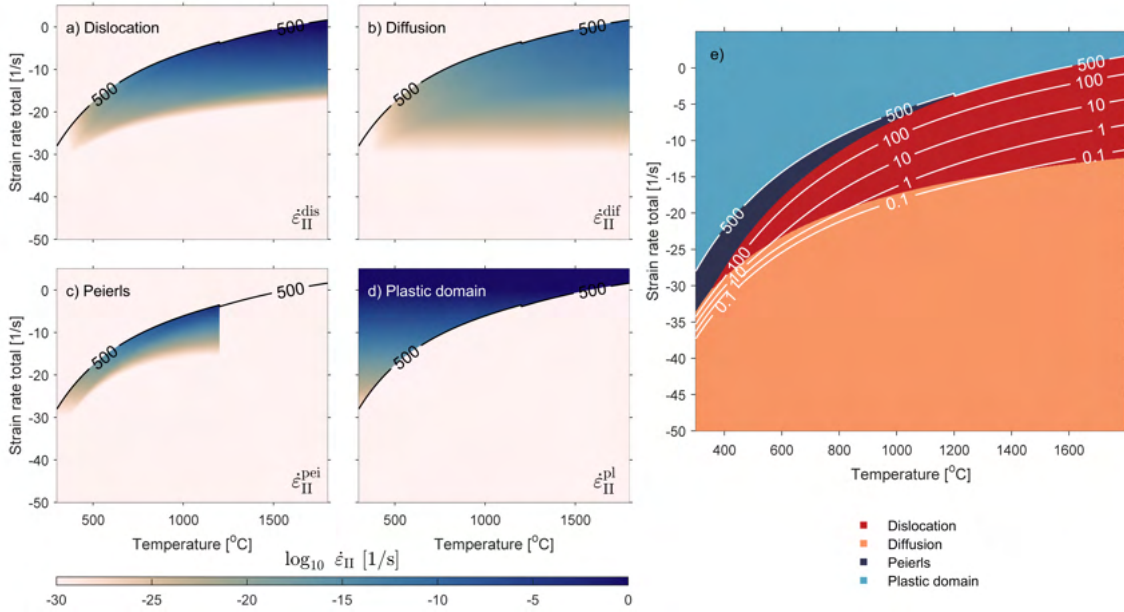


Figure 2.1: Individual strain rates of dissipative deformation mechanisms for (a) dislocation creep, (b) diffusion creep, (c) Peierls creep and (d) plastic deformation as function of temperature and total strain rate for the applied rheology of the mantle. In panels (a-d), the highest individual strain rates for each deformation mechanism are shown in dark blue, while the slower are in light beige. Calculations made at a pressure of 1 GPa with a grain size of 5 mm. The panel (e) shows the corresponding dominant deformation mechanism map as identified by the legend. The black and white curves are lines of constant stresses with label values in MPa. For illustrative purposes a brittle-plastic yield stress of 500 MPa is assumed.

2.2.2 Calculation of slab pull and gravitational potential energy

We quantify two types of forces around subduction zones, one resulting from slab pull force and one resulting from spatial variations of the gravitational potential energy.

We calculate the slab pull force (per unit length) through time with the following integral for a specific time step (approximated by a sum for the numerical calculation):

$$\vec{F}_{SP} = \int_{H_{Sb}}^{H_{LAB}} \Delta\rho g dV \approx \sum \Delta\rho g dx dz n^{\text{lith}} \quad (2.16)$$

where $\Delta\rho$ is the density difference between the density at each point (either the density of the lithosphere or the density of the asthenosphere) and the reference density depth profile on the left side of the model, and dx and dz are the numerical grid spacings, respectively.

We calculate the slab pull only in the asthenosphere, between the bottom of the model (H_{Sb}) and the initial depth of the lithosphere–asthenosphere–boundary (H_{LAB}). We consider only numerical cells that include lithospheric material for the calculation of the slab pull force by using the integer n^{lith} , which is 1 for cells including lithospheric material and 0 otherwise.

The gravitational potential energy per unit area (GPE) corresponds to the depth-integrated lithostatic pressure $P_{\text{L}} \text{ Nm}^{-2}$, which is calculated as

$$P_{\text{L}}(x, z) = \int_z^{St(x)} \rho(x, z') g dz' \quad (2.17)$$

The GPE is then

$$GPE(x) = \int_{Sb}^{St(x)} P_{\text{L}}(x, z) dz + const \quad (2.18)$$

where $St(x)$ is the topography of the model which can vary in the horizontal (x) direction, z is the depth and Sb is the base of the model (for details see Schmalholz et al., 2014). To calculate the topography in our simulations, we apply a numerical algorithm, which includes an Eulerian-Lagrangian free surface implementation, which allows resolving topographic variations at the sub-grid level (Duretz et al., 2016).

The along-profile variation of GPE, ΔGPE , is calculated by subtracting a reference GPE value from all other values. We choose here the GPE value on the left model side as reference value. Along-profile variation of ΔGPE can be due to a horizontal variation of density or a variation of the topography. The ΔGPE provides an estimate for the horizontal driving force per unit length (e.g. Molnar and Lyon-Caen, 1988; Schmalholz et al., 2014, 2019) in the subduction system associated to the density variation at depth due to subduction and to the associated spatial variation of topography. Regions with a negative ΔGPE are under compression and regions with a positive ΔGPE are under extension.

2.3 Model configuration

2.3.1 Configuration of the thermo-mechanical models

The size of the model domain is 3'200 km in width and 660 km in height with a numerical resolution of 1 km by 1 km, yielding 2.112 million cells. The time step is calculated according to a Courant criterion of 0.4 in the model. We fixed the initial thickness of the lithosphere to 80 km following the seismic study from Kawakatsu et al. (2009) which localized the lithosphere-asthenosphere-boundary (LAB) at this depth for the Pacific lithosphere subducting below Japan. A 5 km thick layer of weak material (cohesion of $1 \cdot 10^6$ Pa and internal friction angle of 0° ; see Table 2.1) is placed on the top of the lithosphere to mimic weak hydrated crust (Cramer et al., 2012). The main aim of this modelling study is to quantify stresses and determine dominant deformation mechanisms in flexural lithospheric regions. Therefore, we apply a simple density and temperature model for the sub-lithospheric region. Initially, the temperature of the asthenospheric mantle (T_{ast}) is homogeneous and for simplicity fixed at $1'450^\circ\text{C}$. For the temperature of the lithospheric mantle, we consider also for simplicity a linear gradient from 0°C at the surface to the temperature of the asthenospheric mantle (T_{ast}) at the LAB (80 km depth). The initiation of subduction was facilitated by prescribing an oblique weak zone with an initial thickness of 10 km in the horizontal middle of the model (Fig. 2.2b). The weak zone is characterized by a low plastic strength (see eq. 2.7 and Table 2.1) and has the same properties as the weak upper layer.

We use dry olivine for the viscous flow laws of the lithosphere and asthenosphere with the rheological parameters reported in Table 2.1 (Hirth and Kohlstedt, 2003; Goetze and Evans, 1979 regularized by Kameyama et al., 1999). We employ the dry olivine flow law because the weaker wet olivine is commonly too weak in numerical subduction models and does not generate a coherent slab, but rather generates the dripping of the mantle lithosphere (e.g. Burov, 2010).

We consider two end-member subduction configurations to compare the stress and deformation mechanism in forced and free subduction models. In the forced subduction model, subduction is driven by a horizontal velocity acting at the sides of the lithosphere. Therefore,

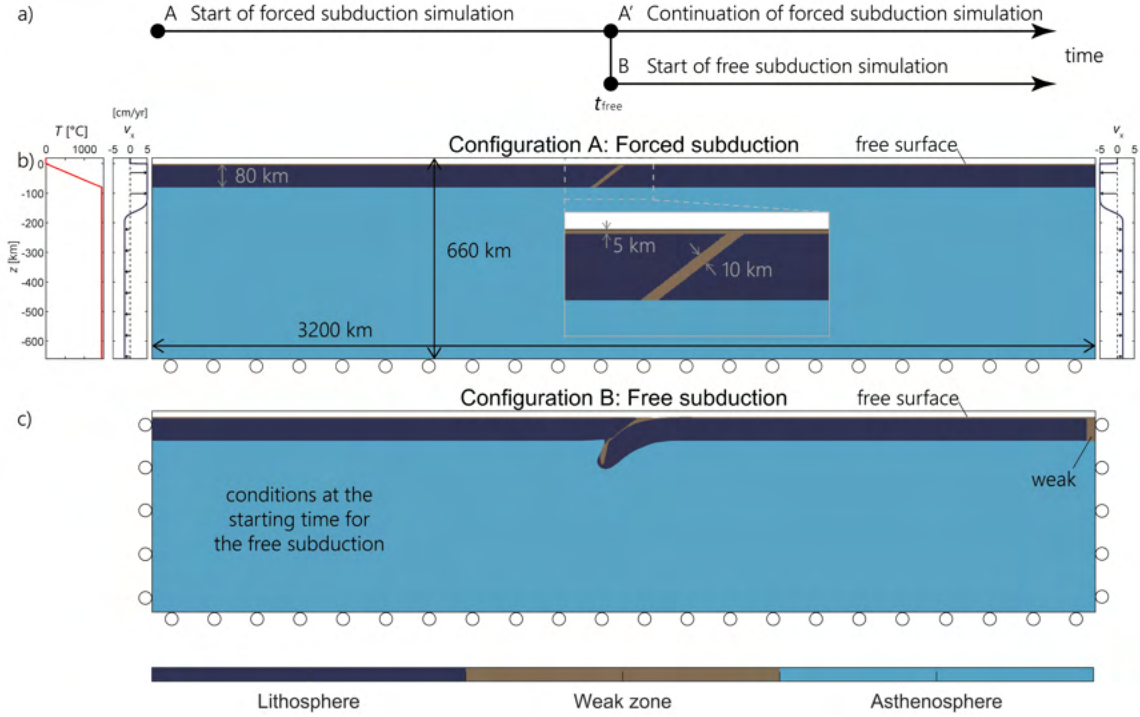


Figure 2.2: Panel (a) shows the time-line sketch of our simulations. Panels (b) and (c) show the model configurations (b) for the forced subduction and (c) for the free subduction. Dark blue areas indicate the lithosphere. Brown areas indicate the initial weak zone. Light blue areas indicate the asthenosphere. Weak domain's size in panel (c) is 30 km.

the slab velocity is controlled by the applied boundary velocity. In contrast, subduction is only driven by the negative buoyancy of the dense lithosphere in a free subduction model. Therefore, the slab velocity can evolve freely and is controlled by the interaction of buoyancy, flexural and viscous resistance stresses in and around the slab. In the forced subduction model, we apply a symmetrical horizontal velocity on the lithosphere at both sides of the model (Fig. 2.2b). We choose symmetrical boundary conditions (Chertova et al., 2012) to have a straight slab as imaged in Japan with tomography (Liu and Zhao, 2016). The total convergence velocity is $10 \text{ cm}\cdot\text{yr}^{-1}$, as observed in Japan for the Pacific plate (Gripp and Gordon, 1990). These velocity profiles are implemented by specifying a material in-flux in the top part of the model sides until a depth of twice the thickness of the lithosphere. To ensure conservation of the mass, an equivalent out-flux is applied in the lower part of the model sides (Fig. 2.2b). For the boundary conditions, we use free slip at the model bottom and specific velocity profiles at the left and right model sides (Fig. 2.2b). At the top of the crust

we use a free surface boundary condition (Duretz et al., 2016, Fig. 2.2b), because previous numerical studies show that the surface topography is controlled by the geometry, rheology and density of the slab (e.g. Zhong and Gurnis, 1994) and that a free surface condition is required to calculate realistic stresses in subducting slabs (Crameri et al., 2017).

For our model configuration (Fig. 2.2b), subduction will not initiate without horizontal boundary velocities, because there is initially no slab and, hence, no slab pull. Therefore, we initiate subduction in all the simulations with a weak zone in the lithosphere and with external velocities compressing the lithosphere (e.g. Toth and Gurnis, 1998). This model scenario is comparable to the compression-induced mode according to the classification of subduction initiation modes of Stern and Gerya (2018). To initiate free subduction, we first impose boundary velocities and then set the boundary velocities to zero once the slab is large enough to drive subduction without imposed boundary velocities. To constrain the moment when slab pull forces are sufficient to drive subduction, we perform several simulations in which we set the boundary velocities to zero after different simulation times (Fig. 2.2c), implying the absence of material flux across lateral boundaries. We also include a weak domain (30 km thick) adjacent to right model boundary, which decouples the lithosphere from the lateral boundary and avoids prescribing a slab-retreat dominated subduction (Fig. 2.2c). To determine the conditions required for free subduction development, we start the model with forced subduction, save the configuration at different times (Fig. 2.2a) and then use the saved configurations in the free subduction model to evaluate whether subduction continues or not. To test the impact of the applied boundary conditions, we also performed two simulations with different boundary conditions: one forced subduction simulation for which the horizontal velocity is only applied at the right model side and one free subduction simulation for which we add a weak zone at both lateral model sides. An overview of the performed simulations is given in Table 2.2.

Table 2.2: The main model differences of the nine simulations performed for this study.

Simulations	Type	t_{free}	Elasticity	Friction angle Lithosphere	Boundary velocity	Boundary weak zone
S0 (Ref)	forced	-	yes, $G = 3 \cdot 10^{10}$	30°	both sides	none
S1	free	1.25 Ma	yes, $G = 3 \cdot 10^{10}$	30°	none	right side
S2	free	1.17 Ma	yes, $G = 3 \cdot 10^{10}$	30°	none	right side
S3	forced	-	yes, $G = 3 \cdot 10^{12}$	30°	both sides	none
S4	forced	-	yes, $G = 3 \cdot 10^{13}$	30°	both sides	none
S5	forced	-	yes, $G = 3 \cdot 10^{10}$	5°	both sides	none
S6	forced	-	yes, $G = 3 \cdot 10^{10}$	1°	both sides	none
S7	forced	-	yes, $G = 3 \cdot 10^{10}$	30°	right side	none
S8	free	1.25 Ma	yes, $G = 3 \cdot 10^{10}$	30°	none	left and right side

2.3.2 Configuration for the gravity anomaly calculations

With the simulation results we also compute synthetic gravity anomalies in order to compare them with real data, in particular across the Mariana trench. For the gravity anomaly calculations, we use the algorithm of Won and Bevis (1987), based on the method of Talwani et al. (1959). The calculation uses the model geometry and corresponding density field of the numerical mesh at the final time step. To avoid edge effects, the model sides have been extended to great distances (10'000 km each side), which ensures the far-field fit of the gravity field. The topography in our model corresponds to the seafloor, therefore, we add a water layer of 5 km thickness with respect to the far-field, undeformed seafloor with a density of $1'000 \text{ kg}\cdot\text{m}^{-3}$. We then calculate the gravity contribution of all numerical elements at virtual measurement stations (10 km spacing) at sea-level to obtain a synthetic free-air anomaly profile, which can be then compared to the anomaly profile obtained from natural data.

2.4 Results

We performed nine simulations whose characteristics and differences are listed in Table 2.2. We employed the colour-maps “lapaz” and “vik” of Cramer (2018) for the visualization.

2.4.1 Quantification of slab pull force and gravitational potential energy

We first compare three different simulations (Fig. 2.3) using identical material parameters, namely simulation S0 for forced subduction scenario (Figs. 2.3a-c) and simulations S1 and S2 for free subduction scenarios (Figs. 2.3d-i). The only difference between S1 and S2 is the time at which we set the horizontal boundary velocities to zero. The time at which free subduction starts is termed t_{free} and it is equal to 1.25 Ma in S1 and 1.17 Ma in S2. In S0 (Figs. 2.3a-c), subduction develops with a relative retreat of the trench to the right of the model. This retreat is caused by the velocity imposed on the left side of the box. This trench retreat is not observed in S1 and S2 because no more lithosphere is created on the left side of the box due to the change of boundary conditions (Figs. 2.3d-i). The evolution of slab geometry differs between models S0 and S1. At the beginning of the simulations (Figs. 2.3a and d) slabs are similar in both models. The time of these two panels (Figs. 2.3a and d) is not identical because for S1 we display the first time step of the free subduction simulation, which has a different numerical time step (due to the Courant criterion which is velocity dependent) than the forced subduction simulation. With progressive time, the dip and curvature of the slabs evolve differently. S0 shows a more straight and vertical slab with a smaller curvature in the deeper regions, while S1 shows a slab dip in the opposite direction than the one in the shallower region (Fig. 2.3f). This curl-type motion is associated with the configuration of the free subduction model, which requires the asthenospheric material to fill the region of the detached slab at the top right region of the model.

Figures 2.3g-i shows a scenario of a failed model of free subduction development (S2). The only difference between S1 and S2 is the time at which the horizontal boundary velocities are set to zero (t_{free}). These simulations show that the difference between a successful or failed free subduction simulation is linked to the slab pull force, associated only to the negative buoyancy of the slab after t_{free} . To determine the slab pull force required to develop a free subduction in our model configuration and to evaluate the impact of rheological parameters, we first calculate the slab pull force for three different forced subduction simulations (Fig. 2.4b), namely S0, S4 and S5 (Table 2.2).

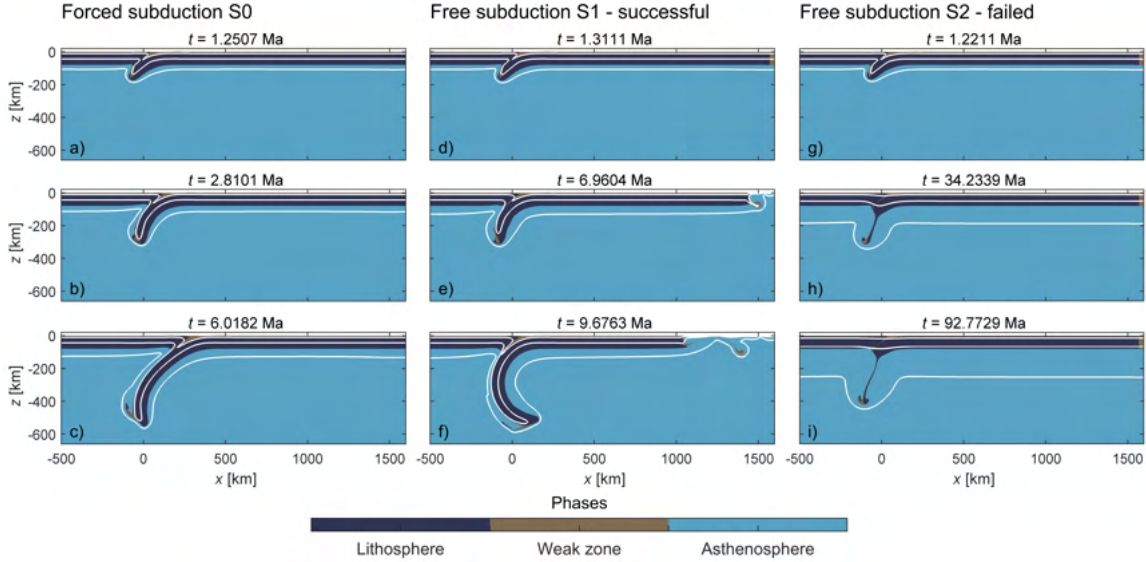


Figure 2.3: Visualisations of the forced subduction model in panels (a-c), the free subduction model where the subduction continues (successful) with $t_{\text{free}} = 1.25$ Ma in panels (d-f), and the free subduction model where the subduction stops and delaminates (failed) with $t_{\text{free}} = 1.17$ Ma in panels (g-i). Material parameters are similar in all three simulations. The time evolution is chosen for different slab length. Panels (a), (d) and (g) show results for a slab of 75 km, the length of the slab required to initiate the free subduction. Panels (b), (e) and (h) show results for a slab of 310 km and subplots (c), (f) and (i) show results for a slab of 550 km. White lines show the isothermal contours for 200, 800 and 1'440°C.

In S4 we increased the shear modulus to $G = 3 \cdot 10^{13}$ Pa, in order to decrease the impact of elasticity, and in S5 we reduced the friction angle to 5° . The three simulations show a similar increase of the slab pull force as function of time up to ca. 4 Ma (Fig. 2.4b). After 4 Ma, S5 differs from the other two simulations and shows a larger slab pull for the same time. We apply several free subduction starting times (t_{free} corresponding to squares and circles in Fig. 2.4a) for the reference forced subduction simulation S0 in order to evaluate the required slab pull force for free subduction (Fig. 2.4a). For the applied model configuration, a slab pull force larger than $1.8 \text{ TN} \cdot \text{m}^{-1}$ is required to develop a free subduction in the case of S0. The time to generate this slab pull force in S0 is ca. 1.15 Ma using a horizontal boundary velocity of $5 \text{ cm} \cdot \text{yr}^{-1}$ at each side of the model. If the slab pull is not large enough before the horizontal boundary velocities are set to zero, then the subduction slows down and ceases, temperature conduction heats up the slab, as illustrated by the shift of the isotherm for 1'440°C in the asthenosphere (Fig. 2.3h), and the base of the lithosphere starts to delaminate.

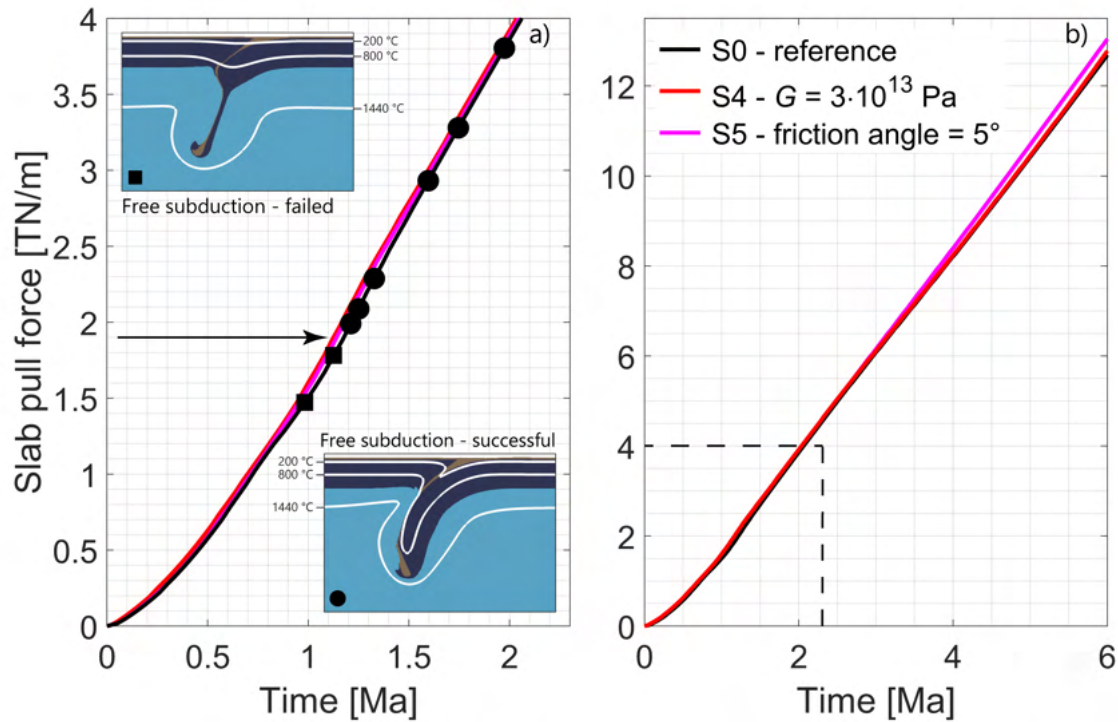


Figure 2.4: Diagrams showing the evolution of slab pull force with time, panel (a) is a zoom from panel (b). These diagrams evaluate the conditions required to develop a free subduction from the forced subduction simulation of reference S0 (in black). Free subduction simulations start after a period during which plates are pushed until initiation of free subduction. The different points in panel (a) show the slab pull force for different starting times (t_{free} , see Fig. 2a). This t_{free} is the duration of plate push to initiate the subduction in the initial part of the free subduction model simulation. Squares show conditions where free subduction failed, while circles show conditions where free subduction occurs. Black arrow indicates the minimum slab pull force needed to obtain a successful free subduction in S0 model. Inset figures, similar to panels (e) and (h) from Fig. 3, show examples of successful and failed free subduction models. White lines show the isothermal contours for 200, 800 and 1440°C.

In contrast, when slab pull is larger than $1.9 \text{ TN}\cdot\text{m}^{-1}$ in S0, the subduction continues. The vertical velocities associated with the delamination for a failed free subduction model are significantly slower than velocities of the subducting slab (compare times in Figs. 2.3c, f and i).

The quantification of along-profile variations of GPE, ΔGPE , in the lithosphere–asthenosphere system allows quantifying the along-profile variation of horizontal driving forces in the system. Hence, regions under overall horizontal compression or extension are identified and the corresponding horizontal forces are quantified. To investigate these

forces around the modelled subduction system, we quantify the relative contribution of (i) density variations below the initial lithospheric thickness due to subduction and (ii) topography variations due to lithospheric flexure to ΔGPE . To quantify contributions due to sub-lithospheric density variations we calculate ΔGPE by integrating P_L from the model bottom up to a depth of 80 km, the initial lithosphere thickness. The relative variation of the total ΔGPE and the topography agree in the right side of the subduction trench for both forced and free subduction model (Figs. 2.5 and 2.6).

This agreement indicates that the variation of total ΔGPE is controlled by the variation of topography created by the flexure of the lithosphere, and that the flexure of the subducting plate does not affect the density field below the lithosphere. In contrast, relative variations of total ΔGPE and the topography on the upper plate side of the trench do not agree. If a significant slab has developed, then the variation of total ΔGPE on the upper plate side of the trench agrees with the ΔGPE beneath 80 km because the variation in total ΔGPE is there controlled by deep density variations due to subduction of the cold slab. The GPE calculation shows that the subduction system is characterized by three regions with respect to ΔGPE variations and associated horizontal driving forces: (1) extensional horizontal driving forces related to the flexural bulge of the subducting plate, (2) compressive horizontal driving forces in the trench region associated to the negative topography of the trench region and (3) extensional horizontal driving forces in the overriding plate region related to deep density variations caused by the subducted plate (Figs. 2.5 and 2.6). The maximal difference in total GPE for the forced subduction is ca. $80 \text{ TN}\cdot\text{m}^{-1}$ and for the free subduction ca. $110 \text{ TN}\cdot\text{m}^{-1}$ (Fig. 2.5c and 2.6c). The division of these values by the model height of 660 km provides a minimum estimate for the vertical average of the horizontal differential stress caused by subduction-related variations of GPE. These vertically-averaged horizontal differential stresses are ca. 121 MPa and 167 MPa for the forced and free subduction, respectively. These vertically-averaged differential stresses are required to maintain the subduction zone and to avoid that the subduction system disappears immediately and returns to a state of static equilibrium, which is characterised by vertical density variations only and no topography.

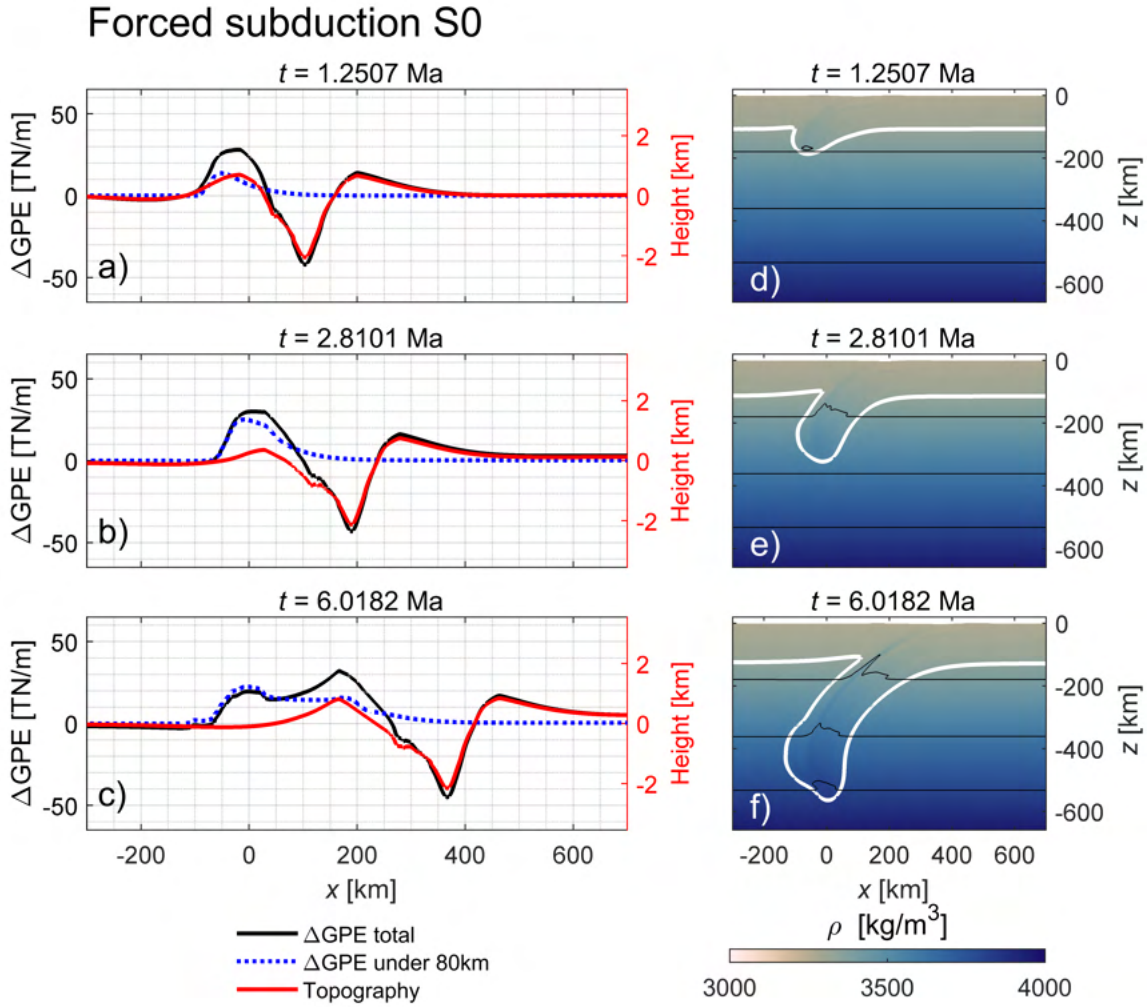


Figure 2.5: Panels (a-c) show the evolution in time, same condition then Figs 2.3a-c, of the variations of total ΔGPE , ΔGPE beneath 80 km and topography for the forced subduction model. Vertical left (black) axes are for the ΔGPE values and vertical right (red) axes are for topography values. Panels (d-f) show the evolution of density in the region of the subduction zone at corresponding model times. White line is a temperature iso-contour for 1440°C representing the LAB. Black lines are iso-contours of density (3400 , 3600 and 3800 $\text{kg}\cdot\text{m}^{-3}$).

2.4.2 Analyses of strain rate, deformation mechanisms, effective viscosity and horizontal deviatoric stress

Strain rate

We quantify the strain rate field with the square root of the second invariant of the deviatoric strain rate tensor, $\dot{\epsilon}_{II}$, for the forced (Figs. 2.7a-c, S0) and the free subduction model (Figs.

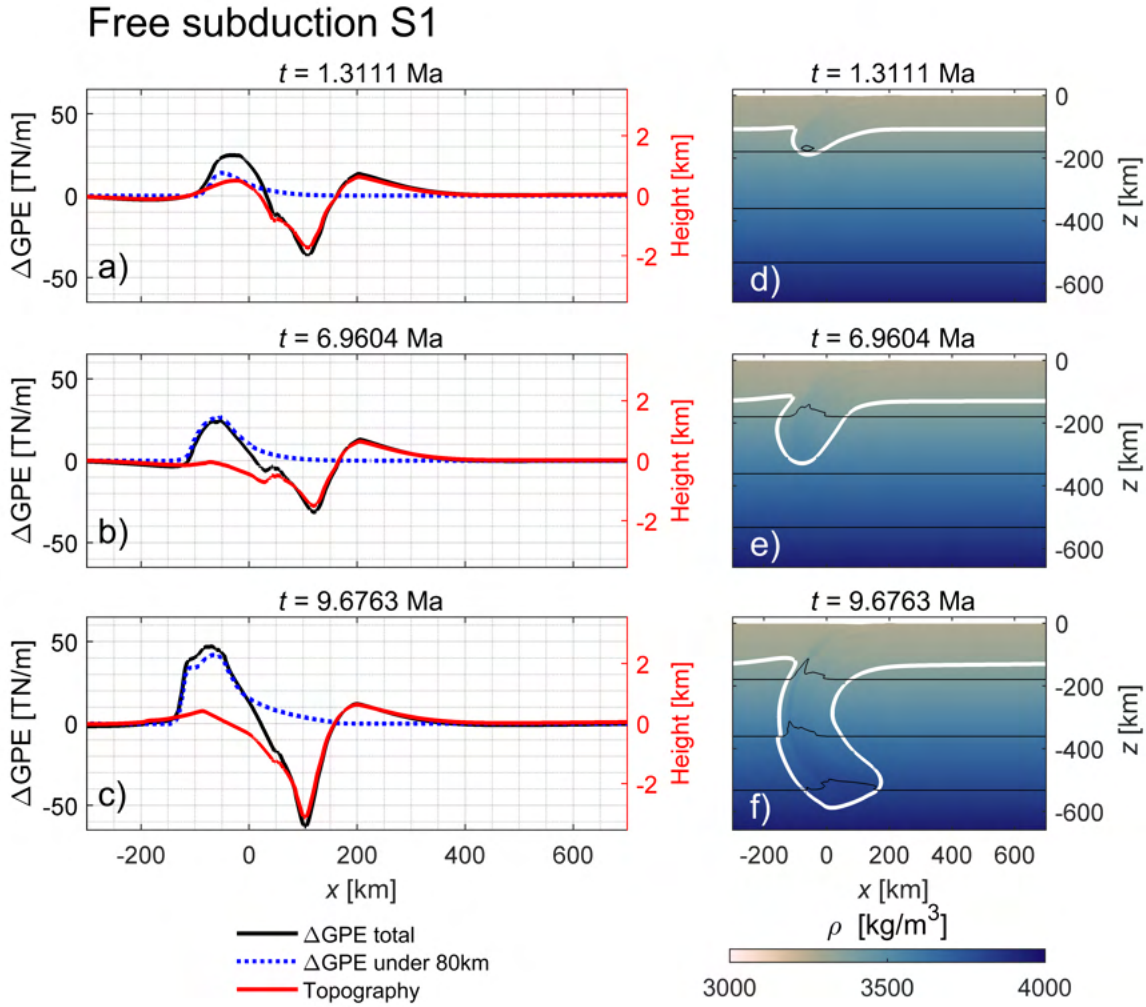


Figure 2.6: Panels (a-c) show the evolution in time, same condition then Figs 2.3d-f, of the variations of total ΔGPE , ΔGPE beneath 80 km and topography for the free subduction model. Vertical left (black) axes are for the ΔGPE values and vertical right (red) axes are for topography values. Panels (d-f) show the evolution of density in the region of the subduction zone at corresponding model times. White line is a temperature iso-contour for 1440°C representing the LAB. Black lines are iso-contours of density (3400, 3600 and 3800 kg·m⁻³).

2.7d-f, S1). High values of $\dot{\epsilon}_{II}$ indicate regions of intense deformation whereas low values indicate regions of little deformation. The distribution and magnitude of $\dot{\epsilon}_{II}$, hence, indicates, for example, whether the deformation around a subduction system and within the slab is either more or less homogeneous or strongly heterogeneous. For both S0 and S1 the strain rates in the upper region of the lithosphere are small away from the subduction zone (Fig. 2.7). These low strain rate regions feature high viscosity, dominantly elastic deformation

(see following sections, Figs. 2.9 and 2.10) and an essentially rigid, plate-like behaviour. In S0, strain rates are generally highest in the lower region of the lithosphere and in the upper regions of the asthenosphere (Figs. 2.7a-c). These high strain rates are due to the applied horizontal boundary velocity profile, which move material into the model domain in the upper model region and, to conserve mass, move material out of the model in the lower regions (see Fig. 2.2b). For S1, the strain rates in the upper plate region, in the front of the subducting slab, are significantly smaller because no material in- and out-flow is considered (Figs 2.7d-f). However, strain rates are also high in the lower regions of the subducting plate (right model region) where the underlying asthenosphere is being sheared by the subducting plate (Figs. 2.7d-f).

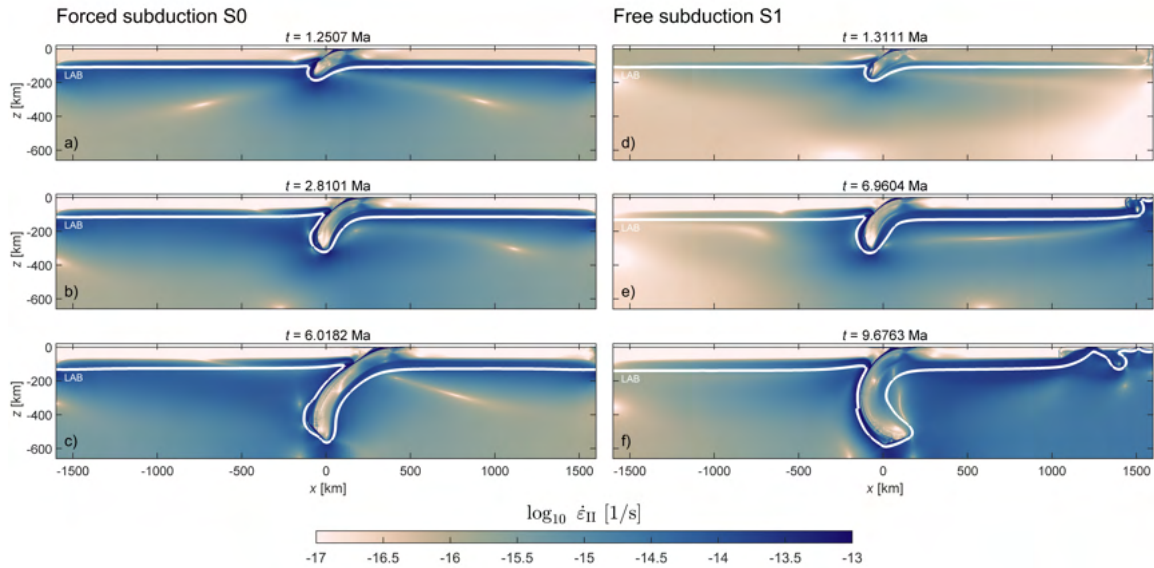


Figure 2.7: Second strain rate invariant evolution for the forced subduction model, (a-c), and for the free subduction model, (d-f), same configuration as Figs 2.3a-f. White lines show the thermally controlled LAB defined as the 1440°C isotherm.

Deformation mechanisms

To study the relative importance of the five modelled deformation mechanisms, namely elastic deformation, frictional-plastic deformation, diffusion creep, dislocation creep, and Peierls creep we plot the individual strain rates for each deformation mechanism separately using Equation (2.6) (Fig. 2.8).

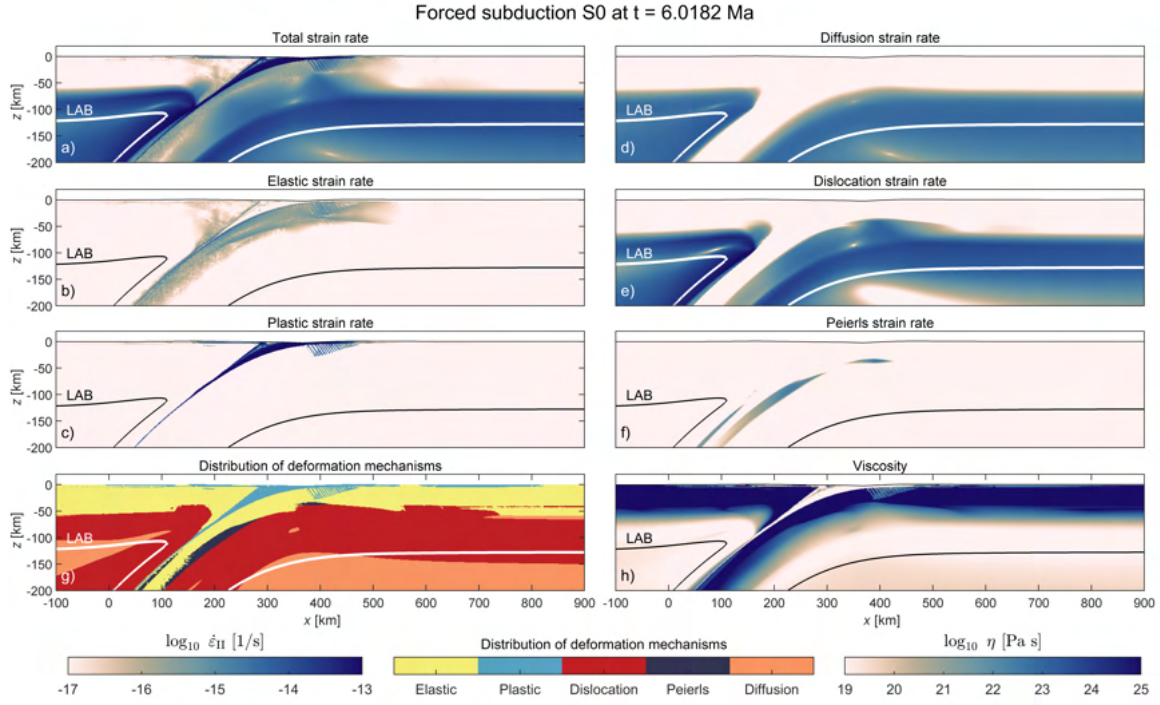


Figure 2.8: Zoom into the subduction zone of the forced subduction model for the time step corresponding to Fig. 2.7c. In panels (a-f) the results of individual strain rates for the different deformation mechanisms are displayed. Panel (a) shows total strain rate, (b) elastic strain rate, (c) plastic strain rate, (d) diffusion strain rate, (e) dislocation strain rate and (f) Peierls strain rate. Panel (g) shows distribution of deformation mechanism (elastic domain in yellow, plastic domain in light blue, dislocation creep in red, Peierls creep in dark blue and diffusion creep in orange) and panel (h) shows effective viscosity (Equation 2.15). White or black lines correspond to the thermally controlled LAB (1440°C isotherm).

Figure 2.8a shows the total strain rate corresponding to the results shown in Figure 2.7c for S0. Strain rates due to elastic deformation are significant in the upper regions of the lithosphere in the subduction zone (Fig. 2.8b). Strain rates due to frictional-plastic deformation are significant (i) in the weak zone between the overriding and subducting plate and (ii) in the uppermost region of the subducting plate where the plate starts to subduct (Fig. 2.8c). This region corresponds to the outer hinge zone of the subducting plate. In the lower region of the lithosphere and upper region of the asthenosphere, both diffusion and dislocation creep are significant (Figs. 2.8d and e). Strain rates due to dislocation creep are generally higher than the ones for diffusion creep. High strain rates due to dislocation creep are in the mantle lithosphere and in the mantle wedge corner (Fig. 2.8e). Strain rates caused by Peierls creep are significant only (i) in small areas in the region where the plate subducts and (ii) in a small

area around the hinge region of the subducting plate (Fig. 2.8f). Around the subduction zone, each of the five deformation mechanisms is dominant in some region (Fig. 2.8g). Therefore, all five deformation mechanisms are important for lithosphere deformation around the subduction zone. For comparison, the corresponding effective viscosity field is also shown (Fig. 2.8h). Upper regions of the lithosphere with high effective viscosity correspond generally to regions in which elastic deformation is dominant. Low viscosity regions correspond to regions in which dislocation and diffusion creep is dominant.

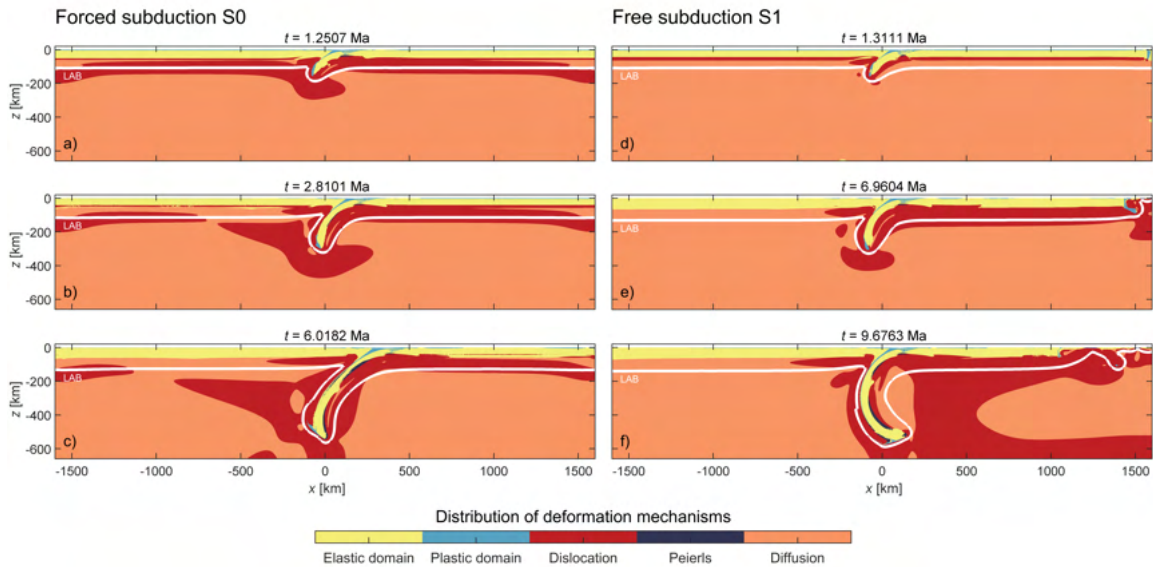


Figure 2.9: Distribution of deformation mechanism evolution for the forced subduction model, (a-c), and for the free subduction model, (d-f), same time as Figs 2.3a-f. White lines correspond to the thermally controlled LAB (1'440°C isotherm).

Considering the entire model domain, the distribution of dominant deformation mechanism is similar for S0 and S1 (Fig. 2.9) except for dislocation creep. The deformation associated with dislocation creep corresponds to the region with the highest strain rate in Fig. 2.7. Frictional-plastic deformation is dominant in three different regions: in a thin zone (ca. 5 km thick) on the top of the lithosphere corresponding to the model weak crust, in the triangular weak zone mimicking an accretionary prism between the subducting and overriding plates, and in the outer hinge zone caused by flexure of the downgoing slab. In this hinge zone, frictional-plastic deformation associated with the development of normal-fault-type shear zones propagates downwards to ca. 30 km depth. Elastic deformation is dominant in the upper regions of

the lithosphere down to a depth of ca. 60 km, measured orthogonally from the top of the lithosphere. Elastic deformation is dominant in the subducting slab to depths of more than 500 km (Figs 2.9c and f).

Effective viscosity

The effective viscosity has contributions from all the considered viscous and plastic deformation mechanisms and thus depends on the strain rate, temperature and pressure. Since these quantities vary in space and time, it is not trivial to predict lithospheric regions, which are mechanically strong or weak, or to predict the absolute values of the effective viscosity. In our simulations, the effective viscosity varies by six orders of magnitude (Fig. 2.10). The viscosity below the lithosphere, in regions unaffected by the subducted slab, exhibits an increase as function of increasing pressure with depth. This increase from ca. 10^{19} to 10^{22} Pa·s at the base of the model is due to the increase of pressure with depth controlled by the activation volume, V (Table 2.1). Overall, the effective viscosity distribution is similar for S0 and S1.

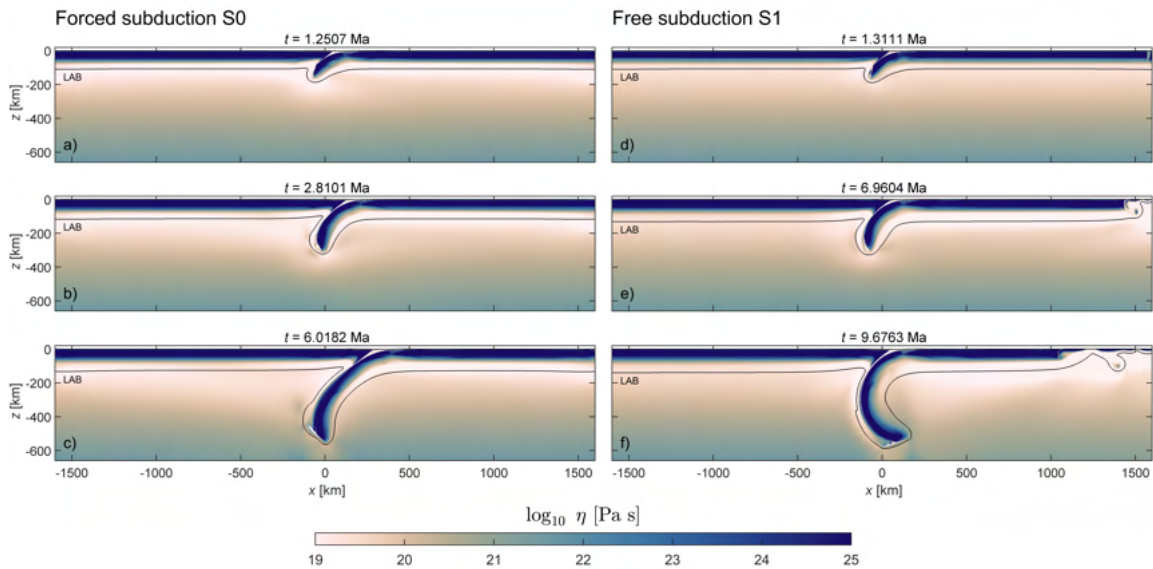


Figure 2.10: Effective viscosity evolution for the forced subduction model, (a-c), and for the free subduction model, (d-f), same time as Figs 2.3a-f. Black lines correspond to the thermally controlled LAB (1440°C isotherm).

Horizontal deviatoric stress

To identify regions in horizontal compression or extension and to quantify stress magnitudes we analyse the distribution of the horizontal deviatoric stress, τ_{xx} . The bending of the slab around the subduction zone causes flexural stresses and this bending also generates a topographic high, the so-called flexural fore-bulge, in the slab region in front of the subduction zone (e.g. Turcotte and Schubert, 2014). Therefore, we also analyse in the following this topographic bulge to assess how much topographic variation is associated with the calculated stress distribution and magnitudes. The link between surface topography and rheological behaviour of the subducting slab has been also demonstrated by previous studies (e.g. Zhong and Gurnis, 1994; Crameri et al., 2017). Absolute values of τ_{xx} are largest in the upper part of the lithosphere where the subducting lithosphere is bending and is colder (Fig. 2.11).

During the initial stages of subduction, both S0 and S1 show the characteristic pattern of bending (e.g. Burov, 2011; his figure 5), or flexure, around the hinge zone of the subducting plate (Figs. 2.11a and d). The outer hinge region is under extension (positive τ_{xx}) and the inner hinge region is under compression (negative τ_{xx}). When subduction evolves and slabs become longer, the plate straightens back, or unbends, causing a stress pattern in the opposite sense (Figs. 2.11c and f; e.g. Faccenda et al., 2012): the upper part of the lithosphere is under compression and the lower part under extension. In S0, the horizontal regions of the subducting plate are under compression during the initial stages of subduction (Fig. 2.11a). With progressive subduction, the stress state of the horizontal region changes from compression to extension and extensive values of τ_{xx} become larger with progressive subduction (Figs. 2.11b and c). This change in stress state is likely due to the increasing slab pull, which starts pulling the subducting plate once it is larger than the compressive stresses due to the applied boundary velocities. The orientation and magnitude of the principal stresses, σ_1 and σ_3 , confirm the result of distribution of τ_{xx} (Figs. 2.11g and h). If the horizontal regions of the lithosphere are in compression, then σ_1 is approximately horizontal (Fig. 2.11g). For extension, σ_3 is horizontal. The orientation of the principal stresses shows that these principal stresses are always either parallel or orthogonal to the local dip of the

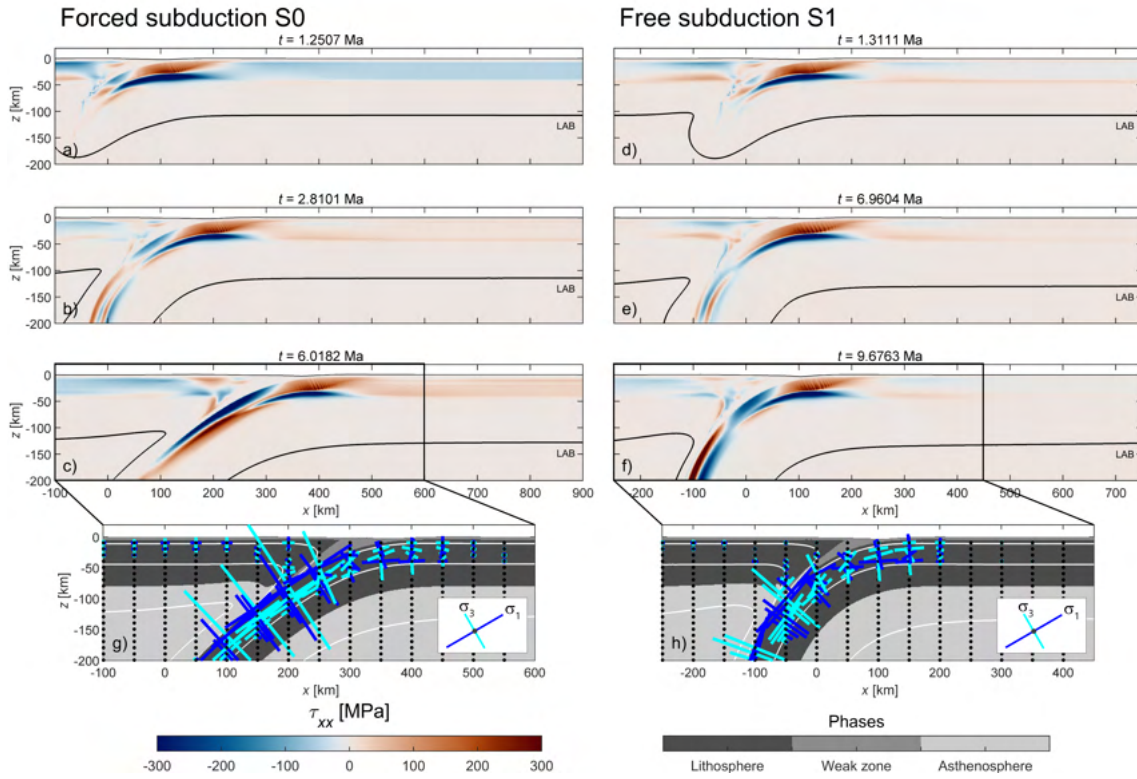


Figure 2.11: Comparison of horizontal deviatoric stress between the forced subduction model (panels a-c) and the free subduction model (panels d-f) depicted at similar time as Figs 2.3a-f. Black lines correspond to the thermally controlled LAB (1440°C isotherm). Areas in red, positive values, show regions associated with extension while areas in blue, negative values, show compression. Panels (g) and (h) show the principal stresses σ_1 in blue and σ_3 in cyan associated, respectively, to panels (c) and (f). The background shows phases and white lines show the isothermal contours for 200, 800 and 1440°C .

subducting plate so that the strong regions of the slab act as a stress guide (Figs. 2.11g and h).

Impact of elasticity

Rocks generally deform visco-elastically, and the time scale over which elastic stresses are relaxed can be estimated to the first order by the so-called Maxwell relaxation time, which is the ratio of the effective viscosity to the shear modulus, η/G . Using 10^{23} Pa·s as representative, average effective viscosity for the slab and $3 \cdot 10^{12}$ Pa for G provides a relaxation time of ca. 100 kyr. One could, therefore, argue that elastic stresses are largely relaxed during subduction processes with durations of several millions of years and that, hence, elasticity

might not be important for slab deformation during subduction (e.g. Schmeling et al., 2008). To study the impact of elasticity in our models, we performed two forced subduction simulations: one with a shear modulus, G in Equation (2.6), which is two orders of magnitude larger than in the reference simulation, i.e. $3 \cdot 10^{12}$ Pa, and one with a shear modulus, which is three orders of magnitude larger than in the reference simulation, i.e. $3 \cdot 10^{13}$ Pa (Fig. 2.12). In the simulations with unrealistically high shear modulus of $3 \cdot 10^{12}$ and $3 \cdot 10^{13}$ Pa the elastic behaviour is significantly less dominant because the Maxwell relaxation time, during which elastic stresses relax, is significantly shorter (e.g. Jaquet et al., 2016).

We compare the topography of the subducting plate from the three numerical simulations with the analytically calculated flexural geometry fitting the Mariana trench (Turcotte and Schubert, 2014) and obtain reasonable agreement (Fig. 2.12a). However, the height of the flexural bulge, ca. 800 m, is higher in the reference simulation than in the simulations with $G = 3 \cdot 10^{12}$ Pa and $G = 3 \cdot 10^{13}$ Pa, ca. 400 m. The lateral topographic variation around the bulge region is considerably smaller in the simulations with unrealistically high values of G , indicating that elasticity has a strong impact on the flexural behaviour in the bulge region. The depth of the trench is similar for the three simulations.

The overall distribution of the horizontal deviatoric stress, τ_{xx} , in the subducting plate is similar for the three simulations (Fig. 2.12b to d). However, the absolute values of τ_{xx} are smallest for the reference simulation and the reduction of the impact of elasticity increases stress values (Figs. 2.12b-d). In the simulation with $G = 3 \cdot 10^{13}$ Pa, the overriding plate exhibits significant larger compressive stresses than in the simulation with a standard elastic shear modulus. The regions dominated by elastic deformation are replaced mostly by the frictional-plastic deformation mechanism when the impact of elasticity is reduced (Figs. 2.12e-g), except in the deeper regions of the subducting lithosphere where elastic deformation is replaced by Peierls creep (Figs. 2.12e-g). The results show that the implementation of elasticity significantly affects both the magnitude of stresses and the distribution of non-elastic deformation mechanisms.

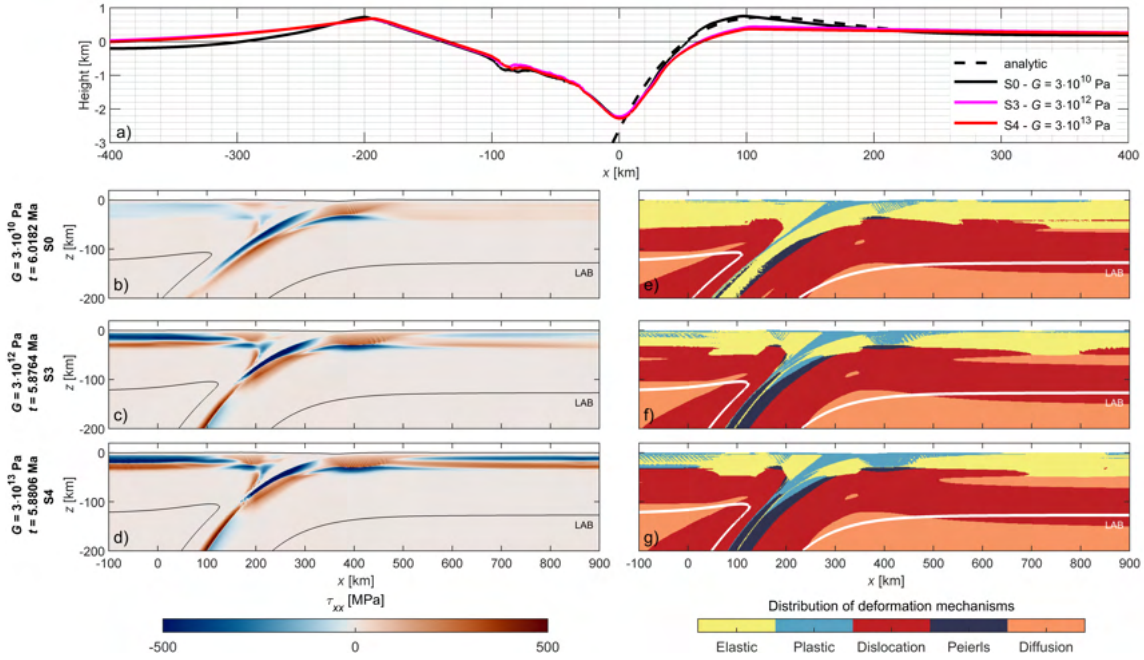


Figure 2.12: Comparison between three forced subduction models with different elasticity parameters. Results of simulation S0 correspond to the black topography profile in panel (a), the horizontal deviatoric stress in panel (b) and the distribution of deformation mechanisms in panel (e). Results of simulation S3, with an unrealistically high shear modulus of $G = 3 \cdot 10^{12}$, correspond to the pink topography profile in panel (a), the horizontal deviatoric stress in panel (c) and the distribution of deformation mechanisms in panel (f). Results of simulation S4, with an unrealistically high shear modulus of $G = 3 \cdot 10^{13}$, correspond to the red topography profile in panel (a), the horizontal deviatoric stress in panel (d) and the distribution of deformation mechanisms in panel (g). Time step for panels (b) and (e) are the same as in Fig. 2.3c. Time step for panels (c and f) and (d and g) are chosen to have approximately the same depth of the slab as in panels (b and e) for reference. The dashed line in panel (a) shows the best fit of elastic flexure from the analytical formula from Turcotte and Schubert (2014) (Fig. 3.35 and equation 3.159, $x_b = 55$ km and $w_b = 0.5$ km). In panel (a) the horizontal position of the zero was displaced to match the position of the trench (but not for the other panels). In panels (b-d) areas in red, positive values, show regions associated with extension while areas in blue, negative values, show compression. In panels (b-g) white or black lines correspond to the thermally controlled LAB ($1'440^\circ\text{C}$ isotherm).

Impact of friction angle

The absolute magnitudes of stress, especially maximal values, in the mantle lithosphere are still contentious. One reason for this is that different laboratory flow laws for mantle rocks predict stresses that can be up to one order of magnitude different for the same temperature, strain rate and pressure (e.g. Mei et al., 2010; Jain et al., 2017). Furthermore, different authors apply stress cut-offs in the mantle, for example, to match tectonic plate size distribution in

mantle convection simulations (e.g. Mallard et al., 2016) or apply reduced friction angles ($\leq 15^\circ$), which further reduce with progressive plastic strain (down to 2°), in order to indirectly consider the weakening effects of fluids or other strain softening mechanisms (e.g. Erdős et al., 2014). Moreover, since the effective friction angle depends on fluid pressure, the appropriate friction angle for the mantle lithosphere is debated and, hence, different friction angles are often used for the mantle lithosphere in numerical models of subduction (e.g. Li et al., 2010). To test the impact of absolute stress magnitudes, we performed two more simulations with a reduced friction angle for the lithosphere (Fig. 2.13). The friction angle is reduced to limit maximal stress values but not to mimic any particular natural process. The standard value for the friction angle is 30° and we decrease this angle to 5° (Figs. 2.13c and f) and 1° (Figs. 2.13d and g) in the two additional simulations. The reduction of friction angle changes the topographic profiles around the flexural bulge of the subducting plate (Fig. 2.13a). A friction angle to 5° generates a shorter flexural wavelength whereas a friction angle of 1° does not generate a realistic flexural topography at all. These results are in broad agreement with results of Cramer et al. (2017) who, amongst others, also show a larger bulge and flexural wavelength with larger friction angle (their figure S10).

The reduction of friction angles reduces, as expected, the maximal absolute values of τ_{xx} (Figs. 2.13b-d) and changes the distribution of dominant deformation mechanism (Figs. 2.13e-g). In the simulation with a friction angle of 1° a continued subduction cannot be established because the slab is thinned in the trench region and detaches, or breaks-off (Fig. 2.13g). The reduction of stress magnitudes makes the slab mechanically so weak that the slab pull force cannot be transmitted anymore to the horizontal regions of the lithosphere, the slab pull cannot drive horizontal plate motion anymore so that the slab detaches. For a friction angle of 5° maximal absolute deviatoric stress magnitudes are between 50 and 100 MPa. Also, for a friction angle of 5° the region with dominant frictional-plastic deformation is significantly larger than for a friction angle of 30° (Fig. 2.13e and f). Particularly, the region of slab unbending (between 50 and 100 km depth and $200 \text{ km} < x < 250 \text{ km}$ in Fig. 2.13f) shows significant frictional-plastic deformation, which is not the case for a friction angle of 30° (between 50 and 100 km depth and $200 \text{ km} < x < 250 \text{ km}$ in Fig. 2.13e). Maximal absolute

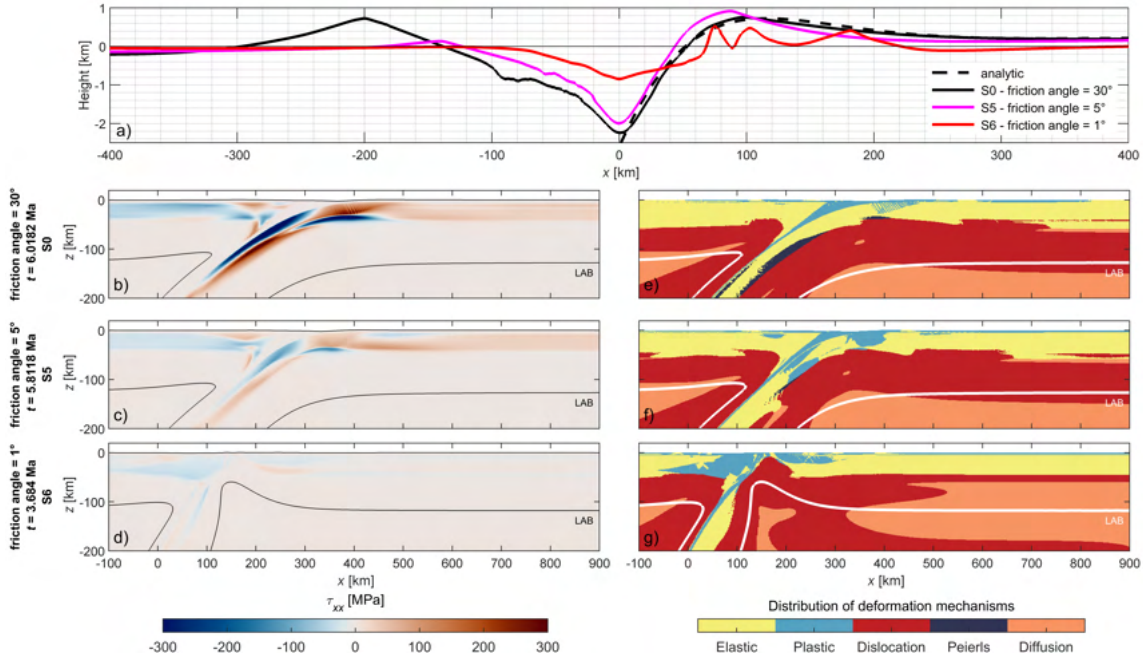


Figure 2.13: Comparison between three forced subduction models where we change the friction angle of the lithosphere. Results of simulation S0 correspond to the black topography profile in panel (a), the horizontal deviatoric stress in panel (b) and the distribution of deformation mechanisms in panel (e). Results of simulation S5 correspond to the pink topography profile in panel (a), the horizontal deviatoric stress in panel (c) and the distribution of deformation mechanisms in panel (f). Results of simulation S6 correspond to the red topography profile in panel (a), the horizontal deviatoric stress in panel (d) and the distribution of deformation mechanisms in panel (g). Time step for panels (b) and (e) are the same as in Fig. 2.3c. Time step for panels (c and f) and (d and g) are chose to have the same depth of the slab than in panels (b and e) as reference. Same references as in Fig. 2.12 for the dashed line in panel (a). The horizontal position of the zero in panel (a) is displaced to correspond to the position of the trench (but not for the other panels). In panels (b-d) areas in red, positive values, show regions associated with extension while areas in blue, negative values, show compression. In panels (b-g) white or black lines correspond to the thermally controlled LAB (1440°C isotherm).

deviatoric stress magnitudes of a few hundred MPa seem to be required in order to generate a flexural wavelength corresponding to the Mariana trench, as is the case in the model with standard elastic shear modulus.

Impact of boundary conditions

We have also performed a forced subduction simulation (S7, Table 2.2) and a free subduction simulation (S8) using different boundary conditions than in reference models (S0, S1). In S7 we apply a horizontal velocity only at the right model side, but with a value of $10 \text{ cm}\cdot\text{yr}^{-1}$

so that the absolute convergence velocity is identical to the one of S0. After ca. 2.8 Ma the stress field and the slab geometry are similar for S0 and S7 (Fig. 2.14a and c). However, after ca. 4 Ma the slab geometry and, hence, the associated stress field are different (Fig. 2.14b and d). In S8 we apply a weak zone at both lateral model sides so that the slab and overriding plate can detach from both lateral model sides. After ca. 6.9 Ma and ca. 8 Ma both simulations S1 and S8 exhibit a similar slab geometry and stress field. These additional simulations indicate that the applied boundary conditions have a significant impact on the forced subduction simulations but not on the free subduction simulations.

Figure 2.14: (Next page.) Colour plot of horizontal deviatoric stress for forced and free subduction with different boundary conditions. Panels (a) and (b) show results of forced simulation S0 corresponding to the model where horizontal boundary velocities are applied on both sides of the model. Panels (c) and (d) show results of the same forced simulation, except that a horizontal boundary velocity is only applied on the right side of the model (simulation S7, Table 2.2). This velocity is twice as large as the one of model S0 to maintain the same absolute convergence velocity. Panels (e) and (f) show results of free simulation S1 corresponding to the model where the lateral detachment of the slab by a weak zone is implemented at the right side of the model. Panels (g) and (h) show results of a free simulation where this detachment is applied at both sides of the model (S8). Time step for panels (a), (b), (e) and (f) same as Figs 2.3b, c, e and f. Time step for panels (c), (d), (g) and (h) are chose to have the same corresponding depth of the slab (310 km and 425 km) for comparison. The areas in red, positive values, show regions associated with extension while areas in blue, negative values, show compression. Black lines correspond to the thermally controlled LAB (1'440°C isotherm).

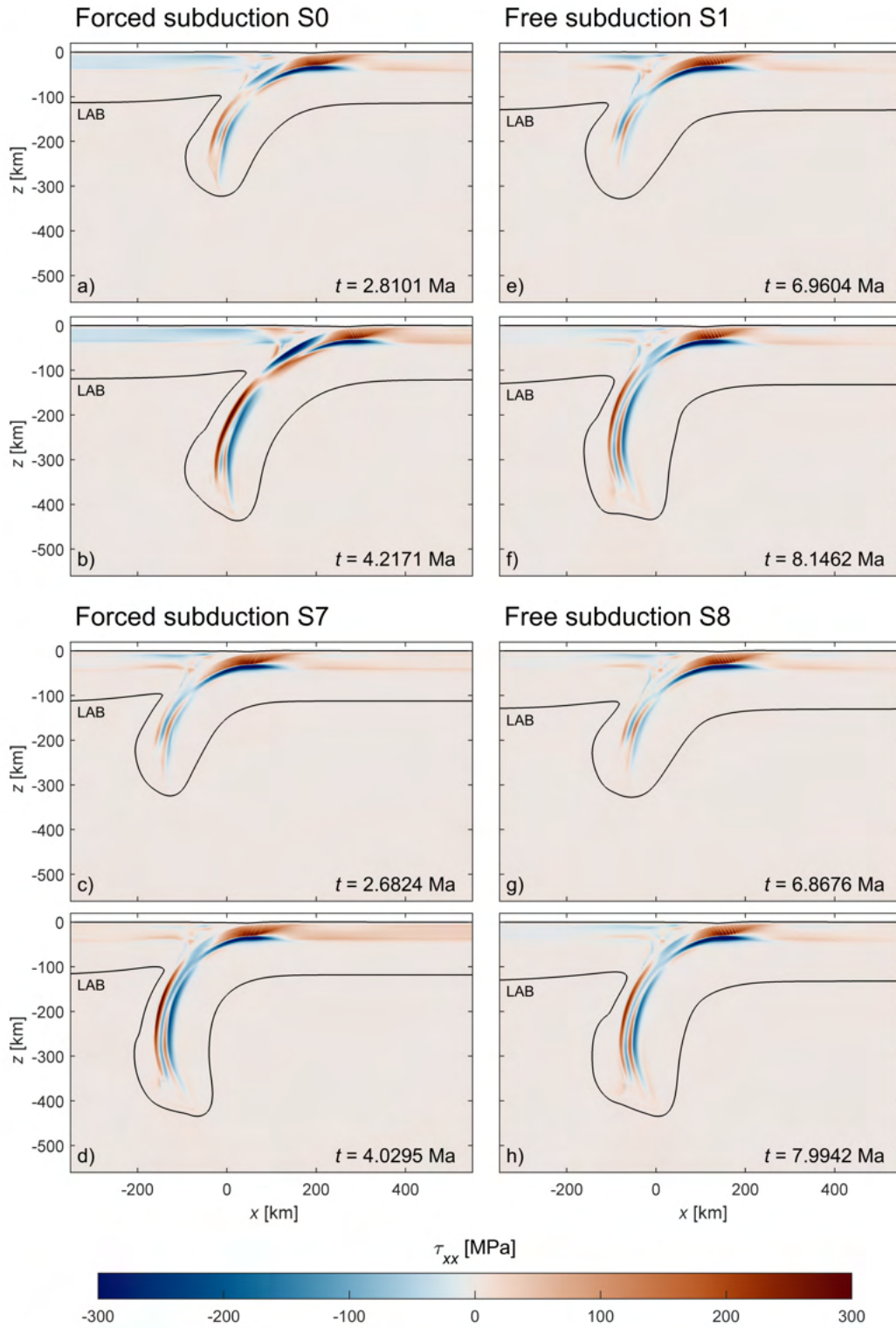


Figure 2.14: (Caption previous page.)

2.5 Discussion

The deformation behaviour, the thermal structure and the mineral composition of the lithosphere are only approximately known and, hence, published numerical subduction models commonly differ in terms of the applied flow laws, temperature and density fields. Our models were not designed to closely match a specific subduction system and we used standard rheological models, and simple density and temperature fields. However, we assume that our mathematical model, the model configuration, the applied boundary conditions, the temperature field, the densities and the applied rheological model, including the different creep flow laws, generate a subduction process, which should be comparable, to the first order, to a natural ocean-ocean subduction system. To test whether the modelled effective deformation behaviour, such as flexure of the slab, and the modelled slab pull, controlled by the model density field, are indeed in broad agreement with natural observations, we compare our model results with a major subduction system, namely with real data from the Mariana subduction zone. We chose the Mariana trench because it is a prominent subduction zone and has been frequently used for the comparison with mathematical subduction models (e.g. Funicello et al., 2003; Turcotte and Schubert, 2014). We first compare topography of the ocean floor to assess the flexural behaviour of the lithosphere. Secondly, we compare modelled gravity anomalies with anomalies derived from data measured in the field in order to assess the density field (Figs. 2.15 and 2.16).

For the topography comparison, we use the seafloor topography data from the Mariana trench (Funicello et al., 2003; Turcotte and Schubert, 2014). For the visual comparison between natural and calculated topography profiles, we have used the position of the trench ($x = 0$) as a reference (Fig. 2.15). The first-order topography of both forced and free subduction models fits the natural topography and the analytical solution of Turcotte and Schubert (2014). Therefore, the applied flow laws and rheological behaviour of our model lithosphere, controlling the height of the flexural bulge and the flexural wavelength, broadly agree with the flexural behaviour of a natural oceanic lithosphere.

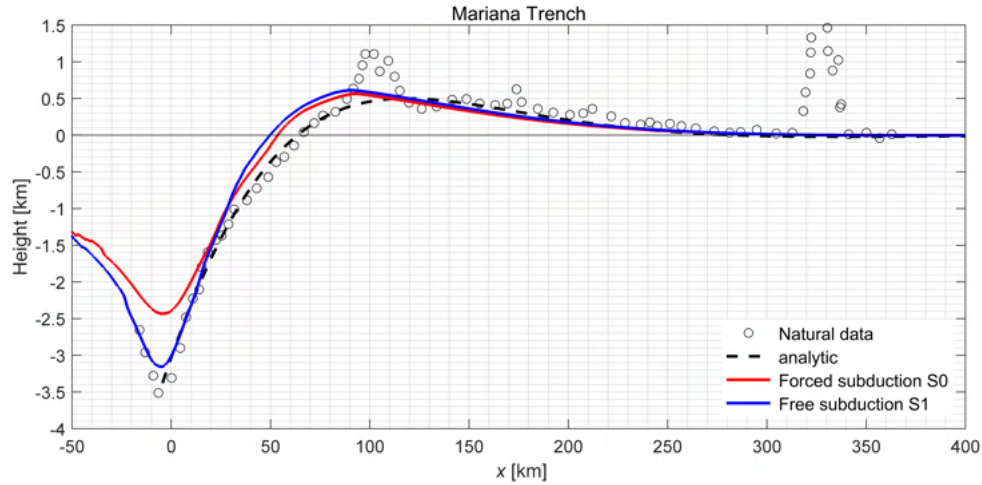


Figure 2.15: Comparison of the topography of the Mariana trench with modelled topography for the forced (S0) and free (S1) subduction models. The dashed line shows the best fit of elastic flexure from Turcotte and Schubert (2014) (Fig. 3.35 and equation 3.159, $x_b = 55$ km and $w_b = 0.5$ km). For comparison all topography profiles are co-located at the trench.

For the gravimetric comparison, we use the global WGM2012 model for free-air gravity anomaly, which has a resolution of $2' \times 2'$ (Bonvalot et al., 2012), and compare it with the synthetic free-air gravity anomalies calculated for our model density field (Fig. 2.16). We extract ten gravity anomaly profiles perpendicular to the trench from the WGM2012 (Fig. 2.16a). From the numerical models, we calculate two free-air anomaly profiles, one for the forced and one for the free subduction model (Fig. 2.16b). For comparison, we have co-located all gravity anomaly profiles at the trench (Fig. 2.16b). Our modelled free-air gravity anomalies agree with the long-wavelength variation of the observed anomaly. Modelled anomalies exhibit a similar width and amplitude in their spatial variation compared with the natural free-air gravity anomalies. The shorter wavelength variations and peaks in the natural gravity anomalies are due to the natural seafloor topography, reflecting the formation and deformation of the volcanic arc to the West of the Mariana trench and the seamounts to the East on the Pacific plate (Fig. 2.16a). These peaks vary across the selected 10 observed profiles and our model has not aimed at reproducing such short wavelength variations.

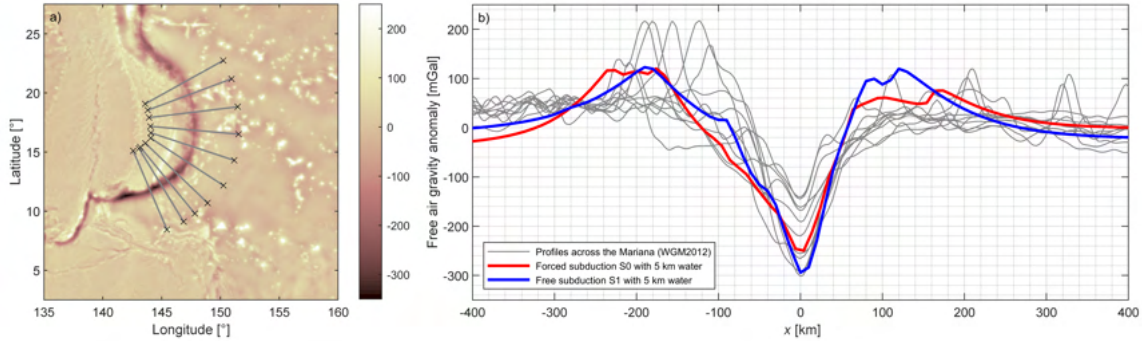


Figure 2.16: Free-air gravity anomaly comparison. Panel (a) shows the location of 10 different profiles across the Mariana Trench, with the WGM2012 free-air anomaly map in the background. Panel (b) shows in grey the observed profiles across the Mariana Trench, in red the synthetic profile from the forced subduction model for the time step corresponding to Fig. 3c, and in blue the synthetic profile from the free subduction model for the time step corresponding to Fig. 3f. A zoom on the trench was chosen for the horizontal position and all profiles were centred on the trench.

The comparison of model and natural topography allows evaluating the applicability of the modelled flexural behaviour of the lithosphere to nature. This modelled flexural behaviour and the associated topography is controlled by the considered deformation mechanisms, the flow laws and material parameters (e.g. Zhong and Gurnis, 1994; Crameri et al., 2017). Consequently, the topography comparison allows evaluating whether the employed flow laws and material parameters are applicable to natural cases. However, since natural topography can vary significantly between different subduction zones, different subduction zones likely exhibit different rheological and density characteristics (e.g. Crameri et al., 2019). The free surface implementation is therefore, well suited for the comparison of model and natural topography. A modelled free surface topography is also essential for the calculation of along-profile variations of ΔGPE (Figs. 2.5 and 2.6). The topography controls gravity anomalies, which further depend on the density field. We calculate the density with an equation of state (EOS), which depends on T and P (see Equation 2.4). We do not consider mineral phase transformation, which could affect the localization of deformation in this compressive setting (e.g. Hetényi et al., 2011). The comparison of gravity anomaly profiles from our model with natural free-air gravity anomaly profiles obtained across the Mariana trench shows that both of our model density fields are appropriate; at least for the considered natural subduction zone (Fig. 2.16).

Our simulations show differences in the forced and free subduction models. However, with respect to topography (e.g. bulge) or gravity anomalies, these differences are not significant (Figs. 2.15 and 2.16). The maximal amplitude of the modelled gravity anomaly profile for the free subduction model is larger than the one for the forced subduction model. However, considering the lateral variability of natural gravity anomaly profiles across the Mariana trench, both models fit the natural data to a good level. Alternative to gravity anomalies, ΔGPE profiles show larger differences between forced and free subduction models, because for a more vertical slab the ΔGPE anomaly is narrower (Figs. 2.5 and 2.6).

The calculated stress field (Fig. 2.11) shows that the subducting plate's outer bend of the hinge zone is under extension and the inner bend is under compression. This deformation distribution is expected for the subducting plate, but our model allows quantifying the contribution of individual deformation mechanism. The flexural behaviour varies along the subducting plate and in the downgoing plate the outer region of the plate is under compression and the inner one under extension (Fig. 2.11). This variation of flexural behaviour along the subducting slab is in agreement with analytical results of Ribe (2010) who shows that the sign of the rate of curvature changes along the slab. Ribe (2010) considered a simpler, linear viscous behaviour of the slab. The comparison with our results, considering five deformation mechanisms and temperature dependent flow laws, indicates that a linear viscous model can capture the first order flexural behaviour of a subducting slab. Regions with high compressive deviatoric stresses of several hundreds of MPa in the downgoing slab next to the subduction interface (Figs 2.11c and f) can be important for the interpretation of exhumed (ultra-)high pressure rocks. Subducted crustal rock units in the outer regions of subducting slabs could experience high stress and, hence, tectonic overpressure (e.g. Schmalholz and Podladchikov, 2013; Moulas et al., 2019) before they are detached from the subducting plate and return to the surface. If the stress and, hence, the internal resistance of the slab is reduced, then a continuous subduction is not possible anymore because the slab detaches, and the slab pull force cannot be transferred anymore to the horizontal region of the lithospheric plate (Figs. 2.13d and g). This behaviour is consistent with the "shallow breakoff" of Duretz et al. (2011a), which systematically occurred for weak slabs (young plates). This result agrees also with

predictions of the analytical model of Ribe (2010) who shows that the subduction velocity approaches the Stokes velocity of a detached object when the internal resistance of the slab becomes smaller than the external resistance of the material surrounding the slab.

Stress magnitude and distribution in subducting plates are one of the controlling parameters of intra-slab processes such as earthquakes, metamorphism or fluid transfer. Our results show that in a subducting lithosphere all five considered deformation mechanisms are active and contribute to shape the total stress field (Fig. 2.8). Particularly, our results show that elastic deformation is the dominant deformation behaviour in large regions of the subducted slab (Fig. 2.8g). Therefore, models aiming to calculate the intra-plate stress field and intra-plate processes should consider the impact of elastic deformation on the stress field.

Our model results can contribute to a better understanding of the development of faults during plate flexure, and its importance for the hydration of the subducting plate. Several mechanisms have been proposed to bring water from the surface into the mantle, such as bending-related faulting (e.g. Ranero et al., 2003; Faccenda et al., 2008, 2009), thermal cracking (Korenaga, 2017) or seismic pumping (Sibson et al., 1975). The length and distribution of faults, which could develop by plate flexure, is therefore important to assess the water budget of the subducting plate. Furthermore, Peacock (2001) suggested that dehydration of antigorite (serpentine) by dehydration reactions could be an explanation for intermediate-depth earthquakes. To constrain the depth of faulting, and therefore the maximum depth where water could be added to the subducting plate is fundamental to test whether part of the earthquakes observed between 15 to 25 km depth could be explained by metamorphic dehydration reaction or not (Peacock, 2001). Our model predicts the formation of faults in the outer hinge zone of the subducting plate (Figs. 2.8g and 2.9). These faults develop in a zone of ca. 100 km width around the bulge. These frictional-plastic faults reach a depth of ca. 40 km. However, the spatial extent of faulting is highly dependent on the elasticity and plasticity parameters in the model. Figure 2.12 shows that the extent of plastic deformation changes drastically if the elastic deformation behaviour is modified.

Flexure of the subducting plate has been also proposed as an important mechanism for the formation of petit-spot volcanoes (Hirano et al., 2006). Petit-spot volcanoes represent small volumes of alkaline magmas that have been emitted on the top of the downgoing Pacific plate in front of Japan (Hirano et al., 2006). These magmas are emitted 300 to 600 km away from the trench, which could correspond to the region where the plate starts to bend (Hirano et al., 2006). Petit-spot volcanoes are, therefore, interpreted as the products of deformation-driven melt segregation of melt initially present at the base of the lithosphere. Since their first observation in front of Japan, petit-spot volcanoes have been identified in several subduction zone, such as Tonga (Hirano et al., 2008), Chile (Hirano et al., 2013), and Sunda trenches (Taneja et al., 2015), or as an accreted petit-spot in Costa Rica (Buchs et al., 2013). These observations suggest that petit-spot volcanism is a global process around subduction zones. In this context, the deformation behaviour and its changes along the lithosphere-asthenosphere-boundary are critical to understand how low degrees of volatile rich melts can be extracted from the base of the lithosphere. Earlier models suggest that large flexural curvatures imposed on the pre-flexed lithosphere might instigate brittle fracturing even at the base of the lithosphere (Hirano et al., 2006; Yamamoto et al., 2014). Our Figure 2.8g shows, however, that deformation around the base of the lithosphere (from 50 km depth to the LAB) is likely controlled by diffusion and dislocation creep. Propagation of brittle faults down to the base of the lithosphere is, therefore, unlikely. Consequently, percolation of melts within the basal viscous region of the lithosphere, before its extraction by faults when the melts reach the elastic domain, seems a more realistic model for petit-spot formation. A possible mechanism of melt transport in the viscous region could be ascent in the form of porosity waves (e.g. Connolly and Podladchikov, 2007). The viscous percolation model is in agreement with recent multiple saturation laboratory experiments which show that petit-spot melts equilibrate last with the mantle phases (olivine, orthopyroxene, and clinopyroxene) at pressures between 1.8 and 2.1 GPa and at temperatures around 1'280–1'290°C, which are P-T conditions corresponding to the lithosphere rather than the top of the asthenosphere (Machida et al., 2017). Another argument in favour for the ascent and equilibration of low degree melts at the base of the lithosphere is the presence in petit-spot lavas with xenoliths

showing evidence of metasomatic enrichment (Pilet et al., 2016). One important question concerning petit-spot formation is which process or parameter initiates melt percolation in the basal part of the lithosphere. The porosity at the base of the lithosphere is frequently considered as too small to allow for silicate melt percolation. Our numerical model allows quantifying the extension produced by plate flexure. Figure 2.11 suggests that the base of the lithosphere where the plate starts to bend is slightly in extension, but the effect is very limited at depths greater than 50 km where absolute magnitudes of τ_{xx} are significantly less than 10 MPa. Nevertheless, the current model considers a homogeneous dry-olivine lithology and future models considering additionally wet or higher-porosity domains at the base of the lithosphere, i.e., in the low seismic velocity zone, will be important to constrain the effect of plate flexure on the stress state at the base of the lithosphere.

2.6 Conclusions

We performed 2D thermo-mechanical numerical simulations of subduction, considering both forced and free subduction regimes as well as a composite rheological model including elasticity, frictional-plasticity, diffusion, dislocation and Peierls creep. In the forced subduction regime, we initiate subduction by applying horizontal boundary velocities. The initiation by a forced subduction must generate an embryonic slab to continue a free subduction simulation, for which boundary velocities are set to zero and subduction is driven by buoyancy forces of the slab. For our configuration, the embryonic slab should produce a slab pull force (per unit length) of at least $1.8 \text{ TN}\cdot\text{m}^{-1}$ so that free subduction can occur.

We show that the five employed deformation mechanisms are all important for the evolution of the subducting lithospheric plate for both forced and free subduction. Particularly, elastic deformation is important because it affects the flexural behaviour, the magnitude and distribution of deviatoric stresses and the distribution of dominant deformation mechanisms. Simulations with an unrealistic, reduced impact of elasticity show significantly larger stress magnitudes and larger regions with high stresses in the subducting and overriding plate than corresponding simulations with appropriate elasticity. For our model configuration, the sim-

ulations with elasticity also fit best the natural flexural bulge and wavelength of the Mariana subduction zone. Therefore, including elasticity in numerical subduction models seems important for an appropriate calculation of stresses, of the distribution of deformation mechanisms and of flexure in a subduction system.

We also show that a subduction system generates along-profile variations of GPE corresponding to horizontal driving forces in the lithosphere-asthenosphere system. These GPE variations result from either topography variations associated to plate flexure or from deeper density variations caused by subduction of the lithosphere into the asthenosphere. For both forced and free subduction models the GPE variations cause compressive forces in the trench region and extensive forces in front and behind the trench region. These latter likely have strong impact on driving petrological processes such as melt migration across the lithosphere, at significant distance from the trench.

Although our models were not specifically designed for reproducing a particular subduction zone, the simulation results closely match natural seafloor topography and free-air gravity anomalies across the Mariana trench. This fit indicates that our model density field and the applied rheological model generate buoyancy and flexural stresses in agreement with this particular natural subduction zone. Calculated maximal absolute values of deviatoric stresses in the bending and subducting lithosphere are approximately 500 MPa. If absolute magnitudes of maximal deviatoric stresses are significantly less than 100 MPa, caused for example by a reduced friction angle, continuation of subduction does not occur because the denser subducting slab detaches from the lithosphere. Hence, deviatoric stress magnitudes of several hundreds of MPa are required for a continuous subduction. The uppermost region of the oblique, subducting slab shows high compressive stress, due to unbending, directly next to the subduction interface. Such high compressive stress may affect metamorphic reactions in rock units before they are detached from the subducting slab and exhumed to the surface.

2.7 Acknowledgements

We thank Fabio Crameri and an anonymous reviewer for very helpful and constructive reviews. This work was supported by the University of Lausanne.

Bibliography

- Babeyko, A., Sobolev, S., 2008. High-resolution numerical modeling of stress distribution in visco-elasto-plastic subducting slabs. *Lithos* 103 (1-2), 205–216.
- Bonvalot, S., Balmino, G., Briais, A., Kuhn, M., Peyrefitte, A., Vales, N., Biancale, R., Gabalda, G., Reinquin, F., Sarrailh, M., 2012. World Gravity Map. Commission for the Geological Map of the World. Eds. BGI-CGMW-CNES-IRD, Paris.
- Buchs, D. M., Pilet, S., Cosca, M., Flores, K. E., Bandini, A. N., Baumgartner, P. O., 2013. Low-volume intraplate volcanism in the Early/Middle Jurassic Pacific basin documented by accreted sequences in Costa Rica. *Geochemistry, Geophysics, Geosystems* 14 (5), 1552–1568.
- Burov, E., 2010. The equivalent elastic thickness (T_e), seismicity and the long-term rheology of continental lithosphere: Time to burn-out “crème brûlée”? *Tectonophysics* 484 (1-4), 4–26.
- Burov, E. B., 2011. Rheology and strength of the lithosphere. *Marine and Petroleum Geology* 28 (8), 1402–1443.
- Chertova, M. V., Geenen, T., van den Berg, A., Spakman, W., 2012. Using open sidewalls for modelling self-consistent lithosphere subduction dynamics. *Solid Earth* 3 (2), 313–326.
- Connolly, J. A. D., Podladchikov, Y. Y., 2007. Decompaction weakening and channeling instability in ductile porous media: Implications for asthenospheric melt segregation. *Journal of Geophysical Research* 112 (B10).
- Crameri, F., 2018. Scientific colour-maps. Zenodo.

- Cramer, F., Conrad, C. P., Montési, L., Lithgow-Bertelloni, C. R., 2019. The dynamic life of an oceanic plate. *Tectonophysics*.
- Cramer, F., Lithgow-Bertelloni, C., Tackley, P., 2017. The dynamical control of subduction parameters on surface topography. *Geochemistry, Geophysics, Geosystems* 18 (4), 1661–1687.
- Cramer, F., Tackley, P. J., Meilick, I., Gerya, T. V., Kaus, B. J. P., 2012. A free plate surface and weak oceanic crust produce single-sided subduction on Earth. *Geophysical Research Letters* 39 (3).
- Duret, T., Gerya, T. V., May, D. A., 2011a. Numerical modelling of spontaneous slab breakoff and subsequent topographic response. *Tectonophysics* 502 (1-2), 244–256.
- Duret, T., Gerya, T. V., Spakman, W., 2014. Slab detachment in laterally varying subduction zones: 3-D numerical modeling. *Geophysical Research Letters* 41 (6), 1951–1956.
- Duret, T., May, D., Yamato, P., 2016. A free surface capturing discretization for the staggered grid finite difference scheme. *Geophysical Journal International* 204 (3), 1518–1530.
- Duret, T., May, D. A., Gerya, T. V., Tackley, P. J., 2011b. Discretization errors and free surface stabilization in the finite difference and marker-in-cell method for applied geodynamics: A numerical study. *Geochemistry, Geophysics, Geosystems* 12 (7).
- Erdős, Z., Huisman, R. S., van der Beek, P., Thieulot, C., 2014. Extensional inheritance and surface processes as controlling factors of mountain belt structure: Inherited structural control on orogens. *Journal of Geophysical Research: Solid Earth* 119 (12), 9042–9061.
- Faccenda, M., Burlini, L., Gerya, T. V., Mainprice, D., 2008. Fault-induced seismic anisotropy by hydration in subducting oceanic plates. *Nature* 455 (7216), 1097–1100.
- Faccenda, M., Gerya, T. V., Burlini, L., 2009. Deep slab hydration induced by bending-related variations in tectonic pressure. *Nature Geoscience* 2 (11), 790–793.

- Faccenda, M., Gerya, T. V., Mancktelow, N. S., Moresi, L., 2012. Fluid flow during slab unbending and dehydration: Implications for intermediate-depth seismicity, slab weakening and deep water recycling. *Geochemistry, Geophysics, Geosystems* 13 (1).
- Farrington, R. J., Moresi, L.-N., Capitanio, F. A., 2014. The role of viscoelasticity in subducting plates. *Geochemistry, Geophysics, Geosystems* 15 (11), 4291–4304.
- Funiciello, F., Morra, G., Regenauer-Lieb, K., Giardini, D., 2003. Dynamics of retreating slabs: 1. Insights from two-dimensional numerical experiments. *Journal of Geophysical Research: Solid Earth* 108 (B4).
- Garel, F., Goes, S., Davies, D. R., Davies, J. H., Kramer, S. C., Wilson, C. R., 2014. Interaction of subducted slabs with the mantle transition-zone: A regime diagram from 2-D thermo-mechanical models with a mobile trench and an overriding plate. *Geochemistry, Geophysics, Geosystems* 15 (5), 1739–1765.
- Gerya, T., 2011. Future directions in subduction modeling. *Journal of Geodynamics* 52 (5), 344–378.
- Gerya, T., 2019. *Introduction to Numerical Geodynamic Modelling*, 2nd Edition. Cambridge University Press, Cambridge.
- Goetze, C., Evans, B., 1979. Stress and temperature in the bending lithosphere as constrained by experimental rock mechanics. *Geophysical Journal of the Royal Astronomical Society* 59 (3), 463–478.
- Gripp, A. E., Gordon, R. G., 1990. Current plate velocities relative to the hotspots incorporating the NUVEL-1 global plate motion model. *Geophysical Research Letters* 17 (8), 1109–1112.
- Gurnis, M., Hall, C., Lavier, L., 2004. Evolving force balance during incipient subduction. *Geochemistry, Geophysics, Geosystems* 5 (7).

- Hassani, R., Jongmans, D., Chéry, J., 1997. Study of plate deformation and stress in subduction processes using two-dimensional numerical models. *Journal of Geophysical Research: Solid Earth* 102 (B8), 17951–17965.
- Hetényi, G., Godard, V., Cattin, R., Connolly, J. A., 2011. Incorporating metamorphism in geodynamic models: the mass conservation problem: Metamorphism and mass conservation. *Geophysical Journal International* 186 (1), 6–10.
- Hirano, N., Koppers, A. A. P., Takahashi, A., Fujiwara, T., Nakanishi, M., 2008. Seamounts, knolls and petit-spot monogenetic volcanoes on the subducting Pacific Plate. *Basin Research* 20 (4), 543–553.
- Hirano, N., Machida, S., Abe, N., Morishita, T., Tamura, A., Arai, S., 2013. Petit-spot lava fields off the central Chile trench induced by plate flexure. *Geochemical Journal* 47 (2), 249–257.
- Hirano, N., Takahashi, E., Yamamoto, J., Abe, N., Ingle, S. P., Kaneoka, I., Hirata, T., Kimura, J.-I., Ishii, T., Ogawa, Y., Machida, S., Suyehiro, K., 2006. Volcanism in Response to Plate Flexure. *Science, New Series* 313 (5792), 1426–1428.
- Hirth, G., Kohlstedt, D., 2003. Rheology of the upper mantle and the mantle wedge: A view from the experimentalists. *Washington DC American Geophysical Union Geophysical Monograph Series* 138, 83–105.
- Holt, A. F., Becker, T. W., Buffett, B. A., 2015. Trench migration and overriding plate stress in dynamic subduction models. *Geophysical Journal International* 201 (1), 172–192.
- Jain, C., Korenaga, J., Karato, S.-i., 2017. On the Yield Strength of Oceanic Lithosphere. *Geophysical Research Letters* 44 (19), 9716–9722.
- Jaquet, Y., Duretz, T., Schmalholz, S. M., 2016. Dramatic effect of elasticity on thermal softening and strain localization during lithospheric shortening. *Geophysical Journal International* 204 (2), 780–784.

- Kameyama, M., Yuen, D. A., Karato, S.-I., 1999. Thermal-mechanical effects of low-temperature plasticity (the Peierls mechanism) on the deformation of a viscoelastic shear zone. *Earth and Planetary Science Letters* 168 (1-2), 159–172.
- Kawakatsu, H., Kumar, P., Takei, Y., Shinohara, M., Kanazawa, T., Araki, E., Suyehiro, K., 2009. Seismic Evidence for Sharp Lithosphere-Asthenosphere Boundaries of Oceanic Plates 324, 5.
- Kearey, P., Klepeis, K. A., Vine, F. J., 2009. *Global tectonics*, 3rd Edition. Wiley-Blackwell, Oxford ; Chichester, West Sussex ; Hoboken, NJ.
- Korenaga, J., 2017. On the extent of mantle hydration caused by plate bending. *Earth and Planetary Science Letters* 457, 1–9.
- Čížková, H., van Hunen, J., van den Berg, A., 2007. Stress distribution within subducting slabs and their deformation in the transition zone. *Physics of the Earth and Planetary Interiors* 161 (3-4), 202–214.
- Li, Z. H., Gerya, T. V., Burg, J.-P., 2010. Influence of tectonic overpressure on P - T paths of HP-UHP rocks in continental collision zones: thermomechanical modelling. *Journal of Metamorphic Geology* 28 (3), 227–247.
- Liu, X., Zhao, D., 2016. P and S wave tomography of Japan subduction zone from joint inversions of local and teleseismic travel times and surface-wave data. *Physics of the Earth and Planetary Interiors* 252, 1–22.
- Machida, S., Kogiso, T., Hirano, N., 2017. Petit-spot as definitive evidence for partial melting in the asthenosphere caused by CO₂. *Nature Communications* 8, 14302.
- Mallard, C., Coltice, N., Seton, M., Müller, R. D., Tackley, P. J., 2016. Subduction controls the distribution and fragmentation of Earth's tectonic plates. *Nature* 535, 140.
- Mei, S., Suzuki, A. M., Kohlstedt, D. L., Dixon, N. A., Durham, W. B., 2010. Experimental constraints on the strength of the lithospheric mantle. *Journal of Geophysical Research* 115 (B8).

- Molnar, P., England, P., Martinod, J., 1993. Mantle dynamics, uplift of the Tibetan Plateau, and the Indian Monsoon. *Reviews of Geophysics* 31 (4), 357–396.
- Molnar, P., Lyon-Caen, H., 1988. Some simple physical aspects of the support, structure, and evolution of mountain belts. In: *Geological Society of America Special Papers*. Vol. 218. Geological Society of America, pp. 179–208.
- Moresi, L., Dufour, F., Mühlhaus, H.-B., 2003. A Lagrangian integration point finite element method for large deformation modeling of viscoelastic geomaterials. *Journal of Computational Physics* 184 (2), 476–497.
- Moulas, E., Schmalholz, S. M., Podladchikov, Y., Tajčmanová, L., Kostopoulos, D., Baumgartner, L., 2019. Relation between mean stress, thermodynamic, and lithostatic pressure. *Journal of Metamorphic Geology* 37 (1), 1–14.
- Peacock, S. M., 2001. Are the lower planes of double seismic zones caused by serpentine dehydration in subducting oceanic mantle? *Geology* 29 (4), 299.
- Pilet, S., Abe, N., Rochat, L., Kaczmarek, M.-A., Hirano, N., Machida, S., Buchs, D. M., Baumgartner, P. O., Müntener, O., 2016. Pre-subduction metasomatic enrichment of the oceanic lithosphere induced by plate flexure. *Nature Geoscience* 9 (12), 898–903.
- Plümper, O., John, T., Podladchikov, Y. Y., Vrijmoed, J. C., Scambelluri, M., 2016. Fluid escape from subduction zones controlled by channel-forming reactive porosity. *Nature Geoscience* 10, 150.
- Popov, A., Sobolev, S., 2008. SLIM3D: A tool for three-dimensional thermomechanical modeling of lithospheric deformation with elasto-visco-plastic rheology. *Physics of the Earth and Planetary Interiors* 171 (1-4), 55–75.
- Ranero, C. R., Phipps Morgan, J., McIntosh, K., Reichert, C., 2003. Bending-related faulting and mantle serpentinization at the Middle America trench. *Nature* 425 (6956), 367–373.
- Ribe, N. M., 2010. Bending mechanics and mode selection in free subduction: a thin-sheet analysis. *Geophysical Journal International* 180 (2), 559–576.

- Schellart, W. P., Freeman, J., Stegman, D. R., Moresi, L., May, D., 2007. Evolution and diversity of subduction zones controlled by slab width. *Nature* 446, 308.
- Schmalholz, S. M., Duretz, T., 2017. Impact of grain size evolution on necking in calcite layers deforming by combined diffusion and dislocation creep. *Journal of Structural Geology* 103, 37–56.
- Schmalholz, S. M., Duretz, T., Hetényi, G., Medvedev, S., 2019. Distribution and magnitude of stress due to lateral variation of gravitational potential energy between Indian lowland and Tibetan plateau. *Geophysical Journal International* 216 (2), 1313–1333.
- Schmalholz, S. M., Fletcher, R. C., 2011. The exponential flow law applied to necking and folding of a ductile layer: Exponential flow law applied to folding and necking. *Geophysical Journal International* 184 (1), 83–89.
- Schmalholz, S. M., Medvedev, S., Lechmann, S. M., Podladchikov, Y., 2014. Relationship between tectonic overpressure, deviatoric stress, driving force, isostasy and gravitational potential energy. *Geophysical Journal International* 197 (2), 680–696.
- Schmalholz, S. M., Podladchikov, Y. Y., 2013. Tectonic overpressure in weak crustal-scale shear zones and implications for the exhumation of high-pressure rocks. *Geophysical Research Letters* 40 (10), 1984–1988.
- Schmalholz, S. M., Podladchikov, Y. Y., Schmid, D. W., 2001. A spectral/finite difference method for simulating large deformations of heterogeneous, viscoelastic materials. *Geophysical Journal International* 145 (1), 199–208.
- Schmeling, H., Babeyko, A., Enns, A., Faccenna, C., Funiciello, F., Gerya, T., Golabek, G., Grigull, S., Kaus, B., Morra, G., Schmalholz, S., van Hunen, J., 2008. A benchmark comparison of spontaneous subduction models—Towards a free surface. *Physics of the Earth and Planetary Interiors* 171 (1-4), 198–223.
- Sibson, R. H., Moore, J. M. M., Rankin, A. H., 1975. Seismic pumping—a hydrothermal fluid transport mechanism. *Journal of the Geological Society* 131 (6), 653–659.

- Sobolev, S. V., Babeyko, A. Y., Koulakov, I., Oncken, O., 2006. Mechanism of the Andean Orogeny: Insight from Numerical Modeling. In: *The Andes: Active Subduction Orogeny. Frontiers in Earth Sciences*. Springer, Berlin, Heidelberg, pp. 513–535.
- Stern, R. J., 2002. Subduction zones. *Reviews of Geophysics* 40 (4), 1012.
- Stern, R. J., Gerya, T., 2018. Subduction initiation in nature and models: A review. *Tectonophysics* 746, 173–198.
- Talwani, M., Worzel, J. L., Landisman, M., 1959. Rapid gravity computations for two-dimensional bodies with application to the Mendocino submarine fracture zone. *Journal of Geophysical Research* 64 (1), 49–59.
- Taneja, R., O'Neill, C., Lackie, M., Rushmer, T., Schmidt, P., Jourdan, F., 2015. $^{40}\text{Ar}/^{39}\text{Ar}$ geochronology and the paleoposition of Christmas Island (Australia), Northeast Indian Ocean. *Gondwana Research* 28 (1), 391–406.
- Toth, J., Gurnis, M., 1998. Dynamics of subduction initiation at preexisting fault zones. *Journal of Geophysical Research: Solid Earth* 103 (B8), 18053–18067.
- Turcotte, D., Schubert, G., 2014. *Geodynamics*, 3rd Edition. Cambridge, UK: Cambridge University Press.
- Won, I. J., Bevis, M., 1987. Computing the gravitational and magnetic anomalies due to a polygon: Algorithms and Fortran subroutines. *Geophysics* 52 (2), 232–238.
- Yamamoto, J., Korenaga, J., Hirano, N., Kagi, H., 2014. Melt-rich lithosphere-asthenosphere boundary inferred from petit-spot volcanoes. *Geology* 42 (11), 967–970.
- Yamato, P., Agard, P., Burov, E., Le Pourhiet, L., Jolivet, L., Tiberi, C., 2007. Burial and exhumation in a subduction wedge: Mutual constraints from thermomechanical modeling and natural P-T-t data (Schistes Lustrés, western Alps). *Journal of Geophysical Research* 112 (B7).
- Yamato, P., Husson, L., Braun, J., Loiselet, C., Thieulot, C., 2009. Influence of surrounding plates on 3D subduction dynamics. *Geophysical Research Letters* 36 (7).

-
- Youngs, R. R., Chiou, S.-J., Silva, W. J., Humphrey, J. R., 1997. Strong Ground Motion Attenuation Relationships for Subduction Zone Earthquakes. *Seismological Research Letters* 68 (1), 58–73.
- Zhong, S., Gurnis, M., 1994. Controls on trench topography from dynamic models of subducted slabs. *Journal of Geophysical Research: Solid Earth* 99 (B8), 15683–15695.

CHAPTER 3

Melt migration and chemical differentiation by reactive porosity waves

**Annelore Bessat¹, Sébastien Pilet¹, Yuri Y. Podladchikov¹ and Stefan M.
Schmalholz¹**

¹Institute of Earth Sciences, University of Lausanne, 1015 Lausanne, Switzerland.

Abstract

The extraction of low-degree melt from its sources and its transport across the ductile part of the mantle is a key process in the Earth sciences since it is essential for the formation of oceanic crust at mid-ocean ridges, of small to large volcanoes in intraplate settings or for arc magmatism. Metasomatic enrichment of the lithospheric mantle demonstrates that such low-degree melts chemically interact with the lithosphere. However, the mechanism of melt migration in the ductile mantle and the involved coupling of physical and chemical processes remain unclear. Here, we present a thermo-hydro-mechanical-chemical (THMC) transport model for melt migration, coupled to thermodynamic results obtained from Gibbs energy minimisation, to investigate the impact of chemical differentiation on melt migration. We study melt migration by porosity waves within a deformable viscous mantle and use a simple ternary thermodynamic system of forsterite-fayalite-silica for the solid and melt phases. We solve the one-dimensional (1D) THMC transport model numerically with a pseudo-transient finite difference method and Gibbs energy minimisations with linear programming routines using MATLAB. Model variables, such as solid and melt densities or mass concentrations of MgO and SiO₂ in solid and melt, are all fully variable and mobile, and are functions of pressure (P), temperature (T) and total silica mass fraction of the system ($C_T^{\text{SiO}_2}$). These variables are pre-computed with Gibbs energy minimisation and implemented in the THMC porosity wave transport code via parameterized equations, determining the P - T - $C_T^{\text{SiO}_2}$ dependence of the model variables. We consider pressure (P) and temperature (T) conditions relevant around the lithosphere-asthenosphere boundary and employ adiabatic and conductive geotherms. The results show that the total silica concentration and the geotherm have a strong impact on melt migration by reactive porosity waves. We perform a systematic series of 1D simulations to quantify the impact of the initial distribution of porosity and total silica mass fraction on the melt velocity. We further discuss preliminary results of two 2D reactive porosity wave simulations showing blob-like and channel-like porosity waves.

3.1 Introduction

The extraction of melt from its sources and melt transport across the mantle to the surface is a key process in Earth sciences (e.g. McKenzie, 1984; Spiegelman et al., 2001; Keller and Suckale, 2019). The different geodynamic settings with magmatism observed around the world, such as mid-ocean ridges (MORs), volcanic arcs and intraplate volcanism, indicate that asthenospheric melts are extracted under significantly distinct pressure, temperature and rheological conditions. The main difference between melt extraction at intraplate settings and at MORs is the presence of the lithospheric mantle for the intraplate settings. The geochemical signature of MOR basalt (MORB) presumably depends on magma source composition, melt-extraction and differentiation processes intervening between the magma source and the crust (e.g. Langmuir et al., 1992). MORBs are produced and migrate in the asthenosphere and temperature (T) and pressure (P) variations are, hence, controlled by the mantle adiabat. In contrast, asthenospheric melts produced in intraplate settings need to cross the continental or oceanic lithosphere before their extraction to the surface. The lithosphere is characterized by a strong temperature gradient and the associated vertical rheological variations from viscous to elasto-plastic domains (e.g. Burov, 2011). Melt migration in the ductile domain is presumably controlled by porous flow in a viscous solid (McKenzie, 1984), while hydrous fracture propagating into the brittle domain allow melt transport to the surface (e.g. Shaw, 1980; Keller et al., 2013). For intraplate volcanoes, only few studies have focused on the mechanism of extraction and transport of melt across a thick and cold lithosphere, considering a visco-elasto-plastic deformation behavior (e.g. Keller et al., 2013). Hence, many aspects of the thermo-hydro-mechanical (THM) process of melt migration across the lithosphere remain still little constrained.

In addition to THM processes, melt migration can be affected by chemical (C) reactions, leading to a reactive melt flow (e.g. Jackson et al., 2018). For example, low-viscosity magma, like carbonatite or volatile-rich low degree silicate melts, can rise in the upper mantle. However, such low-degree melts cannot transport significant heat (McKenzie, 1985) and if such melts rise in the lithospheric mantle with a considerable geothermal gradient, then these melts likely

interact with the surrounding solid mantle, cool, and crystallize. This melt-solid interaction is frequently referred to as metasomatism and was documented by various xenoliths sampled by kimberlites or intraplate basalts worldwide (e.g. Best, 1974; Lloyd and Bailey, 1975; Francis, 1976; Irving, 1980). Metasomatic processes are important to understand the chemical evolution of the continental lithosphere (e.g. Griffin et al., 2009) and the petrogenesis of alkaline lavas (e.g. Lloyd and Bailey, 1975; Wass and Roge, 1980; Pilet et al., 2008). However, the origin of the metasomatic agent(s), the process by which low degree melts percolate across the lithosphere, and whether metasomatic processes represent a global mechanism at the asthenosphere-lithosphere boundary (LAB) are still a matter of debate. Therefore, we aim here to investigate coupled THMC processes during melt migration around the LAB. From a geometrical point of view, there are two general styles of flow during melt migration in a viscous domain: (1) a spatially distributed flow, characterised by a pervasive percolation of melt between the crystals of the solid rock (e.g. olivine or pyroxene crystals in a peridotite) and (2) a spatially focused flow where melt migration is localized in channels, which is documented in the mantle by the presence of metasomatic veins (Wilshire, 1987; Harte et al., 1993). According to the lithosphere thermal gradient, rising melt cools progressively and crystallizes mineral phases which are segregated within the lithospheric mantle, producing metasomatic cumulates sampled by intraplate lavas or observed in mantle outcrops (e.g. Nielson and Noller, 1987; Wilshire, 1987; Nielson and Wilshire, 1993; Harte et al., 1993). Both distributed and focused flows involve a change in the composition of the melt due to its interaction with the solid. For distributed flow, the change of composition is achieved by the infiltrating melt that reacts with the peridotite through an exchange of elements (so-called cryptic metasomatism; Wilshire, 1987). For focused flow, the change in melt composition occurs through differentiation as phases crystallise (so called percolative fractional crystallization; Harte et al., 1993). Most models for the metasomatic enrichment were developed based on observations made in the brittle part of the lithosphere. How metasomatic agents move into the ductile part of the mantle, how such melt interacts with the solid and how channelizing is generated are questions still debated.

The rise of large coherent magma bodies in a viscous solid can be described by diapiric flow (e.g. Cruden, 1988; Weinberg and Podladchikov, 1994; Miller and Paterson, 1999). However, the physical process of melt extraction and migration in partially molten viscous rock is commonly described by two-phase flow models whereby the melt, representing the fluid phase, flows through the pore space of the viscous rock, representing the solid phase (e.g. McKenzie, 1984). There are several extraction processes for melt migration in a porous, ductile rock: (1) porous flow, described by Darcy's law, controlled by the rate of melt expulsion whereby the characteristics of solid deformation are of minor importance (e.g. Walker et al., 1978; Ahern and Turcotte, 1979), (2) melt transport by porosity waves for which volumetric deformation of the viscous solid is essential (e.g. McKenzie, 1984; Scott and Stevenson, 1984; Spiegelman, 1993; Connolly and Podladchikov, 1998, 2007; Keller et al., 2013; Yarushina and Podladchikov, 2015; Omlin et al., 2017; Jordan et al., 2018), (3) melt migration by reaction infiltration instabilities controlled by depth-dependent solubilities (e.g. Aharonov et al., 1995, 1997; Kelemen et al., 1997; Spiegelman et al., 2001; Weatherley and Katz, 2012; Jones and Katz, 2018) and (4) extraction by shear localization and melt segregation generating melt bands (e.g. Stevenson, 1989; Katz et al., 2006; Holtzman and Kohlstedt, 2007). We focus here on melt migration by porosity waves. Connolly and Podladchikov (1998) show that employing a visco-elastic volumetric deformation of the solid enables porosity waves to travel through rock in the limit of zero initial connected porosity. Low-porosity (i.e. few percent) scenarios are most relevant for melt migration across the viscous lithosphere. The application of decompaction weakening (e.g. Connolly and Podladchikov, 1998, 2007) and the consideration of viscous shear deformation of the solid (Räss et al., 2019) enables a significant channelization of porosity waves for two- and three-dimensional (2D and 3D) flow. Furthermore, Omlin et al. (2017) show that the coupling of the kinetics of chemical reactions with fluid flow may enable porosity waves also to potentially arise in low-temperature regimes, so that the porosity waves are not necessarily limited to the high-temperature viscous regions (Chakraborty, 2017). Moreover, Jordan et al. (2018) show that mass, and hence melt, can be transported in 2D and 3D porosity waves; a fact that has been doubted based on 1D porosity

wave studies. Therefore, porosity waves are a potential mechanism to transport significant melt in a channelized style across the LAB and the lithospheric mantle.

Here, we present a new numerical THMC model to investigate reactive melt migration by porosity waves in a viscous solid coupled to heat transfer and to chemical differentiation of major elements in the melt and solid. Chemical differentiation of major elements is important for melt migration because it changes the density of the melt and solid. Such density variations do not occur for trace element transport by porosity waves (e.g. Jordan et al., 2018) applied to study, for example, the chromatographic separation occurring during percolation (Korzhinskii, 1965; Hofmann, 1972), because trace elements do not alter the density of melt and solid. The importance of chemical differentiation for the rise of magma in the crust has been highlighted recently by Jackson et al. (2018). We couple our THMC model with thermodynamic results calculated by Gibbs energy minimisation. We perform this minimisation with a self-developed MATLAB code using a linear programming algorithm. The P and T conditions are chosen to reflect conditions at the LAB. We consider a simple ternary system composition of MgO, FeO and SiO₂ based on the olivine phase diagram system, forsterite (Mg₂SiO₄) and fayalite (Fe₂SiO₄). We consider conditions for which the system is always between solidus and liquidus so that both melt and solid phase are present simultaneously. We extend this binary system by adding more SiO₂ using experimental data of peridotite in equilibrium with melt at 3 GPa (Davis et al., 2011). All model variables determined by thermodynamic calculations (e.g. solid and melt densities, mass fractions of MgO and SiO₂ of the melt and the solid) are a function of P , T and chemical SiO₂ composition of the system ($C_T^{\text{SiO}_2}$). These variables and their dependence of P , T and SiO₂ are precomputed and used in the THMC reactive transport model, so that they can evolve freely with evolving P , T and SiO₂. The model, hence, allows quantifying the impact of variations in the chemical composition on melt migration.

The aims of this study are (i) to present a new numerical THMC-thermodynamic model for coupled melt migration and chemical differentiation by reactive porosity waves, (ii) to explain specific features of coupling chemical differentiation with porosity waves and (iii) to discuss potential applications of our model to melt migration around the LAB. We present the model

derivation and some systematic results for 1D and show two representative results for 2D showing blob- and channel-type reactive porosity waves.

3.2 Mathematical model

We develop a 1D mathematical model for THMC reactive transport by porosity waves. The model is based on the concepts of continuum mechanics, two-phase flow and equilibrium thermodynamics and follows the same approach in deriving a closed system of equations as described in Yarushina and Podladchikov (2015); Malvoisin et al. (2015) or Schmalholz et al. (2020). The complete THMC model consists of two parts: a THMC model for reactive transport of melt by porosity waves, consisting of a system of partial differential equations, and a thermodynamic model, based on Gibbs energy minimisation, which provides the required solid and melt densities, solid and melt mass fractions of MgO and SiO₂, and solid and melt thermal energies, and their respective dependencies on P , T and $C_T^{\text{SiO}_2}$.

3.2.1 Thermodynamic model

We apply a thermodynamic model to determine the stable phases for a range of P , T and composition (X). We start with a simple binary system of olivine (Fig. 3.1a) between forsterite, the olivine magnesium-rich end-member (Mg₂SiO₄), and fayalite, the olivine iron-rich end-member (Fe₂SiO₄).

We minimize the Gibbs free energy, G , to determine the equilibrium of the binary system. The Gibbs free energies used for the minimisation are from the thermodynamic database of Holland and Powell (1998). To calculate this minimisation, we use the linear programming “linprog” algorithm from MATLAB. We consider a pressure range of 0.1 GPa to 4.9 GPa and a temperature range of 1’200°C to 1’700°C. The X composition varies from 0 to 1, with 0 corresponding to 100% of fayalite and 0% of forsterite and 1 corresponding to 0% fayalite and 100% of forsterite. There are four mineral phases for this solid-melt system; for the solid part there are forsterite (fo) and fayalite (fa) as well as for the melt (liquid) part there are forsterite

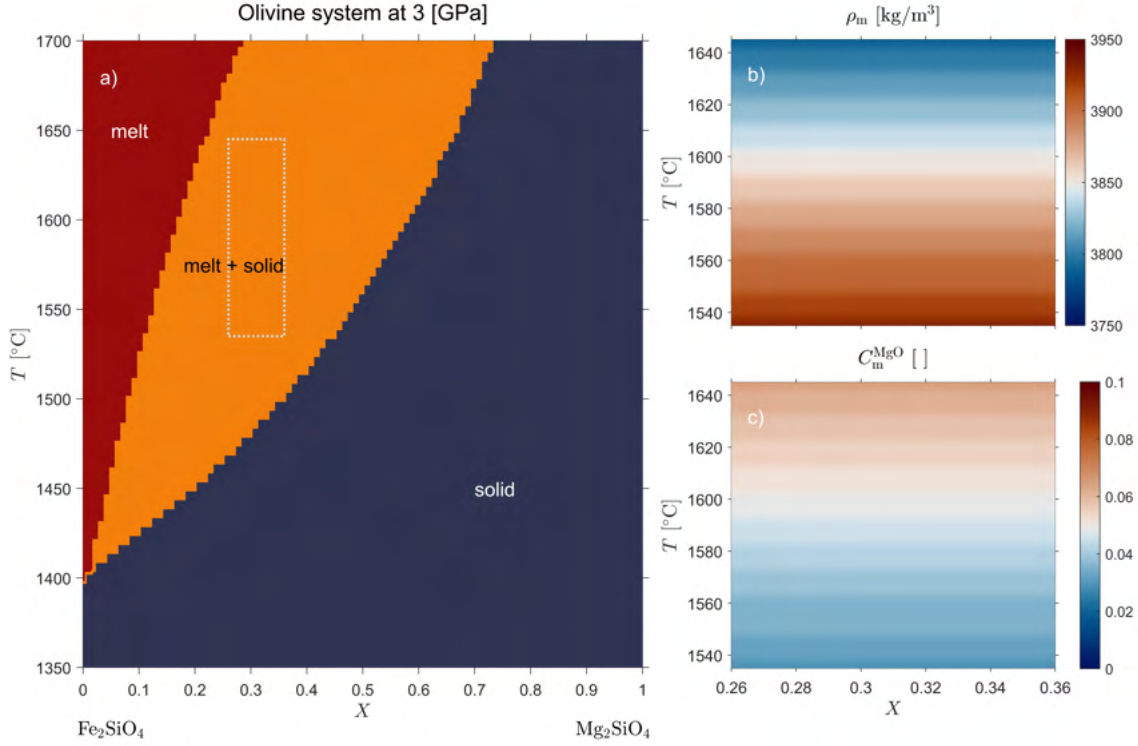


Figure 3.1: Panel (a) shows the binary system of olivine for a pressure of 3 GPa. Blue area shows where solid is stable, red area shows where melt is stable and orange area shows where both solid and melt are stable. Dashed square indicates the region used to calculate thermodynamic variables employed in the THMC model. Panels (b) and (c) show respectively, the melt density and the melt mass fraction of magnesium (in the dashed region), which are independent on X in the region of interest.

(foL) and fayalite (faL) (see Holland and Powell, 1998 for nomenclature). Figure 3.1a shows the result of the minimisation and emphasizes where the phases are stable for a pressure of 3 GPa. After the minimisation of G , in each point of the P - T - X domain, we extract several quantities for the melt (with subscript m) and the solid (with subscript s; all listed in Table 3.1): Gibbs energy, G_m and G_s in $[\text{J}\cdot\text{mol}^{-1}]$, volume, V_m and V_s in $[\text{m}^3\cdot\text{mol}^{-1}]$, entropy, S_m and S_s in $[\text{J}\cdot\text{mol}^{-1}\cdot\text{K}^{-1}]$ and specific heat capacity, c_{p_m} and c_{p_s} in $[\text{J}\cdot\text{mol}^{-1}\cdot\text{K}^{-1}]$. We calculate the extensive quantities from the Gibbs energies, volume $V_{m,s} = \frac{dG_{m,s}}{dP}$ and entropy $S_{m,s} = -\frac{dG_{m,s}}{dT}$. The specific heat capacity $c_{p_{m,s}} = T\frac{dS_{m,s}}{dT}$. To have all parameters in mass units of kilogram, and not in mole, we divide all quantities by their respective melt or solid molar mass, m_m and m_s in $[\text{kg}\cdot\text{mol}^{-1}]$. With the volume per unit mass, we can then calculate melt and solid density, $\rho_{m,s} = \frac{1}{V_{m,s}}$ in $[\text{kg}\cdot\text{m}^{-3}]$. In addition, several molar fractions (in mole

units) can be obtained from Gibbs minimisation, like melt concentrations of forsterite and fayalite, $C_{m,[mol]}^{foL}$ and $C_{m,[mol]}^{faL}$, and solid concentrations of forsterite and fayalite, $C_{s,[mol]}^{fo}$ and $C_{s,[mol]}^{fa}$. We transform them into mass fractions in order to use them in the mass conservation equations of the THMC model. The details of this transformation are presented in Appendix C, equations C1 to C3.

In the solid-melt THMC model, we focus on the thermodynamic region where melt and solid coexist (orange area in Fig. 3.1a). In the considered P - T - X domain, this region has a pressure range of 2.4001 GPa to 3.5001 GPa, a temperature range of 1'535°C (1'808.15 K) to 1'645°C (1'918.15 K) and a composition range of 0.26 to 0.36. Figures 3.1b and 3.1c show that the variation in melt density (ρ_m) and in melt mass fraction of magnesium (C_m^{MgO}), respectively, are independent of composition in this range. Accordingly, all other thermodynamic parameters used in the THMC model are also independent of composition, such as solid density (ρ_s), solid mass fraction of magnesium (C_s^{MgO}) and melt and solid mass fractions of silica ($C_m^{SiO_2}, C_s^{SiO_2}$). Therefore, we can reduce our binary P - T - X domain to a P - T domain for all considered parameters. The independency of densities and mass fractions on composition X is a result of the Gibbs phase rule (e.g. Müller, 2007) because there is no degree of freedom for a system with two components (fo and fa) and two phases (solid and melt) for a given temperature and pressure. Figure 3.2 shows the variation of thermodynamic parameters used in the THMC code as function of temperature and pressure. All parameters show an essentially linear variation with P and T (Figure 3.2).

The essentially linear variation allows making a linear approximation for all six parameters by calculating two values, α and β , whereby α quantifies the variation of a variable with respect to a variation of temperature, for a constant pressure of reference P_0 , and β quantifies the variation of the variable with respect to a variation of pressure, for a constant temperature of reference T_0 . The α and β for the six variables are calculated, for example, for the melt density by (see Fig. 3.2a for details):

$$\alpha_{\rho_m} = \left(\frac{\rho_m(2, P_0) - \rho_m(1, P_0)}{\Delta T} \right) / \rho_{m,0} \quad (3.1)$$

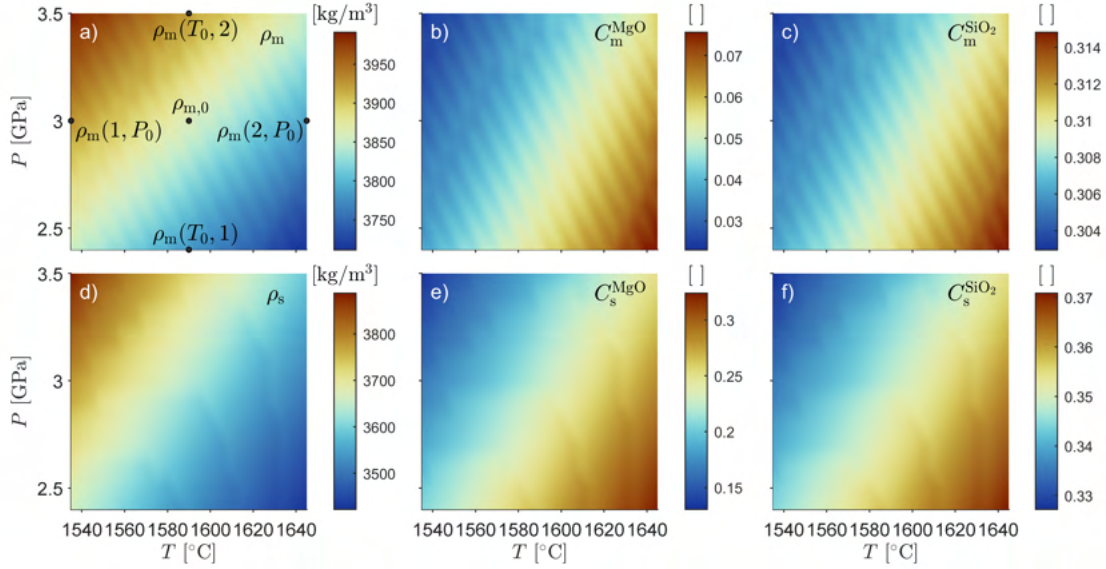


Figure 3.2: Variation of thermodynamic variables used in the THMC transport code. Variables are calculated by Gibbs free energy minimization. Enlargement of the region of coexistence between melt and solid (orange area in Fig. 3.1a). All parameters depend on temperature and pressure: panel (a) for melt density, panel (d) for solid density, panel (b) for mass fraction of magnesium in melt, panel (e) for mass fraction of magnesium in solid, panel (c) for mass fraction of silica in melt and panel (f) for mass fraction of silica in solid. Black points in panel (a) are used to calculate α and β in equations 3.1 and 3.2.

$$\beta_{\rho_m} = \left(\frac{\rho_m(T_0, 2) - \rho_m(T_0, 1)}{\Delta P} \right) / \rho_{m,0} \quad (3.2)$$

where ΔT and ΔP are the temperature and pressure differences of domain P - T , $\rho_m(2, P_0) - \rho_m(1, P_0)$ is density variation as function of temperature, $\rho_m(T_0, 2) - \rho_m(T_0, 1)$ is density variation as function of pressure and $\rho_{m,0}$ is the density at the reference point T_0 and P_0 . The same procedure is applied for the other five parameters: the resulting α , β and corresponding reference points are given in Table 3.2. Figure 3.3 shows the results of this approximation for each variable.

A particular result for olivine in the considered pressure and temperature range is that solid density is smaller than melt density (Figs. 3.2 and 3.3). This is a known phenomenon in the forsterite-fayalite system for high temperature (e.g. Herzberg et al., 1982). For melt to rise, it should have a smaller density than the solid. To obtain smaller melt densities, we add another composition dimension to our P - T domain, which is the total silica mass fraction

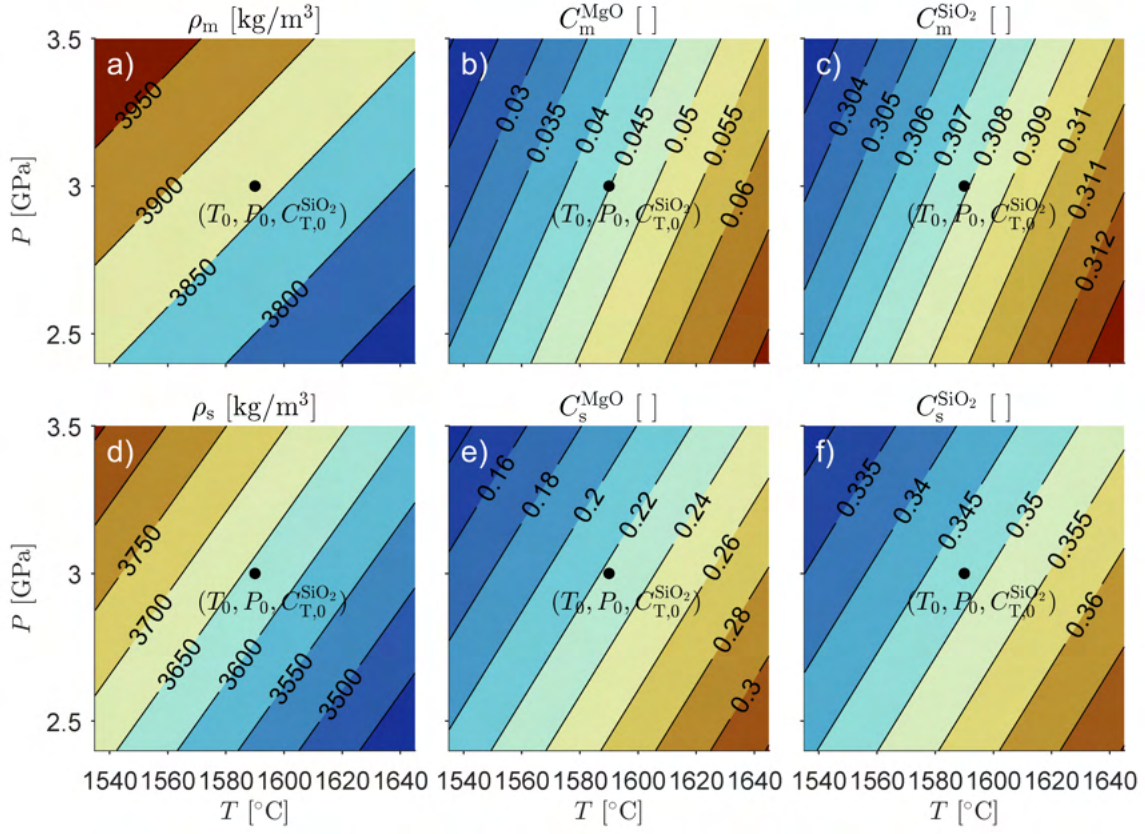


Figure 3.3: Linear approximation of data obtained by thermodynamics with α and β . All variations are in function of temperature and pressure: panel (a) for melt density, panel (d) for solid density, panel (b) for mass fraction of magnesium in melt, panel (e) for mass fraction of magnesium in solid, panel (c) for mass fraction of silica in melt and panel (f) for mass fraction of silica in solid. Black point in the centre of each panel is the reference point at T_0 , P_0 and $C_{T,0}^{\text{SiO}_2}$. $C_{T,0}^{\text{SiO}_2}$ corresponds to the total mass fraction of silica in the olivine.

$C_T^{\text{SiO}_2}$. Adding more silica to the olivine system allows to change the melt and solid densities of the system to a more realistic value for a peridotitic system. For simplicity, we did not included pyroxenes in our thermodynamic calculation.

The total silica mass fraction ($C_T^{\text{SiO}_2}$) is calculated at the reference point T_0 and P_0 as follows:

$$C_{T,0}^{\text{SiO}_2} = \frac{C_{m,0}^{\text{SiO}_2} + C_{s,0}^{\text{SiO}_2}}{C_{m,0}^{\text{MgO}} + C_{s,0}^{\text{MgO}} + C_{m,0}^{\text{FeO}} + C_{s,0}^{\text{FeO}} + C_{m,0}^{\text{SiO}_2} + C_{s,0}^{\text{SiO}_2}} \quad (3.3)$$

By increasing the total silica mass fraction, the density of melt will become smaller than the density of solid, allowing the melt to percolate towards the surface. We use an experiment by

Davis et al. (2011) which provides the composition of a peridotite in equilibrium with the first magma produced by partial melting at a pressure of 3 GPa and a temperature of 1'450 °C. These experimental compositions are reported as “KLB-1ox” for the solid, and “0% melt” for melt in Table 1 of Davis et al. (2011). The combination of these data and the values obtained by our thermodynamic olivine model allows calculating a γ parameter that quantifies the variation of the six variables, ρ_m , ρ_s , C_m^{MgO} , C_s^{MgO} , $C_m^{\text{SiO}_2}$, $C_s^{\text{SiO}_2}$, as function of the total silica mass fraction in the system. To calculate γ for mass fractions of magnesium or silica for melt and solid, we transform MgO, FeO and SiO₂ oxides weight percent of “KLB-1ox” and “0% melt” into oxides mass fractions (here shown for MgO, same procedure for FeO and SiO₂):

$$C_{m,\text{exp}}^{\text{MgO}} = \frac{C_{0\% \text{melt}, [\text{wt}\%]}^{\text{MgO}}}{C_{0\% \text{melt}, [\text{wt}\%]}^{\text{MgO}} + C_{0\% \text{melt}, [\text{wt}\%]}^{\text{FeO}} + C_{0\% \text{melt}, [\text{wt}\%]}^{\text{SiO}_2}} \quad (3.4a)$$

$$C_{s,\text{exp}}^{\text{MgO}} = \frac{C_{\text{KLB-1ox}, [\text{wt}\%]}^{\text{MgO}}}{C_{\text{KLB-1ox}, [\text{wt}\%]}^{\text{MgO}} + C_{\text{KLB-1ox}, [\text{wt}\%]}^{\text{FeO}} + C_{\text{KLB-1ox}, [\text{wt}\%]}^{\text{SiO}_2}} \quad (3.4b)$$

The total silica mass fraction of experiment, $C_{T,\text{exp}}^{\text{SiO}_2}$, is calculated in the same way as shown in equation 3.3. Then we calculate the γ (here shown for C_m^{MgO} and C_s^{MgO} , same procedure for $C_m^{\text{SiO}_2}$ and $C_s^{\text{SiO}_2}$ shown in Appendix C, equation 3.C4) by:

$$\gamma_{C_m^{\text{MgO}}} = \left(\frac{C_{m,\text{exp}}^{\text{MgO}} - C_{m,0}^{\text{MgO}}}{C_{T,\text{exp}}^{\text{SiO}_2} - C_{T,0}^{\text{SiO}_2}} \right) / C_{m,0}^{\text{MgO}} \quad (3.5a)$$

$$\gamma_{C_s^{\text{MgO}}} = \left(\frac{C_{s,\text{exp}}^{\text{MgO}} - C_{s,0}^{\text{MgO}}}{C_{T,\text{exp}}^{\text{SiO}_2} - C_{T,0}^{\text{SiO}_2}} \right) / C_{s,0}^{\text{MgO}} \quad (3.5b)$$

To calculate γ for melt and solid densities we proceed in the same way:

$$\gamma_{\rho_m} = \left(\frac{\rho_{m,\text{exp}} - \rho_{m,0}}{C_{T,\text{exp}}^{\text{SiO}_2} - C_{T,0}^{\text{SiO}_2}} \right) / \rho_{m,0} \quad (3.6a)$$

$$\gamma_{\rho_s} = \left(\frac{\rho_{s,\text{exp}} - \rho_{s,0}}{C_{T,\text{exp}}^{\text{SiO}_2} - C_{T,0}^{\text{SiO}_2}} \right) / \rho_{s,0} \quad (3.6b)$$

The values for the melt and solid densities, $\rho_{m,\text{exp}}$ and $\rho_{s,\text{exp}}$, are not provided in Davis et al. (2011). We calculate these densities using the values included in our thermodynamic data base and the mineral mode reported in Table 1 of Davis et al. (2011) (see Appendix C for the detail of these calculations).

Figure 3.4 shows the linear approximation using γ for the different variables between the forsterite-fayalite binary olivine system, $C_{T,0}^{\text{SiO}_2}=0.33$, and the experiment of Davis et al. (2011), $C_{T,\text{experiment}}^{\text{SiO}_2}=0.56$. Figure 3.4a shows the relative change of solid and melt densities and the value of $C_T^{\text{SiO}_2}=0.41$, indicated by the vertical black dashed line, for which melt and solid densities are equal.

To calculate the melt and solid thermal energies, U_m and U_s , required for the temperature calculation, we only consider, for simplicity, their variation with respect to temperature and density. We use values for the respective melt and solid specific heat at the reference point T_0 and P_0 , $c_{p_{m,0}}$ and $c_{p_{s,0}}$ (values are given in Table 3.2), and calculate the thermal energies by:

$$U_m = \rho_m \cdot c_{p_{m,0}} \cdot T \quad (3.7a)$$

$$U_s = \rho_s \cdot c_{p_{s,0}} \cdot T \quad (3.7b)$$

We apply this simplification of the thermal solid and melt energies because in our model the temperature deviation from the initial thermal gradient is small because we remain in the region of coexistence of melt and solid.

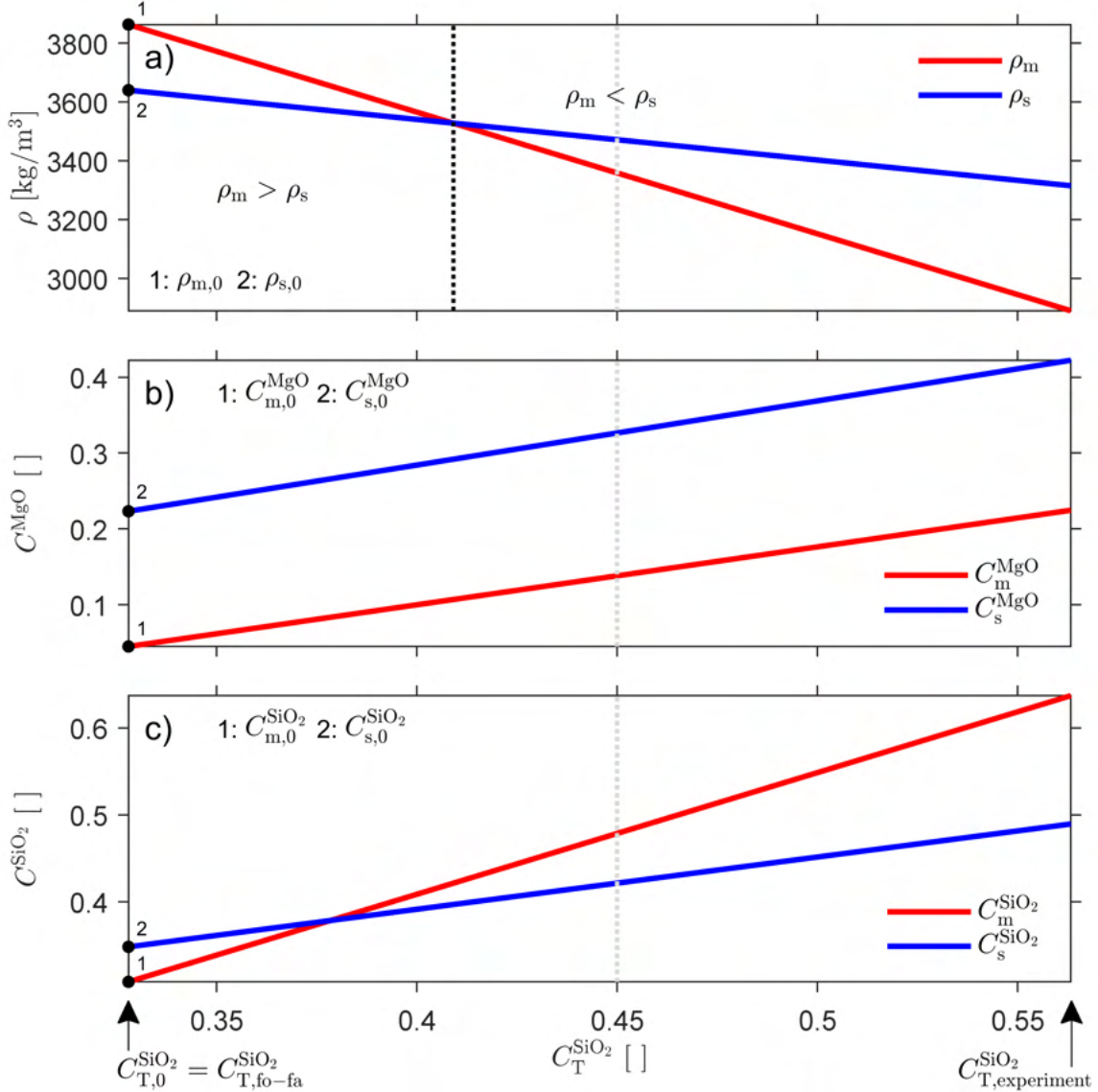


Figure 3.4: Linearized dependence of thermodynamic variables on total silica mass fraction, $C_T^{\text{SiO}_2}$. Panel (a) densities, melt in red and solid in blue, panel (b) mass fractions of magnesium, melt in red and solid in blue and panel (c) mass fractions of silica, melt in red and solid in blue. Black points are reference values of each variable at T_0 , P_0 and $C_{T,0}^{\text{SiO}_2}$ in Figure 3.3. $C_{T,\text{experiment}}^{\text{SiO}_2}$ corresponds to the total mass fraction of silica in the experiment of Davis et al. (2011). The black dashed line indicates at which total silica mass fraction the melt density becomes smaller than the solid density. The grey dashed line shows the value selected in the THMC model as the initial total silica mass fraction.

In summary, the thermodynamic model calculates eight variables: solid and melt densities, solid and melt mass fractions of MgO and SiO₂, and solid and melt specific heat. The densities and mass fractions are all a function of pressure, temperature and total SiO₂ concentration and these dependencies will be quantified below by a total of 18 parameters, namely 6 different values each for α , β and γ (Table 3.2). These 18 parameters will be used in the THMC transport model.

Table 3.1: Parameters used in the thermodynamic and THMC model

Symbol	Meaning	Units
ρ_m, ρ_s, ρ_T	melt, solid and total densities	$\text{kg}\cdot\text{m}^{-3}$
$C_m^{\text{MgO}}, C_s^{\text{MgO}}, C_m^{\text{SiO}_2}, C_s^{\text{SiO}_2}$	mass fractions of magnesium or silica for melt and solid	[]
U_m, U_s	melt, solid internal energy	$\text{J}\cdot\text{mol}^{-1}$
c_{p_m}, c_{p_s}	melt, solid specific heat capacity	$\text{J}\cdot\text{kg}^{-1}\cdot\text{K}^{-1}$
$\lambda_m, \lambda_s, \lambda_T$	melt, solid and total thermal conductivity	$\text{W}\cdot\text{m}^{-1}\cdot\text{K}^{-1}$
G_m, G_s	melt, solid Gibbs energies	$\text{J}\cdot\text{mol}^{-1}$
V_m, V_s	melt, solid volumes	$\text{m}^3\cdot\text{mol}^{-1}$
S_m, S_s	melt, solid entropy	$\text{J}\cdot\text{mol}^{-1}\cdot\text{K}^{-1}$
m_m, m_s	melt, solid molar mass	$\text{kg}\cdot\text{mol}^{-1}$
k	permeability	m^2
φ	porosity	[]
v_m, v_s	melt, solid velocity	$\text{m}\cdot\text{s}^{-1}$
σ_{xx}	total stress	Pa
τ	deviatoric stress	Pa
g	gravitational acceleration	$\text{m}\cdot\text{s}^{-2}$
P_T, P_m, P_e	total pressure, melt pressure and effective pressure	Pa
η_s, η_v, η_m	shear viscosity, compaction viscosity and melt viscosity	Pa·s
t	time	s
T	temperature	K

3.2.2 Thermo-Hydro-Mechanical-Chemical model

The applied THMC model is based on a system of conservation equations. The general derivation of these conservation equations is given in the appendix and below only the applied equations are given. The conservation of total mass is

$$\frac{\partial}{\partial t}(\rho_m \varphi + \rho_s(1 - \varphi)) = -\frac{\partial}{\partial x}(\rho_m \varphi v_m + \rho_s(1 - \varphi)v_s) \quad (3.8)$$

where t is the time, φ is the porosity, x is the spatial coordinate (here the direction parallel to gravity) and v_m and v_s are the melt and solid velocity, respectively. The equation conservation of total mass of MgO is

$$\frac{\partial}{\partial t}(C_m^{\text{MgO}} \rho_m \varphi + C_s^{\text{MgO}} \rho_s(1 - \varphi)) = -\frac{\partial}{\partial x}(C_m^{\text{MgO}} \rho_m \varphi v_m + C_s^{\text{MgO}} \rho_s(1 - \varphi)v_s) \quad (3.9)$$

and of conservation of total mass of SiO₂ is

$$\frac{\partial}{\partial t}(C_m^{\text{SiO}_2} \rho_m \varphi + C_s^{\text{SiO}_2} \rho_s(1 - \varphi)) = -\frac{\partial}{\partial x}(C_m^{\text{SiO}_2} \rho_m \varphi v_m + C_s^{\text{SiO}_2} \rho_s(1 - \varphi)v_s) \quad (3.10)$$

For the conservation of the total masses of MgO and SiO₂, we consider only the advective part of the conservation equation because we assume that diffusion processes are much slower than advection processes (corresponding Péclet number $\gg 1$). The conservation of thermal energy is

$$\frac{\partial}{\partial t}(U_m \varphi + U_s(1 - \varphi)) = -\frac{\partial}{\partial x}(U_m \varphi v_m + U_s(1 - \varphi)v_s - \lambda_T \frac{\partial T}{\partial x}) \quad (3.11)$$

where $\lambda_T = (\lambda_m \varphi + \lambda_s(1 - \varphi))$ and λ_m and λ_s are the thermal conductivity of melt and solid, respectively. The conservation of linear momentum of the solid is given by

$$\frac{\partial \sigma_{xx}}{\partial x} = \rho_T g \quad (3.12)$$

where σ_{xx} is the total stress, $\rho_T = \rho_m \varphi + \rho_s(1 - \varphi)$ is the total density and g is the gravitational acceleration. The total stress is given by

$$\sigma_{xx} = -P_T + \tau \quad (3.13)$$

where P_T is the total pressure (i.e. the mean stress) and τ is the deviatoric stress. The conservation of linear momentum of fluid, also known as Darcy's law, is given by

$$\varphi(v_m - v_s) = -\frac{k\varphi^3}{\eta_m} \left(\frac{\partial P_m}{\partial x} + \rho_m g \right) \quad (3.14)$$

where k is the permeability coefficient in a Kozeny-Carman type model, η_m is the melt viscosity and P_m is the melt pressure. We use the melt pressure as thermodynamic pressure for the thermodynamic calculations. The system is closed by two constitutive equations. The first equation is used to calculate the total pressure,

$$P_T = P_m - \frac{\partial v_s}{\partial x} (1 - \varphi) \eta_v \quad (3.15)$$

where η_v is the solid volumetric viscosity (i.e. compaction viscosity). We consider in the equation for P_T only a viscous volumetric deformation since an additional reversible elastic volumetric deformation is generated by the considered thermodynamic reactions, specifically the variation of density with melt pressure. Temporal variations of P_m are related via a compressibility, β , to temporal variations of the densities (Table 3.2 and eq. 3.2). These density variations are considered in the mass conservation equations and, hence, affect the volumetric deformation. Therefore, the temporal variation of P_m is indirectly related via the compressibility and density to the divergence of solid velocities, which effectively corresponds to a reversible elastic relation between melt pressure and divergence of solid velocity (e.g. $\beta \frac{\partial P_m}{\partial t} = -\frac{\partial v_s}{\partial x}$). Elastic volumetric deformation is, hence, considered indirectly in our THMC model by the consideration of reversible equilibrium reactions. The second constitutive equation is used to calculate (τ) by

$$\tau = 2\eta_s \frac{\partial v_s}{\partial x} \quad (3.16)$$

where η_s is the shear viscosity of the solid. For more details on the development of all equations, see Appendix A.

3.2.3 Coupled THMC and thermodynamic model and numerical method

The entire system of equations describing the THMC and thermodynamic models has a total of 14 unknowns; 8 unknowns are determined by the thermodynamic model, namely ρ_m , ρ_s , C_m^{MgO} , C_s^{MgO} , $C_m^{\text{SiO}_2}$, $C_s^{\text{SiO}_2}$, U_m and U_s , and 6 unknowns are determined by the THMC model, namely P_m , φ , $C_T^{\text{SiO}_2}$, T , v_m , v_s . In the thermodynamic model the unknowns are determined by T , P_m and $C_T^{\text{SiO}_2}$ using pre-computed results from Gibbs energy minimizations (i.e. phase diagrams of the 8 thermodynamic variables) whereas in the THMC model the unknowns are calculated by numerically solving a system of coupled partial differential equations.

We use a standard staggered grid finite difference (FD) method (e.g. Gerya, 2019) to solve the partial differential equations of the THMC model. The numerical algorithm consists of a standard time loop with an internal pseudo-transient (PT) iterative loop to determine P_m , φ , $C_T^{\text{SiO}_2}$, T and v_s . This PT method (e.g. Duretz et al., 2019; Räss et al., 2019; Schmalholz et al., 2020) solves non-linear system of equations in an iterative way without the need of inverting a numerical coefficient matrix. To use the PT method, we transform the conservation equations in pseudo-transient equations by adding a pseudo-transient time derivative, with PT time step Δt^{PT} , for each unknown variable, P_m , φ , $C_T^{\text{SiO}_2}$, T and v_s . The PT equations are

$$\frac{\partial P_m}{\partial \Delta t_P^{\text{PT}}} = -\frac{\partial}{\partial t}(\rho_m \varphi + \rho_s(1 - \varphi)) - \frac{\partial}{\partial x} \left(-\rho_m \frac{k\varphi^3}{\eta_m} \left(\frac{\partial P_m}{\partial x} + \rho_m g \right) + \rho_T v_s \right) \quad (3.17a)$$

$$\frac{\partial \varphi}{\partial \Delta t_\varphi^{\text{PT}}} = -\frac{\partial}{\partial t} (C_m^{\text{MgO}} \rho_m \varphi + C_s^{\text{MgO}} \rho_s (1 - \varphi)) - \frac{\partial}{\partial x} (C_m^{\text{MgO}} \rho_m \varphi v_m + C_s^{\text{MgO}} \rho_s (1 - \varphi) v_s) \quad (3.17b)$$

$$\frac{\partial C_T^{\text{SiO}_2}}{\partial \Delta t_{C_T^{\text{SiO}_2}}^{\text{PT}}} = -\frac{\partial}{\partial t} (C_m^{\text{SiO}_2} \rho_m \varphi + C_s^{\text{SiO}_2} \rho_s (1 - \varphi)) - \frac{\partial}{\partial x} (C_m^{\text{SiO}_2} \rho_m \varphi v_m + C_s^{\text{SiO}_2} \rho_s (1 - \varphi) v_s) \quad (3.17c)$$

$$\frac{\partial T}{\partial \Delta t_T^{\text{PT}}} = -\frac{\partial}{\partial t}(U_m \varphi + U_s(1 - \varphi)) - \frac{\partial}{\partial x}(U_m \varphi v_m + U_s(1 - \varphi)v_s - \lambda_T \frac{\partial T}{\partial x}) \quad (3.17d)$$

$$\frac{\partial v_s}{\partial \Delta t_{v_s}^{\text{PT}}} = \frac{\partial}{\partial x}(-P_T + \tau) - \rho_T g \quad (3.17e)$$

When the PT time derivatives on the left-hand sides of the above equation are zero, the corresponding equations of the right-hand side are solved. In practice, the iteration will continue in the PT iteration loop as long as PT time derivatives are not smaller than a specified numerical tolerance error. In the FD method, we use numerical time steps representing the physical time step Δt to approximate the time derivatives, which control the physical time evolution (i.e. the “real” time derivatives). We employ five PT time steps to solve for P_m , Δt_P^{PT} , for φ , $\Delta t_\varphi^{\text{PT}}$, for $C_T^{\text{SiO}_2}$, $\Delta t_{C_T^{\text{SiO}_2}}^{\text{PT}}$, for T , Δt_T^{PT} and for v_s , $\Delta t_{v_s}^{\text{PT}}$. The choice of these numerical PT time steps is crucial for a stable convergence of the PT iterative solution but does not affect the result after the convergence. The values of the PT time steps are given in Appendix B, Table 3.3. The melt velocity can be directly calculated from Darcy’s law (eq. 3.14), which does not require the solution of an additional differential equation.

3.2.4 Model configuration and characteristic values

The algorithm is programmed in such way that all parameters are dimensionless, with the goal to have the best possible numerical stability and convergence of the algorithm. For that purpose, we define independent and dependent model parameters. We choose four independent parameters that are used to determine all other parameters, namely (1) melt density times gravitational acceleration, $\rho_m g = 1$ [Pa·m⁻¹], (2) permeability divided by melt viscosity, $\frac{k}{\eta_m} = 1$ [m²·Pa⁻¹·s⁻¹], (3) solid volumetric viscosity, $\eta_v = 1$ [Pa·s] and (4) temperature, $T^A = 1$ [K]. Next, we specify the following characteristic scales of the model: the characteristic length, $L_c = \sqrt{\frac{k}{\eta_m} \cdot \eta_v} = 1$ [m], the characteristic time, $t_c = \frac{\eta_v}{\rho_m g \cdot L_c} = 1$ [s], the characteristic stress, $P_c = \rho_m g \cdot L_c = 1$ [Pa], the characteristic power, $E_c = \frac{\rho_m g \cdot L_c^4}{t_c} = 1$ [W], the characteristic thermal conductivity, $\lambda_c = \frac{E_c}{L_c \cdot T^A} = 1$ [W·K⁻¹·m⁻¹], and the characteristic density times specific heat, $\rho C p_c = \frac{\rho_m g \cdot L_c}{T^A} = 1$ [Pa·K⁻¹]. The characteristic length L_c of the model, also known

as compaction length in the context of porosity waves (e.g. McKenzie, 1985; Connolly and Podladchikov, 2007), corresponds to the characteristic distance over which deformation occurs. Next, we define several dimensionally dependent scales to configure the model. These scales must be chosen in such way that the considered process can be numerically resolved and that the applied parameters are applicable to the considered process. Therefore, we apply a model height $Lx = 100 \cdot L_c$ and a width of perturbations in the initial distribution of porosity and/or total concentration of SiO_2 , $w = 10 \cdot L_c$ so that the characteristic compaction for the two-phase flow can occur within the model domain and is affected by the size of initial perturbations. Furthermore, the solid density times gravitational acceleration $\rho_s g = \frac{\rho_{s,0}}{\rho_{m,0}} \cdot \rho_m g = 0.9423 \cdot \rho_m g$, which is a relation calculated for the reference point in the olivine system (see Fig. 3.3a and d). The shear viscosity is considered equal to the compaction viscosity $\eta_s = \eta_v = 1$. The thermal conductivity of melt and solid $\lambda_m = \lambda_s = 483 \cdot \lambda_c$, which applies to a natural conductivity of 3 [$\text{W} \cdot \text{m}^{-1} \cdot \text{K}^{-1}$] if we assume a natural $L_c = 1$ km, $\eta_v = 1.25 \cdot 10^{20}$ [$\text{Pa} \cdot \text{s}$] and $T^A = 1860$ [K] and reference melt density (Table 3.2). Similarly, the product of density times specific heat for melt and solid can be determined with reference values in Table 3.2 as $\rho C p_m = 205 \cdot \rho C p_c = 205$ and $\rho C p_s = \frac{\rho_{s,0}}{\rho_{m,0}} \cdot \frac{C p_{s,0}}{C p_{m,0}} \cdot \rho C p_m = 0.9014 \cdot \rho C p_m = 184.7906 \cdot \rho C p_{cm}$.

To further configure the model, we define four initial profiles, namely for temperature, porosity, total silica mass fraction and total pressure (Fig. 3.5). First, we apply a constant porosity profile with a value of 0.02 and a constant total silica mass fraction profile with a value of 0.45 (in Fig. 3.4 this silica mass fraction corresponds to the grey dashed lines in the region where melt density is lower than solid density). We then add a perturbation to the porosity and/or the total silica mass fraction profiles in the form of a Gaussian with its maximum at a depth of $x = -20$ (Fig. 3.5g and h). For the simulations presented below, we apply five perturbation amplitudes for porosity, $\Delta\varphi$ (0.005, 0.01, 0.02, 0.03 and 0.04) and five for total silica mass fraction $\Delta C_T^{\text{SiO}_2}$ (0, 0.25, 0.5, 0.75 and 1; see Fig. 3.6 for the systematic scheme of simulations). We define the temperature profile in the model with a temperature difference ΔT_{model} of 2 between the bottom and the top of our model (Fig. 3.5d). For the initial pressure profile, we calculate the lithostatic pressure across the model with the model total densities and obtain a pressure difference ΔP_{model} of approximately 90 for all simulations. We performed

two series of systematic simulations with two different thermal gradients, one representing an adiabatic and one a conductive gradient. In order to adapt our temperature and pressure profiles in the model to realistic natural profiles, we must rescale the α and β parameters with a temperature ratio ($\Delta T_{\text{nature}}/\Delta T_{\text{model}}$) and a pressure ratio ($\Delta P_{\text{nature}}/\Delta P_{\text{model}}$). ΔT_{nature} is different depending on whether it represents an adiabatic or conductive gradient. We apply a natural pressure variation, ΔP_{nature} , across our model equal to 1 [GPa], which corresponds to the pressure range chosen for the thermodynamic data (Figs 3.2 and 3.3). Thus, we can determine a certain model height ($h = P/\rho_T g$, with $\rho_T = \rho_{m,0}\varphi + \rho_{s,0}(1 - \varphi)$ and $\varphi=0.02$) that we can use to calculate a natural temperature difference, $\Delta T_{\text{nature},1}$, corresponding to a realistic adiabatic gradient. We found $h \sim 28$ [km] and $\Delta T_{\text{nature},1} \sim 15$ [K] for an adiabatic gradient between 0.5-0.55 [$^{\circ}\text{C}\cdot\text{km}^{-1}$]. To define the second, larger natural temperature difference $\Delta T_{\text{nature},2}$ representing a conductive gradient at the base of the lithosphere, we multiplied $\Delta T_{\text{nature},1}$ by ten, thus $\Delta T_{\text{nature},2}=150$ [K].

3.3 Results

We first present results from the thermodynamic model which consist essentially of the determined values of α , β and γ for the thermodynamic variables (Table 3.2). Subsequently, we show results from the THMC model.

3.3.1 Linearization of thermodynamic results

The parameters α , β and γ are used to linearize the dependency of the thermodynamic variables on temperature, pressure and total silica content. For example, for the melt density the linearized relation is

$$\rho_m = \rho_{m,0} + \alpha_{\rho_m} \Delta T + \beta_{\rho_m} \Delta P + \gamma_{\rho_m} \Delta C_T^{\text{SiO}_2} \quad (3.18)$$

The calculated values of all α , β and γ are presented in Table 3.2. If values of α , β and γ are positive, then the corresponding parameter will increase with the respective increase of

temperature, pressure or total silica mass fraction (e.g. in Fig. 3.3, ρ_m increase with increasing pressure, since β_{ρ_m} is positive). Consequently, if values α , β and γ are negative, then the associated parameter will decrease with the respective increasing temperature, pressure or total silica mass fraction (e.g. in Fig. 3.3, ρ_m decrease with increasing temperature, α_{ρ_m} is negative). The determined values of α , β and γ provide a transparent overview on the relative importance and interdependence of the parameters. For example, the α for solid density α_{ρ_s} and for solid mass fraction of silica $\alpha_{C_s^{\text{SiO}_2}}$ are 2 to 5 times larger than values of α for melt density α_{ρ_m} and for melt mass fraction of silica $\alpha_{C_m^{\text{SiO}_2}}$. This relationship is opposite for magnesium mass fraction where α for the melt, $\alpha_{C_m^{\text{MgO}}}$, is 1.5 times larger than the solid one, $\alpha_{C_s^{\text{MgO}}}$. We observe the same trend for β , where β_{ρ_s} and $\beta_{C_s^{\text{SiO}_2}}$ are 1.5 to 4 times larger than β_{ρ_m} and $\beta_{C_m^{\text{SiO}_2}}$ and $\beta_{C_m^{\text{MgO}}}$ is slightly larger than $\beta_{C_s^{\text{MgO}}}$. For the γ the situation is different, because all γ values for melt (γ_{ρ_m} , $\gamma_{C_m^{\text{MgO}}}$ and $\gamma_{C_m^{\text{SiO}_2}}$) are 2.5 to 4.5 times larger than γ values for solid (γ_{ρ_s} , $\gamma_{C_s^{\text{MgO}}}$ and $\gamma_{C_s^{\text{SiO}_2}}$). This difference in dependence on P , T and $C_T^{\text{SiO}_2}$ between variables related to melt and solid is between a factor of 1.5 and 4.5 and it is, hence, important to consider this difference in the THMC models.

We use the linearized relations employing parameters α , β and γ , instead of the results obtained directly from the Gibbs free energy minimization (Fig. 3.2), mainly because of computational efficiency, since direct usage of Gibbs energy minimisation results would require numerical interpolations in order to calculate the thermodynamic variables used in the THMC model. Such data interpolations are computationally time consuming, especially if the algorithm is extended to 2D (see below) or 3D.

The initial density profile of the model impacts the melt migration. For a constant chemical composition, the initial density profile is controlled by the initial variation of P and T , but with opposite trend: from the top to the bottom of the model, the melt and solid densities increase with increasing pressure but decrease with increasing temperature. We determine for the applied values of ΔT and ΔP the critical value of ΔT , for which the density is constant with depth. We use the equation

Table 3.2: Values for linear approximation of thermodynamic variables. Values are calculated from Gibbs free energy minimisation and experiment of Davis et al. (2011), see section 3.2.1 for details.

	Adopted values for linear approximation, subscript 0 indicate at reference point:			
P_0	$3.0001 \cdot 10^9$	[Pa]		
T_0	1863.15	[K]		
$C_{T,0}^{\text{SiO}_2}$	0.3280	[]		
Value at reference point			alpha [K ⁻¹]	beta [Pa ⁻¹]
$\rho_{m,0}$	$3.8631 \cdot 10^3$	[kg·m ⁻³]	α_{ρ_m}	β_{ρ_m}
$\rho_{s,0}$	$3.6401 \cdot 10^3$	[kg·m ⁻³]	α_{ρ_s}	β_{ρ_s}
$C_{m,0}^{\text{MgO}}$	0.0449	[]	$\alpha_{C_m^{\text{MgO}}}$	$\beta_{C_m^{\text{MgO}}}$
$C_{m,0}^{\text{MgO}}$	0.2232	[]	$\alpha_{C_s^{\text{MgO}}}$	$\beta_{C_s^{\text{MgO}}}$
$C_{s,0}^{\text{SiO}_2}$	0.3079	[]	$\alpha_{C_m^{\text{SiO}_2}}$	$\beta_{C_m^{\text{SiO}_2}}$
$C_{s,0}^{\text{SiO}_2}$	0.3481	[]	$\alpha_{C_s^{\text{SiO}_2}}$	$\beta_{C_s^{\text{SiO}_2}}$
$c_{p_{m,0}}$	$1.2481 \cdot 10^3$	[J·kg ⁻¹ ·K ⁻¹]		
$c_{p_{s,0}}$	$1.1940 \cdot 10^3$	[J·kg ⁻¹ ·K ⁻¹]		
			gamma []	
			γ_{ρ_m}	γ_{ρ_m}
			γ_{ρ_s}	γ_{ρ_s}
			$\gamma_{C_m^{\text{MgO}}}$	$\gamma_{C_m^{\text{MgO}}}$
			$\gamma_{C_s^{\text{MgO}}}$	$\gamma_{C_s^{\text{MgO}}}$
			$\gamma_{C_m^{\text{SiO}_2}}$	$\gamma_{C_m^{\text{SiO}_2}}$
			$\gamma_{C_s^{\text{SiO}_2}}$	$\gamma_{C_s^{\text{SiO}_2}}$

$$\rho = \rho_0 + \alpha\Delta T + \beta\Delta P \quad (3.19)$$

and reformulate the equation to

$$\frac{\Delta\rho}{\alpha} = \Delta T + \frac{\beta}{\alpha}\Delta P \quad (3.20)$$

We assume no density variation (isochoric system) with a variation of T and P , i.e. $\frac{\Delta\rho}{\alpha} = 0$ and solve the remaining equation for ΔT which yields

$$\Delta T = -\frac{\beta}{\alpha}\Delta P \quad (3.21)$$

If the applied ΔT is larger than the above expression, then the density is decreasing with depth in the model (the initial density variation is controlled by the temperature variation) and if ΔT is smaller, then the density increases with depth, controlled by the pressure variation. The above analysis can also be applied to the mass fractions. Choosing ΔP of 1 [GPa] and using α and β values from Table 3.2, we obtain for the melt density a critical $\Delta T=98.2$ [K], for the solid density a critical $\Delta T=72.5$ [K], for magnesium melt mass fraction a critical $\Delta T=45.3$ [K], for magnesium solid mass fraction a critical $\Delta T=63.2$ [K], for silica melt mass fraction a critical $\Delta T=45.6$ [K] and for silica solid mass fraction a critical $\Delta T=62.6$ [K]. We note that all values of critical ΔT are between $\Delta T_{\text{nature},1}$ and $\Delta T_{\text{nature},2}$, respectively, that is the temperature differences applied for the adiabatic and the conductive gradient. Therefore, the applied initial adiabatic and conductive geotherms cause a fundamentally different initial variation of densities and mass fractions with depth.

3.3.2 THMC model results: comparison of initial profiles, maximum melt velocity and evolution over time

We performed 50 simulations with one time step only to determine the initial profiles of all the involved model variables, because the initial profiles of, for example, the solid and melt

velocities represent already an interesting result that needs to be calculated iteratively due to the nonlinear coupling of the model variables. For four of these simulations we also calculate the evolution with time to investigate the upward melt migration by reactive porosity waves.

Comparison of initial profiles

We first compare initial profiles from four different simulations, namely simulations termed S05 with an initial porosity perturbation only and simulations S15 with an initial porosity and total silica mass fraction perturbations, both for the two temperature gradients, namely a conductive gradient (Figs 3.5 and 3.12) and an adiabatic gradient (Figs Figs 3.13 and 3.14). The four simulations show similar profiles for melt and total pressure (Fig. 3.5a), effective pressure, $P_e = P_m - P_T$ (Fig. 3.5c), temperature (Fig. 3.5d), porosity (Fig. 3.5g) and solid velocity (Fig. 3.5i). The effective pressure shows which part of the model is in compression (P_e is negative) and which part is in dilation (P_e is positive). The main difference between the four simulations is the maximum magnitudes of the peaks of corresponding profiles. Maximum magnitudes are larger in the two S15 simulations (Figs 3.5 and 3.14), with an initial perturbation in porosity and in total silica mass fraction, than in the two S05 simulations (Figs 3.12 and 3.13), with an initial perturbation only in porosity. Differences between the four simulations are visible in the calculated profiles of densities (Fig. 3.5b), of magnesium and silica mass fractions (Figs. 3.5e and h) and of melt velocity (Fig. 3.5f). There is a significant difference between simulations with a conductive gradient (Figs 3.5 and 3.12) and simulations with an adiabatic gradient (Figs 3.13 and 3.14). Across the model, density profiles for the conductive gradient (panel b in Figs. 3.5 and 3.12) decrease with increasing depth, whereas for the adiabatic gradient (panel b in Figs. 3.13 and 3.14), densities increase with increasing depth. This trend is reversed for melt and solid mass fraction of magnesium and silica (panels e and h in Figs 3.5, 3.12-3.14). For the conductive gradient, melt and solid mass fraction of magnesium and silica increase with increasing depth and with the adiabatic gradient, melt and solid mass fraction of magnesium and silica decrease with increasing depth. The calculated total magnesium mass fraction (black line in panel e in Fig. 3.5 and 3.12-3.14) follows the trend of melt and solid mass fractions of magnesium. The calculated total silica

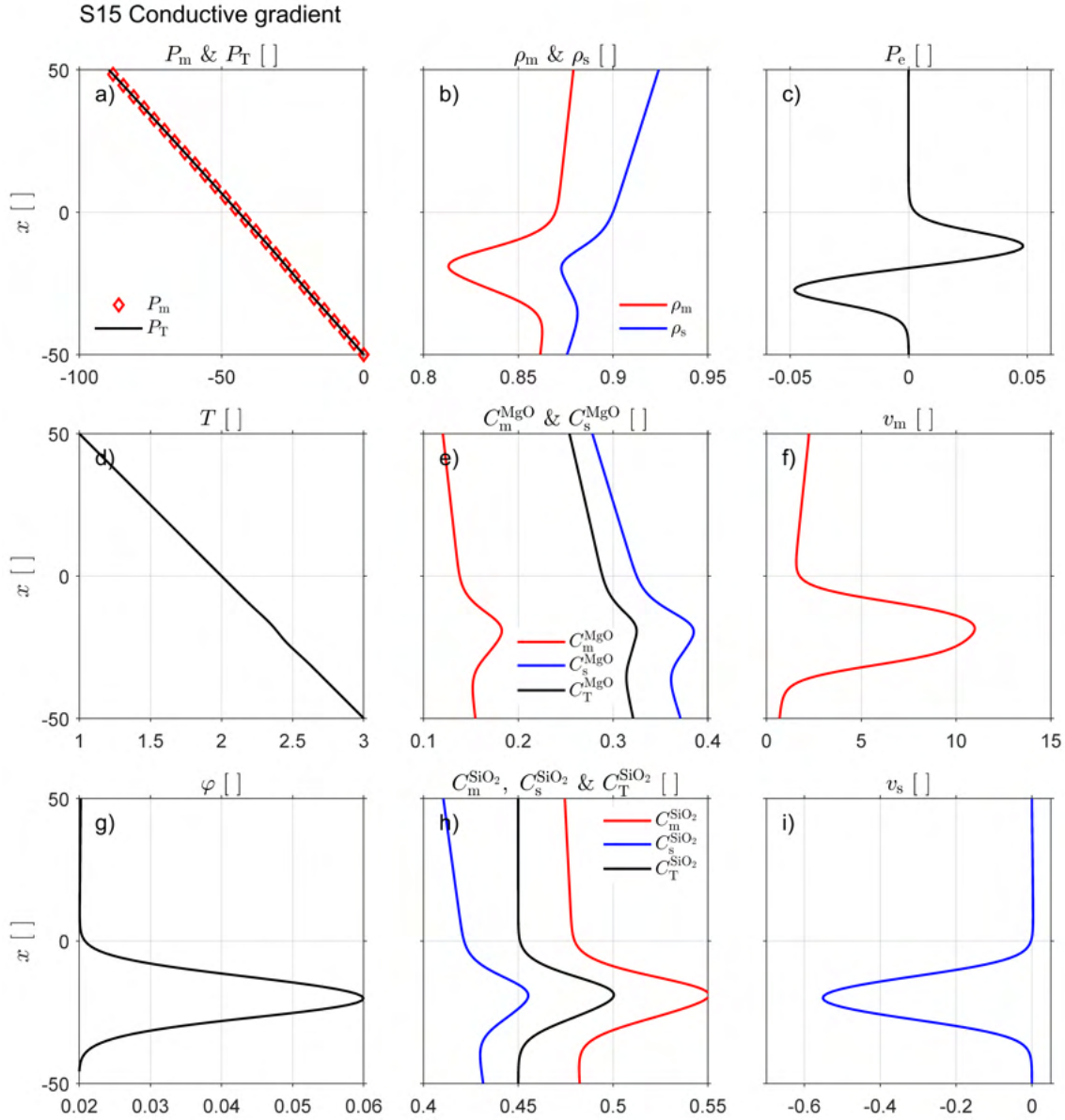


Figure 3.5: Initial profiles of simulation S15 for a conductive gradient. All variables are dimensionless. Panel (a) shows melt pressure (red diamond) and total pressure (black line). Panel (b) shows melt density (red line) and solid density (blue line). Panel (c) shows effective pressure, positive values indicate decompaction while negative values indicate compaction. Panel (d) shows temperature. Panel (e) shows magnesium mass fraction in melt (red line) and in solid (blue line) and total magnesium mass fraction (black line). Panel (f) shows melt velocity. Panel (g) shows porosity. Panel (h) shows silica mass fraction in melt (red line) and in the solid (blue line) and total silica mass fraction (black line). Panel (i) shows solid velocity.

mass fraction (black line in panel h in Fig. 3.5 and 3.12-3.14) remains constant except in the region of the perturbation where the maximum value changes according to the applied initial perturbations. The melt velocity profiles (panel f in Fig. 3.5 and 3.12-3.14) exhibit the maximum melt velocity at the position where the maximum initial perturbation in porosity and/or total silica mass fraction is applied. The maximum melt velocity is greater when both porosity and total silica mass fraction profiles exhibit initial perturbations (simulation S15, Figs 3.5 and 3.14). A difference also exist in the overall slope of the melt velocity profiles between the two different temperature gradients in all four simulations. The melt velocity decreases with depth for the conductive gradient (Figs 3.5 and 3.12) and increases with depth for the adiabatic gradient (Figs 3.13 and 3.14). The initial melt velocity profile shows positive values indicating upward motion of the melt (Figs 3.5, 3.12-3.14 panel e). In the region where the initial perturbation in porosity and silica mass fraction is applied the melt velocity is largest. In this region, the solid velocity is negative indicating compaction in the region where the melt is moving upward, or where melt is extracted (Figs 3.5, 3.12-3.14 panel i). Also, the absolute magnitudes of the melt velocities around the maximal initial perturbation are approximately one order of magnitude larger than absolute magnitudes of the solid velocities.

Comparison of maximum melt velocity

Figure 3.6 compares maximum melt velocities of the respective initial profiles for 50 simulations. We made 25 simulations with an adiabatic gradient (Fig. 3.6a) and 25 simulations with a conductive gradient (Fig. 3.6b). For each thermal gradient, we applied 5 perturbation amplitudes for the initial porosity, $\Delta\varphi$, and 5 amplitudes for the initial total silica mass fraction, $\Delta C_T^{\text{SiO}_2}$. The four simulations selected for investigating the time evolution, i.e. S05 and S15, are represented by the points circled in red (Fig. 3.6). The greater the amplitudes of the perturbations, the greater the maximum melt velocity. The maximum melt velocity occurs when both perturbation amplitudes are maximal, which applies for both thermal gradients. The maximal melt velocities are slightly larger for an adiabatic gradient (Fig. 3.6). The curved velocity contours in figure 3.6 indicate a nonlinear dependence between the maximal

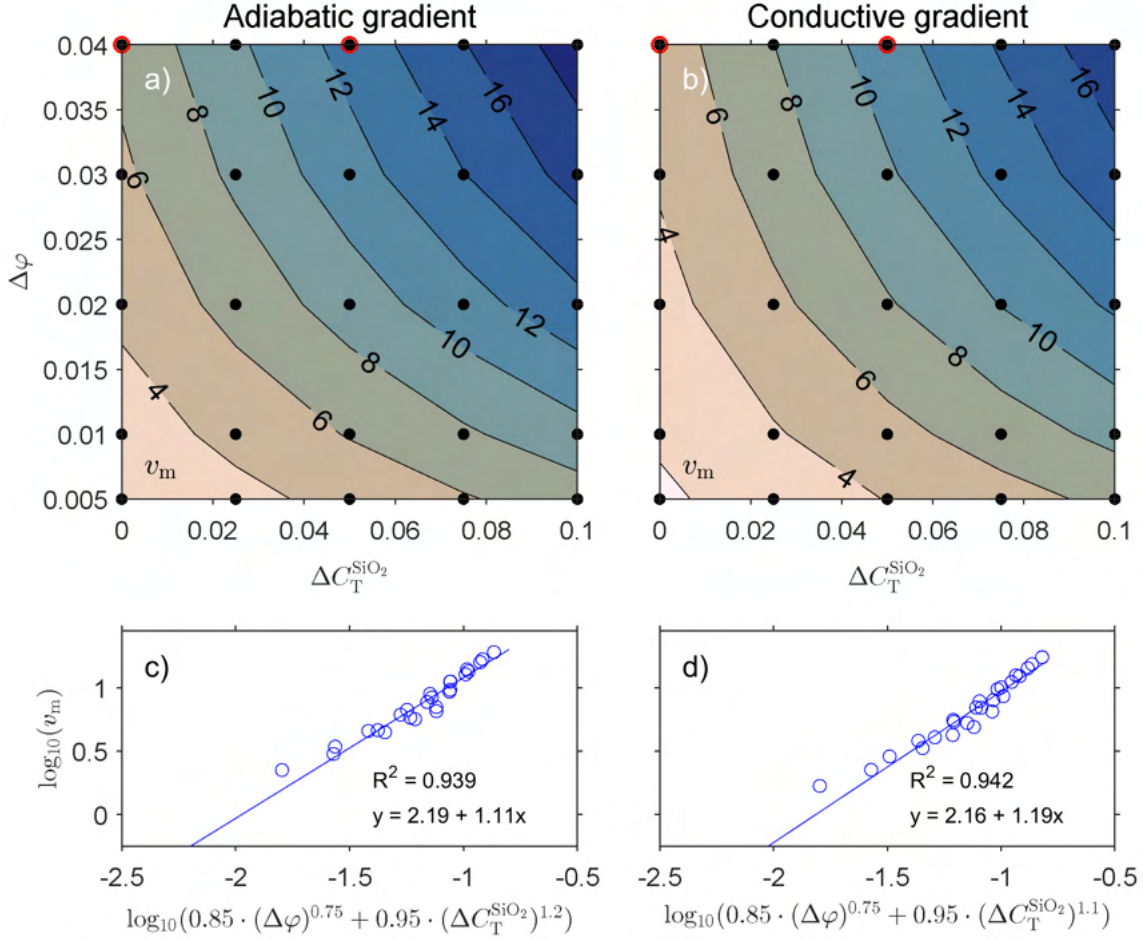


Figure 3.6: Panels (a) and (b) show maximal initial melt velocities as function of initial porosity, $\Delta\varphi$, and total silica mass fraction, $\Delta C_T^{\text{SiO}_2}$, perturbation amplitudes. (a) for adiabatic gradient and (b) for conductive gradient. Black lines show the velocity contours and red circles indicate the initial perturbations for four simulations for which the time evolution has been calculated; respectively simulations S05 (top left in panels a and b) and S15 (top in the middle in panels a and b) for both temperature gradients. Panels (c) and (d) show the power law relationship between melt velocity and a combination of porosity and total silica mass fraction perturbation amplitude, (c) for adiabatic gradient and (d) for conductive gradient. In each panel, blue points represent the 25 systematic simulations and the blue line the linear regression line.

melt velocity and $\Delta\varphi$ and $\Delta C_T^{\text{SiO}_2}$. However, the 25 maximal melt velocities for each thermal gradient can be collapsed from the two dimensional space ($\Delta\varphi - \Delta C_T^{\text{SiO}_2}$) onto a one dimensional space (Fig. 3.6c and d). The equations of this data collapse are obtained by a linear best fit of the 25 data points and are given as label of the horizontal axis. The two best-fit equations show that the difference in maximal melt velocity for the two thermal gradients is only due to a different sensitivity to $\Delta C_T^{\text{SiO}_2}$, with exponents 1.1 and 1.2, because the expo-

nents of $\Delta\varphi$ are identical for the two thermal gradients (Fig. 3.6c and d). Overall, for the chosen parameters, a perturbation in total silica mass fraction has a similar impact on the maximal melt velocity as a perturbation in the initial porosity.

Time evolution and reactive porosity wave propagation

Figure 3.7 shows the time evolution of the S15 simulation with a conductive gradient. The additional figures 3.15 to 3.17 show the three other simulations, namely S05 with a conductive gradient, and S05 and S15 with an adiabatic gradient. The evolution of porosity (Fig. 3.7a) and of effective pressure (Fig. 3.7b) corresponds to the typical evolution of 1D porosity waves (e.g. Connolly and Podladchikov, 2013; Jordan et al., 2018). During porosity wave propagation, the maximum porosity always corresponds to an effective pressure of zero (Fig. 3.7a and b). The compaction at the base of the high porosity region (where P_e is minimum) allows the melt to rise upward into the high porosity region under decompression (where P_e is maximum). Comparing all porosity profiles (panel a in Fig. 3.7 and 3.15 to 3.17), for the two S05 simulations (Figs 3.15 and 3.16), the maximum porosity decreases slightly with progressive time and then remains constant, whereas for the two S15 simulations (Figs 3.7 and 3.17), the maximum porosity increases and then decreases slightly. The two simulations with an adiabatic gradient (Figs 3.16 for S05 and 3.17 for S15) show a stabilisation of the maximum melt velocity over time, while the two simulations with a conductive gradient (Figs 3.15 for S05 and 3.7 for S15) show a slight increase in melt velocity over time. For the four simulations (Figs 3.7 and 3.15 to 3.17), the variations of melt density and total silica mass fraction are small over time compare to the total magnesium mass fraction which show a slightly greater variation, especially for simulations with an adiabatic gradient (Figs 3.16 and 3.17).

Figure 3.8 shows the time evolution of the melt density (panel a), the total magnesium mass fraction (panel b) and the total silica mass fraction (panel c) at depth $x=10$ [] for the four simulations. The variation in melt density (Fig. 3.8a) for the two S05 simulations (conductive in light blue and adiabatic in grey) and the two S15 simulations (conductive in

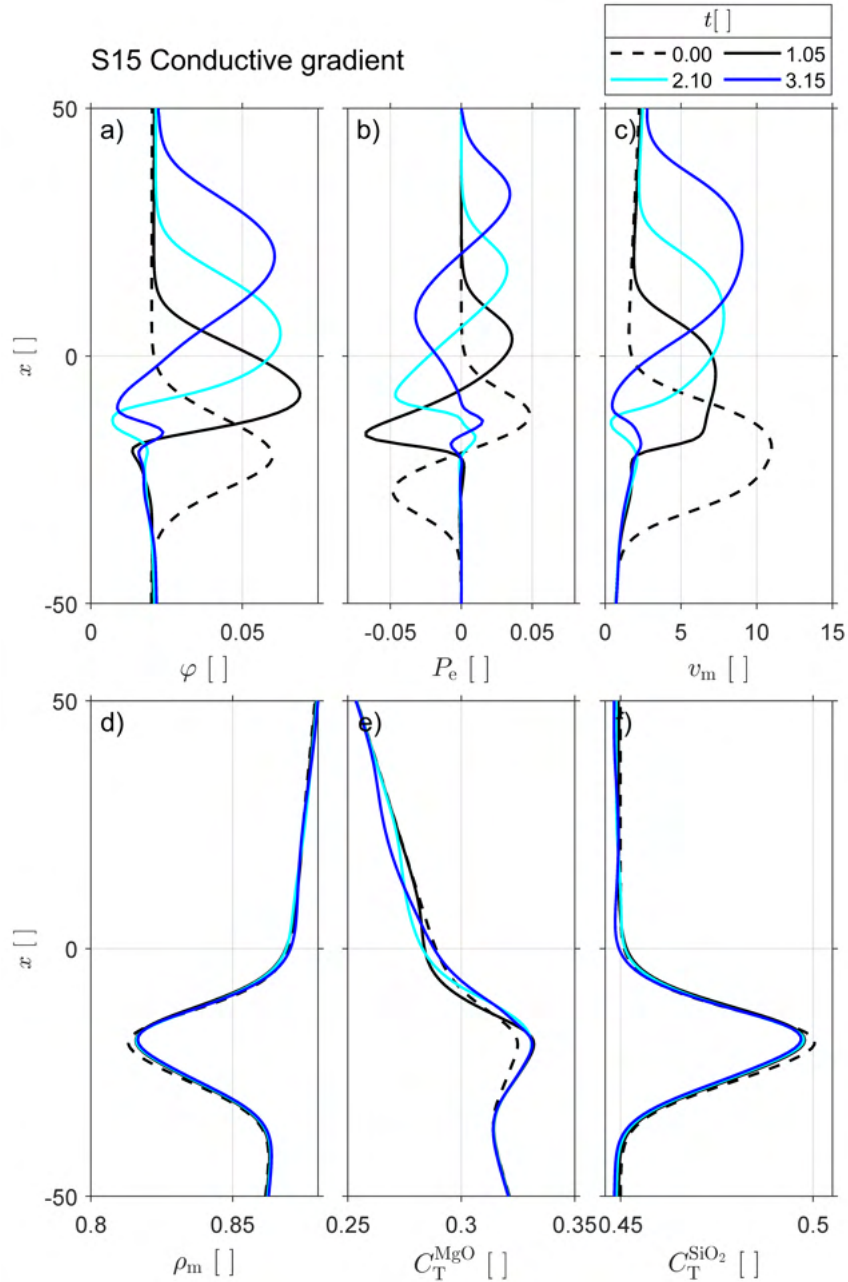


Figure 3.7: Time evolution of six variables in simulation S15 Conductive gradient; all variables are dimensionless. Panel (a) shows porosity, panel (b) shows effective pressure, panel (c) shows melt velocity, panel (d) shows melt density, panel (e) shows total magnesium mass fraction and panel (f) shows total silica mass fraction. Four time steps are chosen at different dimensional times: $t = 0$ with dashed line (corresponding to the initial profiles in figure 3.5 for each variables), $t = 1.05$ with black line, $t = 2.10$ with light blue and $t = 3.15$ with dark blue (see legend).

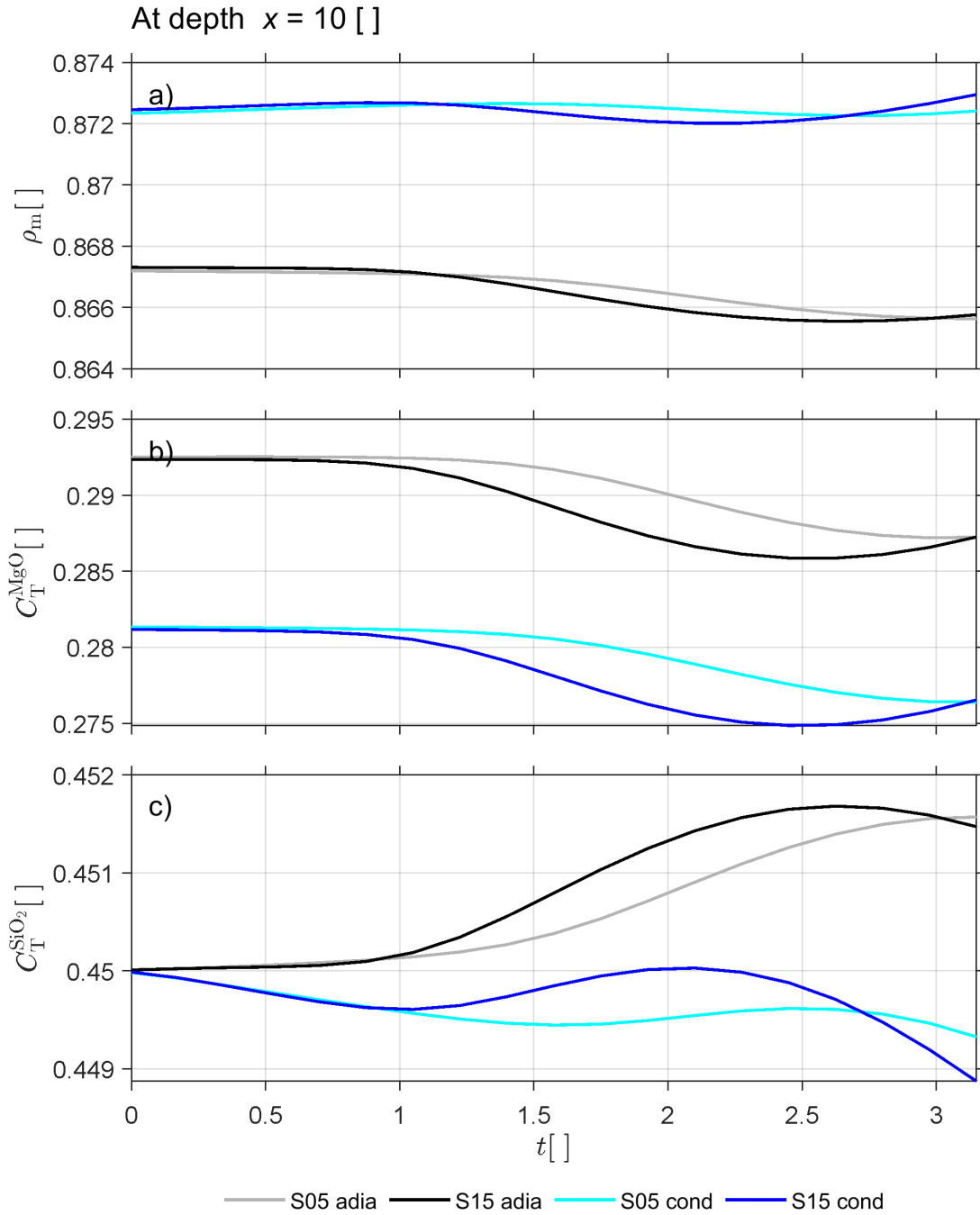


Figure 3.8: Time evolution, at a fixed depth of $x = 10$, of three variables for the four simulations indicated by red circles in figure 3.6: simulation S05 for adiabatic gradient in grey, simulation S15 for adiabatic gradient in black, simulation S05 for conductive gradient in light blue and simulation S15 for conductive gradient in dark blue. All variables are dimensionless. Panel (a) shows melt density. Panel (b) shows total magnesium mass fraction and panel (c) shows total silica mass fraction.

dark blue and adiabatic in black) is very similar. The main difference is the magnitude of the initial value at time $t=0$ for the two different thermal gradients. The initial value for the conductive gradient is larger than the initial value for the adiabatic gradient (ρ_m of S05 and S15 conductive $>$ ρ_m of S05 and S15 adiabatic). Similar variations are observed for total magnesium mass fraction (panel b) for the two S05 simulations (conductive in light blue and adiabatic in grey) and the two S15 simulations (conductive in dark blue and adiabatic in black). For melt density, the magnitude of the initial value at time $t=0$ between the two thermal gradients are different. The initial value for the adiabatic gradient is larger than the initial value for the conductive gradient (C_T^{MgO} of S05 and S15 adiabatic $>$ C_T^{MgO} of S05 and S15 conductive). For the variation of the total silica mass fraction (panel c), the initial value is identical for all four simulations since this value is specified as initial condition. The local variation of the total silica mass fraction over time is larger than the initial value (at $t = 0$) for the simulations with an adiabatic gradient (black and grey lines) and is smaller for the simulations with a conductive gradient (dark and light blue lines). The maximum peaks of the two S15 simulations (black and dark blue lines) arrive before the maximum peaks of the two S05 simulations (grey and light blue lines). This is consistent with the fact that S15 simulations have a greater initial perturbation, hence the melt velocity is larger and the maximum peaks arrive first.

3.4 Discussion

3.4.1 Mobility and mass transport

In the modelled chemical system, the mass fractions of MgO and SiO₂ in the melt and solid are variable and are functions of pressure, temperature and total silica content. Our model can be considered as fully mobile since there are no restrictions on the mobility of MgO and SiO₂ so that MgO and SiO₂ can be freely exchanged between solid and melt. This full mobility is an elaboration compared to existing studies on reactive transport with fluid-rock interactions, who assume that some chemical components are immobile and fixed to the solid phase (e.g. Plümper et al., 2016; Beinlich et al., 2020). Furthermore, in our model the total mass of

MgO and SiO₂ can locally change permanently due to mass transport by melt migration since the total mass of SiO₂ can change locally permanently. In contrast, other studies on melt migration with chemical differentiation consider the silica mass fraction as a function of temperature only (e.g. Jackson et al., 2018). Therefore, for a given temperature the silica mass fraction cannot change by transport. In our model, the mobility and mass transport are enabled by a freely evolving porosity, which is calculated from the conservation equation for the total mass of MgO. For example, inside the considered partial melting region of the olivine phase diagram (Fig. 3.1), the densities (Fig. 3.1b) and mass fractions of MgO of solid and melt (Fig.3.1c) are fixed for a given temperature and pressure, independent on the composition X (Gibbs phase rule). The total mass of MgO is calculated by the mass fractions, densities and porosity. If the total mass of MgO is locally modified due to an advective melt flux, and densities and mass fractions of MgO are fixed, then the porosity of the system must change to enable and balance the mass transport.

3.4.2 Magnesium in melt

For the applied simple chemistry, our thermodynamic model predicts an increase of the magnesium mass fraction in the melt, C_m^{MgO} , with increasing pressure (Figs. 3.5 and 3.12). Partial melting experiments of peridotite have shown also that the MgO mass fraction in the melt increases with pressure (Fig. 3.9). The black line in figure 3.9 represents the numerically modelled profile of C_m^{MgO} for a conductive thermal gradient (simulation S15). Therefore, despite the applied simplified chemistry for the mantle composition, the modelled gradient of C_m^{MgO} shows a similar trend than the experimental data. Our model shows smaller absolute values of C_m^{MgO} than the experiments, which is due to the applied simplified chemistry.

3.4.3 2D reactive porosity wave model, channelization and melt-rock interaction

A characteristic feature of porosity wave propagation in 2D and 3D is the possibility to change the shape of the propagating wave, which can be either blob-like (Fig. 3.10 a-h)

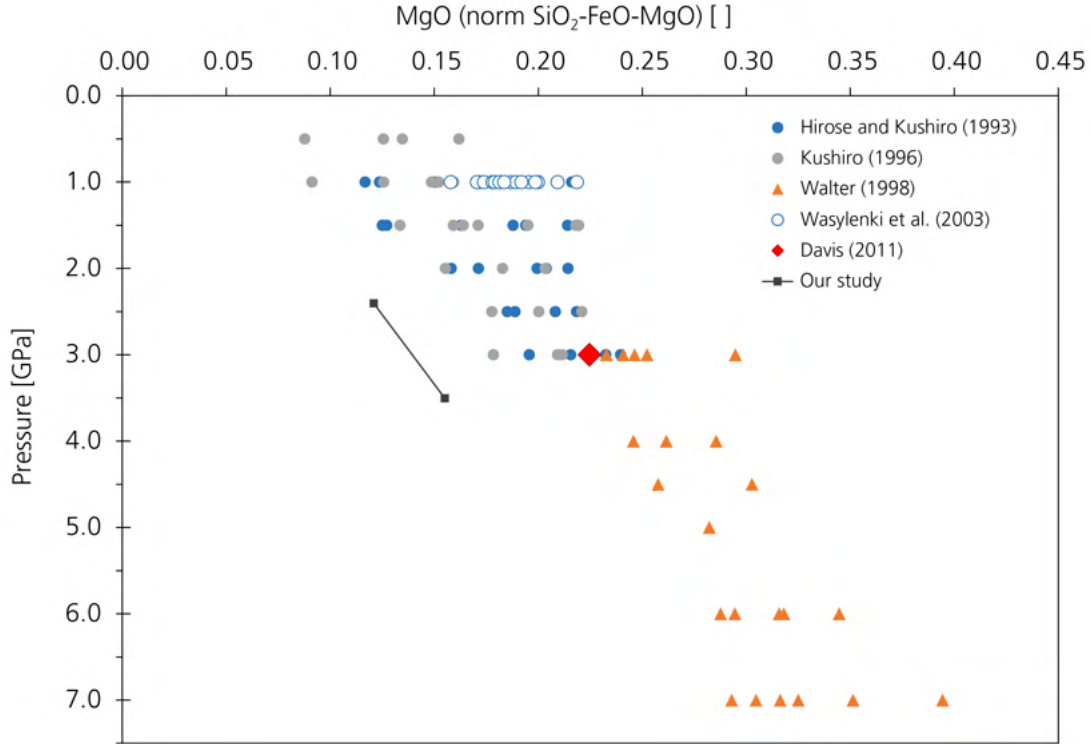


Figure 3.9: Magnesium melt mass fractions of five partial melting experiments of peridotite vs. pressure. Filled blue circles are data from Hirose and Kushiro (1993). Filled grey circles are data from Kushiro (1996). Filled orange triangles are data from Walter (1998). Filled white circles are data from Wasylenki et al. (2003). The filled red diamond is 0% melt from Davis et al. (2011). The horizontal evolution of MgO at each pressure correspond to the increase in partial melting rate. The black line shows the overall gradient of MgO mass fraction in the melt resulting from our study without the perturbation (corresponding to the C_m^{MgO} profile in Figure 3.5e).

or channel-like (Fig. 3.10 i-p) (e.g. Connolly and Podladchikov, 2007; Räss et al., 2019). The shape of the propagating wave is controlled by the ratio of shear to bulk viscosity ratio (η_s/η_v) and the ratio of decompaction to compaction bulk viscosity (η_d/η_v) (e.g. Räss et al., 2019). A value of $\eta_d/\eta_v < 1$ is termed decompaction weakening. If both viscosity ratios are equal to one, the propagation is a blob-like for a circular initial perturbation in porosity. If decompaction weakening is significant, then the propagating porosity wave forms a channel (e.g. Connolly and Podladchikov, 2007; Räss et al., 2019). 2D and 3D models of porosity waves are important to study the mass transport of melt because the effective mass transport predicted by 1D models is less compared to predictions of 2D models (Jordan et al., 2018).

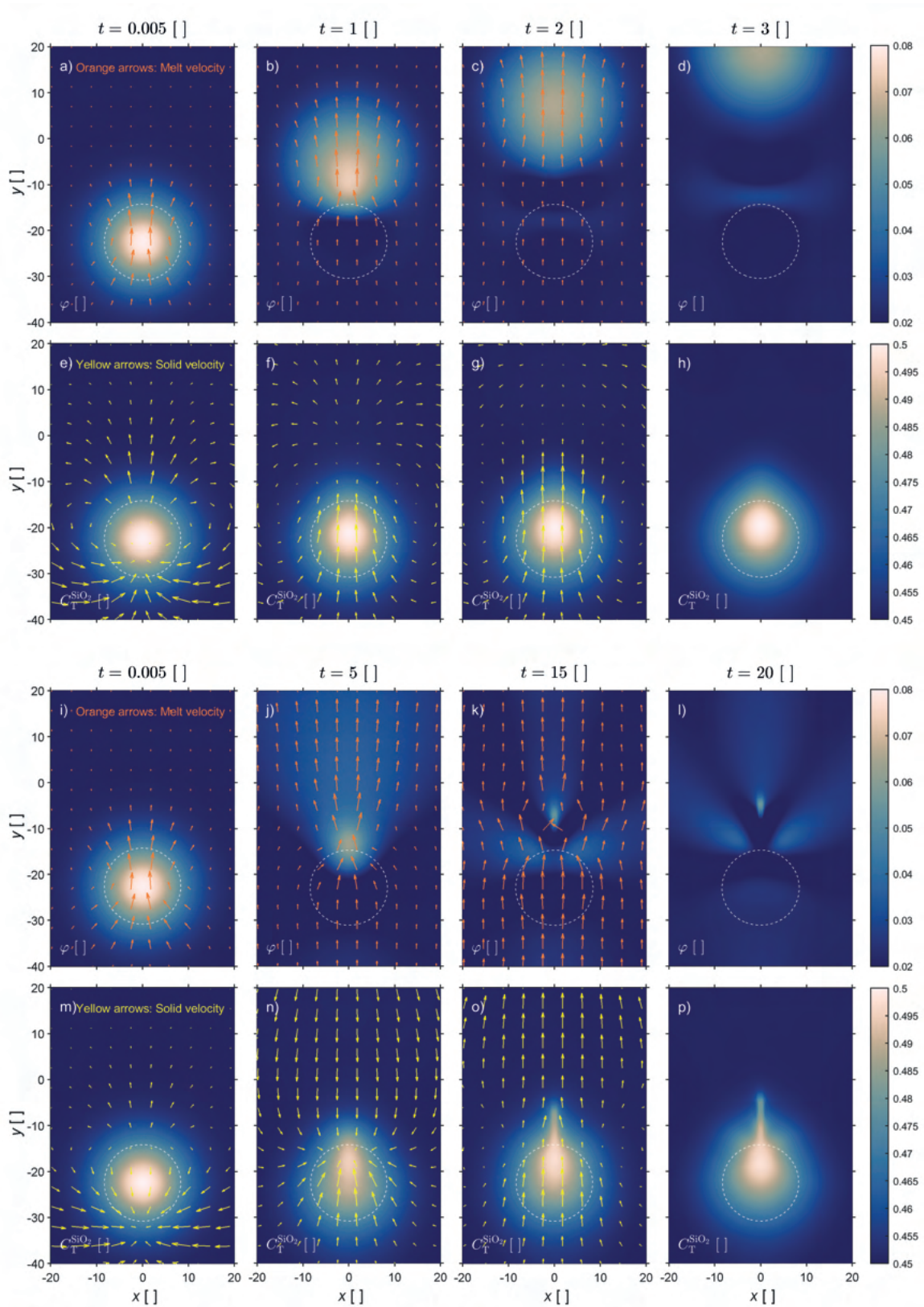


Figure 3.10: (Caption next page.)

Figure 3.10: (Previous page.) Time evolution of two 2D melt migration models by reactive porosity waves. Panels (a-d) show the porosity and panels (e-h) the total silica mass fraction for the blob-like simulation at four time steps (0.005, 1, 2 and 3). $(\eta_s/\eta_v)=1$ and $(\eta_d/\eta_v)=1$ for the blob-like simulation. Panels (i-l) show the porosity and panels (m-p) the total silica mass fraction for the channel-like simulation at four time steps (0.005, 5, 15 and 20). $(\eta_s/\eta_v)=25$ and $(\eta_d/\eta_v)=\eta_v/100=0.1$ for the channel-like simulation. Orange arrows show melt velocity, yellow arrows show solid velocity and dashed circles the position of initial perturbations. All variables are dimensionless.

The presented 1D THMC transport model is straightforward expandable to 2D and 3D. The main difference compared to the 1D model is that the deformation of the viscous solid must be calculated with a 2D model for viscous flow including both shear and normal deviatoric stresses. For all other conservation equations simply the 2D advective and diffusive fluxes must be added. We present here first results of two 2D models to show the localization of flow from a blob-like (Fig. 3.10 a-d) to a channel-like geometry (Fig. 3.10 i-l), and associated evolutions of the total silica content (Fig. 3.10 e-h and m-p). The 2D models employ mostly the same parameters as the 1D model, but, for example, the initial perturbation of the porosity has the form of a 2D Gaussian. For the model with blob-like geometry, we apply $\eta_s/\eta_v = 1$ and $\eta_d/\eta_v = 1$ and for the model with channel-like geometry $\eta_s/\eta_v = 25$ and $\eta_d/\eta_v = 0.1$.

Panels (d), (h), (l) and (p) in Fig. 3.10 show the chemical exchange between melt and solid in both simulations by the different evolution of the porosity and the total silica mass fraction. This exchange enables an enrichment of total silica in the solid and a differentiation of the melt in the pores.

The migration of melt by either blob-like or by channelized flow is an important process to consider for understanding metasomatism in a ductile region. Following the schematic illustration of Harte et al. (1993) (Fig. 3.11), the focusing of melt arriving in a rock to be eventually metasomatised (indicated by black arrows) has an impact on the type of metasomatism; from a pervasive metasomatism (Fig. 3.11a), through the formation of veins (Fig. 3.11b) to channels (Fig. 3.11c). Another important aspect is the melt-rock equilibration at every time step in the model. In the 2D simulation presented in figure 3.10, blob-like migration shows the importance of reaction as the chemical anomaly doesn't rise with the porosity but is accommodated by the solid via melt-rock reaction. This is illustrated by the

Modal metasomatism: various degrees of channelizing of the melt flow

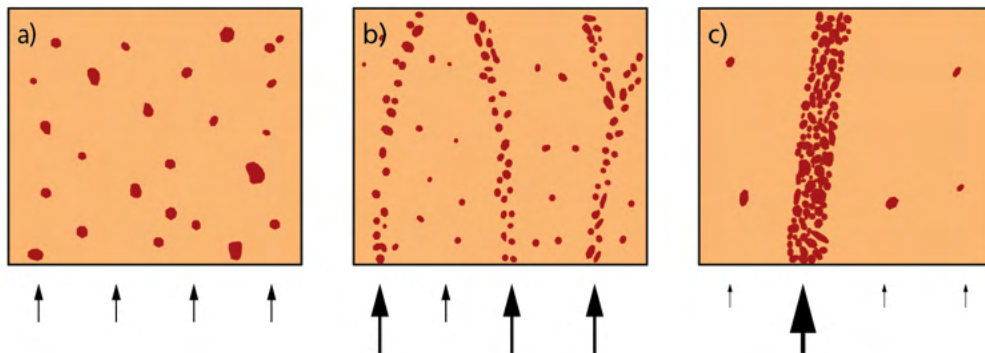


Figure 3.11: Schematic illustration showing the various degrees of channelizing of the melt flow in function of the distribution of melt flux. Redrawn from Harte et al. (1993)

comparison between the location of the porosity perturbation in figure 3.10d and the zone with higher total SiO_2 mass fraction, which is still close to the initial perturbation indicated by the dashed circle. In contrast, in the channel-like migration the porosity is focusing and allows the chemical perturbation to rise (Fig. 3.10l and p). The combination of melt-rock reaction with the type of melt migration seems therefore fundamental to understand the type of metasomatism recorded in the lithospheric mantle.

An example of melt-rock reaction has been recently considered by Tomlinson and Kamber (2021) to explain the formation and evolution of the subcontinental cratonic lithospheric mantle. Xenoliths sampled by kimberlites have revealed that the cratonic lithosphere is heterogeneous and contains olivine with high magnesium content (Fo₉₂₋₉₄), which requires extensive melting (Boyd and Mertzman, 1987; Herzberg, 1993). One interesting feature of this peridotite xenolith suite is the lower MgO/SiO_2 ratio for a given magnesium number (Mg#) of Archean subcontinental cratonic lithosphere regarding younger subcontinental lithospheric mantle. While various hypotheses have been proposed to explain this feature (e.g. Boyd and Mertzman, 1987; Herzberg, 1993), Tomlinson and Kamber (2021) suggest that silica enrichment in cratonic lithosphere could be associated to the migration of komatiite magma produced in episodic hot asthenospheric upwellings, which interact with previously depleted peridotite. Their melt-peridotite interaction is supported by THERMOCALC calculations, but no physical aspect on melt migration is considered. Although our thermodynamic cal-

culatation does not yet allow to predict natural melt-peridotite chemical interactions due to our simplified chemical system, which does not take into account pyroxene crystallization or dissolution, the mechanical aspects of our model provide some new insights of melt-percolation within the lithospheric mantle, supporting potential channelization of melt passing through a cratonic lithosphere.

3.4.4 Estimates of melt velocity

We can use the characteristic values of L_c and t_c to calculate a dimensional melt velocity from the numerically calculated dimensionless melt velocity, by applying representative values for melt viscosity, volumetric viscosity and porosity. Using a porosity φ of 2%, the effective permeability is in the order of $k = 10^{-7} \cdot \varphi^3 = 8 \cdot 10^{-13} \text{ [m}^2\text{]}$ (e.g. Connolly and Podladchikov, 2007). We assume values for melt viscosity η_m between 0.1 and 10 [Pa·s] (e.g. McKenzie, 1989). We further assume that the volumetric viscosity η_v is identical to the shear viscosity around the LAB and use 10^{19} [Pa·s], in agreement with numerical lithosphere subduction simulations of Bessat et al. (2020). The applied melt density is the reference density ($\rho_{m,0} = 3.8631 \cdot 10^3 \text{ [kg}\cdot\text{m}^{-3}\text{]}$). Taking a typical dimensionless velocity of 12 from the two simulations S15 (red dots in the top middle in Fig. 3.6a and b), we obtain a dimensional melt velocity between 1 to 115 [$\text{m}\cdot\text{yr}^{-1}$]. Modifying the porosity φ to 1 and 0.5%, and the associated permeability, and using a melt viscosity η_m of 0.1 [Pa·s], which seems more realistic for low degree melts rising in the lithosphere, we obtain velocities between 14.3 [$\text{m}\cdot\text{yr}^{-1}$] and 1.8 [$\text{m}\cdot\text{yr}^{-1}$] for a porosity of 1 and 0.5%, respectively. Using a larger melt viscosity η_m of 10 [Pa·s], as used by Connolly et al. (2009) to estimate melt velocity at mid ocean ridges, we obtain 14 [$\text{cm}\cdot\text{yr}^{-1}$] and 1.8 [$\text{cm}\cdot\text{yr}^{-1}$], respectively. These estimated melt velocities agree to first order with melt transport velocities deduced from centrifuge experiments by Connolly et al. (2009), which are 2 to 150 [$\text{m}\cdot\text{yr}^{-1}$] and considered applicable for melt rising at mid-ocean-ridges.

3.5 Conclusions

We present a new numerical model for two-phase melt migration in a deformable viscous solid coupled to chemical differentiation. The model is based on the coupling of a thermo-hydro-mechanical-chemical (THMC) transport model with thermodynamic results that have been precomputed by Gibbs energy minimization. For the considered system of forsterite-fayalite-silica, the solid and melt densities and the mass fractions of MgO and SiO₂ in both solid and melt are fully mobile, and all densities and mass fractions vary with temperature, pressure and total silica content. Therefore, the model is suitable to investigate chemical differentiation, metasomatism and melt-rock interaction during melt migration. The developed 1D and 2D THMC transport model can generate porosity waves. The initial variation of porosity and total silica content has a strong impact on the melt velocity. Also, the employed thermal gradient in the model, either adiabatic or conductive, has an impact on the melt velocity, with higher velocities for an adiabatic gradient. For conditions applicable to the lithosphere-asthenosphere boundary, the densities for an adiabatic gradient generally increase with depth and increasing pressure, while for a conductive gradient the densities decrease with increasing depth. The thermal gradient, therefore, has a considerable impact on the vertical variation of solid and melt densities and mass fractions and, hence, on the chemical differentiation during melt migration. Application of a range of typical lithosphere values for porosity, permeability, melt and compaction viscosities provides reasonable melt velocities between 10 [cm·yr⁻¹] and 100 [m·yr⁻¹]. The 2D version of the model can generate blob-like and channel-like porosity waves. First 2D results show that the total silica mass transport is more efficient by channel-like porosity waves than by blob-like porosity waves, which has important implications for understanding metasomatism during melt migration across the ductile lithosphere. The thermodynamic results show that the sensitivity of solid and melt densities to variations in P , T and $C_T^{\text{SiO}_2}$, expressed by the coefficients α , β and γ , can be considerably different. The same applies for the solid and melt mass fractions of MgO and SiO₂. Particularly, the sensitivity to chemical variations in $C_T^{\text{SiO}_2}$ is considerably different for the corresponding densities and considered mass fractions of the solid and melt phases.

Hence, it is important to treat the dependencies of densities and mass fractions of solid and melt phase on variations in P , T and $C_T^{\text{SiO}_2}$ independently in a THMC melt migration model and determine these dependencies with thermodynamic calculations.

Bibliography

- Aharonov, E., Spiegelman, M., Kelemen, P., 1997. Three-dimensional flow and reaction in porous media: Implications for the earth's mantle and sedimentary basins. *Journal of Geophysical Research: Solid Earth* 102 (B7), 14821–14833.
- Aharonov, E., Whitehead, J. A., Kelemen, P. B., 1995. Channeling instability of upwelling melt in the mantle. *Journal of Geophysical Research* 100 (B10), 20,433–20,450.
- Ahern, J., Turcotte, D., 1979. Magma migration beneath an ocean ridge. *Earth and Planetary Science Letters* 45 (1), 115–122.
- Beinlich, A., John, T., Vrijmoed, J. C., Tominaga, M., Magna, T., Podladchikov, Y. Y., 2020. Instantaneous rock transformations in the deep crust driven by reactive fluid flow. *Nature Geoscience* 13 (4), 307–311.
- Bessat, A., Duretz, T., Hetényi, G., Pilet, S., Schmalholz, S. M., 2020. Stress and deformation mechanisms at a subduction zone: insights from 2-d thermomechanical numerical modelling. *Geophysical Journal International* 221 (3), 1605–1625.
- Best, M., 1974. Mantle-derived amphibole within inclusions in alkalic-basaltic lavas. *Journal of Geophysical Research* 79 (14), 2107–2113.
- Boyd, F., Mertzman, S., 1987. Composition and structure of the kaapvaal lithosphere, southern africa. *Magmatic processes: physicochemical principles* 1, 3–12.
- Burov, E. B., 2011. Rheology and strength of the lithosphere. *Marine and Petroleum Geology* 28 (8), 1402–1443.
- Chakraborty, S., 2017. A New Mechanism for Upper Crustal Fluid Flow Driven by Solitary Porosity Waves in Rigid Reactive Media? *Geophysical Research Letters* 44 (20), 10324–10327.
- Connolly, J. A. D., Podladchikov, Y. Y., 1998. Compaction-driven fluid flow in viscoelastic rock. *Geodinamica Acta* 11 (2-3), 55–84.

- Connolly, J. A. D., Podladchikov, Y. Y., 2007. Decompaction weakening and channeling instability in ductile porous media: Implications for asthenospheric melt segregation. *Journal of Geophysical Research* 112 (B10).
- Connolly, J. A. D., Podladchikov, Y. Y., 2013. A Hydromechanical Model for Lower Crustal Fluid Flow. In: *Metasomatism and the Chemical Transformation of Rock*. Springer Berlin Heidelberg, Berlin, Heidelberg, pp. 599–658.
- Connolly, J. A. D., Schmidt, M. W., Solferino, G., Bagdassarov, N., 2009. Permeability of asthenospheric mantle and melt extraction rates at mid-ocean ridges. *Nature* 462 (7270), 209–212.
- Cruden, A. R., 1988. Deformation around a rising diapir modeled by creeping flow past a sphere. *Tectonics* 7 (5), 1091–1101.
- Davis, F., Hirschmann, M., Humayun, M., 2011. The composition of the incipient partial melt of garnet peridotite at 3GPa and the origin of OIB. *Earth and Planetary Science Letters* 308 (3-4), 380–390.
- Duretz, T., Räss, L., Podladchikov, Y., Schmalholz, S., 2019. Resolving thermomechanical coupling in two and three dimensions: spontaneous strain localization owing to shear heating. *Geophysical Journal International* 216 (1), 365–379.
- Francis, D., 1976. The origin of amphibole in lherzolite xenoliths from nunivak island, alaska. *Journal of Petrology* 17 (3), 357–378.
- Gerya, T., 2019. *Introduction to Numerical Geodynamic Modelling*, 2nd Edition. Cambridge University Press, Cambridge.
- Griffin, W., O'reilly, S. Y., Afonso, J. C., Begg, G., 2009. The composition and evolution of lithospheric mantle: a re-evaluation and its tectonic implications. *Journal of Petrology* 50 (7), 1185–1204.

- Harte, B., Hunter, R., Kinny, P., 1993. Melt geometry, movement and crystallization, in relation to mantle dykes, veins and metasomatism. *Philosophical Transactions of the Royal Society of London. Series A: Physical and Engineering Sciences* 342 (1663), 1–21.
- Herzberg, C. T., 1993. Lithosphere peridotites of the Kaapvaal craton. *Earth and Planetary Science Letters* 120 (1-2), 13–29.
- Herzberg, C. T., Baker, M. B., Wendlandt, R. F., 1982. Olivine flotation and settling experiments on the join Mg_2SiO_4 - Fe_2SiO_2 . *Contributions to Mineralogy and Petrology* 80 (4), 319–323.
- Hirose, K., Kushiro, I., 1993. Partial melting of dry peridotites at high pressures: Determination of compositions of melts segregated from peridotite using aggregates of diamond. *Earth and Planetary Science Letters* 114 (4), 477–489.
- Hofmann, A., 1972. Chromatographic theory of infiltration metasomatism and its application to feldspars. *American Journal of Science* 272 (1), 69–90.
- Holland, T. J. B., Powell, R., 1998. An internally consistent thermodynamic data set for phases of petrological interest. *Journal of Metamorphic Geology* 16 (3), 309–343.
- Holtzman, B. K., Kohlstedt, D. L., 2007. Stress-driven melt segregation and strain partitioning in partially molten rocks: Effects of stress and strain.
- Irving, A. J., 1980. Petrology and geochemistry of composite ultramafic xenoliths in alkalic basalts and implications for magmatic processes within the mantle. *American Journal of Science* 280 (2), 389–426.
- Jackson, M. D., Blundy, J., Sparks, R. S. J., 2018. Chemical differentiation, cold storage and remobilization of magma in the Earth's crust. *Nature* 564 (7736), 405–409.
- Jones, R. D. W., Katz, R. F., 2018. Reaction-infiltration instability in a compacting porous medium. *Journal of Fluid Mechanics* 852, 5–36.
- Jordan, J. S., Hesse, M. A., Rudge, J. F., 2018. On mass transport in porosity waves. *Earth and Planetary Science Letters* 485, 65–78.

- Katz, R. F., Spiegelman, M., Holtzman, B., 2006. The dynamics of melt and shear localization in partially molten aggregates. *Nature* 442 (7103), 676–679.
- Kelemen, P. B., Hirth, G., Shimizu, N., Spiegelman, M., Dick, H. J. B., 1997. A review of melt migration processes in the adiabatically upwelling mantle beneath oceanic spreading ridges. *Philosophical Transactions of the Royal Society A: Mathematical, Physical and Engineering Sciences* 355, 283–318.
- Keller, T., May, D. A., Kaus, B. J. P., 2013. Numerical modelling of magma dynamics coupled to tectonic deformation of lithosphere and crust. *Geophysical Journal International* 195 (3), 1406–1442.
- Keller, T., Suckale, J., 2019. A continuum model of multi-phase reactive transport in igneous systems. *Geophysical Journal International* 219 (1), 185–222.
- Korzhinskii, D., 1965. The theory of systems with perfectly mobile components and processes of mineral formation. *American Journal of Science* 263 (3), 193–205.
- Kushiro, I., 1996. Partial melting of fertile mantle peridotite at high pressures: an experimental study using aggregates of diamond. *Geophysical Monograph-American Geophysical Union* 95, 109–122.
- Langmuir, C. H., Klein, E. M., Plank, T., 1992. Petrological Systematics of Mid-Ocean Ridge Basalts: Constraints on Melt Generation Beneath Ocean Ridges. In: *Mantle Flow and Melt Generation at Mid-Ocean Ridges*. American Geophysical Union (AGU), pp. 183–280.
- Lloyd, F. E., Bailey, D. K., 1975. Light element metasomatism of the continental mantle: The evidence and the consequences. *Physics and Chemistry of the Earth* 9, 389–416.
- Malvoisin, B., Podladchikov, Y. Y., Vrijmoed, J. C., 2015. Coupling changes in densities and porosity to fluid pressure variations in reactive porous fluid flow: Local thermodynamic equilibrium. *Geochemistry, Geophysics, Geosystems* 16 (12), 4362–4387.
- McKenzie, D., 1984. The Generation and Compaction of Partially Molten Rock. *Journal of Petrology* 25 (3), 713–765.

- McKenzie, D., 1985. The extraction of magma from the crust and mantle. *Earth and Planetary Science Letters* 74 (1), 81–91.
- McKenzie, D., 1989. Some remarks on the movement of small melt fractions in the mantle. *Earth and Planetary Science Letters* 95 (1-2), 53–72.
- Miller, R. B., Paterson, S. R., 1999. In defense of magmatic diapirs. *Journal of Structural Geology* 21 (8), 1161–1173.
- Müller, I., 2007. *A History of Thermodynamics: The Doctrine of Energy and Entropy*. Springer-Verlag, Berlin Heidelberg.
- Nauman, E. B., He, D. Q., 2001. Nonlinear diffusion and phase separation. *Chemical Engineering Science*, 20.
- Nielson, J. E., Noller, J. S., 1987. Processes of mantle metasomatism; Constraints from observations of composite peridotite xenoliths. *Geological Society of America* 215, 61–76.
- Nielson, J. E., Wilshire, H., 1993. Magma transport and metasomatism in the mantle: A critical review of current geochemical models. *American Mineralogist* 78, 1117–1134.
- Omlin, S., Malvoisin, B., Podladchikov, Y. Y., 2017. Pore fluid extraction by reactive solitary waves in 3-d. *Geophysical Research Letters* 44 (18), 9267–9275.
- Pilet, S., Baker, M. B., Stolper, E. M., 2008. Metasomatized Lithosphere and the Origin of Alkaline Lavas. *Science* 320 (5878), 916–919.
- Plümper, O., John, T., Podladchikov, Y. Y., Vrijmoed, J. C., Scambelluri, M., 2016. Fluid escape from subduction zones controlled by channel-forming reactive porosity. *Nature Geoscience* 10, 150.
- Räss, L., Duretz, T., Podladchikov, Y. Y., 2019. Resolving hydromechanical coupling in two and three dimensions: spontaneous channelling of porous fluids owing to decompaction weakening. *Geophysical Journal International* 218 (3), 1591–1616.

- Schmalholz, S. M., Moulas, E., Plümper, O., Myasnikov, A. V., Podladchikov, Y. Y., 2020. 2D Hydro-Mechanical-Chemical Modeling of (De)hydration Reactions in Deforming Heterogeneous Rock: The Periclase-Brucite Model Reaction. *Geochemistry, Geophysics, Geosystems* 21 (11).
- Scott, D. R., Stevenson, D. J., 1984. Magma solitons. *Geophysical Research Letters* 11 (11), 1161–1164.
- Shaw, H. R., 1980. Chapter 6. The Fracture Mechanisms of Magma Transport From The Mantle to The Surface. In: *Physics of Magmatic Processes*. Princeton University Press, pp. 201–264.
- Spiegelman, M., 1993. Physics of Melt Extraction: Theory, Implications and Applications. *Philosophical Transactions of the Royal Society of London Series A* 342, 23–41.
- Spiegelman, M., Kelemen, P. B., Aharonov, E., 2001. Causes and consequences of flow organization during melt transport: The reaction infiltration instability in compactible media. *Journal of Geophysical Research: Solid Earth* 106 (B2), 2061–2077.
- Stevenson, D. J., 1989. Spontaneous small-scale melt segregation in partial melts undergoing deformation. *Geophysical Research Letters* 16 (9), 1067–1070.
- Tomlinson, E. L., Kamber, B. S., 2021. Depth-dependent peridotite-melt interaction and the origin of variable silica in the cratonic mantle. *Nature Communications* 12 (1), 1082.
- Walker, D., Stolper, E. M., Hays, J. F., 1978. A numerical treatment of melt/solid segregation: Size of the eucrite parent body and stability of the terrestrial low-velocity zone. *Journal of Geophysical Research: Solid Earth* 83 (B12), 6005–6013.
- Walter, M. J., 1998. Melting of Garnet Peridotite and the Origin of Komatiite and Depleted Lithosphere 39 (1), 32.
- Wass, S. Y., Roge, N. W., 1980. Mantle metasomatism—precursor to continental alkaline volcanism. *Geochimica et Cosmochimica Acta* 44 (11), 1811–1823.

- Wasylenki, L. E., Baker, M. B., Kent, A. J. R., Stolper, E. M., 2003. Near-solidus Melting of the Shallow Upper Mantle: Partial Melting Experiments on Depleted Peridotite. *Journal of Petrology* 44 (7), 1163–1191.
- Weatherley, S. M., Katz, R. F., 2012. Melting and channelized magmatic flow in chemically heterogeneous, upwelling mantle. *Geochemistry, Geophysics, Geosystems* 13 (5).
- Weinberg, R. F., Podladchikov, Y., 1994. Diapiric ascent of magmas through power law crust and mantle. *Journal of Geophysical Research: Solid Earth* 99 (B5), 9543–9559.
- Wilshire, H., 1987. A model of mantle metasomatism. *Mantle Metasomatism and Alkaline Magmatism*. Geological Society of America, Special Papers 215, 47–60.
- Yarushina, V. M., Podladchikov, Y. Y., 2015. (De)compaction of porous viscoelastoplastic media: Model formulation. *Journal of Geophysical Research: Solid Earth* 120 (6), 4146–4170.

Appendix A. THMC model equations, additional explanation

A general conservation equation without a source term in 1D for any variable, here named B (per unit volume), has the form:

$$\frac{\partial B}{\partial t} = -\frac{\partial}{\partial x}q_A - \frac{\partial}{\partial x}q_D \quad (3.A1)$$

where t is the time, q_A is the advective flux and q_D is the diffusive flux. The advective flux corresponds to the transport of B with its velocity v_b :

$$q_A = Bv_b \quad (3.A2)$$

A porous medium, with porosity φ , is composed of a solid skeleton (solid phase) with density ρ_s and a melt phase in the pores with density ρ_m . The total mass of the medium, having total density ρ_T , is the sum of the mass of melt in pores and the mass of the solid:

$$B = \rho_m\varphi + \rho_s(1 - \varphi) = \rho_T \quad (3.A3)$$

The advective flux for the total mass is:

$$q_A = \rho_m\varphi v_m + \rho_s(1 - \varphi)v_s \quad (3.A4)$$

where v_m and v_s are the melt and solid velocities, respectively. There is no diffusive flux in the conservation of the total mass, hence:

$$q_D = 0 \quad (3.A5)$$

Therefore, the conservation equation for total mass is:

$$\frac{\partial}{\partial t}(\rho_m\varphi + \rho_s(1 - \varphi)) = -\frac{\partial}{\partial x}(\rho_m\varphi v_m + \rho_s(1 - \varphi)v_s) \quad (3.A6)$$

The force balance for the melt follows Darcy's law:

$$\varphi(v_m - v_s) = -\frac{k\varphi^3}{\eta_m} \left(\frac{\partial P_m}{\partial x} + \rho_m g \right) \quad (3.A7)$$

where k is the permeability, η_m is the melt viscosity, P_m is the melt pressure and g is the gravitational acceleration. To introduce the Darcy's force balance in the total mass conservation equation, it is useful to modify equation (3.A6) by subtracting and adding v_s to v_m :

$$\frac{\partial}{\partial t}(\rho_m \varphi + \rho_s(1 - \varphi)) = -\frac{\partial}{\partial x}(\rho_m \varphi(v_m - v_s + v_s) + \rho_s(1 - \varphi)v_s) \quad (3.A8)$$

Equation (3.A8) can be rewritten as:

$$\frac{\partial}{\partial t}(\rho_m \varphi + \rho_s(1 - \varphi)) = -\frac{\partial}{\partial x} \left(-\rho_m \frac{k\varphi^3}{\eta_m} \left(\frac{\partial P_m}{\partial x} + \rho_m g \right) + \rho_m \varphi v_s + \rho_s(1 - \varphi)v_s \right) \quad (3.A9)$$

Equation (3.A9) can be simplified by collecting terms in front of v_s :

$$\frac{\partial}{\partial t}(\rho_m \varphi + \rho_s(1 - \varphi)) = -\frac{\partial}{\partial x} \left(-\rho_m \frac{k\varphi^3}{\eta_m} \left(\frac{\partial P_m}{\partial x} + \rho_m g \right) + \rho_T v_s \right) \quad (3.A10)$$

The total mass of magnesium (MgO) considers the concentration of MgO in the melt and in the solid:

$$B = C_m^{\text{MgO}} \rho_m \varphi + C_s^{\text{MgO}} \rho_s(1 - \varphi) = M_T^{\text{MgO}} \quad (3.A11)$$

where C_m^{MgO} and C_s^{MgO} are, respectively, the mass fractions (C_m^{MgO} = mass of MgO in the melt / total mass of melt; C_s^{MgO} = mass of MgO in the solid / total mass of solid) of MgO in the melt and in the solid. The advective flux for the total mass of MgO is:

$$q_A = C_m^{\text{MgO}} \rho_m \varphi v_m + C_s^{\text{MgO}} \rho_s(1 - \varphi)v_s \quad (3.A12)$$

Assuming an ideal solution, the diffusive flux is described by Fick's law that describes the molecular diffusion of MgO in the melt and in the solid:

$$q_D = -D_m^{\text{MgO}} \rho_m \varphi \frac{\partial C_m^{\text{MgO}}}{\partial x} - D_s^{\text{MgO}} \rho_s (1 - \varphi) \frac{\partial C_s^{\text{MgO}}}{\partial x} \quad (3.A13)$$

where D_m^{MgO} and D_s^{MgO} are the effective diffusivities of MgO in the melt and in the solid (e.g. Nauman and He, 2001). Therefore, the conservation equation for total mass of MgO is:

$$\begin{aligned} \frac{\partial}{\partial t} (C_m^{\text{MgO}} \rho_m \varphi + C_s^{\text{MgO}} \rho_s (1 - \varphi)) = & -\frac{\partial}{\partial x} (C_m^{\text{MgO}} \rho_m \varphi v_m + C_s^{\text{MgO}} \rho_s (1 - \varphi) v_s) \\ & - D_m^{\text{MgO}} \rho_m \varphi \frac{\partial C_m^{\text{MgO}}}{\partial x} - D_s^{\text{MgO}} \rho_s (1 - \varphi) \frac{\partial C_s^{\text{MgO}}}{\partial x} \end{aligned} \quad (3.A14)$$

The total mass per unit of volume SiO_2 considers the concentration of SiO_2 in the melt and in the solid:

$$B = C_m^{\text{SiO}_2} \rho_m \varphi + C_s^{\text{SiO}_2} \rho_s (1 - \varphi) = M_T^{\text{SiO}_2} \quad (3.A15)$$

where $C_m^{\text{SiO}_2}$ and $C_s^{\text{SiO}_2}$ are, respectively, the mass fractions ($C_m^{\text{SiO}_2} = \text{mass of SiO}_2 \text{ in the melt} / \text{total mass of melt}$; $C_s^{\text{SiO}_2} = \text{mass of SiO}_2 \text{ in the solid} / \text{total mass of solid}$) of SiO_2 in the melt and in the solid. The advective flux for the total mass of SiO_2 is:

$$q_A = C_m^{\text{SiO}_2} \rho_m \varphi v_m + C_s^{\text{SiO}_2} \rho_s (1 - \varphi) v_s \quad (3.A16)$$

For an ideal solution, the diffusive flux is described by Fick's law that describes the molecular diffusion of SiO_2 in the melt and in the solid:

$$q_D = -D_m^{\text{SiO}_2} \rho_m \varphi \frac{\partial C_m^{\text{SiO}_2}}{\partial x} - D_s^{\text{SiO}_2} \rho_s (1 - \varphi) \frac{\partial C_s^{\text{SiO}_2}}{\partial x} \quad (3.A17)$$

where $D_m^{\text{SiO}_2}$ and $D_s^{\text{SiO}_2}$ are the effective diffusivities of SiO_2 in the melt and in the solid (e.g. Nauman and He, 2001). Therefore, conservation equation for total mass of SiO_2 is:

$$\begin{aligned} \frac{\partial}{\partial t} (C_m^{\text{SiO}_2} \rho_m \varphi + C_s^{\text{SiO}_2} \rho_s (1 - \varphi)) = & -\frac{\partial}{\partial x} (C_m^{\text{SiO}_2} \rho_m \varphi v_m + C_s^{\text{SiO}_2} \rho_s (1 - \varphi) v_s \\ & - D_m^{\text{SiO}_2} \rho_m \varphi \frac{\partial C_m^{\text{SiO}_2}}{\partial x} - D_s^{\text{SiO}_2} \rho_s (1 - \varphi) \frac{\partial C_s^{\text{SiO}_2}}{\partial x}) \end{aligned} \quad (3.A18)$$

The total thermal energy of the medium is:

$$U_m(P, T) = \int_{T_{\text{ref}}}^T (c_{p_m}(P, T') \rho_m(P, T')) dT' \quad (3.A19a)$$

$$U_s(P, T) = \int_{T_{\text{ref}}}^T (c_{p_s}(P, T') \rho_s(P, T')) dT' \quad (3.A19b)$$

$$B = U_m \varphi + U_s (1 - \varphi) = U_T \quad (3.A19c)$$

where c_{p_m} and c_{p_s} are specific heat capacity of the melt and the solid and T is the temperature.

The advective flux for thermal energy is:

$$q_A = U_m \varphi v_m + U_s (1 - \varphi) v_s \quad (3.A20)$$

Assuming that the temperature in the solid and fluid is identical, the diffusive flux is described by Fourier's law:

$$q_D = -\lambda_T \frac{\partial T}{\partial x} \quad (3.A21)$$

where $\lambda_T = (\lambda_m \varphi + \lambda_s (1 - \varphi))$ and λ_m and λ_s are the thermal conductivity of melt and solid, respectively. The conservation equation for the energy takes the form of:

$$\frac{\partial}{\partial t} (U_m \varphi + U_s (1 - \varphi)) = -\frac{\partial}{\partial x} (U_m \varphi v_m + U_s (1 - \varphi) v_s - \lambda_T \frac{\partial T}{\partial x}) \quad (3.A22)$$

The other mechanical equations that close the system of equations are presented in section 3.2.2, equations 3.12, 3.13, 3.15 and 3.16.

Appendix B. Additional figures and tables

Table 3.3: Numerical pseudo-transient time step used in the THMC simulations

Pseudo-transient time step	
for the melt pressure	$\Delta t_P^{\text{PT}} = \frac{1}{2} \frac{dx^2}{\max(k/\eta_m \cdot (\varphi/\varphi_0)^3)}$
for the porosity	$\Delta t_\varphi^{\text{PT}} = -dt$
for the total silica content	$\Delta t_{C_T^{\text{SiO}_2}}^{\text{PT}} = dt$
for the temperature	$\Delta t_T^{\text{PT}} = \frac{1}{4.1} \frac{dx^2}{\max(\lambda_m/\rho_T c_{pm})}$
for the solid velocity	$\Delta t_{v_s}^{\text{PT}} = \frac{1}{6} \frac{dx^2}{\eta_s}$

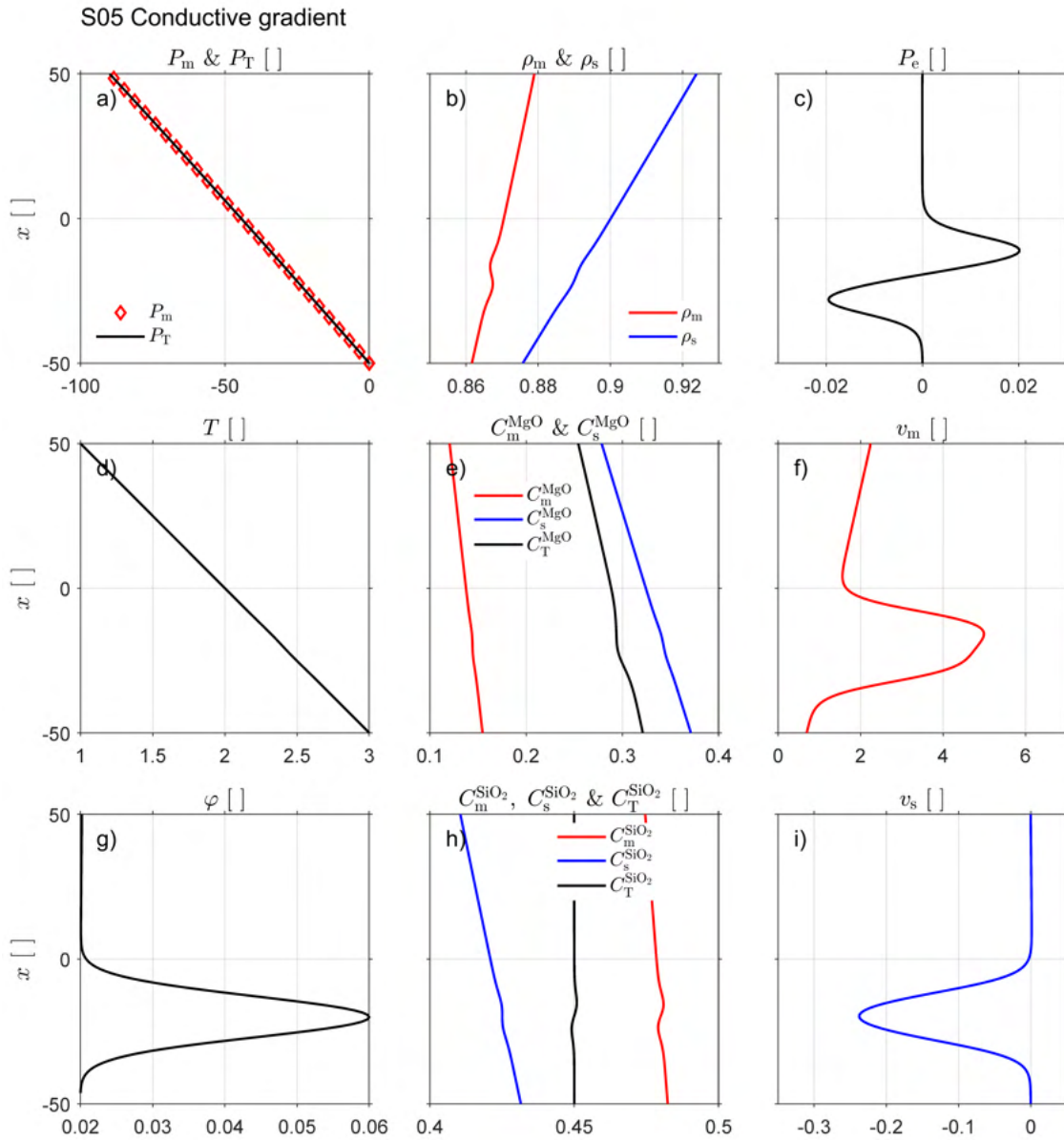


Figure 3.12: Initial profiles of simulation S05 Conductive gradient, all variables are dimensionless. Panel (a) shows melt pressure (red diamond) and total pressure (black line). Panel (b) shows melt density (red line) and solid density (blue line). Panel (c) shows effective pressure, positive values indicate decompaction while negative values indicate compaction. Panel (d) shows temperature. Panel (e) shows magnesium mass fraction in melt (red line) and in solid (blue line) and total magnesium mass fraction (black line). Panel (f) shows melt velocity. Panel (g) shows porosity. Panel (h) shows silica mass fraction in melt (red line) and in the solid (blue line) and total silica mass fraction (black line). Panel (i) shows solid velocity.

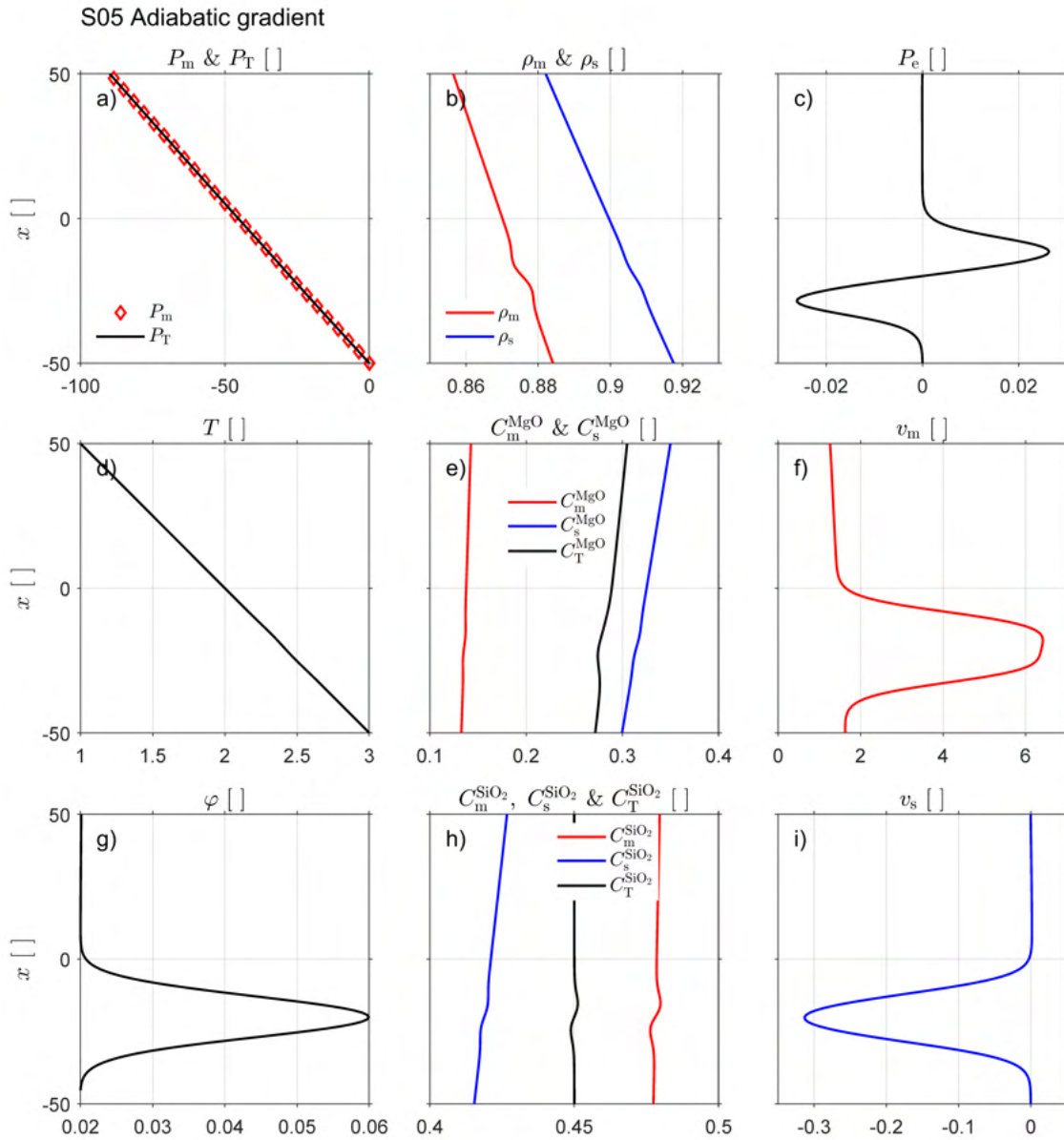


Figure 3.13: Initial profiles of simulation S05 Adiabatic gradient, all variables are dimensionless. Panel (a) shows melt pressure (red diamond) and total pressure (black line). Panel (b) shows melt density (red line) and solid density (blue line). Panel (c) shows effective pressure, positive values indicate decompaction while negative values indicate compaction. Panel (d) shows temperature. Panel (e) shows magnesium mass fraction in melt (red line) and in solid (blue line) and total magnesium mass fraction (black line). Panel (f) shows melt velocity. Panel (g) shows porosity. Panel (h) shows silica mass fraction in melt (red line) and in the solid (blue line) and total silica mass fraction (black line). Panel (i) shows solid velocity.

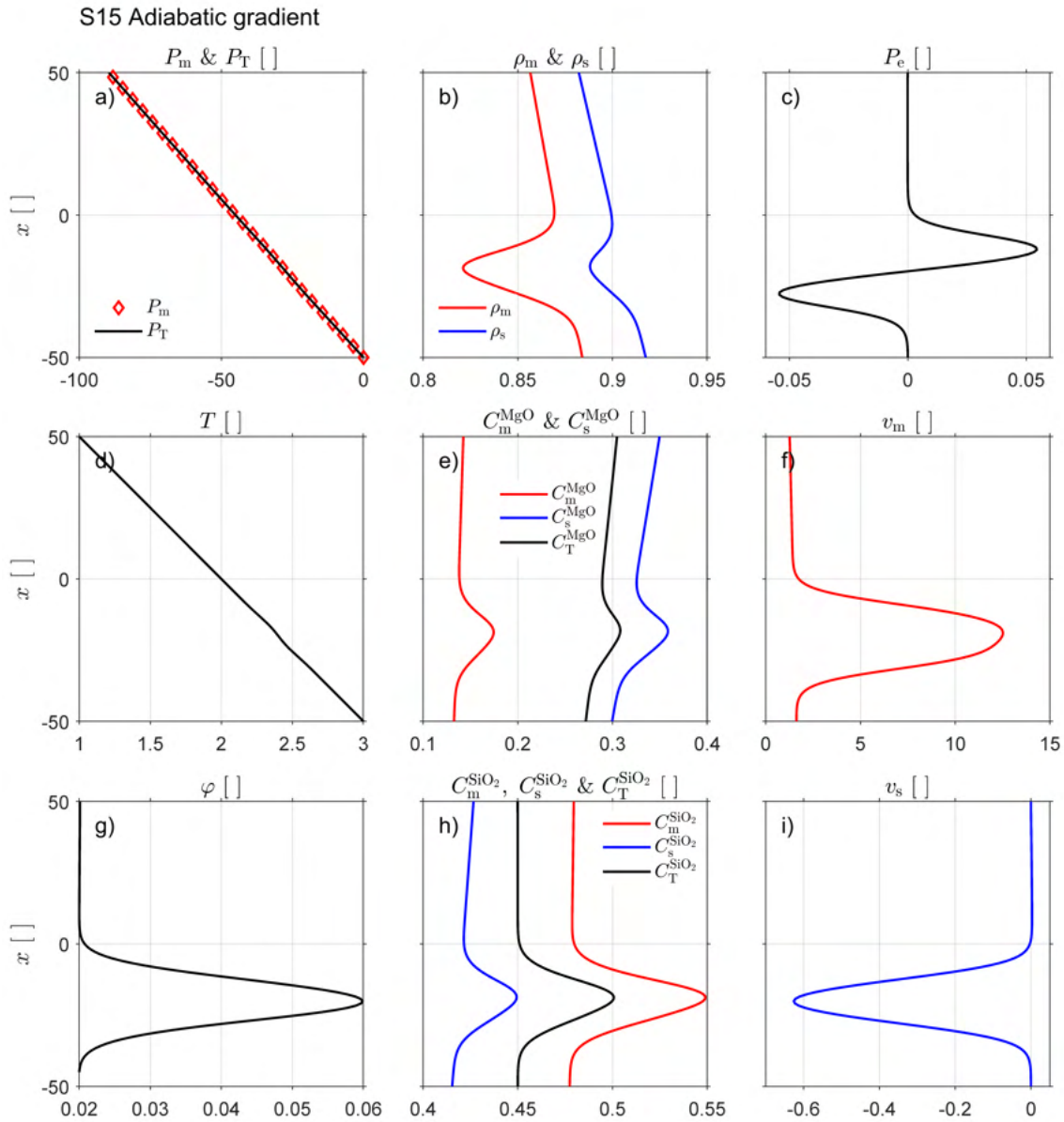


Figure 3.14: Initial profiles of simulation S15 Adiabatic gradient, all variables are dimensionless. Panel (a) shows melt pressure (red diamond) and total pressure (black line). Panel (b) shows melt density (red line) and solid density (blue line). Panel (c) shows effective pressure, positive values indicate decompaction while negative values indicate compaction. Panel (d) shows temperature. Panel (e) shows magnesium mass fraction in melt (red line) and in solid (blue line) and total magnesium mass fraction (black line). Panel (f) shows melt velocity. Panel (g) shows porosity. Panel (h) shows silica mass fraction in melt (red line) and in the solid (blue line) and total silica mass fraction (black line). Panel (i) shows solid velocity.

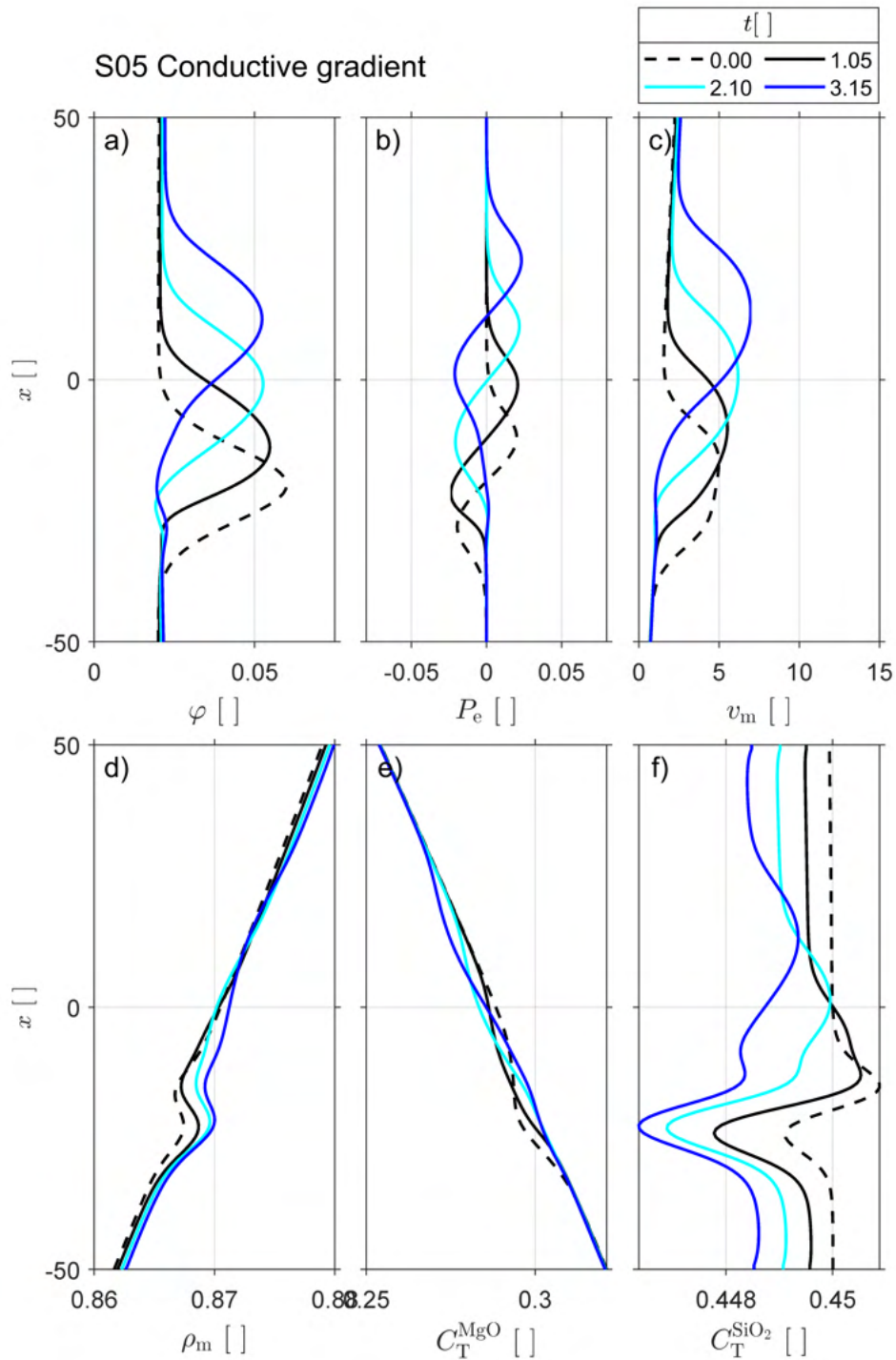


Figure 3.15: Evolution in time of six variables in simulation S05 Conductive gradient, all variables are dimensionless. Panel (a) shows porosity, panel (b) shows effective pressure, panel (c) shows melt velocity, panel (d) shows melt density, panel (e) shows total magnesium mass fraction and panel (f) shows total silica mass fraction. Four time steps are chosen at different dimensional times: $t = 0$ with dashed line (corresponding to the initial profiles in figure 3.12 for each variables), $t = 1.05$ with black line, $t = 2.10$ with light blue and $t = 3.15$ with dark blue (see legend).

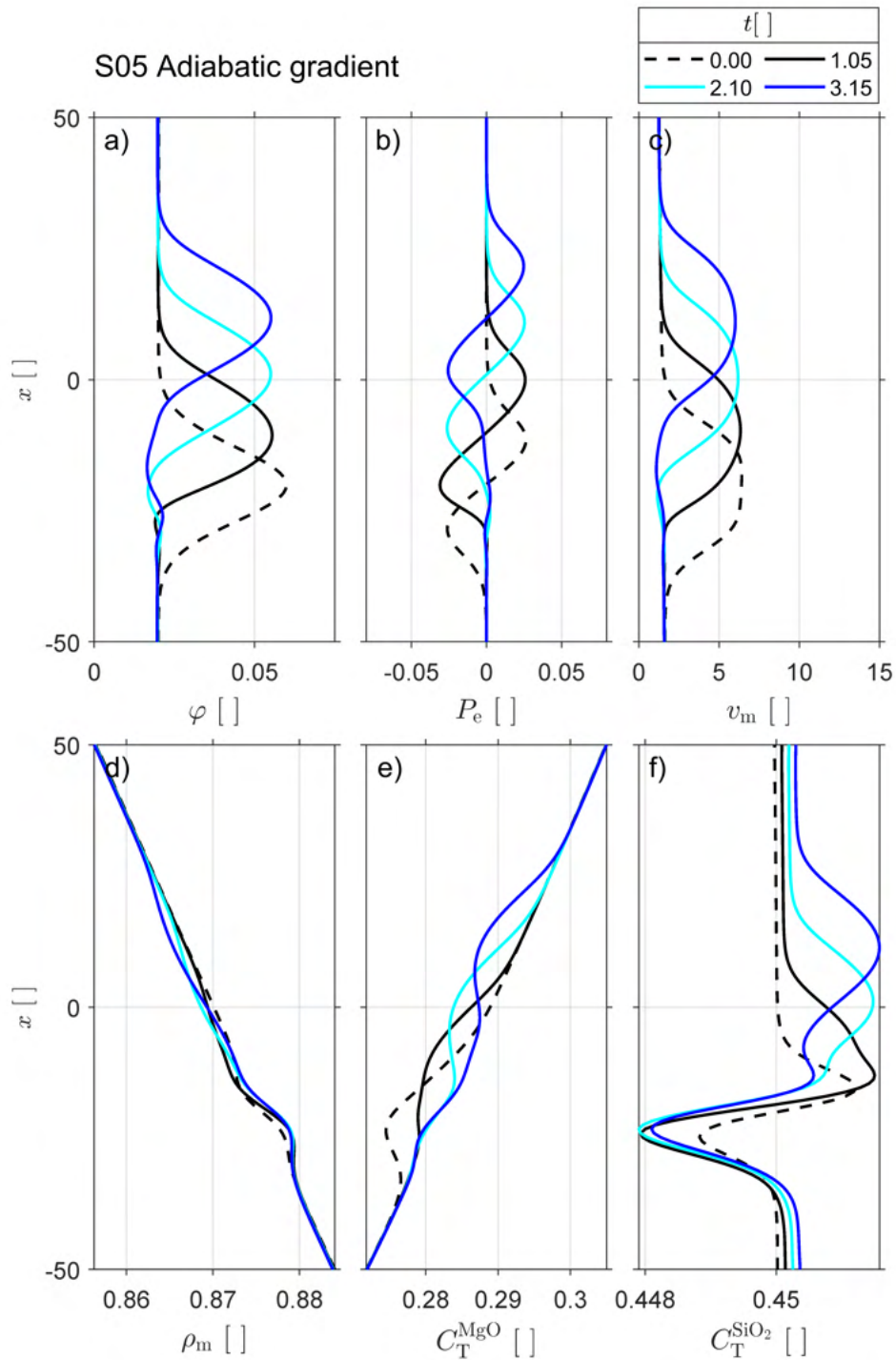


Figure 3.16: Evolution in time of six variables in simulation S05 Adiabatic gradient, all variables are dimensionless Panel (a) shows porosity, panel (b) shows effective pressure, panel (c) shows melt velocity, panel (d) shows melt density, panel (e) shows total magnesium mass fraction and panel (f) shows total silica mass fraction. Four time steps are chosen at different dimensional times: $t = 0$ with dashed line (corresponding to the initial profiles in figure 3.13 for each variables), $t = 1.05$ with black line, $t = 2.10$ with light blue and $t = 3.15$ with dark blue (see legend).

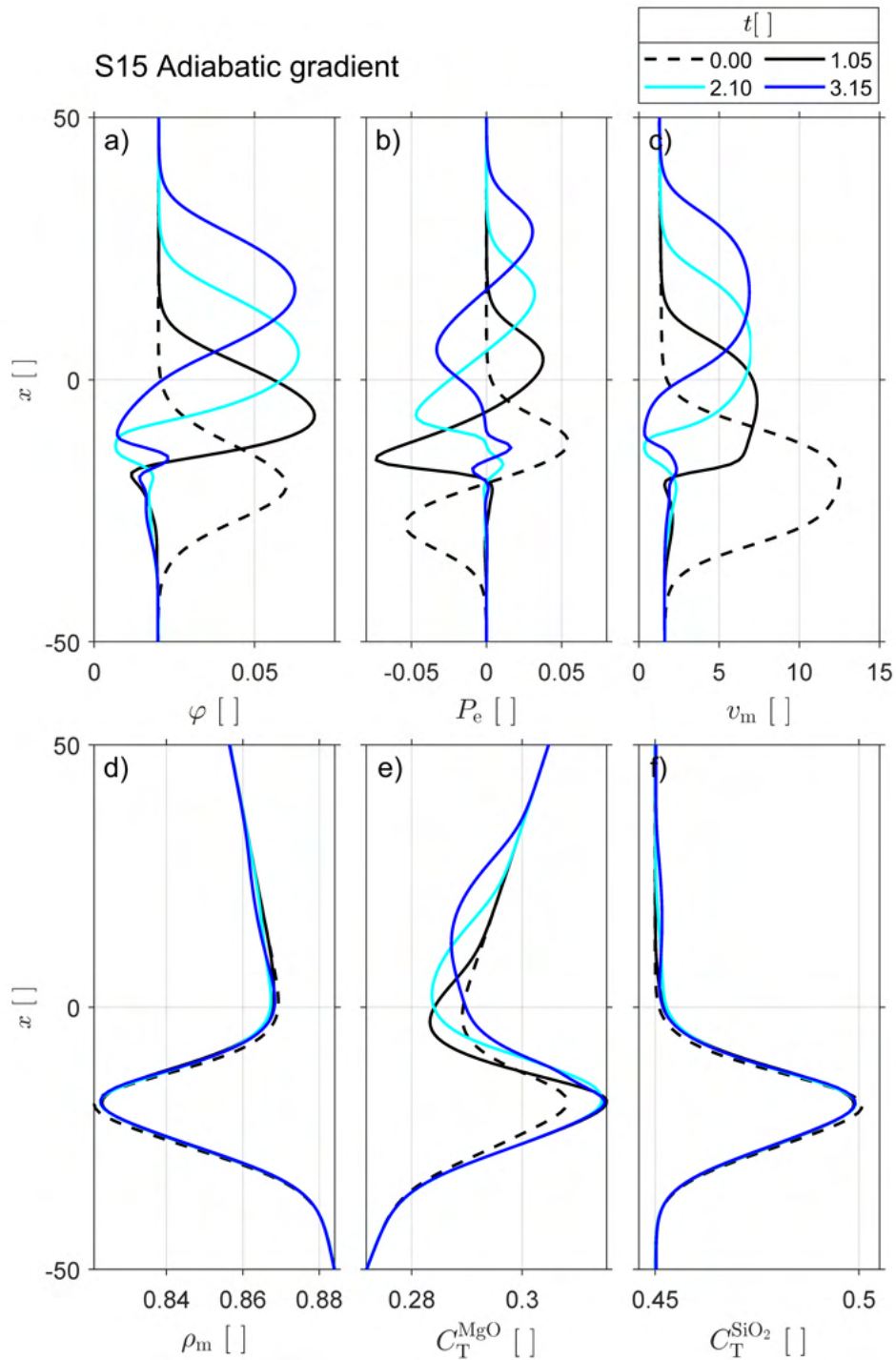


Figure 3.17: Evolution in time of six variables in simulation S15 Adiabatic gradient, all variables are dimensionless. Panel (a) shows porosity, panel (b) shows effective pressure, panel (c) shows melt velocity, panel (d) shows melt density, panel (e) shows total magnesium mass fraction and panel (f) shows total silica mass fraction. Four time steps are chosen at different dimensional times: $t = 0$ with dashed line (corresponding to the initial profiles in figure 3.14 for each variables), $t = 1.05$ with black line, $t = 2.10$ with light blue and $t = 3.15$ with dark blue (see legend).

Appendix C. Thermodynamic part, additional explanation

Transformation from molar fractions into mass fractions

To use molar concentrations in the mass conservation equations of the THMC transport model, we first transform these concentrations into olivine phase mass fractions:

$$C_m^{\text{foL}} = \frac{C_{m,[\text{mol}]}^{\text{foL}} \cdot m_m^{\text{foL}}}{(C_{m,[\text{mol}]}^{\text{foL}} \cdot m_m^{\text{foL}}) + (C_{m,[\text{mol}]}^{\text{faL}} \cdot m_m^{\text{faL}})} \quad (3.C1a)$$

$$C_m^{\text{faL}} = \frac{C_{m,[\text{mol}]}^{\text{faL}} \cdot m_m^{\text{faL}}}{(C_{m,[\text{mol}]}^{\text{foL}} \cdot m_m^{\text{foL}}) + (C_{m,[\text{mol}]}^{\text{faL}} \cdot m_m^{\text{faL}})} \quad (3.C1b)$$

$$C_s^{\text{fo}} = \frac{C_{s,[\text{mol}]}^{\text{fo}} \cdot m_s^{\text{fo}}}{(C_{s,[\text{mol}]}^{\text{fo}} \cdot m_s^{\text{fo}}) + (C_{s,[\text{mol}]}^{\text{fa}} \cdot m_s^{\text{fa}})} \quad (3.C1c)$$

$$C_s^{\text{fa}} = \frac{C_{s,[\text{mol}]}^{\text{fa}} \cdot m_s^{\text{fa}}}{(C_{s,[\text{mol}]}^{\text{fo}} \cdot m_s^{\text{fo}}) + (C_{s,[\text{mol}]}^{\text{fa}} \cdot m_s^{\text{fa}})} \quad (3.C1d)$$

where m_m^{foL} , m_m^{faL} , m_s^{fo} and m_s^{fa} are, respectively, the molar mass of forsterite and fayalite liquid for the melt part and forsterite and fayalite for the solid part. We transform these olivine phase mass fractions into oxide mass fractions of MgO, FeO and SiO₂:

$$C_{m,i}^{\text{MgO}} = C_m^{\text{foL}} \cdot M_r^{\text{MgO}} \cdot nb^{\text{MgO}} \quad (3.C2a)$$

$$C_{m,i}^{\text{FeO}} = (1 - C_m^{\text{foL}}) \cdot M_r^{\text{FeO}} \cdot nb^{\text{FeO}} \quad (3.C2b)$$

$$C_{m,i}^{\text{SiO}_2} = (C_m^{\text{foL}} + 1 - C_m^{\text{foL}}) \cdot M_r^{\text{SiO}_2} \cdot nb^{\text{SiO}_2} \quad (3.C2c)$$

where M_r^{MgO} , M_r^{FeO} and $M_r^{\text{SiO}_2}$ are molecular weight (i.e. relative molecular mass) of oxides ($M_r^{\text{MgO}} = 0.0403$ [kg·mol⁻¹], $M_r^{\text{FeO}} = 0.0708$ [kg·mol⁻¹] and $M_r^{\text{SiO}_2} = 0.0601$ [kg·mol⁻¹]), nb^{MgO} , nb^{FeO} and nb^{SiO_2} correspond to the number of times each oxide is in the olivine

formula ($nb^{\text{MgO}} = nb^{\text{FeO}} = 2$ and $nb^{\text{SiO}_2} = 1$), subscript i indicates that the oxide mass fractions $C_{m,i}^{\text{MgO}}$, $C_{m,i}^{\text{FeO}}$ and $C_{m,i}^{\text{SiO}_2}$ are not normalised. For the normalization, each oxide mass fraction is divided by the sum of these three oxide mass fractions:

$$C_m^{\text{MgO}} = \frac{C_{m,i}^{\text{MgO}}}{C_{m,i}^{\text{MgO}} + C_{m,i}^{\text{FeO}} + C_{m,i}^{\text{SiO}_2}} \quad (3.C3a)$$

$$C_m^{\text{FeO}} = \frac{C_{m,i}^{\text{FeO}}}{C_{m,i}^{\text{MgO}} + C_{m,i}^{\text{FeO}} + C_{m,i}^{\text{SiO}_2}} \quad (3.C3b)$$

$$C_m^{\text{SiO}_2} = \frac{C_{m,i}^{\text{SiO}_2}}{C_{m,i}^{\text{MgO}} + C_{m,i}^{\text{FeO}} + C_{m,i}^{\text{SiO}_2}} \quad (3.C3c)$$

C_m^{MgO} , C_m^{FeO} and $C_m^{\text{SiO}_2}$ are the oxide mass fractions that we use in the THMC model. We proceed with the same approach to calculate the values for the solid part, C_s^{MgO} , C_s^{FeO} and $C_s^{\text{SiO}_2}$.

Calculation of γ

We calculate the γ for $C_m^{\text{SiO}_2}$ and $C_s^{\text{SiO}_2}$ as follow :

$$\gamma_{C_m^{\text{SiO}_2}} = \left(\frac{C_{m,\text{exp}}^{\text{SiO}_2} - C_{m,0}^{\text{SiO}_2}}{C_{T,\text{exp}}^{\text{SiO}_2} - C_{T,0}^{\text{SiO}_2}} \right) / C_{m,0}^{\text{SiO}_2} \quad (3.C4a)$$

$$\gamma_{C_s^{\text{SiO}_2}} = \left(\frac{C_{s,\text{exp}}^{\text{SiO}_2} - C_{s,0}^{\text{SiO}_2}}{C_{T,\text{exp}}^{\text{SiO}_2} - C_{T,0}^{\text{SiO}_2}} \right) / C_{s,0}^{\text{SiO}_2} \quad (3.C4b)$$

For the density calculation, we use the thermodynamic data of Holland and Powell (1998) and the different minerals and liquids Mg-Fe end-members are recalculated from experimental data of Davis et al. (2011). In these calculations, we use the following end-members: for the solid part, forsterite (fo) (Mg_2SiO_4) and fayalite (fa) (Fe_2SiO_4) for olivine; enstatite (en) ($\text{Mg}_2\text{Si}_2\text{O}_6$) and ferrosilite (fs) ($\text{Fe}_2\text{Si}_2\text{O}_6$) for orthopyroxene; diopside (di) ($\text{CaMgSi}_2\text{O}_6$)

and hedenbergite (hed) ($\text{CaFeSi}_2\text{O}_6$) for clinopyroxene; pyrope (py) ($\text{Mg}_3\text{Al}_2\text{Si}_3\text{O}_{12}$) and almandine (alm) ($\text{Fe}_3\text{Al}_2\text{Si}_3\text{O}_{12}$) for garnet. We consider also quartz (q) (SiO_2). For the melt part, we consider forsterite liquid (foL), fayalite liquid (faL) and quartz liquid (qL). The abbreviations in brackets correspond to the nomenclature of Holland and Powell (1998).

CHAPTER 4

General conclusion and perspectives

The aim of this thesis is to better understand the formation of petit-spot volcanoes that are located on oceanic lithosphere adjacent to subduction zones. The mechanism by which melt migrates through oceanic lithosphere to form petit-spot is debated. This thesis focuses on two aspects of melt migration through oceanic lithosphere: (1) understanding mechanical constraints on plate flexure and deformation (and thus melt migration-) mechanisms of oceanic lithosphere as it bends to enter the subduction zone; and (2) melt extraction. The first study (chapter 2) aims to quantify stresses and deformation mechanisms to understand what is happening mechanically in the flexed oceanic plate near a subducting plate. This study shows that elasto-plastic deformation (yellow and light blue regions in Figure 4.1) is the dominant mechanism in the upper part of the lithosphere and subducting slab (from ca. 5 to 60 km depth from the top of the slab), while viscous deformation mechanisms (red, orange and dark blue regions in Figure 4.1) dominate in the lower part of the lithosphere and in the asthenosphere. This indicates that the transition from viscous to brittle deformation is independent of the thermal definition of the lithosphere-asthenosphere-boundary indicated by the white line in Figure 4.1.

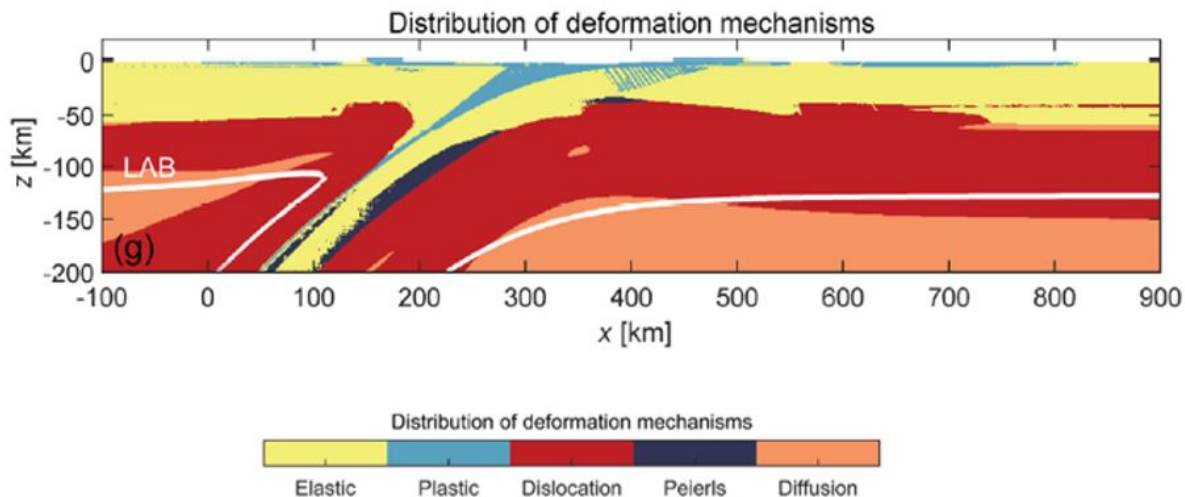


Figure 4.1: Distribution of deformation mechanisms for the forced subduction S0 simulation at $t = 6.0182$ Ma, zoom into Fig. 2.10 of chapter 2, panel (g). Elastic domain is in yellow, plastic domain is in light blue, and viscous domain is the combination of dislocation creep in red, Peierls creep in dark blue and diffusion creep in orange. The white line correspond to the thermally controlled lithosphere-asthenosphere-boundary (1440°C isotherm).

The magnitude and distribution of deviatoric stress, τ_{xx} , which illustrate regions under compression (τ_{xx} negative, areas in blue in Figure 4.2) or under extension (τ_{xx} positive, areas in red in Figure 4.2), shows that absolute values are maximum in the upper part of the lithosphere at the location where subducting lithosphere is bending. We note that flexure of the plate has little effect on the base of the lithosphere, where deviatoric stresses are small (near 0 MPa). A comparison between deviatoric stresses in the bending plate with deformation mechanisms suggests that large stresses are absent in lower, viscous half of the lithosphere.

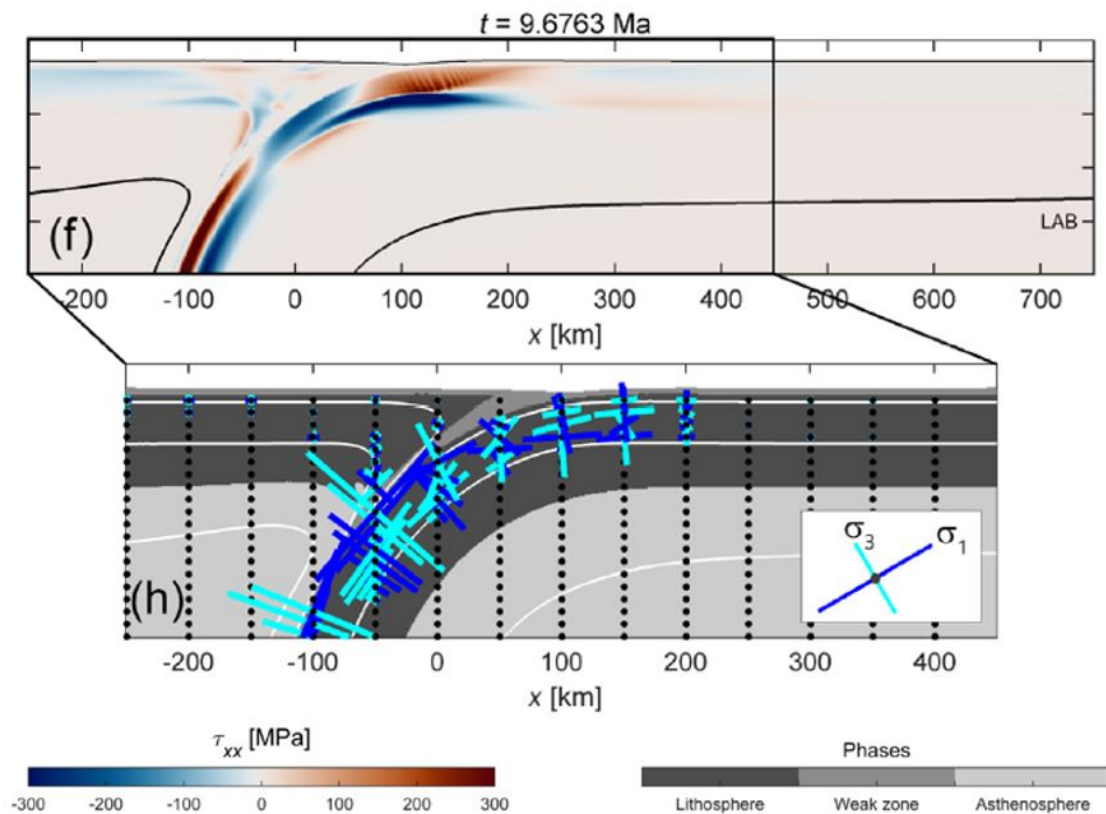


Figure 4.2: Panel (f) shows horizontal deviatoric stress for the free subduction S1 simulation at $t = 9.6763$ Ma (zoom into Fig. 2.11 of chapter 2). Areas in red show regions under extension and areas in blue show regions under compression. Black line correspond to the thermally controlled LAB (1440°C isotherm). Panel (h) shows principal stresses σ_1 in blue and σ_3 in cyan associated to panel (f). The background shows phases and white lines show the isothermal contours for 200, 800 and 1440°C.

According to Hirano et al. (2006) (Figure 4.3), upward flexural bending of the plate causes extension of the base of the lithosphere seawards of the flexural bulge. Hirano et al. (2006)

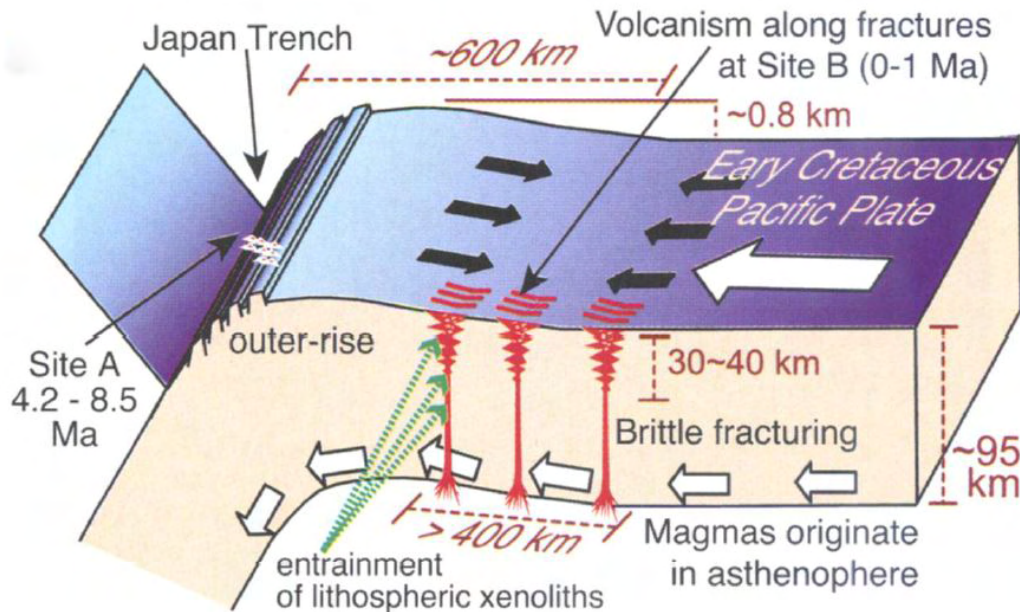


Figure 4.3: Schematic figure from Hirano et al. (2006, Fig. 3c of their paper), illustrating the conceptual model for the formation of petit-spot volcanism. Asthenospheric magmas escape to the surface due to extension at the base of the lithosphere made by the flexure of the subduction plate.

suggest that this extension is expected to cause brittle fracturing of the entire lithosphere, leading the extraction of low-degree melts from the base of the lithosphere to the surface. Our results have implications for the interpretations of Hirano et al. (2006) for the formation of petit-spot volcanoes. Firstly, our models do not predict a brittle domain at the base of the lithosphere; instead, the lower part of oceanic lithosphere deforms viscously, and does not enable the formation of brittle fractures to promote melt extraction. Secondly, the models do not predict extension at the base of lithosphere as a result of plate flexure; the models show that horizontal deviatoric stresses are low.

Our quantification of horizontal deviatoric stresses (in Figure 4.2f) have, nevertheless, direct implications for the location of petit-spot volcanoes at the surface. (1) A zone of extension in the oceanic plate between about 250 to 450 km from the trench at a depth of 40 to 50 km could promote the extraction of melts from mid-lithospheric depths, because the upper part of oceanic lithosphere down to this depth is dominated by elasto-plastic deformation, potentially allowing fractures to develop (Figure 4.2). (2) The extension region in the upper

part of the bulge (100 to 150 km from the trench, Fig. 4.2) could promote brittle fracturing, explaining the volcanoes found on the bulge region by Sato et al. (2017). This model for melt extraction would require for melts to be stored at mid-lithospheric depth (Figure 4.4). This model calls, therefore, into question the initial location of the melt which is observed at the surface. Sato et al. (2017) suggest that melts that produce petit-spot volcanoes at the top of the bulge originate from the base of the lithosphere. Our simulations show that the base of the lithosphere is under compression (blue area below the bulge in fig.4.2), potentially excluding melt migration from the base of the lithosphere. Alternatively, magma producing petit-spot volcanoes at the bulge originates from melt storage at mid-lithospheric depth as illustrated by the magma pocket schematically drawn for other petit-spots in Sato et al. (2017) (Figure 4.4). The question of how to explain the presence of melts at mid-lithospheric depth remains; are these melts produced at this location or do these melt pockets correspond to deeper melts that accumulated there?

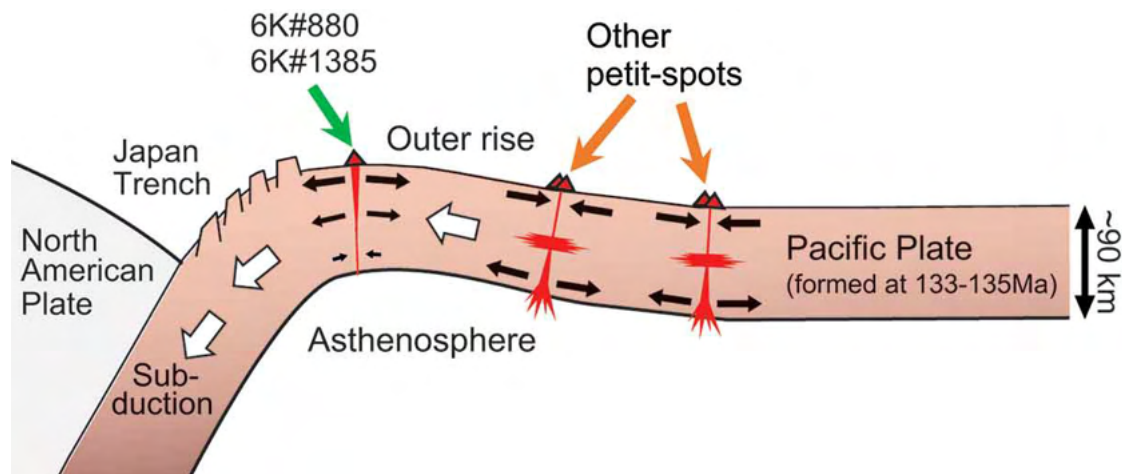


Figure 4.4: Schematic figure from Sato et al. (2017, Fig. 7 of their paper), illustrating the formation of petit-spot volcanoes on the bulge of the subduction zone. The black arrows indicate the main deformation mechanisms inferred by Sato and co-authors. For these basalts (6K#880/1385), the mechanism of extraction from the base of the lithosphere remains enigmatic.

An alternative to the existing model for petit-spot formation is a two-step model where melt first percolates through the lower lithosphere, stalls in the mid-lithosphere, and is extracted from mid-lithospheric depth. This alternative was first proposed by Buchs et al. (2013) in order to explain the high K/Na ratio observed in petit-spot lava from Japan and from alkaline

sills from Costa-Rica interpreted as an accreted petit-spot volcano on the western margin of Central America. This alternative model is supported by multiple saturation experiments on petit-spot primitive lava, supporting an equilibration of petit-spot magma with peridotite at lithospheric P-T condition (1.8-2.1 GPa and temperature of 1'280-1'290°C). Our numerical simulations support this hypothesis of a two-step model by showing that viscous deformation is dominant in the lower lithosphere. Low-degree melts originated from the sub-lithospheric low-velocity zone are therefore likely to rise by percolation across the ductile part of the lithosphere, before to be extracted to the surface by tectonic stress. Melt percolation across the ductile part of the oceanic plate has implications for the chemical composition of rising melt and peridotite composing the lithospheric mantle. Melts percolating across the lower lithosphere are expected to interact chemically with peridotite, while the conductive geotherm of the lithosphere implies cooling and potentially crystallisation of the initial rising magma. Buchs et al. (2013) have already pointed out the role of this metasomatic process to explain the chemistry of petit-spot emitted lavas. In their model, they proposed “(1) *peridotite melts are continuously extracted from the low-velocity zone at the base of the oceanic lithosphere (in the stability field of garnet) and percolate through the lower lithosphere producing metasomatic phlogopite pyroxenite veins at depth; (2) that tectonic stress triggering lithosphere cracking allows melts from the low-velocity zone to interact with the phlogopite-pyroxenite veins, re-melting and mix them, before reaching the surface to produce potassic lavas.*”

Various types of metasomatism are documented in mantle xenoliths and mantle outcrops. The different types of metasomatic enrichment associated to melt percolation across the mantle are illustrated in Figure 4.5, which is modified from original figures from Wilshire (1987) and Harte et al. (1993). Modal metasomatism is evidenced by the presence of newly formed phases such as pyroxenes, amphibole and phlogopite in peridotite and by the formation of hydrous and anhydrous metasomatic veins (Conqu  r  , 1971; Dawson and Smith, 1982; Nielson and Noller, 1987; Bodinier et al., 1990; Harte et al., 1993). In contrast, cryptic metasomatism is characterized by chemical enrichment of peridotite without the occurrence of new or additional major constituents. Various models have been proposed that relate cryptic and modal metasomatism including veins to a continuum process (Nielson and Noller, 1987; Wilshire,

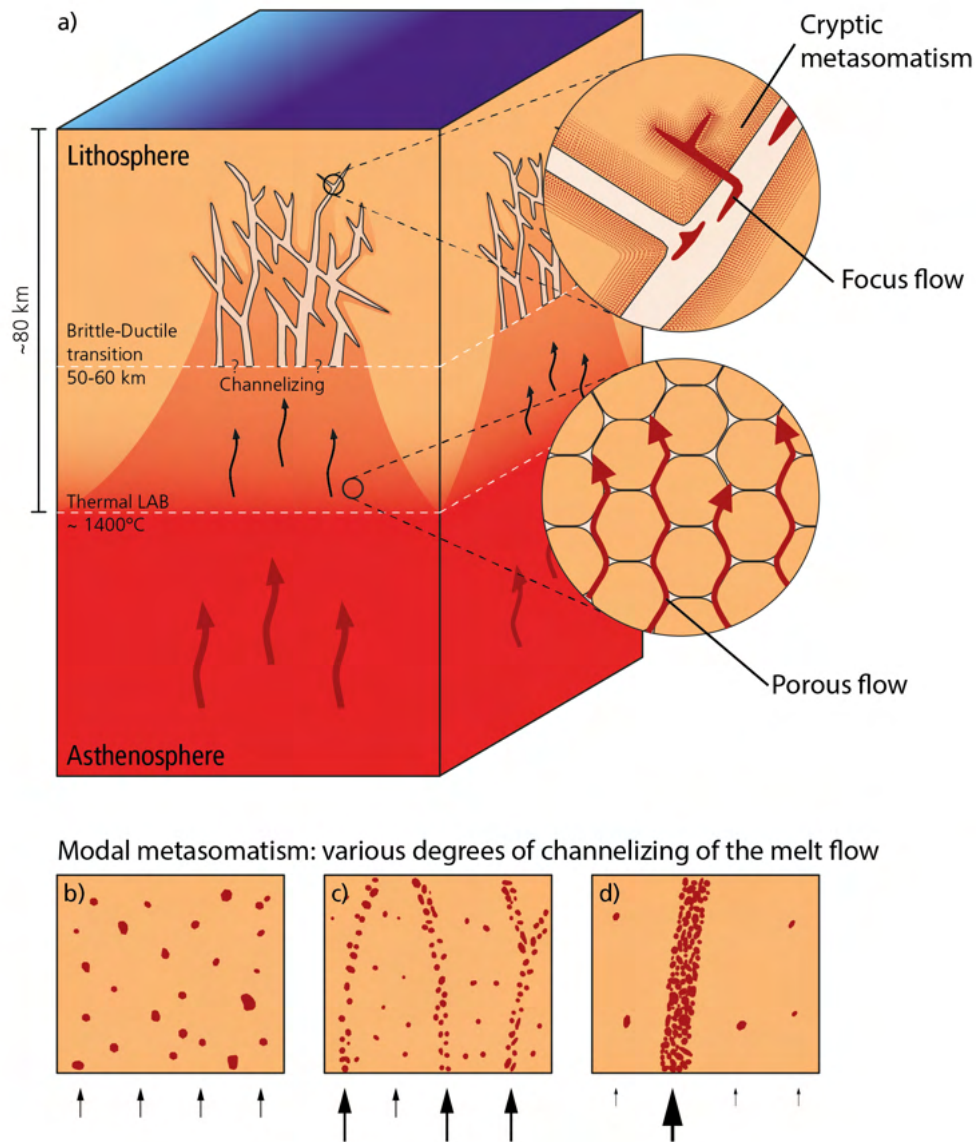


Figure 4.5: a) Schematic drawing of the different processes associated to the metasomatic enrichment of the lithosphere based on figures from Wilshire (1987) and Harte et al. (1993). Low-degree melts from the asthenosphere start to rise in the ductile domain of the lithosphere by porous flow or porosity waves. A channelizing mechanism (b to d) is expected close to ductile-brittle transition allowing melts to rise by focus flow in the top part of the lithosphere. This later process is documented by the various metasomatic cumulates and associated cryptic enrichment in surrounding peridotite sampled by intraplate alkaline magmas.

1987; Nielson and Wilshire, 1993; Harte et al., 1993). For example, Harte et al. (1993) suggest that the percolation and differentiation of basaltic liquid across the lithosphere generates a continuum from anhydrous (pyroxene + garnet \pm olivine) to hydrous (pyroxene + amphibole

± phlogopite) veins plus cryptic metasomatic enrichment in the adjacent peridotite. The formation of metasomatic cumulates is associated to focus flow allowing veins of a few tens of centimeters to form, while cryptical metasomatism seems associated to pervasive flow (Foley, 1992b), also referred to as porous flow (Fig. 4.5). The link between vein formation and the chromatographic chemical enrichment in the surrounding mantle has been illustrated, e.g. in outcrops of mantle rocks in the Lherz peridotite massif (McPherson et al., 1996; Woodland et al., 1996; Bodinier, 2004) or using constraints on the timing of metasomatism observed in metasomatized peridotite and metasomatic cumulate xenoliths from the Kaapvaal craton lithosphere (Konzett et al., 2000). Metasomatic imprint is also observed in oceanic settings (Pilet et al., 2016). Metasomatism could occur during the cooling of the oceanic lithosphere in the periphery of ridges, or by tectonic processes including plume activity (Roden et al., 1984; Wulff-Pedersen et al., 1996; Grégoire et al., 2000; Neumann et al., 2002; Delpech et al., 2004; Shaw et al., 2006).

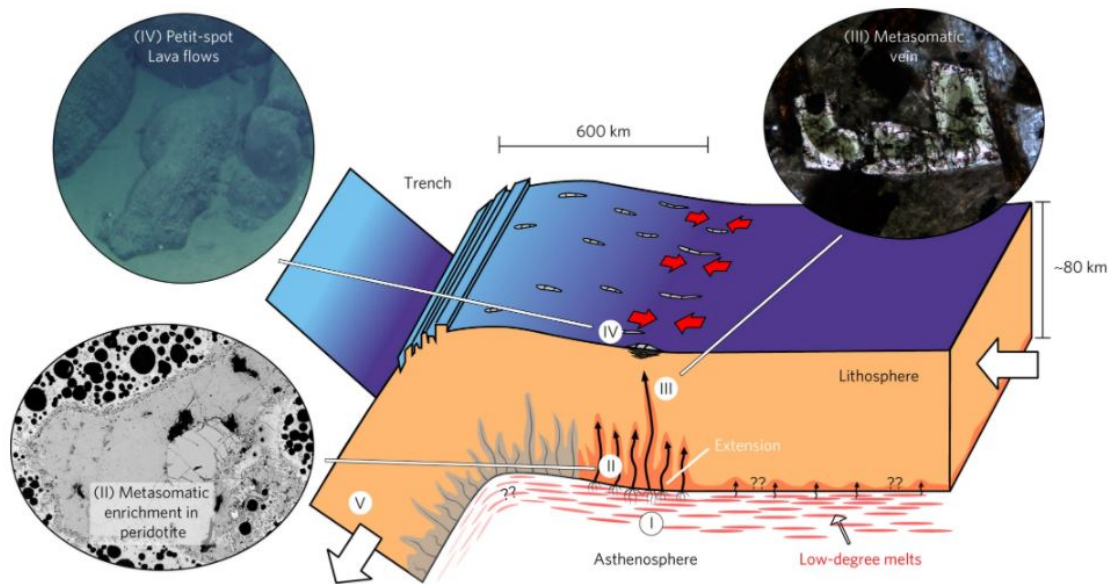


Figure 4.6: Redrawn of Fig.3 from Pilet et al. (2016). Illustration of the metasomatism in an oceanic lithospheric mantle due to plate flexure. See text for explanation of the different stage of the model.

The study of Pilet et al. (2016) on mantle xenolith samples from Japanese petit-spot lavas shows evidence for metasomatic enrichment of the Pacific oceanic lithosphere associated to the

generation of petit-spot volcanoes. Figure 4.6 illustrates the different stages of melt migration deduced from their mineral analyses. The authors assume the presence of low-degree melts at the base of the lithosphere (I), associated to plate flexure; this melt starts to percolate across the lithospheric mantle producing cryptic metasomatism observed in mantle xenoliths (II) and the formation of metasomatic veins (III) illustrated by "green-core" cpx observed in some petit-spot lavas. If most of the initial melts from the base of the lithosphere remain trapped in the lithosphere, some melts could reach the surface producing petit-spot volcanoes (IV). This figure also illustrates that metasomatized lithosphere could be recycled into the convecting mantle potentially producing some of the chemical mantle heterogeneities sample in oceanic islands (Pilet et al., 2005, 2008, 2011).

The location of the different deformation mechanisms within the oceanic plate, combined with quantification of stresses associated to plate flexure (chapter 2), supports the two-step model proposed in previous studies (e.g. Buchs et al., 2013; Pilet et al., 2016; Machida et al., 2017) with initial melt migration across the lower lithosphere and the potential extraction of the melts from mid-lithosphere depth. Nevertheless, insights from our numerical modeling, and chemical constraints on petit-spot lava and enclosing xenoliths, raise new questions about the mechanical aspect of melt migration within the ductile domain. Our study on porosity waves provides new information on this aspect.

Our second study (chapter 3) focuses on magma transport by porosity waves in a viscous domain, to constrain the mechanical aspects of melt transport coupled with chemistry. Although melt migration has been studied extensively in mid-ocean ridges, few studies could be applied to magma rising within the lithospheric mantle. The main difference between the two settings is the thermal gradient, which is convective in the asthenosphere, and conductive in the lithosphere. When melts rises in the asthenosphere, the thermal difference for melt rising from 100 km to the surface is around 30-50°C (mantle adiabat 1°C/0.1GPa, Langmuir et al. 1992). This difference could be several hundreds of degrees for melt rising in the lithosphere, and this could modify the physical and chemical behaviour of the rising melts. Our numerical models include a first-order description of the chemical changes involved with magma transport by porosity waves. At this stage, the chemical system in our models is simplified

(forsterite-fayalite-silica) and is not directly applicable to melt rising across a peridotite matrix, as the system requires pyroxene component in addition to forsterite and silicate. Our 1D simulations show that melts can move by porosity waves supporting results from Jordan et al. (2018), and that the total silica concentration and the geotherm have strong impacts on melt migration. These simulations allow us also to calculate velocity of the melt. For melts characterized by a viscosity varying from 0.1 to 10 Pa·s, i.e. from alkaline to tholeiitic melt composition (McKenzie, 1989), we obtain melt velocity between 1 to 115 m·yr⁻¹, which is in the same velocity range as magma rising below mid-ocean ridges estimated by Connolly et al. (2009) based on high pressure, high temperature experiments in centrifuge (2-150 m·yr⁻¹). Nevertheless, the rise of magma within the ductile part of the lithosphere is dependent on mantle porosity, which is held constant in our model at 2%. Such porosity is difficult to estimate, but it was considered to be low (<1%) in the lithospheric mantle suggesting that our estimate of melt velocity may be overestimated. A recent thermal study of Repac et al. (2020) shows the importance of velocity of the rising melt to be able to cross the lithosphere without crystallizing. Using a simple approach taking into account only the thermal diffusivity between melt and peridotite matrix, Repac et al. (2020) show that the velocity of a magma rising need to be higher than 10 km·yr⁻¹ to avoid cooling and crystallizing at depth. Even if the higher velocity calculated in our simulation (115 m·yr⁻¹) is selected, such melt is therefore likely to cool and crystallize during its ascent through the lithosphere.

Our porosity wave simulations for the rise of magma within the lithosphere may be fundamental to understand the formation of the alkaline magmas observed worldwide as metasomatic processes seem critical to explain the chemistry of these lavas. Lloyd and Bailey (1975) were the first to suggest that different types of alkaline rocks observed in continental settings are generated by the melting of metasomatized lithosphere at various depths. Considering that pressure controls the type of hydrous metasomatized phase present in the lithosphere (e.g. Konzett and Ulmer, 1999), they linked the formation of K-rich lavas to the melting of deep lithosphere enclosing mica while the Na-magmas are produced at shallower depth (<80-90 km) in presence of amphibole. Their hypothesis is supported by different studies, which suggest that K-rich magmas are produced by the melting of phlogopite-pyroxenites (Foley,

1992a; Prelević et al., 2010) while several models implying the melting of lithosphere enclosing amphibole have been proposed to explain the formation of sodic alkaline magma in continental settings (Wass and Roge, 1980; Pilet et al., 2002, 2004; Ma et al., 2011; Mayer et al., 2013; Rooney et al., 2014). However, the hypothesis of melting of metasomatized lithosphere is not very popular for the generation of oceanic island basalts (OIB) (e.g. Hofmann, 1997) where an asthenospheric source is considered as a more realistic hypothesis. Various models have been proposed such as melting of silica deficient pyroxenite, (e.g. Hirschmann et al., 2003), melting of peridotite in presence of CO₂, (Dasgupta et al., 2007), or eclogite melt (peridotite reaction in presence of CO₂ (Mallik and Dasgupta, 2014)). Our numerical simulations for melt rising within the lithosphere suggest, however, that even for melts characterized by low viscosity ($\sim 1-0.1$ Pa·s), the velocity of such melts is not sufficient to cross the lithosphere without cooling and crystallizing. This supports the two-step model proposed by Pilet et al. (2008, 2011) suggesting that alkaline magmas are not produced directly from the asthenosphere, but from the re-melting of metasomatic veins formed by the differentiation of low-degree asthenospheric melts percolating through the lithosphere.

Our different simulations open new perspectives for understanding the mechanism of petit-spot formation and magma migration in the ductile domain. We propose the following points to improve our model:

1. The chemistry used for the porosity wave models is very simple but it highlights the importance of taking into account the interaction and the change of composition between melt and solid in the melt migration process, particularly on density. It is important to include a more complex chemistry in future models, by adding pyroxene phases in the calculation of thermodynamics to simulate a more realistic peridotite.
2. We propose to add reactions for the crystallisation of the different mineral phases, such as amphibole or phlogopite, that crystallise during metasomatism and their thermal contribution in the heat budget on the rising melt.
3. The numerical method chosen for the porosity wave model allows us to extend the 1D model to two dimensions, as seen in the discussion of chapter 3, but eventually also

to three dimensions. The 3D models would allow to estimate and quantify the volume of melt that would percolate in a porous medium representative of the base of the lithosphere.

4. An important parameter for melt transport that could be tested is the viscosity of the melt. Our current model includes a fixed viscosity. In future models, we can vary viscosity according to the temperature, and study the effect on the velocity of the rising melt.
5. In our melt transport model, no deformation of the solid is applied at this time. A future step could be the addition of horizontal extension or compression to study the impact of this deformation on the melt velocity.

Finally, the two models, the subduction model and the melt percolation model, can be coupled, to simulate the formation of petit-spot volcanoes and intraplate volcanism.

Bibliography

- Bodinier, J.-L., 2004. Silicate, Hydrous and Carbonate Metasomatism at Lherz, France: Contemporaneous Derivatives of Silicate Melt-Harzburgite Reaction. *Journal of Petrology* 45 (2), 299–320.
- Bodinier, J. L., Vasseur, G., Vernieres, J., Dupuy, C., Fabries, J., 1990. Mechanisms of Mantle Metasomatism: Geochemical Evidence from the Lherz Orogenic Peridotite. *Journal of Petrology* 31 (3), 597–628.
- Buchs, D. M., Pilet, S., Cosca, M., Flores, K. E., Bandini, A. N., Baumgartner, P. O., 2013. Low-volume intraplate volcanism in the Early/Middle Jurassic Pacific basin documented by accreted sequences in Costa Rica. *Geochemistry, Geophysics, Geosystems* 14 (5), 1552–1568.
- Connolly, J. A. D., Schmidt, M. W., Solferino, G., Bagdassarov, N., 2009. Permeability of asthenospheric mantle and melt extraction rates at mid-ocean ridges. *Nature* 462 (7270), 209–212.
- Conqu er , F., 1971. Les pyrox enolites   amphibole et les amphibololites associ es aux lherzolites du gisement de Lherz (Ari ge, France): un exemple du r le de l’eau au cours de la cristallisation fractionn e des liquides issus de la fusion partielle de lherzolites. *Contributions to Mineralogy and Petrology* 33 (1), 32–61.
- Dasgupta, R., Hirschmann, M. M., Smith, N. D., 2007. Partial Melting Experiments of Peridotite + CO₂ at 3 GPa and Genesis of Alkalic Ocean Island Basalts. *Journal of Petrology* 48 (11), 2093–2124.
- Dawson, J. B., Smith, J., 1982. Upper-Mantle Amphiboles - a Review. *Mineral. Mag.* 45, 35–46.
- Delpech, G., Gr goire, M., O’Reilly, S. Y., Cottin, J. Y., Moine, B., Michon, G., Giret, A., 2004. Feldspar from carbonate-rich silicate metasomatism in the shallow oceanic mantle under Kerguelen Islands (South Indian Ocean). *Lithos* 75 (1), 209–237.

- Foley, S., 1992a. Petrological characterization of the source components of potassic magmas: geochemical and experimental constraints. *Lithos* 28 (3), 187–204.
- Foley, S., 1992b. Vein-plus-wall-rock melting mechanisms in the lithosphere and the origin of potassic alkaline magmas. *Lithos* 28 (3-6), 435–453.
- Grégoire, M., Lorand, J. P., O'Reilly, S. Y., Cottin, J. Y., 2000. Armalcolite-bearing, Ti-rich metasomatic assemblages in harzburgitic xenoliths from the Kerguelen Islands: implications for the oceanic mantle budget of high-field strength elements. *Geochimica et Cosmochimica Acta* 64 (4), 673–694.
- Harte, B., Hunter, R., Kinny, P., 1993. Melt geometry, movement and crystallization, in relation to mantle dykes, veins and metasomatism. *Philosophical Transactions of the Royal Society of London. Series A: Physical and Engineering Sciences* 342 (1663), 1–21.
- Hirano, N., Takahashi, E., Yamamoto, J., Abe, N., Ingle, S. P., Kaneoka, I., Hirata, T., Kimura, J.-I., Ishii, T., Ogawa, Y., Machida, S., Suyehiro, K., 2006. Volcanism in Response to Plate Flexure. *Science, New Series* 313 (5792), 1426–1428.
- Hirschmann, M. M., Kogiso, T., Baker, M. B., Stolper, E. M., 2003. Alkalic magmas generated by partial melting of garnet pyroxenite. *Geology* 31 (6), 481–484.
- Hofmann, A. W., 1997. Mantle geochemistry: the message from oceanic volcanism. *Nature* 385 (6613), 219–229.
- Jordan, J. S., Hesse, M. A., Rudge, J. F., 2018. On mass transport in porosity waves. *Earth and Planetary Science Letters* 485, 65–78.
- Konzett, J., Armstrong, R. A., Günther, D., 2000. Modal metasomatism in the Kaapvaal craton lithosphere: constraints on timing and genesis from U–Pb zircon dating of metasomatized peridotites and MARID-type xenoliths. *Contributions to Mineralogy and Petrology* 139 (6), 704–719.

- Konzett, J., Ulmer, P., 1999. The Stability of Hydrous Potassic Phases in Lherzolitic Mantle—an Experimental Study to 9.5 GPa in Simplified and Natural Bulk Compositions. *Journal of Petrology* 40 (4), 629–652.
- Langmuir, C. H., Klein, E. M., Plank, T., 1992. Petrological Systematics of Mid-Ocean Ridge Basalts: Constraints on Melt Generation Beneath Ocean Ridges. In: *Mantle Flow and Melt Generation at Mid-Ocean Ridges*. American Geophysical Union (AGU), pp. 183–280.
- Lloyd, F. E., Bailey, D. K., 1975. Light element metasomatism of the continental mantle: The evidence and the consequences. *Physics and Chemistry of the Earth* 9, 389–416.
- Ma, G. S.-K., Malpas, J., Xenophontos, C., Chan, G. H.-N., 2011. Petrogenesis of Latest Miocene-Quaternary Continental Intraplate Volcanism along the Northern Dead Sea Fault System (Al Ghab-Homs Volcanic Field), Western Syria: Evidence for Lithosphere-Asthenosphere Interaction. *Journal of Petrology* 52 (2), 401–430.
- Machida, S., Kogiso, T., Hirano, N., 2017. Petit-spot as definitive evidence for partial melting in the asthenosphere caused by CO₂. *Nature Communications* 8, 14302.
- Mallik, A., Dasgupta, R., 2014. Effect of variable CO₂ on eclogite-derived andesite and lherzolite reaction at 3 GPa—Implications for mantle source characteristics of alkalic ocean island basalts. *Geochemistry, Geophysics, Geosystems* 15 (4), 1533–1557.
- Mayer, B., Jung, S., Romer, R. L., Stracke, A., Haase, K. M., Garbe-Schönberg, C.-D., 2013. Petrogenesis of Tertiary Hornblende-bearing Lavas in the Rhön, Germany. *Journal of Petrology* 54 (10), 2095–2123.
- McKenzie, D., 1989. Some remarks on the movement of small melt fractions in the mantle. *Earth and Planetary Science Letters* 95 (1-2), 53–72.
- McPherson, E., Thirlwall, M. F., Parkinson, I. J., Menzies, M. A., Bodinier, J. L., Woodland, A., Bussod, G., 1996. Geochemistry of metasomatism adjacent to amphibole-bearing veins in the Lherz peridotite massif. *Chemical Geology* 134 (1), 135–157.

- Neumann, E.-R., Wulff-Pedersen, E., Pearson, N. J., Spencer, E. A., 2002. Mantle Xenoliths from Tenerife (Canary Islands): Evidence for Reactions between Mantle Peridotites and Silicic Carbonatite Melts inducing Ca Metasomatism. *Journal of Petrology* 43 (5), 825–857.
- Nielson, J. E., Noller, J. S., 1987. Processes of mantle metasomatism; Constraints from observations of composite peridotite xenoliths. *Geological Society of America* 215, 61–76.
- Nielson, J. E., Wilshire, H., 1993. Magma transport and metasomatism in the mantle: A critical review of current geochemical models. *American Mineralogist* 78, 1117–1134.
- Pilet, S., Abe, N., Rochat, L., Kaczmarek, M.-A., Hirano, N., Machida, S., Buchs, D. M., Baumgartner, P. O., Müntener, O., 2016. Pre-subduction metasomatic enrichment of the oceanic lithosphere induced by plate flexure. *Nature Geoscience* 9 (12), 898–903.
- Pilet, S., Baker, M. B., Müntener, O., Stolper, E. M., 2011. Monte Carlo Simulations of Metasomatic Enrichment in the Lithosphere and Implications for the Source of Alkaline Basalts. *Journal of Petrology* 52 (7-8), 1415–1442.
- Pilet, S., Baker, M. B., Stolper, E. M., 2008. Metasomatized Lithosphere and the Origin of Alkaline Lavas. *Science* 320 (5878), 916–919.
- Pilet, S., Hernandez, J., Bussy, F., Sylvester, P., 2004. Short-term metasomatic control of Nb/Th ratios in the mantle sources of intraplate basalts. *Geology* 32 (2), 113–116.
- Pilet, S., Hernandez, J., Sylvester, P., Pujol, M., 2005. The metasomatic alternative for ocean island basalt chemical heterogeneity. *Earth and Planetary Science Letters* 236 (1-2), 148–166.
- Pilet, S., Hernandez, J., Villemant, B., 2002. Evidence for high silicic melt circulation and metasomatic events in the mantle beneath alkaline provinces: the Na-Fe-augitic green-core pyroxenes in the tertiary alkali basalts of the Cantal massif (French Massif Central). *Min & Petrol* 76, 39–62.
- Prelević, D., Akal, C., Romer, R. L., Foley, S. F., 2010. *Terra Nova* 22 (6), 443–452.

- Repac, M., Panter, K. S., Podladchikov, Y., Pilet, S., 2020. Metasomatism and physical properties of the lithosphere-asthenosphere boundary: a combined petrological and numerical study. AGU.
- Roden, M. K., Hart, S. R., Frey, F. A., Melson, W. G., 1984. Sr, Nd and Pb isotopic and REE geochemistry of St. Paul's Rocks: the metamorphic and metasomatic development of an alkali basalt mantle source. *Contributions to Mineralogy and Petrology* 85 (4), 376–390.
- Rooney, T. O., Nelson, W. R., Dosso, L., Furman, T., Hanan, B., 2014. The role of continental lithosphere metasomes in the production of HIMU-like magmatism on the northeast African and Arabian plates. *Geology* 42 (5), 419–422.
- Sato, Y., Hirano, N., Machida, S., Yamamoto, J., Nakanishi, M., Ishii, T., Taki, A., Yasukawa, K., Kato, Y., 2017. Direct ascent to the surface of asthenospheric magma in a region of convex lithospheric flexure. *International Geology Review* 60 (10), 1231–1243.
- Shaw, C. S. J., Heidelbach, F., Dingwell, D. B., 2006. The origin of reaction textures in mantle peridotite xenoliths from Sal Island, Cape Verde: the case for “metasomatism” by the host lava. *Contributions to Mineralogy and Petrology* 151 (6), 681.
- Wass, S. Y., Roge, N. W., 1980. Mantle metasomatism—precursor to continental alkaline volcanism. *Geochimica et Cosmochimica Acta* 44 (11), 1811–1823.
- Wilshire, H., 1987. A model of mantle metasomatism. *Mantle Metasomatism and Alkaline Magmatism*. Geological Society of America, Special Papers 215, 47–60.
- Woodland, A. B., Kornprobst, J., McPherson, E., Bodiner, J.-L., Menzies, M. A., 1996. Metasomatic interactions in the lithospheric mantle: petrologic evidence from the Lherz massif, French Pyrenees. *Chemical Geology* 134 (1-3), 83–112.
- Wulff-Pedersen, E., Neumann, E.-R., Jensen, B. B., 1996. The upper mantle under La Palma, Canary Islands: formation of Si-K-Na-rich melt and its importance as a metasomatic agent. *Contributions to Mineralogy and Petrology* 125 (2), 113–139.

APPENDIX A

Code for gravimetry calculations

Code gravimetry

```
% ===== GRAVIMETRY ===== %
% ReadMDoodz_GraviAL_FreeAir_para
% Method for gravimetry calculation with Free Air correction
% Annelore 26.02.2019

function Main
clear all, close all, clc

%% Subduction simulation file number of interest
time_step = 1420;

%% Chargement des données/Upload of data
file_suffix = '';
time = 0;
filename = ['Output', num2str(time_step, '%05d'), file_suffix, '.gzip.h5'];
PhToposave = ['PhTopo_Gravi_FreeAir_', num2str(time_step, '%05d'), file_suffix, '.mat'];

% Domaine
params = hdf5read(filename, '/Model/Params');
xg_coord = hdf5read(filename, '/Model/xg_coord');
xg_coord = cast(xg_coord, 'double');
zg_coord = hdf5read(filename, '/Model/zg_coord');
zg_coord = cast(zg_coord, 'double');
xc_coord = hdf5read(filename, '/Model/xc_coord');
xc_coord = cast(xc_coord, 'double');
zc_coord = hdf5read(filename, '/Model/zc_coord');
zc_coord = cast(zc_coord, 'double');
xvz_coord = hdf5read(filename, '/Model/xvz_coord');
xvz_coord = cast(xvz_coord, 'double');
zvx_coord = hdf5read(filename, '/Model/zvx_coord');
zvx_coord = cast(zvx_coord, 'double');
VizGrid.x = hdf5read(filename, '/VizGrid/xviz');
VizGrid.x = cast(VizGrid.x, 'double');
VizGrid.z = hdf5read(filename, '/VizGrid/zviz');
VizGrid.z = cast(VizGrid.z, 'double');

nx = params(4);
nz = params(5);
ncx = nx-1;
ncz = nz-1;
time0 = time;
time = params(1);
t_vec = time;

if params(1) < 60
    TimeLabel = [' t = ' num2str(time) ' s '];
elseif time >= 60 && time < 3600
    TimeLabel = [' t = ' num2str(time/60) ' min '];
elseif time >= 3600 && time < 24*3600
    TimeLabel = [' t = ' num2str(time/3600) ' h '];
elseif time >= 24*3600 && time < 365.25*24*3600
    TimeLabel = [' t = ' num2str(params(1)/24/3600) ' j '];
elseif time >= 365.25*24*3600 && time < 1e3*365.25*24*3600
    TimeLabel = [' t = ' num2str(params(1)/365/24/3600) ' a '];
elseif time >= 1e3*365.25*24*3600 && time < 1e6*365.25*24*3600
    TimeLabel = [' t = ' num2str(time/1e3/365.25/24/3600) ' ka '];
elseif time >= 1e6*365.25*24*3600
    TimeLabel = [' t = ' num2str(time/1e6/365.25/24/3600) ' Ma '];
end
```

```

% Spacing
L = xg_coord(end) - xg_coord(1);
H = zg_coord(end) - zg_coord(1);
vol = H*L;
dx = xg_coord(2) - xg_coord(1);
dz = zg_coord(2) - zg_coord(1);

if L < 1e-6
    xg_plot = xg_coord/1e-0;
    zg_plot = zg_coord/1e-0;
    xc_plot = xc_coord/1e-0;
    zc_plot = zc_coord/1e-0;
    xvz_plot = xvz_coord/1e-0;
    zvx_plot = zvx_coord/1e-0;
    VizGrid.x_plot = VizGrid.x/1e-0;
    VizGrid.z_plot = VizGrid.z/1e-0;
    xlabel = ['x [nm]'];
    ylabel = ['z [nm]'];
elseif L < 1e3
    xg_plot = xg_coord/1e0;
    zg_plot = zg_coord/1e0;
    xc_plot = xc_coord/1e0;
    zc_plot = zc_coord/1e0;
    xvz_plot = xvz_coord/1e0;
    zvx_plot = zvx_coord/1e0;
    VizGrid.x_plot = VizGrid.x/1e0;
    VizGrid.z_plot = VizGrid.z/1e0;
    xlabel = ['x [m]'];
    ylabel = ['z [m]'];
else
    xg_plot = xg_coord/1e3;
    zg_plot = zg_coord/1e3;
    xc_plot = xc_coord/1e3;
    zc_plot = zc_coord/1e3;
    xvz_plot = xvz_coord/1e3;
    zvx_plot = zvx_coord/1e3;
    VizGrid.x_plot = VizGrid.x/1e3;
    VizGrid.z_plot = VizGrid.z/1e3;
    xlabel = ['x [km]'];
    ylabel = ['z [km]'];
end

% Adaptive min max axis
dt = time - time0;

[Zg2,Xg2] = ndgrid(zg_coord,xg_coord);
[Zc2,Xc2] = ndgrid(zc_coord,xc_coord);

% --- Chargement des donnees ---
rho_s = hdf5read(filename, '/Vertices/rho_s');
rho_s = cast(rho_s, 'double');
rho_node = reshape(rho_s,params(4)-0,params(5)-0)';

rho_n = hdf5read(filename, '/Centers/rho_n');
rho_n = cast(rho_n, 'double');
rho_center = reshape(rho_n,params(4)-1,params(5)-1)';

xtopo = hdf5read(filename, '/Topo/x');
xtopo = cast(xtopo, 'double');

ztopo = hdf5read(filename, '/Topo/z');
ztopo = cast(ztopo, 'double');

```

```

height      = hdf5read(filename, '/Topo/height');
height2     = height-mean(height);

% height2 = topo with correction of the topo mean value

%% Parameter for sea level and water density
sealevel    = 5000; % sea level in m for the free air correction
topomer     = sealevel*ones(size(height2)); % vector of the sea level
rho_water   = 1000; % density of the water kg/m3

%% Identification des éléments:
isavephtopo = 1; % Save "identification des éléments"
% isavephtopo:
% possible to save time, put 1 the first time you run the code than put 0.

if isavephtopo == 1
    phtopo = zeros(size(rho_center));

    % Définition du polygone
    xv = [xg_coord(1) xg_coord' xg_coord(end) xg_coord(1)];
    zv = [zg_coord(1) height2' zg_coord(1) zg_coord(1)];

    % Scannage du domaine: intérieur du polygone = 1, extérieur = 0
    for i = 1:ncz
        for j = 1:ncx
            xq = Xc2(i,j);
            zq = Zc2(i,j);
            in = inpolygon(xq,zq,xv,zv);
            phtopo(i,j) = in;
        end
    end

    % Cas des cellules juste sous la topographie: = 2
    for k = 1:ncx
        iphtopo = max(find(phtopo(:,k)>0));
        phtopo(iphtopo,k) = 2;
    end

    % Cas des cellules extérieur du polygone mais sous le niveau de la mer = 3
    for k = 1:ncx
        iphtopo = max(find(phtopo(:,k)>0));
        i_sealevel = max(find(zc_coord <= (sealevel-dx/2)));
        phtopo(iphtopo+1:i_sealevel,k) = 3;
    end

    save(PhToposave, 'phtopo')
else
    load(PhToposave)
end

%% Calcul pour la gravimétrie

% 1a - copie des coordonnées et création du maillage de gravité
ffield_left = -10000000;
ffield_right = 10000000;
xg_gravi = xg_coord;
xg_gravi(1) = xg_coord(1) +ffield_left;
xg_gravi(end) = xg_coord(end)+ffield_right;
zg_gravi = -zg_coord;
height_gravi = -height2;
topomer_gravi = -topomer;

```

```

% 1b - position des points de mesure sur la topographie
pzoomX_left   = -100000;           % position zoom x left
pzoomX_right  =  900000;           % position zoom x right
nxm           = 101;               % nb de station de mesure sur
                                   la topo
dxm           = (pzoomX_right-pzoomX_left)/(nxm-1); % distance entre les stations
                                   de mesure
datapts.x     = pzoomX_left:dxm:pzoomX_right;      % coordonnées x des stations

for i = 1:nxm
    i_xm       = max(find(xg_gravi'<=datapts.x(i))); % indice de position x des
                                                       stations
    datapts.z(i) = topomer_gravi(i_xm);             % coordonnées z des stations
end

% 2 - shift des coordonnées, de la topographie et des points de mesure
decal_x      = 0; % m
decal_z      = 0;
xg_gravi_decal = xg_gravi + decal_x;
zg_gravi_decal = zg_gravi - decal_z;
height_gravi_decal = height_gravi - decal_z;
topomer_gravi_decal = topomer_gravi - decal_z;
datapts_decal.x = datapts.x + decal_x;
datapts_decal.z = datapts.z - decal_z;

% 3 - calcul de l'anomalie de gravité
anom_local   = zeros(1,nxm);
G            = 6.67259e-11; % constante gravitationnelle universelle in m^3/kg/s^2

% Configuration du cluster pour le calcul en parallèle
myCluster    = parcluster;
num_pool     = min(ncz,38); % !/\ Put 2 on the computer !/\
myCluster.NumWorkers = num_pool ;
saveProfile(myCluster);
myPool       = parpool(myCluster,num_pool,'IdleTimeout', 5200);

tic;
parfor jj = 1:ncz
    for ii = 1:ncx
        geometry = [];
        if phtopo(jj,ii) == 1 % CAS GENERAL
            % sens horaire
            %
            % X1 X4 X3 X2 X1
            geometry.x = [ xg_gravi_decal(ii) xg_gravi_decal(ii) xg_gravi_decal(ii+1)
                          xg_gravi_decal(ii+1) xg_gravi_decal(ii)];
            %
            % Z1 Z4 Z3 Z2 Z1
            geometry.z = [ zg_gravi_decal(jj) zg_gravi_decal(jj+1) zg_gravi_decal(jj+1)
                          zg_gravi_decal(jj) zg_gravi_decal(jj)];

            densanom = rho_center(jj,ii);
            anom_incr = calcgrav(geometry,densanom,datapts_decal);
            anom_local = anom_local + anom_incr.z;

        elseif phtopo(jj,ii) == 2 % CAS SOUS LA TOPO
            % sens horaire
            %
            % X1 X4 X3 X2 X1
            geometry.x = [ xg_gravi_decal(ii) xg_gravi_decal(ii) xg_gravi_decal(ii+1)
                          xg_gravi_decal(ii+1) xg_gravi_decal(ii)];
            %
            % Z1 Z4 Z3 Z2 Z1
            geometry.z = [ zg_gravi_decal(jj) height_gravi_decal(ii)
                          height_gravi_decal(ii+1) zg_gravi_decal(jj)
                          zg_gravi_decal(jj)];
        end
    end
end

```

```

densanom = rho_center(jj,ii);
anom_incr = calcgrav(geometry,densanom,datapts_decal);
anom_local = anom_local + anom_incr.z;

end
end
end

% CAS DANS L'EAU
% sens horaire
%
% topo left 1 sealevel left-right topo right-left
geometry.x = [ xg_gravi_decal(1) xg_gravi_decal -xg_gravi_decal ];
% topo left 1 sealevel left-right topo right-left
geometry.z = [ height_gravi_decal(1) topomer_gravi_decal -height_gravi_decal ];

densanom = rho_water;
anom_incr = calcgrav(geometry,densanom,datapts_decal);
anom_local = anom_local + anom_incr.z;

%% Save DATA
timecal = toc;
Anomasave =
['Anoma_Gravi_FreeAir_para_',num2str(time_step,'%05d'),'_',num2str(nxm,'%03d'),file_suffi
x, '.mat'];
save(Anomasave)
delete(myPool);
end

%% -- Fonctions -----
function VizGrid = PhaseMap( filename, VizGrid )
VizGrid.ph = hdf5read(filename,'/VizGrid/compo'); VizGrid.ph = cast(VizGrid.ph,
'double');
VizGrid.ph = (reshape(VizGrid.ph,length(VizGrid.x),length(VizGrid.z))');
VizGrid.ph(VizGrid.ph== -69) = -1;
end

function PatchCells( ncx, ncy, field, x, y )
imagesc( 0.5*(x(1:end-1) + x(2:end)), 0.5*(y(1:end-1) + y(2:end)), field )

x_tab = zeros(ncx*ncy, 4);
y_tab = zeros(ncx*ncy, 4);
f = zeros(ncx*ncy,1);
ci = 0;

% Plot cells
for ic = 1:ncx
for jc = 1:ncy
ci = ci + 1;

x_arr = [x(ic) x(ic) x(ic+1) x(ic+1)];
y_arr = [y(jc) y(jc+1) y(jc) y(jc+1)];

x_tab(ci,:) = x_arr;
y_tab(ci,:) = y_arr;

f(ci) = field(jc,ic);

end
end
id = [ 1 2 4 3];

% patch(x_tab(:,id)', y_tab(:,id)', repmat(f,1,4)', 'EdgeColor', 'none' );
patch(x_tab(:,id)', y_tab(:,id)', repmat(f,1,4)' );

```

```

end

function [ Arr, xc, zc] = CropCellArray( Arr, xc, zc, crop )
[val,icmin] = min(abs(xc-crop.xmin));
[val,icmax] = min(abs(xc-crop.xmax));
[val,jcmin] = min(abs(zc-crop.zmin));
[val,jcmax] = min(abs(zc-crop.zmax));
xc         = xc(icmin:icmax);
zc         = zc(jcmin:jcmax);
Arr        = Arr(jcmin:jcmax,icmin:icmax);
end

function AddCompoContours( filename, VizGrid, crop, lim )

VizGrid = PhaseMap( filename, VizGrid );

if crop == 1
    [ VizGrid.ph, VizGrid.x_plot, VizGrid.z_plot ] = CropCellArray( VizGrid.ph,
VizGrid.x_plot, VizGrid.z_plot, lim );
end
for i = 0:2:40
    if ( sum (sum (VizGrid.ph == i-1)) ~= 0)
        Vizbuf = VizGrid.ph;
        Vizbuf(VizGrid.ph == i) = 1;
        Vizbuf(VizGrid.ph ~= i) = 69;
        [c, hb] = contour(VizGrid.x_plot, VizGrid.z_plot, Vizbuf, [ 0 1]);
        set(hb, 'Color', 'w', 'LineWidth', 1.0);
    end
end
end
end

% ===== FCT calcgrav ===== %
function anomaly=calcgrav(geometry,densanom,datapts)
% The scientific part of the program: gravity anomaly calculation using the algorithm
described in Won & Bevis (1987).
%
% =input: geometry (m), density-anomaly (kg/m^3) and data points (m)
% =output: gravity anomaly (mGal)
%
% Version as of 20.12.2018
% (C) Gyorgy HETENYI

#####

% loop on datapts
for i=1:length(datapts.x)

    % change co-ordinate system to a local one
    x=geometry.x-datapts.x(i);
    z=geometry.z-datapts.z(i);

    % to prevent numerical errors, when datapoint is at the same altitude (put 1 mm)
    z(z==0)=1e-3;

    % distance coefficients and angles (formulae from Won & Bevis)
    Z=[];
    X=[];
    theta=atan2(z,x);
    r=sqrt(x.^2+z.^2);

    % loop on the vertices of the polygon
    for j=1:length(x)-1

```

```

% make local theta that in case of modification, next loop will still be correct
clear theta1 theta2
theta1=theta(j);
theta2=theta(j+1);

% CASE 1
if z(j)*z(j+1)<0
    % CASE 1A
    if ( x(j)*z(j+1) ) < ( x(j+1)*z(j) ) && z(j+1)>=0
        theta1=theta1+2*pi;
    end
    % CASE 1B
    if ( x(j)*z(j+1) ) > ( x(j+1)*z(j) ) && z(j)>=0
        theta2=theta2+2*pi;
    end
    % CASE 1C
    if ( x(j)*z(j+1) ) == ( x(j+1)*z(j) )
        Z=[Z 0];
        X=[X 0];
    end
end

% CASE 2
if ( x(j)==0 && z(j)==0 ) || ( x(j+1)==0 && z(j+1)==0 ) && ( length(X)==(j-1) )
    X=[X 0];
    Z=[Z 0];
end

% CASE 3
if ( x(j)==x(j+1) ) && ( length(X)==(j-1) )
    Z=[Z x(j) * log( r(j+1)/r(j) )];
    X=[X -x(j) * ( theta1-theta2 )];
end

% GENERAL CASE
if length(X)==(j-1)
    A=( x(j+1)-x(j) )*( x(j)*z(j+1) - x(j+1)*z(j) )/( (x(j+1)-x(j)).^2+ (z(j+1)-z(j)).^2);
    B=( z(j+1)-z(j) )/( x(j+1)-x(j) );
    Z=[Z A*( (theta1-theta2) + B*log( r(j+1)/r(j) ) )];
    X=[X A*( B*(theta2-theta1) + log( r(j+1)/r(j) ) )];
    clear theta1 theta2
end

end

% gravity anomaly calculation and conversion to milliGals
G=6.67259e-11; % in m3/kg/s^2
anomaly.x(i)=2*G*densanom*sum(X)*1e5;
anomaly.z(i)=2*G*densanom*sum(Z)*1e5;

end
#####

```

APPENDIX B

Code for thermodynamic

Code thermodynamic

```
% ===== GIBBS MINIMISATION ===== %
%- Olivine System - low resolution -----
%- Annelore Bessat - last version 15.10.2020 - UpDate 21.01.21 -----
clear all, close all, clc
% = Minimisation with linprog =====
opts          = optimoptions('linprog','Display','off');      % option for linprog fct
%- PHYSICS -----
R              = 8.3144;                                     % [J/K/mol]
Tmin           = 1200 + 273.15;
%- NUMERICS -----
C_sys         = 0:0.01:1;
%- DATA BASE -----
load HP98_ds55_lowres; whos
% Temperature
T_all         = T_HP98_K;
iT            = find( T_all >= Tmin);
dT            = T_all(2)-T_all(1);
T_all         = T_all(iT);
T_all_c       = (T_all(1:end-1)+T_all(2:end))/2;
% Pressure
P_all         = P_HP98_Pa;
iP            = 1:length(P_all);
dP            = P_all(2)-P_all(1);
P_all_c       = (P_all(1:end-1)+P_all(2:end))/2;
% Phase
iphase        = [find(strcmp(phs_names,'fo' ))...
                 ,find(strcmp(phs_names,'fa' ))...
                 ,find(strcmp(phs_names,'foL'))...
                 ,find(strcmp(phs_names,'faL'))];
% J = kg*m^2/s^2 = kg*m^3/m*s^2 = Pa*m^3 | Pa = kg/m*s^2
Molar_mass    = phase_mol_comp(iphase,:)*(ele_wt/1e3)';      % [kg/mol]
Gibbs         = Gibbs_HP98_Pa(iT,:,iphase);                  % [J/mol]
% Volume: Pa*m^3/mol*Pa = m^3/mol
Vol_c         = diff( Gibbs,1,2)/dP;
Vol           = zeros(size(Gibbs));
Vol(:,2:end-1,:) = (Vol_c(:,1:end-1,:) + Vol_c(:,2:end,:) )/2;
Vol(:, 1,:)    = Vol(:, 2,:);
Vol(:,end,:)   = Vol(:,end-1,:);
% Entropy: J/mol*K
S_c           = -diff(Gibbs,1,1)/dT;
S             = zeros(size(Gibbs));
S(2:end-1,:,:) = (S_c(1:end-1,:,:) + S_c(2:end,:,:) )/2;
S( 1,:,:)     = S( 2,:,:) ;
S(end,:,:)    = S(end-1,:,:) ;
Cp_c          = T_all(2:end-1)'.*diff(S_c,1,1)/dT;
Cp            = zeros(size(Gibbs));
Cp(2:end-1,:,:) = Cp_c;
Cp( 1,:,:)    = Cp(2,:,:) ;
Cp(end,:,:)   = Cp(end-1,:,:) ;
rho           = 1./Vol;
H             = Gibbs + T_all'.*S;
U             = Gibbs + T_all'.*S - P_all.*Vol;
TS            = T_all'.*S;
PV            = P_all.*Vol;
for i= 1:4
H(:, :, i)    = H(:, :, i) - H(1,1,i);
U(:, :, i)    = U(:, :, i) - U(1,1,i);
TS(:, :, i)   = TS(:, :, i) - TS(1,1,i);
PV(:, :, i)   = PV(:, :, i) - PV(1,1,i);
end
```

```

%- PREPROCESSING -----
C(:,1)      = C_sys;
C(:,2)      = 1 - C(:,1);
Gibbs_id0   = R*sum(C.*log(C + (C==0)),2);
C_all       = [C_sys C_sys];
M_all       = zeros(size(C_all));
Vol_all     = M_all;
S_all       = M_all;
Gibbs_all   = M_all;
Cp_all      = M_all;
i_sol       = 1:length(C_sys);           % index solid part
i_mlt       = i_sol(end)+[1:length(C_sys)]; % index melt part
M_all(i_sol) = C*squeeze(Molar_mass([1 2])); % [kg/mol]
M_all(i_mlt) = C*squeeze(Molar_mass([3 4]));

for iC = 1:length(C_sys)
    prog = iC/length(C_sys)
    for iT = 1:length(T_all)
        for iP = 1:length(P_all)
            Vol_all(i_sol) = C*squeeze( Vol(iT,iP,[1 2]));
            Vol_all(i_mlt) = C*squeeze( Vol(iT,iP,[3 4]));
            Cp_all(i_sol)  = C*squeeze( Cp(iT,iP,[1 2]));
            Cp_all(i_mlt)  = C*squeeze( Cp(iT,iP,[3 4]));
            S_all(i_sol)   = C*squeeze( S(iT,iP,[1 2])) + Gibbs_id0;
            S_all(i_mlt)   = C*squeeze( S(iT,iP,[3 4])) + Gibbs_id0;
            Gibbs_all(i_sol) = C*squeeze(Gibbs(iT,iP,[1 2])) + T_all(iT)*Gibbs_id0;
            Gibbs_all(i_mlt) = C*squeeze(Gibbs(iT,iP,[3 4])) + T_all(iT)*Gibbs_id0;
            Aeq              = [C_all; ones(1,length(C_all))];
            beq              = [C_sys(iC); 1];
            LB                = zeros(1,length(C_all));
            UB                = ones(1,length(C_all));
            [alph,FVAL,EXITFLAG] = linprog(Gibbs_all,[],[],Aeq,beq,LB,UB,[],opts);
            alph_stb(:,iT,iC) = alph;
            alph_sol(iT,iP,iC) = sum(alph(i_sol));
            alph_mlt(iT,iP,iC) = sum(alph(i_mlt));

            M_sol(iT,iP,iC) = sum( M_all(i_sol).*alph(i_sol)')/sum(alph(i_sol));
            M_mlt(iT,iP,iC) = sum( M_all(i_mlt).*alph(i_mlt)')/sum(alph(i_mlt));
            Vol_sol(iT,iP,iC) = sum( Vol_all(i_sol).*alph(i_sol)')/...
                sum(alph(i_sol))/M_sol(iT,iP,iC);
            Vol_mlt(iT,iP,iC) = sum( Vol_all(i_mlt).*alph(i_mlt)')/...
                sum(alph(i_mlt))/ M_mlt(iT,iP,iC);
            Cp_sol(iT,iP,iC) = (sum( Cp_all(i_sol).*alph(i_sol)')/...
                sum(alph(i_sol)))/M_sol(iT,iP,iC);
            Cp_mlt(iT,iP,iC) = (sum( Cp_all(i_mlt).*alph(i_mlt)')/...
                sum(alph(i_mlt)))/M_mlt(iT,iP,iC);
            S_sol(iT,iP,iC) = sum( S_all(i_sol).*alph(i_sol)')/...
                sum(alph(i_sol))/M_sol(iT,iP,iC);
            S_mlt(iT,iP,iC) = sum( S_all(i_mlt).*alph(i_mlt)')/...
                sum(alph(i_mlt))/M_mlt(iT,iP,iC);
            G_sol(iT,iP,iC) = sum(Gibbs_all(i_sol).*alph(i_sol)')/...
                sum(alph(i_sol))/M_sol(iT,iP,iC);
            G_mlt(iT,iP,iC) = sum(Gibbs_all(i_mlt).*alph(i_mlt)')/...
                sum(alph(i_mlt))/M_mlt(iT,iP,iC);
            U_sol(iT,iP,iC) = G_sol(iT,iP,iC) + T_all(iT)*S_sol(iT,iP,iC) ...
                - P_all(iP)*Vol_sol(iT,iP,iC);
            U_mlt(iT,iP,iC) = G_mlt(iT,iP,iC) + T_all(iT)*S_mlt(iT,iP,iC) ...
                - P_all(iP)*Vol_mlt(iT,iP,iC);

            rho_sol(iT,iP,iC) = 1/Vol_sol(iT,iP,iC);
            rho_mlt(iT,iP,iC) = 1/Vol_mlt(iT,iP,iC);
            CFo_sol_mol(iT,iP,iC) = sum(alph(i_sol).*C_all(i_sol)')/sum(alph(i_sol));
            CFo_mlt_mol(iT,iP,iC) = sum(alph(i_mlt).*C_all(i_mlt)')/sum(alph(i_mlt));
            CFa_sol_mol(iT,iP,iC) = 1 - CFo_sol_mol(iT,iP,iC);
            CFa_mlt_mol(iT,iP,iC) = 1 - CFo_mlt_mol(iT,iP,iC);
        end
    end
end

```

```

% MASS fraction [kg/kg]
CFo_sol(iT,iP,iC) = (CFo_sol_mol(iT,iP,iC)*Molar_mass(1))/...
(CFo_sol_mol(iT,iP,iC)*Molar_mass(1)+(CFa_sol_mol(iT,iP,iC)*Molar_mass(2)));
CFo_mlt(iT,iP,iC) = (CFo_mlt_mol(iT,iP,iC)*Molar_mass(3))/...
((CFo_mlt_mol(iT,iP,iC)*Molar_mass(3)+(CFa_mlt_mol(iT,iP,iC)*Molar_mass(4)));
CFa_sol(iT,iP,iC) = (CFa_sol_mol(iT,iP,iC)*Molar_mass(2))/...
((CFo_sol_mol(iT,iP,iC)*Molar_mass(1)+(CFa_sol_mol(iT,iP,iC)*Molar_mass(2)));
CFa_mlt(iT,iP,iC) = (CFa_mlt_mol(iT,iP,iC)*Molar_mass(4))/...
((CFo_mlt_mol(iT,iP,iC)*Molar_mass(3)+(CFa_mlt_mol(iT,iP,iC)*Molar_mass(4)));
end
end
end

% Transformation from Fo-Fa to oxyde (MgO-FeO-SiO2)
%--- Calculation of concentration in oxydes -----
%
%           MgO   FeO   SiO2
Molecular_wt = [ 40.30 70.85 60.08]/1e3;    % poids moléculaire
nb_ele       = [ 2     2     1   ];        % nombre de fois l'élément dans une olivine
for i = 1:length(C_all)/2
    for j = 1:length(T_all)
        for k = 1:length(P_all)
            % MELT - subscript i = no normalized, n = normalized
            CMgO_mlt_i(j,k,i) = nb_ele(1)*Molecular_wt(1)*CFo_mlt(j,k,i);
                                % concentration MgO in melt no-normalized
            CFeO_mlt_i(j,k,i) = nb_ele(2)*Molecular_wt(2)*(1-CFo_mlt(j,k,i));
                                % concentration FeO in melt no-normalized
            CSiO2_mlt_i(j,k,i) = nb_ele(3)*Molecular_wt(3)*(CFo_mlt(j,k,i)+1
                                -CFo_mlt(j,k,i));
                                % concentration SiO2 in melt no-normalized
            SOM_mlt_i(j,k,i) = CMgO_mlt_i(j,k,i)+CFeO_mlt_i(j,k,i)+CSiO2_mlt_i(j,k,i);
                                % sum for normalisation
            CMgO_mlt_n(j,k,i) = CMgO_mlt_i(j,k,i)/SOM_mlt_i(j,k,i);
                                % concentration MgO in melt normalized
            CFeO_mlt_n(j,k,i) = CFeO_mlt_i(j,k,i)/SOM_mlt_i(j,k,i);
                                % concentration FeO in melt normalized
            CSiO2_mlt_n(j,k,i) = CSiO2_mlt_i(j,k,i)/SOM_mlt_i(j,k,i);
                                % concentration SiO2 in melt normalized
            % SOLID - subscript i = no normalized, n = normalized
            CMgO_sol_i(j,k,i) = nb_ele(1)*Molecular_wt(1)*CFo_sol(j,k,i);
                                % concentration MgO in solid no-normalized
            CFeO_sol_i(j,k,i) = nb_ele(2)*Molecular_wt(2)*(1-CFo_sol(j,k,i));
                                % concentration FeO in solid no-normalized
            CSiO2_sol_i(j,k,i) = nb_ele(3)*Molecular_wt(3)*(CFo_sol(j,k,i)+1
                                -CFo_sol(j,k,i));
                                % concentration SiO2 in solid no-normalized
            SOM_sol_i(j,k,i) = CMgO_sol_i(j,k,i)+CFeO_sol_i(j,k,i)+CSiO2_sol_i(j,k,i);
                                % sum for normalisation
            CMgO_sol_n(j,k,i) = CMgO_sol_i(j,k,i)/SOM_sol_i(j,k,i);
                                % concentration MgO in solid normalized
            CFeO_sol_n(j,k,i) = CFeO_sol_i(j,k,i)/SOM_sol_i(j,k,i);
                                % concentration FeO in solid normalized
            CSiO2_sol_n(j,k,i) = CSiO2_sol_i(j,k,i)/SOM_sol_i(j,k,i);
                                % concentration SiO2 in solid normalized
        end
    end
end
end

save GibbsMin_Ol_Cigar

% ===== ZOOM IN THE CIGAR ===== %
% CODE FOR ZOOM IN DATA OLIVINE CIGAR - low resolution
% Annelore Bessat, last version 05.06.2020
clear all, close all, clc

```

```

%= DATA LOAD AND PREPARATION =====
load GibbsMin_01_Cigar.mat; whos

% Visualisation of cigar to choose Zoom
[T3,P3,C3] = ndgrid(T_all,P_all,C_all(i_sol));

ind_rect = [ 68  90  27  37]; % index of zoom in the data
rect_y    = T_all(ind_rect(1))-273.15;
rect_x    = C_all(ind_rect(3));
rect_ly   = (T_all(ind_rect(2))-273.15)-(T_all(ind_rect(1))-273.15);
rect_lx   = C_all(ind_rect(4))-C_all(ind_rect(3));

for iP = [1 25 36]
    figure(iP)
    pcolor(squeeze(C3(:,iP,:)),squeeze(T3(:,iP,:)-273.15),squeeze(rho_mlt(:,iP,:)))
    shading interp
    title(num2str(P_all(iP)/1e9))
    colorbar
    caxis([3500 4200])
    drawnow
    hold on
    rectangle('Position',[rect_x rect_y rect_lx rect_ly],...
              'LineWidth',2,'LineStyle',':','EdgeColor','k')
end

%= CHOOSE DATA ZOOM =====
% for a pressure between 2.4-3.5 GPa
iT      = 68:90;           % index zoom for temperature
iP      = 25:36;           % index zoom for pressure
iC      = 27:37;           % index zoom for concentration of system

Uz_sol  = U_sol(iT,iP,iC);
Uz_mlt  = U_mlt(iT,iP,iC);
rhoz_sol = rho_sol(iT,iP,iC);
rhoz_mlt = rho_mlt(iT,iP,iC);
Cpz_sol  = Cp_sol(iT,iP,iC);
Cpz_mlt  = Cp_mlt(iT,iP,iC);
CFoz_sol = CFo_sol(iT,iP,iC);
CFoz_sol_mol = CFo_sol_mol(iT,iP,iC);
CFaz_sol  = CFa_sol(iT,iP,iC);
CFaz_sol_mol = CFa_sol_mol(iT,iP,iC);
CFoz_mlt  = CFo_mlt(iT,iP,iC);
CFoz_mlt_mol = CFo_mlt_mol(iT,iP,iC);
CFaz_mlt  = CFa_mlt(iT,iP,iC);
CFaz_mlt_mol = CFa_mlt_mol(iT,iP,iC);
CMgOz_sol = CMgO_sol_n(iT,iP,iC);
CMgOz_mlt = CMgO_mlt_n(iT,iP,iC);
CFeOz_sol = CFeO_sol_n(iT,iP,iC);
CFeOz_mlt = CFeO_mlt_n(iT,iP,iC);
CSiO2z_sol = CSiO2_sol_n(iT,iP,iC);
CSiO2z_mlt = CSiO2_mlt_n(iT,iP,iC);
T3z       = T3(iT,iP,iC);
P3z       = P3(iT,iP,iC);
C3z       = C3(iT,iP,iC);
T_plotz   = T_all(iT)-273.15;
P_plotz   = P_all(iP);

%= 3D(TemperaturePressureConcentration) to 2D(TemperaturePressure) =====
iT      = 1:length(iT);
iP      = 1:length(iP);
iC      = 11;
Uz_sol  = squeeze(      Uz_sol(iT,iP,iC));
Uz_mlt  = squeeze(      Uz_mlt(iT,iP,iC));

```

```

rhoz_sol      = squeeze(    rhoz_sol(iT,iP,iC));
rhoz_mlt      = squeeze(    rhoz_mlt(iT,iP,iC));
Cpz_sol       = squeeze(    Cpz_sol(iT,iP,iC));
Cpz_mlt       = squeeze(    Cpz_mlt(iT,iP,iC));
CFoz_sol      = squeeze(    CFoz_sol(iT,iP,iC));
CFoz_sol_mol  = squeeze(CFoz_sol_mol(iT,iP,iC));
CFaz_sol      = squeeze(    CFaz_sol(iT,iP,iC));
CFaz_sol_mol  = squeeze(CFaz_sol_mol(iT,iP,iC));
CFoz_mlt      = squeeze(    CFoz_mlt(iT,iP,iC));
CFoz_mlt_mol  = squeeze(CFoz_mlt_mol(iT,iP,iC));
CFaz_mlt      = squeeze(    CFaz_mlt(iT,iP,iC));
CFaz_mlt_mol  = squeeze(CFaz_mlt_mol(iT,iP,iC));
CMgOz_sol     = squeeze(    CMgOz_sol(iT,iP,iC));
CMgOz_mlt     = squeeze(    CMgOz_mlt(iT,iP,iC));
CFeOz_sol     = squeeze(    CFeOz_sol(iT,iP,iC));
CFeOz_mlt     = squeeze(    CFeOz_mlt(iT,iP,iC));
CSiO2z_sol    = squeeze(    CSiO2z_sol(iT,iP,iC));
CSiO2z_mlt    = squeeze(    CSiO2z_mlt(iT,iP,iC));
T2dz          = squeeze(    T3z(iT,iP,iC));
P2dz          = squeeze(    P3z(iT,iP,iC));
C2dz          = squeeze(    C3z(iT,iP,iC));
C_ref         = C3z(1,1,iC);

```

```

%= DATA SAVE =====
save ZoomData_O1_Cigar T2dz P2dz C2dz T_plotz P_plotz C_ref      ...
    Uz_sol rhoz_sol CFoz_sol CFoz_sol_mol CFaz_sol CFaz_sol_mol ...
    Uz_mlt rhoz_mlt CFoz_mlt CFoz_mlt_mol CFaz_mlt CFaz_mlt_mol ...
    CMgOz_sol CFeOz_sol CSiO2z_sol Cpz_sol                      ...
    CMgOz_mlt CFeOz_mlt CSiO2z_mlt Cpz_mlt

```

```

% ===== CODE FOR APPROXIMATION ===== %
% CODE FOR APPROXIMATION OF ALPHA, BETA AND GAMMA
% 22.05.2020, Annelore Bessat, Last Update 27.01.2021

```

```

clear all, close all
load ZoomData_O1_Cigar; whos

```

```

% = PARAMETRES APPROXIMATION =====

```

```

%- Point de référence -----
iTref      = round(length(T_plotz)/2);
iPref      = min(find(P_plotz >= 3e9));
Tref_apx   = T2dz(iTref,1); % Tref: 1590°C (middle of zoom domain)
Pref_apx   = P2dz(1,iPref); % Pref: 3 GPa
rho0_mlt   = rhoz_mlt(iTref,iPref);
rho0_sol   = rhoz_sol(iTref,iPref);
Cp0_mlt    = Cpz_mlt(iTref,iPref);
Cp0_sol    = Cpz_sol(iTref,iPref);
U0_mlt     = Uz_mlt(iTref,iPref);
U0_sol     = Uz_sol(iTref,iPref);
CMgO0_mlt  = CMgOz_mlt(iTref,iPref);
CMgO0_sol  = CMgOz_sol(iTref,iPref);
CFeO0_mlt  = CFeOz_mlt(iTref,iPref);
CFeO0_sol  = CFeOz_sol(iTref,iPref);
CSiO20_mlt = CSiO2z_mlt(iTref,iPref);
CSiO20_sol = CSiO2z_sol(iTref,iPref);

```

```

%- Calcul de l'alpha et du beta -----

```

```

alpha_rho_mlt = (( rhoz_mlt(end,iPref)- rhoz_mlt(1,iPref))/(T2dz(end,iPref)- ...
    T2dz(1,iPref)))/ rho0_mlt;
alpha_rho_sol = (( rhoz_sol(end,iPref)- rhoz_sol(1,iPref))/(T2dz(end,iPref)- ...
    T2dz(1,iPref)))/ rho0_sol;
alpha_Cp_mlt  = (( Cpz_mlt(end,iPref)- Cpz_mlt(1,iPref))/(T2dz(end,iPref)- ...
    T2dz(1,iPref)))/ Cp0_mlt;

```

```

alpha_Cp_sol    = (( Cpz_sol(end,iPref)- Cpz_sol(1,iPref))/(T2dz(end,iPref)- ...
                  T2dz(1,iPref)))/ Cp0_sol;
alpha_U_mlt     = Cp0_mlt;
alpha_U_sol     = Cp0_sol;
alpha_CMgO_mlt  = (( CMgOz_mlt(end,iPref)- CMgOz_mlt(1,iPref))/(T2dz(end,iPref)- ...
                  T2dz(1,iPref)))/ CMgO0_mlt;
alpha_CMgO_sol  = (( CMgOz_sol(end,iPref)- CMgOz_sol(1,iPref))/(T2dz(end,iPref)- ...
                  T2dz(1,iPref)))/ CMgO0_sol;
alpha_CFeO_mlt  = (( CFeOz_mlt(end,iPref)- CFeOz_mlt(1,iPref))/(T2dz(end,iPref)- ...
                  T2dz(1,iPref)))/ CFeO0_mlt;
alpha_CFeO_sol  = (( CFeOz_sol(end,iPref)- CFeOz_sol(1,iPref))/(T2dz(end,iPref)- ...
                  T2dz(1,iPref)))/ CFeO0_sol;
alpha_CSiO2_mlt = ((CSiO2z_mlt(end,iPref)-CSiO2z_mlt(1,iPref))/(T2dz(end,iPref)- ...
                  T2dz(1,iPref)))/CSiO20_mlt;
alpha_CSiO2_sol = ((CSiO2z_sol(end,iPref)-CSiO2z_sol(1,iPref))/(T2dz(end,iPref)- ...
                  T2dz(1,iPref)))/CSiO20_sol;

beta_rho_mlt    = (( rhoz_mlt(iTref,end)- rhoz_mlt(iTref,1))/(P2dz(iTref,end)- ...
                  P2dz(iTref,1)))/ rho0_mlt;
beta_rho_sol    = (( rhoz_sol(iTref,end)- rhoz_sol(iTref,1))/(P2dz(iTref,end)- ...
                  P2dz(iTref,1)))/ rho0_sol;
beta_Cp_mlt     = (( Cpz_mlt(iTref,end)- Cpz_mlt(iTref,1))/(P2dz(iTref,end)- ...
                  P2dz(iTref,1)))/ Cp0_mlt;
beta_Cp_sol     = (( Cpz_sol(iTref,end)- Cpz_sol(iTref,1))/(P2dz(iTref,end)- ...
                  P2dz(iTref,1)))/ Cp0_sol;
beta_U_mlt      = 0;
beta_U_sol      = 0;
beta_CMgO_mlt   = (( CMgOz_mlt(iTref,end)- CMgOz_mlt(iTref,1))/(P2dz(iTref,end)- ...
                  P2dz(iTref,1)))/ CMgO0_mlt;
beta_CMgO_sol   = (( CMgOz_sol(iTref,end)- CMgOz_sol(iTref,1))/(P2dz(iTref,end)- ...
                  P2dz(iTref,1)))/ CMgO0_sol;
beta_CFeO_mlt   = (( CFeOz_mlt(iTref,end)- CFeOz_mlt(iTref,1))/(P2dz(iTref,end)- ...
                  P2dz(iTref,1)))/ CFeO0_mlt;
beta_CFeO_sol   = (( CFeOz_sol(iTref,end)- CFeOz_sol(iTref,1))/(P2dz(iTref,end)- ...
                  P2dz(iTref,1)))/ CFeO0_sol;
beta_CSiO2_mlt  = ((CSiO2z_mlt(iTref,end)-CSiO2z_mlt(iTref,1))/(P2dz(iTref,end)- ...
                  P2dz(iTref,1)))/CSiO20_mlt;
beta_CSiO2_sol  = ((CSiO2z_sol(iTref,end)-CSiO2z_sol(iTref,1))/(P2dz(iTref,end)- ...
                  P2dz(iTref,1)))/CSiO20_sol;

```

%- Calcul des paramètres par approximation -----

```

rho_mlt_apx    = rho0_mlt.*(1+( alpha_rho_mlt.*(T2dz-Tref_apx))+ ...
                  ( beta_rho_mlt.*(P2dz-Pref_apx)));
rho_sol_apx    = rho0_sol.*(1+( alpha_rho_sol.*(T2dz-Tref_apx))+ ...
                  ( beta_rho_sol.*(P2dz-Pref_apx)));
CMgO_mlt_apx   = CMgO0_mlt.*(1+( alpha_CMgO_mlt.*(T2dz-Tref_apx))+ ...
                  ( beta_CMgO_mlt.*(P2dz-Pref_apx)));
CMgO_sol_apx   = CMgO0_sol.*(1+( alpha_CMgO_sol.*(T2dz-Tref_apx))+ ...
                  ( beta_CMgO_sol.*(P2dz-Pref_apx)));
CFeO_mlt_apx   = CFeO0_mlt.*(1+( alpha_CFeO_mlt.*(T2dz-Tref_apx))+ ...
                  ( beta_CFeO_mlt.*(P2dz-Pref_apx)));
CFeO_sol_apx   = CFeO0_sol.*(1+( alpha_CFeO_sol.*(T2dz-Tref_apx))+ ...
                  ( beta_CFeO_sol.*(P2dz-Pref_apx)));
CSiO_mlt_apx   = CSiO20_mlt.*(1+(alpha_CSiO2_mlt.*(T2dz-Tref_apx))+ ...
                  ( beta_CSiO2_mlt.*(P2dz-Pref_apx)));
CSiO_sol_apx   = CSiO20_sol.*(1+(alpha_CSiO2_sol.*(T2dz-Tref_apx))+ ...
                  ( beta_CSiO2_sol.*(P2dz-Pref_apx)));
U_mlt_apx      = U0_mlt.*(1+( alpha_U_mlt.*(T2dz-Tref_apx))+ ...
                  ( beta_U_mlt.*(P2dz-Pref_apx)));
U_sol_apx      = U0_sol.*(1+( alpha_U_sol.*(T2dz-Tref_apx))+ ...
                  ( beta_U_sol.*(P2dz-Pref_apx)));
Cp_mlt_apx     = Cp0_mlt.*(1+( alpha_Cp_mlt.*(T2dz-Tref_apx))+ ...
                  ( beta_Cp_mlt.*(P2dz-Pref_apx)));

```

```

Cp_sol_apx      =      Cp0_sol.*(1+(      alpha_Cp_sol.*(T2dz-Tref_apx))+ ...
                        (      beta_Cp_sol.*(P2dz-Pref_apx)));

%% - Data pour calcul du gamma -----
% Data experimental melt "0% melt" (Table 1; Davis 2011)
MgO_m_data_exp = 15.78;
FeO_m_data_exp = 9.72;
SiO_m_data_exp = 44.77;
SOM_mlt_data_exp = MgO_m_data_exp + FeO_m_data_exp + SiO_m_data_exp;
MgO_m_exp       = MgO_m_data_exp/SOM_mlt_data_exp;
FeO_m_exp       = FeO_m_data_exp/SOM_mlt_data_exp;
SiO_m_exp       = SiO_m_data_exp/SOM_mlt_data_exp;
SOM_mlt_exp     = MgO_m_exp + FeO_m_exp + SiO_m_exp;
% Data experimental solid "KLB-10x" (Table 1; Davis 2011)
MgO_s_data_exp = 38.76;
FeO_s_data_exp = 8.09;
SiO_s_data_exp = 44.92;
SOM_sol_data_exp = MgO_s_data_exp + FeO_s_data_exp + SiO_s_data_exp;
MgO_s_exp       = MgO_s_data_exp/SOM_sol_data_exp;
FeO_s_exp       = FeO_s_data_exp/SOM_sol_data_exp;
SiO_s_exp       = SiO_s_data_exp/SOM_sol_data_exp;
SOM_sol_exp     = MgO_s_exp + FeO_s_exp + SiO_s_exp;
% total experimental
SOM_TOT_exp     = SOM_mlt_exp + SOM_sol_exp;
MgO_TOT_exp     = (MgO_m_exp + MgO_s_exp)/SOM_TOT_exp;
FeO_TOT_exp     = (FeO_m_exp + FeO_s_exp)/SOM_TOT_exp;
SiO_TOT_exp     = (SiO_m_exp + SiO_s_exp)/SOM_TOT_exp;

% data melt linprog
MgO_m_data_lp   = CMgO0_mlt;
FeO_m_data_lp   = CFeO0_mlt;
SiO_m_data_lp   = CSiO20_mlt;
SOM_mlt_data_lp = MgO_m_data_lp + FeO_m_data_lp + SiO_m_data_lp;
MgO_m_lp        = MgO_m_data_lp/SOM_mlt_data_lp;
FeO_m_lp        = FeO_m_data_lp/SOM_mlt_data_lp;
SiO_m_lp        = SiO_m_data_lp/SOM_mlt_data_lp;
SOM_mlt_lp      = MgO_m_lp + FeO_m_lp + SiO_m_lp;
% data solid linprog
MgO_s_data_lp   = CMgO0_sol;
FeO_s_data_lp   = CFeO0_sol;
SiO_s_data_lp   = CSiO20_sol;
SOM_sol_data_lp = MgO_s_data_lp + FeO_s_data_lp + SiO_s_data_lp;
MgO_s_lp        = MgO_s_data_lp/SOM_sol_data_lp;
FeO_s_lp        = FeO_s_data_lp/SOM_sol_data_lp;
SiO_s_lp        = SiO_s_data_lp/SOM_sol_data_lp;
SOM_sol_lp      = MgO_s_lp + FeO_s_lp + SiO_s_lp;
% total linprog
SOM_TOT_lp      = SOM_mlt_lp + SOM_sol_lp;
MgO_TOT_lp      = (MgO_m_lp + MgO_s_lp)/SOM_TOT_lp;
FeO_TOT_lp      = (FeO_m_lp + FeO_s_lp)/SOM_TOT_lp;
SiO_TOT_lp      = (SiO_m_lp + SiO_s_lp)/SOM_TOT_lp;

%- Calcul des gammas U CMgO CFeO CSiO2 -----
gamma_CMgO_mlt  = ((MgO_m_exp-MgO_m_lp)/(SiO_TOT_exp-SiO_TOT_lp))/ CMgO0_mlt;
gamma_CMgO_sol  = ((MgO_s_exp-MgO_s_lp)/(SiO_TOT_exp-SiO_TOT_lp))/ CMgO0_sol;
gamma_CFeO_mlt  = ((FeO_m_exp-FeO_m_lp)/(SiO_TOT_exp-SiO_TOT_lp))/ CFeO0_mlt;
gamma_CFeO_sol  = ((FeO_s_exp-FeO_s_lp)/(SiO_TOT_exp-SiO_TOT_lp))/ CFeO0_sol;
gamma_CSiO2_mlt = ((SiO_m_exp-SiO_m_lp)/(SiO_TOT_exp-SiO_TOT_lp))/CSiO20_mlt;
gamma_CSiO2_sol = ((SiO_s_exp-SiO_s_lp)/(SiO_TOT_exp-SiO_TOT_lp))/CSiO20_sol;
gamma_U_mlt     = 0;
gamma_U_sol     = 0;
gamma_Cp_mlt    = 0;
gamma_Cp_sol    = 0;

```

```

%- Calcul des gammas rho -----
% Oxyde transformation (MgO-FeO-SiO2) in mol to find molar fraction - data from Davis et
al. 2011
%--- Data of Davis et al. (Tables 1 and 2) in WT% -----
nameph_D2011 = {'Ol_s_D2011', 'Opx_s_D2011', 'Cpx_s_D2011', 'Grt_s_D2011', 'Liq_m_D2011'};
MgO_D2011     = [ 48.26, 31.16, 21.43, 20.50, 15.78];
FeO_D2011     = [ 10.00, 5.89, 4.82, 6.63, 9.72];
SiO2_D2011    = [ 40.65, 54.28, 52.97, 42.15, 44.77];
SOM_D2011     = MgO_D2011 + FeO_D2011 + SiO2_D2011;
mode_D2011    = [ 60.80, 7.70, 22.60, 8.90]/1e2;
%--- Data normalisation in WT% -----
MgO_D2011_n   = MgO_D2011./SOM_D2011;
FeO_D2011_n   = FeO_D2011./SOM_D2011;
SiO2_D2011_n  = SiO2_D2011./SOM_D2011;
SOM_D2011_n   = MgO_D2011_n + FeO_D2011_n + SiO2_D2011_n;
%--- Transformation in MOLE -----
%
%           MgO   FeO   SiO2
Molecular_wt = [ 40.30 70.85 60.08]/1e3; % poids moléculaire
SOM_TOT_D2011_n_mol = (MgO_D2011_n./Molecular_wt(1))+(FeO_D2011_n./Molecular_wt(2))+ ...
(SiO2_D2011_n./Molecular_wt(3));
MgO_D2011_n_mol = (MgO_D2011_n./Molecular_wt(1))./SOM_TOT_D2011_n_mol;
FeO_D2011_n_mol = (FeO_D2011_n./Molecular_wt(2))./SOM_TOT_D2011_n_mol;
SiO2_D2011_n_mol = (SiO2_D2011_n./Molecular_wt(3))./SOM_TOT_D2011_n_mol;
SOM_test = MgO_D2011_n_mol+FeO_D2011_n_mol+SiO2_D2011_n_mol;
% Liquid
%
%           MgO   FeO   SiO2
%           FoL  =  2   0   1
%           FaL  =  0   2   1
%           QtzL =  0   0   1
nb_mol_Liq = [2 0 1; 0 2 1; 0 0 1];
inv_nmol_Liq = inv(nb_mol_Liq)';
FoL_n_mol = inv_nmol_Liq(1,1)*MgO_D2011_n_mol(5)+inv_nmol_Liq(1,2)* ...
FeO_D2011_n_mol(5)+inv_nmol_Liq(1,3)*SiO2_D2011_n_mol(5);
FaL_n_mol = inv_nmol_Liq(2,1)*MgO_D2011_n_mol(5)+inv_nmol_Liq(2,2)* ...
FeO_D2011_n_mol(5)+inv_nmol_Liq(2,3)*SiO2_D2011_n_mol(5);
QtzL_n_mol = inv_nmol_Liq(3,1)*MgO_D2011_n_mol(5)+inv_nmol_Liq(3,2)* ...
FeO_D2011_n_mol(5)+inv_nmol_Liq(3,3)*SiO2_D2011_n_mol(5);
SOM_Liq = FoL_n_mol + FaL_n_mol + QtzL_n_mol;
FoL_n_mol_nor = FoL_n_mol/SOM_Liq;
FaL_n_mol_nor = FaL_n_mol/SOM_Liq;
QtzL_n_mol_nor = QtzL_n_mol/SOM_Liq;
% Olivine
%
%           MgO   FeO   SiO2
%           Fo   =  2   0   1
%           Fa   =  0   2   1
%           Qtz  =  0   0   1
nb_mol_Ol = [2 0 1; 0 2 1; 0 0 1];
inv_nmol_Ol = inv(nb_mol_Ol)';
Fo_n_mol = inv_nmol_Ol(1,1)*MgO_D2011_n_mol(1)+inv_nmol_Ol(1,2)* ...
FeO_D2011_n_mol(1)+inv_nmol_Ol(1,3)*SiO2_D2011_n_mol(1);
Fa_n_mol = inv_nmol_Ol(2,1)*MgO_D2011_n_mol(1)+inv_nmol_Ol(2,2)* ...
FeO_D2011_n_mol(1)+inv_nmol_Ol(2,3)*SiO2_D2011_n_mol(1);
QtzOl_n_mol = inv_nmol_Ol(3,1)*MgO_D2011_n_mol(1)+inv_nmol_Ol(3,2)* ...
FeO_D2011_n_mol(1)+inv_nmol_Ol(3,3)*SiO2_D2011_n_mol(1);
SOM_Ol = Fo_n_mol + Fa_n_mol + QtzOl_n_mol;
Fo_n_mol_nor = Fo_n_mol/SOM_Ol;
Fa_n_mol_nor = Fa_n_mol/SOM_Ol;
QtzOl_n_mol_nor = QtzOl_n_mol/SOM_Ol;
% Opx
%
%           MgO   FeO   SiO2
%           En   =  2   0   2
%           Fs   =  0   2   2
%           Qtz  =  0   0   1

```



```

nb_mol_Opx      = [2 0 2; 0 2 2; 0 0 1];
inv_nmol_Opx   = inv(nb_mol_Opx)';
En_n_mol       = inv_nmol_Opx(1,1)*MgO_D2011_n_mol(2)+inv_nmol_Opx(1,2)* ...
                FeO_D2011_n_mol(2)+inv_nmol_Opx(1,3)*SiO2_D2011_n_mol(2);
Fs_n_mol       = inv_nmol_Opx(2,1)*MgO_D2011_n_mol(2)+inv_nmol_Opx(2,2)* ...
                FeO_D2011_n_mol(2)+inv_nmol_Opx(2,3)*SiO2_D2011_n_mol(2);
QtzOpx_n_mol   = inv_nmol_Opx(3,1)*MgO_D2011_n_mol(2)+inv_nmol_Opx(3,2)* ...
                FeO_D2011_n_mol(2)+inv_nmol_Opx(3,3)*SiO2_D2011_n_mol(2);
SOM_Opx        = En_n_mol + Fs_n_mol + QtzOpx_n_mol;
En_n_mol_nor   = En_n_mol/SOM_Opx;
Fs_n_mol_nor   = Fs_n_mol/SOM_Opx;
QtzOpx_n_mol_nor = QtzOpx_n_mol/SOM_Opx;
% Cpx
%
%           MgO   FeO   SiO2   CaO
%           Di    =   1    0     2     1
%           Hed    =   0    1     2     1
%           Qtz    =   0    0     1     0
nb_mol_Cpx     = [1 0 2; 0 1 2; 0 0 1];
inv_nmol_Cpx   = inv(nb_mol_Cpx)';
Di_n_mol       = inv_nmol_Cpx(1,1)*MgO_D2011_n_mol(3)+inv_nmol_Cpx(1,2)* ...
                FeO_D2011_n_mol(3)+inv_nmol_Cpx(1,3)*SiO2_D2011_n_mol(3);
Hed_n_mol      = inv_nmol_Cpx(2,1)*MgO_D2011_n_mol(3)+inv_nmol_Cpx(2,2)* ...
                FeO_D2011_n_mol(3)+inv_nmol_Cpx(2,3)*SiO2_D2011_n_mol(3);
QtzCpx_n_mol   = inv_nmol_Cpx(3,1)*MgO_D2011_n_mol(3)+inv_nmol_Cpx(3,2)* ...
                FeO_D2011_n_mol(3)+inv_nmol_Cpx(3,3)*SiO2_D2011_n_mol(3);
SOM_Cpx        = Di_n_mol + Hed_n_mol + QtzCpx_n_mol;
Di_n_mol_nor   = Di_n_mol/SOM_Cpx;
Hed_n_mol_nor  = Hed_n_mol/SOM_Cpx;
QtzCpx_n_mol_nor = QtzCpx_n_mol/SOM_Cpx;
% Grt
%
%           MgO   FeO   SiO2   Al2O3
%           Py    =   3    0     3     1
%           Alm   =   0    3     3     1
%           Qtz   =   0    0     1     0
nb_mol_Grt     = [3 0 3; 0 3 3; 0 0 1];
inv_nmol_Grt   = inv(nb_mol_Grt)';
Py_n_mol       = inv_nmol_Grt(1,1)*MgO_D2011_n_mol(4)+inv_nmol_Grt(1,2)* ...
                FeO_D2011_n_mol(4)+inv_nmol_Grt(1,3)*SiO2_D2011_n_mol(4);
Alm_n_mol      = inv_nmol_Grt(2,1)*MgO_D2011_n_mol(4)+inv_nmol_Grt(2,2)* ...
                FeO_D2011_n_mol(4)+inv_nmol_Grt(2,3)*SiO2_D2011_n_mol(4);
QtzGrt_n_mol   = inv_nmol_Grt(3,1)*MgO_D2011_n_mol(4)+inv_nmol_Grt(3,2)* ...
                FeO_D2011_n_mol(4)+inv_nmol_Grt(3,3)*SiO2_D2011_n_mol(4);
SOM_Grt        = Py_n_mol + Alm_n_mol + QtzGrt_n_mol;
Py_n_mol_nor   = Py_n_mol/SOM_Grt;
Alm_n_mol_nor  = Alm_n_mol/SOM_Grt;
QtzGrt_n_mol_nor = QtzGrt_n_mol/SOM_Grt;

%--- Calculation of mineral pole density -----
% load HP98_ds55_lowres, whos
load('HP98_ds55_lowres.mat', 'T_HP98_K', 'P_HP98_Pa', 'Gibbs_HP98_Pa', 'phs_names', 'phase_mol
_comp', 'ele_wt')
T_all          = T_HP98_K;
P_all          = P_HP98_Pa;
dP             = P_all(2)-P_all(1);
% Temperature and pressure of reference from experimentation
iT_apx        = find(T_all == Tref_apx);
iP_apx        = find(P_all == Pref_apx);
% Phase
iphase         = [find(strcmp(phs_names, 'fo' ))... % ol - Mg2SiO4          1
                 ,find(strcmp(phs_names, 'fa' ))... % - Fe2SiO4          2
                 ,find(strcmp(phs_names, 'en' ))... % opx - Mg2Si2O6       3
                 ,find(strcmp(phs_names, 'fs' ))... % - Fe2Si2O6       4
                 ,find(strcmp(phs_names, 'di' ))... % cpx - CaMgSi2O6       5

```

```
,find(strcmp(phs_names,'hed' ))... % - CaFeSi2O6 6
,find(strcmp(phs_names,'py' ))... % grt - Mg3Al2Si3O12 7
,find(strcmp(phs_names,'alm' ))... % - Fe3Al2Si3O12 8
,find(strcmp(phs_names,'foL' ))... % ol liq - Mg2SiO4 9
,find(strcmp(phs_names,'faL' ))... % - Fe2SiO4 10
,find(strcmp(phs_names,'q' ))... % qtz - SiO2 11
,find(strcmp(phs_names,'qL' )); % qtz liq - SiO2 12
```

```
% Calculation with data base
```

```
Molar_mass = phase_mol_comp(iphase,:)*(ele_wt/1e3)';
```

```
Gibbs_apx = Gibbs_HP98_Pa(iT_apx,:,iphase);
```

```
% Volume
```

```
Vol_c_exp = diff(Gibbs_exp,1,2)/dP; % Pa*m^3/mol/Pa = m^3/mol
```

```
Vol_c_apx = diff(Gibbs_apx,1,2)/dP;
```

```
Vol_exp = zeros(size(Gibbs_exp));
```

```
Vol_apx = zeros(size(Gibbs_apx));
```

```
Vol_exp(:,2:end-1,:) = (Vol_c_exp(:,1:end-1,:) + Vol_c_exp(:,2:end,:)) /2;
```

```
Vol_exp(:, 1,:) = Vol_exp(:, 2,:);
```

```
Vol_exp(:,end,:) = Vol_exp(:,end-1,:);
```

```
Vol_apx(:,2:end-1,:) = (Vol_c_apx(:,1:end-1,:) + Vol_c_apx(:,2:end,:)) /2;
```

```
Vol_apx(:, 1,:) = Vol_apx(:, 2,:);
```

```
Vol_apx(:,end,:) = Vol_apx(:,end-1,:);
```

```
%= PREPROCESSING =====
```

```
Vol_ol_exp = Vol_exp(1,iP_exp,1)* Fo_n_mol_nor + Vol_exp(1,iP_exp,2) *...
Fa_n_mol_nor + Vol_exp(1,iP_exp,11)* QtzOl_n_mol_nor; % MOLAR VOLUME
```

```
Vol_opx_exp = Vol_exp(1,iP_exp,3)* En_n_mol_nor + Vol_exp(1,iP_exp,4) *...
Fs_n_mol_nor + Vol_exp(1,iP_exp,11)*QtzOpx_n_mol_nor;
```

```
Vol_cpx_exp = Vol_exp(1,iP_exp,5)* Di_n_mol_nor + Vol_exp(1,iP_exp,6) *...
Hed_n_mol_nor + Vol_exp(1,iP_exp,11)*QtzCpx_n_mol_nor;
```

```
Vol_grt_exp = Vol_exp(1,iP_exp,7)* Py_n_mol_nor + Vol_exp(1,iP_exp,8) *...
Alm_n_mol_nor + Vol_exp(1,iP_exp,11)*QtzGrt_n_mol_nor;
```

```
Vol_liq_exp = Vol_exp(1,iP_exp,9)*FoL_n_mol_nor + Vol_exp(1,iP_exp,10)*...
FaL_n_mol_nor + Vol_exp(1,iP_exp,12)* QtzL_n_mol_nor;
```

```
Vol_ol_apx = Vol_apx(1,iP_apx,1)* Fo_n_mol_nor + Vol_apx(1,iP_apx,2) *...
Fa_n_mol_nor + Vol_apx(1,iP_apx,11)* QtzOl_n_mol_nor;
```

```
Vol_opx_apx = Vol_apx(1,iP_apx,3)* En_n_mol_nor + Vol_apx(1,iP_apx,4) *...
Fs_n_mol_nor + Vol_apx(1,iP_apx,11)*QtzOpx_n_mol_nor;
```

```
Vol_cpx_apx = Vol_apx(1,iP_apx,5)* Di_n_mol_nor + Vol_apx(1,iP_apx,6) *...
Hed_n_mol_nor + Vol_apx(1,iP_apx,11)*QtzCpx_n_mol_nor;
```

```
Vol_grt_apx = Vol_apx(1,iP_apx,7)* Py_n_mol_nor + Vol_apx(1,iP_apx,8) *...
Alm_n_mol_nor + Vol_apx(1,iP_apx,11)*QtzGrt_n_mol_nor;
```

```
Vol_liq_apx = Vol_apx(1,iP_apx,9)*FoL_n_mol_nor + Vol_apx(1,iP_apx,10)*...
FaL_n_mol_nor + Vol_apx(1,iP_apx,12)* QtzL_n_mol_nor;
```

```
M_ol = Molar_mass(1)*Fo_n_mol_nor + Molar_mass(2) * Fa_n_mol_nor +...
Molar_mass(11)* QtzOl_n_mol_nor; % MOLAR MASS
```

```
M_opx = Molar_mass(3)* En_n_mol_nor + Molar_mass(4) * Fs_n_mol_nor +...
Molar_mass(11)*QtzOpx_n_mol_nor;
```

```
M_cpx = Molar_mass(5)* Di_n_mol_nor + Molar_mass(6) *Hed_n_mol_nor +...
Molar_mass(11)*QtzCpx_n_mol_nor;
```

```
M_grt = Molar_mass(7)* Py_n_mol_nor + Molar_mass(8) *Alm_n_mol_nor +...
Molar_mass(11)*QtzGrt_n_mol_nor;
```

```
M_liq = Molar_mass(9)*FoL_n_mol_nor + Molar_mass(10)*FaL_n_mol_nor +...
Molar_mass(12)* QtzL_n_mol_nor;
```

```
mod_vol_fo_exp = Fo_n_mol_nor*Vol_exp(1,iP_exp, 1)/(Fo_n_mol_nor*...
Vol_exp(1,iP_exp,1)+ Fa_n_mol_nor*Vol_exp(1,iP_exp,2)+ ...
QtzOl_n_mol_nor*Vol_exp(1,iP_exp,11)); % MODE IN VOL%
```

```
mod_vol_fa_exp = Fa_n_mol_nor*Vol_exp(1,iP_exp, 2)/(Fo_n_mol_nor*...
Vol_exp(1,iP_exp,1)+ Fa_n_mol_nor*Vol_exp(1,iP_exp,2)+ ...
QtzOl_n_mol_nor*Vol_exp(1,iP_exp,11));
```

```
mod_vol_qtzol_exp = QtzOl_n_mol_nor*Vol_exp(1,iP_exp,11)/(Fo_n_mol_nor*...
Vol_exp(1,iP_exp,1)+ Fa_n_mol_nor*Vol_exp(1,iP_exp,2)+ ...
QtzOl_n_mol_nor*Vol_exp(1,iP_exp,11));
```

```

mod_vol_en_exp = En_n_mol_nor*Vol_exp(1,iP_exp, 3)/(En_n_mol_nor*...
Vol_exp(1,iP_exp,3)+ Fs_n_mol_nor*Vol_exp(1,iP_exp,4)+ ...
QtzOpx_n_mol_nor*Vol_exp(1,iP_exp,11));
mod_vol_fs_exp = Fs_n_mol_nor*Vol_exp(1,iP_exp, 4)/(En_n_mol_nor*...
Vol_exp(1,iP_exp,3)+ Fs_n_mol_nor*Vol_exp(1,iP_exp,4)+ ...
QtzOpx_n_mol_nor*Vol_exp(1,iP_exp,11));
mod_vol_qtzopx_exp = QtzOpx_n_mol_nor*Vol_exp(1,iP_exp,11)/(En_n_mol_nor*...
Vol_exp(1,iP_exp,3)+Fs_n_mol_nor*Vol_exp(1,iP_exp,4)+ ...
QtzOpx_n_mol_nor*Vol_exp(1,iP_exp,11));
mod_vol_di_exp = Di_n_mol_nor*Vol_exp(1,iP_exp, 5)/(Di_n_mol_nor*...
Vol_exp(1,iP_exp,5)+Hed_n_mol_nor*Vol_exp(1,iP_exp,6)+ ...
QtzCpx_n_mol_nor*Vol_exp(1,iP_exp,11));
mod_vol_hed_exp = Hed_n_mol_nor*Vol_exp(1,iP_exp, 6)/(Di_n_mol_nor*...
Vol_exp(1,iP_exp,5)+Hed_n_mol_nor*Vol_exp(1,iP_exp,6)+ ...
QtzCpx_n_mol_nor*Vol_exp(1,iP_exp,11));
mod_vol_qtzcpx_exp = QtzCpx_n_mol_nor*Vol_exp(1,iP_exp,11)/(Di_n_mol_nor*...
Vol_exp(1,iP_exp,5)+Hed_n_mol_nor*Vol_exp(1,iP_exp,6)+ ...
QtzCpx_n_mol_nor*Vol_exp(1,iP_exp,11));
mod_vol_py_exp = Py_n_mol_nor*Vol_exp(1,iP_exp, 7)/(Py_n_mol_nor*...
Vol_exp(1,iP_exp,7)+Alm_n_mol_nor*Vol_exp(1,iP_exp,8)+ ...
QtzGrt_n_mol_nor*Vol_exp(1,iP_exp,11));
mod_vol_alm_exp = Alm_n_mol_nor*Vol_exp(1,iP_exp, 8)/(Py_n_mol_nor*...
Vol_exp(1,iP_exp,7)+Alm_n_mol_nor*Vol_exp(1,iP_exp,8)+ ...
QtzGrt_n_mol_nor*Vol_exp(1,iP_exp,11));
mod_vol_qtzgrt_exp = QtzGrt_n_mol_nor*Vol_exp(1,iP_exp,11)/(Py_n_mol_nor*...
Vol_exp(1,iP_exp,7)+Alm_n_mol_nor*Vol_exp(1,iP_exp,8)+ ...
QtzGrt_n_mol_nor*Vol_exp(1,iP_exp,11));
mod_vol_fo_apx = Fo_n_mol_nor*Vol_apx(1,iP_apx, 1)/(Fo_n_mol_nor*...
Vol_apx(1,iP_apx,1)+ Fa_n_mol_nor*Vol_apx(1,iP_apx,2)+ ...
QtzOl_n_mol_nor*Vol_apx(1,iP_apx,11));
mod_vol_fa_apx = Fa_n_mol_nor*Vol_apx(1,iP_apx, 2)/(Fo_n_mol_nor*...
Vol_apx(1,iP_apx,1)+ Fa_n_mol_nor*Vol_apx(1,iP_apx,2)+ ...
QtzOl_n_mol_nor*Vol_apx(1,iP_apx,11));
mod_vol_qtzol_apx = QtzOl_n_mol_nor*Vol_apx(1,iP_apx,11)/(Fo_n_mol_nor*...
Vol_apx(1,iP_apx,1)+ Fa_n_mol_nor*Vol_apx(1,iP_apx,2)+ ...
QtzOl_n_mol_nor*Vol_apx(1,iP_apx,11));
mod_vol_en_apx = En_n_mol_nor*Vol_apx(1,iP_apx, 3)/(En_n_mol_nor*...
Vol_apx(1,iP_apx,3)+ Fs_n_mol_nor*Vol_apx(1,iP_apx,4)+ ...
QtzOpx_n_mol_nor*Vol_apx(1,iP_apx,11));
mod_vol_fs_apx = Fs_n_mol_nor*Vol_apx(1,iP_apx, 4)/(En_n_mol_nor*...
Vol_apx(1,iP_apx,3)+ Fs_n_mol_nor*Vol_apx(1,iP_apx,4)+ ...
QtzOpx_n_mol_nor*Vol_apx(1,iP_apx,11));
mod_vol_qtzopx_apx = QtzOpx_n_mol_nor*Vol_apx(1,iP_apx,11)/(En_n_mol_nor*...
Vol_apx(1,iP_apx,3)+ Fs_n_mol_nor*Vol_apx(1,iP_apx,4)+ ...
QtzOpx_n_mol_nor*Vol_apx(1,iP_apx,11));
mod_vol_di_apx = Di_n_mol_nor*Vol_apx(1,iP_apx, 5)/(Di_n_mol_nor*...
Vol_apx(1,iP_apx,5)+Hed_n_mol_nor*Vol_apx(1,iP_apx,6)+ ...
QtzCpx_n_mol_nor*Vol_apx(1,iP_apx,11));
mod_vol_hed_apx = Hed_n_mol_nor*Vol_apx(1,iP_apx, 6)/(Di_n_mol_nor*...
Vol_apx(1,iP_apx,5)+Hed_n_mol_nor*Vol_apx(1,iP_apx,6)+ ...
QtzCpx_n_mol_nor*Vol_apx(1,iP_apx,11));
mod_vol_qtzcpx_apx = QtzCpx_n_mol_nor*Vol_apx(1,iP_apx,11)/(Di_n_mol_nor*...
Vol_apx(1,iP_apx,5)+Hed_n_mol_nor*Vol_apx(1,iP_apx,6)+ ...
QtzCpx_n_mol_nor*Vol_apx(1,iP_apx,11));
mod_vol_py_apx = Py_n_mol_nor*Vol_apx(1,iP_apx, 7)/(Py_n_mol_nor*...
Vol_apx(1,iP_apx,7)+Alm_n_mol_nor*Vol_apx(1,iP_apx,8)+ ...
QtzGrt_n_mol_nor*Vol_apx(1,iP_apx,11));
mod_vol_alm_apx = Alm_n_mol_nor*Vol_apx(1,iP_apx, 8)/(Py_n_mol_nor*...
Vol_apx(1,iP_apx,7)+Alm_n_mol_nor*Vol_apx(1,iP_apx,8)+ ...
QtzGrt_n_mol_nor*Vol_apx(1,iP_apx,11));
mod_vol_qtzgrt_apx = QtzGrt_n_mol_nor*Vol_apx(1,iP_apx,11)/(Py_n_mol_nor*...
Vol_apx(1,iP_apx,7)+Alm_n_mol_nor*Vol_apx(1,iP_apx,8)+ ...
QtzGrt_n_mol_nor*Vol_apx(1,iP_apx,11));

```

```

M_sol = M_ol*mode_D2011(1)+M_opx*mode_D2011(2)+ ...
      M_cpx*mode_D2011(3)+M_grt*mode_D2011(4);

rho_ol_exp = M_ol/ Vol_ol_exp;
rho_opx_exp = M_opx/Vol_opx_exp;
rho_cpx_exp = M_cpx/Vol_cpx_exp;
rho_grt_exp = M_grt/Vol_grt_exp;
Vol_sol_exp = Vol_ol_exp*mode_D2011(1)+Vol_opx_exp*mode_D2011(2)+ ...
             Vol_cpx_exp*mode_D2011(3)+Vol_grt_exp*mode_D2011(4);

rho_sol_exp = M_sol/Vol_sol_exp;
rho_mlt_exp = M_liq/Vol_liq_exp;

rho_ol_apx = M_ol/ Vol_ol_apx;
rho_opx_apx = M_opx/Vol_opx_apx;
rho_cpx_apx = M_cpx/Vol_cpx_apx;
rho_grt_apx = M_grt/Vol_grt_apx;
Vol_sol_apx = Vol_ol_apx*mode_D2011(1)+Vol_opx_apx*mode_D2011(2)+ ...
             Vol_cpx_apx*mode_D2011(3)+Vol_grt_apx*mode_D2011(4);

rho_sol_apx = M_sol/Vol_sol_apx;
rho_mlt_apx = M_liq/Vol_liq_apx;

rho_mlt_lp = rho0_mlt;
rho_sol_lp = rho0_sol;

gamma_rho_mlt_lp = ((rho_mlt_exp-rho_mlt_lp)/(SiO_TOT_exp-SiO_TOT_lp))/rho0_mlt;
                  % avec température de l'expérience
gamma_rho_mlt_apx = ((rho_mlt_apx-rho_mlt_lp)/(SiO_TOT_exp-SiO_TOT_lp))/rho0_mlt;
                  % avec température de l'approximation
gamma_rho_sol_lp = ((rho_sol_exp-rho_sol_lp)/(SiO_TOT_exp-SiO_TOT_lp))/rho0_sol;
gamma_rho_sol_apx = ((rho_sol_apx-rho_sol_lp)/(SiO_TOT_exp-SiO_TOT_lp))/rho0_sol;

% Changement de nom des variables
T_ref = Tref_apx;
T_exp = Tref_exp;
P_ref = Pref_apx;
P_exp = Pref_exp;
gamma_rho_mlt = gamma_rho_mlt_apx;
gamma_rho_sol = gamma_rho_sol_apx;
T_zoom = T_plotz+273.15;
T2 = T2dz;
P_zoom = P_plotz;
P2 = P2dz;
C2 = C2dz;
C_ref = SiO_TOT_lp;

save ApproxData_AlphaBetaGamma T_zoom P_zoom T2 P2 C2 C_ref ...
T_ref P_ref T_exp P_exp SiO_TOT_exp SiO_TOT_lp ...
rho0_mlt U0_mlt CMgO0_mlt CFeO0_mlt CSiO20_mlt Cp0_mlt ...
rho0_sol U0_sol CMgO0_sol CFeO0_sol CSiO20_sol Cp0_sol ...
alpha_rho_mlt alpha_U_mlt alpha_CMgO_mlt alpha_CFeO_mlt alpha_CSiO2_mlt alpha_Cp_mlt ...
alpha_rho_sol alpha_U_sol alpha_CMgO_sol alpha_CFeO_sol alpha_CSiO2_sol alpha_Cp_sol ...
beta_rho_mlt beta_U_mlt beta_CMgO_mlt beta_CFeO_mlt beta_CSiO2_mlt beta_Cp_mlt ...
beta_rho_sol beta_U_sol beta_CMgO_sol beta_CFeO_sol beta_CSiO2_sol beta_Cp_sol ...
gamma_rho_mlt gamma_U_mlt gamma_CMgO_mlt gamma_CFeO_mlt gamma_CSiO2_mlt gamma_Cp_mlt ...
gamma_rho_sol gamma_U_sol gamma_CMgO_sol gamma_CFeO_sol gamma_CSiO2_sol gamma_Cp_sol

```


APPENDIX C

Code for THMC transport

```

ND_6          = 1;                                % rhoCpm/rhoCpc_number; density * specific heat /
                                                  characteristic value

% dimensionally dependent scales
w             = ND_1 * Lc;
Lx           = ND_2 * Lc;
rhosg0       = ND_3 * rhofg0;
etas         = ND_4 * etac0;
lams         = 483 * lamc;
lamf         = 1*lams;
rhoCpm0      = 205 * rhoCpc;
rhoCps0      = ND_3*(Cp0_sol/Cp0_mlt)*rhoCpm0;
%% numerics
dt           = 7e-3*tc;                          % [m/m^2*Pa*s/Pa*m = s]
nx           = 128;
nt           = 500;
niter        = 1000*nx^2;
eiter        = 1e-7;
nout         = 1000*1e0;
nout_it      = 25;
% preprocessing
dx           = Lx/(nx-1);
x            = -Lx/2:dx:Lx/2;
%% initial
hatf         = exp(-(x+0.2*Lx)/w).^2;
Delta_T      = 2*TA; % K ; temperature difference across model
Tgeoeth     = linspace(T0+Delta_T,T0,length(x));
T            = Tgeoeth + 0*TA*hatf;               T_i = T;
phi          = phi0 + phiA*hatf;                 phi_i = phi;
CSit         = CSit0 + CSitA*hatf;              CSit_i = CSit;
rhofg        = rhofg0*ones(1,nx);
rhosg        = rhosg0*ones(1,nx);
rhotg        = rhofg.*phi + rhosg.*(1-phi);
Pt           = -cumtrapz(rhotg)*dx;
Pf           = Pt;
Pf0          = Pf;
P_ref        = mean(Pf);
T_ref        = mean(T);
Vs           = zeros(1,nx+1);
qD           = zeros(1,nx+1);
qC           = zeros(1,nx+1);
qT           = zeros(1,nx+1);
%% action
for it = 1:nt
    for iter = 1:niter
        % Concentration
        CSim    = CSim0 .* (1 + alpha_CSiO2_mlt.*(T-T_ref) + beta_CSiO2_mlt.* ...
            (Pf-P_ref) + gamma_CSiO2_mlt.*(CSit-CSit_ref));
        CSis    = CSis0 .* (1 + alpha_CSiO2_sol.*(T-T_ref) + beta_CSiO2_sol.* ...
            (Pf-P_ref) + gamma_CSiO2_sol.*(CSit-CSit_ref));
        CMgm    = CMgm0 .* (1 + alpha_CMgO_mlt.*(T-T_ref) + beta_CMgO_mlt.* ...
            (Pf-P_ref) + gamma_CMgO_mlt.*(CSit-CSit_ref));
        CMgs    = CMgs0 .* (1 + alpha_CMgO_sol.*(T-T_ref) + beta_CMgO_sol.* ...
            (Pf-P_ref) + gamma_CMgO_sol.*(CSit-CSit_ref));

        % Densities
        rhofg   = rhofg0.*(1 + alpha_rho_mlt.*(T-T_ref) + beta_rho_mlt.* ...
            (Pf-P_ref) + gamma_rho_mlt.*(CSit-CSit_ref));
        rhosg   = rhosg0.*(1 + alpha_rho_sol.*(T-T_ref) + beta_rho_sol.* ...
            (Pf-P_ref) + gamma_rho_sol.*(CSit-CSit_ref));

        % Total densities
        rhotg   = rhofg.*phi + rhosg.*(1-phi);
        rhoMgg  = rhofg.*phi.*CMgm + rhosg.*(1-phi).*CMgs;
        rhoSig  = rhofg.*phi.*CSim + rhosg.*(1-phi).*CSis;

        % Energy

```



```

% Update rho*cp
rhoCpm      = rhoCpm0 .* rhofg/rhofg0;
rhoCps      = rhoCps0 .* rhosg/rhosg0;
rhoCpt      = rhoCpm.*phi + rhoCps.*(1-phi);
Um          = rhoCpm.*T;
Us          = rhoCps.*T;
Ut          = Um.*phi + Us.*(1-phi);
if iter < 3;
    rhotg_old = rhotg;
    rhoMgg_old = rhoMgg;
    rhoSig_old = rhoSig;
    CMgm_old = CMgm;
    CMgs_old = CMgs;
    CSim_old = CSim;
    CSis_old = CSis;
    CSit_old = CSit;
    Ut_old = Ut;
end
if it < 6
    if iter<3
        Pt      = -cumtrapz(rhotg)*dx;
        Pf      = Pt;
        Pf0     = Pf;
        CSim_i  = CSim;
        CSis_i  = CSis;
        CMgm_i  = CMgm;
        CMgs_i  = CMgs;
        rhofg_i = rhofg;
        rhosg_i = rhosg;
    end
end
% MASS CONSERVATION EQUATIONS
% Darcy
perm        = k_etaf*(avx(phi)/phi0).^nperm;
qD(2:end-1) = -perm.*(diff(Pf)/dx + avx(rhofg));
qD([1 end]) = qD([2 end-1]);
% time derivatives
drhotg_dt   = (rhotg - rhotg_old)/dt;
drhocMgg_dt = (rhoMgg - rhoMgg_old)/dt;
drhocSig_dt = (rhoSig - rhoSig_old)/dt;
% mass fluxes
q_rhotg     = expx(avx(rhofg)).*qD + expx(avx(rhotg)).*Vs;
q_rhocMgg   = expx(avx(rhofg.*CMgm)).*qD + expx(avx(rhoMgg)).*Vs;
q_rhocSig   = expx(avx(rhofg.*CSim)).*qD + expx(avx(rhoSig)).*Vs;
% residuals
res_Pf      = -drhotg_dt - diff(q_rhotg)/dx;
res_Phi     = -drhocMgg_dt - diff(q_rhocMgg)/dx;
res_CSit    = -drhocSig_dt - diff(q_rhocSig)/dx;
% update fluid pressure
dt_Pf       = dx^2/max(perm)/4 /2;
dPf         = dt_Pf*res_Pf;
Pf          = Pf + dPf;
Pf([1,end]) = Pt([1,end]);
% update porosity
dPhi        = -dt/1*res_Phi;
phi         = phi + dPhi;
% update concentration Si
dCSi        = dt/1*res_CSit;
CSit        = CSit + dCSi;
% Melt velocity; Used e.g. for advection-only of concentrations
Vm          = qD./expx(avx(phi)) + Vs;
% CONSERVATION OF LINEAR MOMENTUM, force balance for solid deformation
etac        = etac0;

```

```

Pt          = Pf - diff(Vs)/dx.*(1-phi).*etas;
tau         = 2*etas*diff(Vs)/dx;
dt_visc    = dx^2/etas/6/1;
dVx        = dt_visc*( diff(-Pt + tau)/dx - avx(rhotg) );
Vs(2:end-1) = Vs(2:end-1) + dVx;
% CONSERVATION OF ENERGY, heat transfer
dUtdt      = (Ut-Ut_old)/dt;
lam        = lamf*phi + lams*(1-phi);
qT(2:end-1) = -avx(lam).*diff(T)/dx+ avx(Um).*qD(2:end-1)+ avx(Ut).*Vs(2:end-1);
qT([1 end]) = qT([2 end-1]);
res_Ut     = -dUtdt - diff(qT)/dx;
dt_Ut      = dx^2/max(lam./rhoCpt)/4.1;
Ut2T       = 1./rhoCpt/10;
dT         = dt_Ut*Ut2T.*res_Ut;
T          = T + dT;
% check exit creteria
errs       = [ max(abs(dPf(2:end-1))) /max(abs(Pf(2:end-1))) ...
              ,max(abs(dPhi)) /max(abs(phi)) ...
              ,max(abs(dVx)) /max(abs(Vs)) ...
              ,max(abs(dT)) /max(abs(T)) ...
              ,max(abs(dCSi)) /max(abs(CSit)) ];
if mod(iter,nout) == 1e10
    figure(1)
    semilogy(iter,max(abs(dPf(2:end-1))) /max(abs(Pf(2:end-1))) , 'd');hold on
    semilogy(iter,max(abs(dPhi)) /max(abs(phi)) , 's');
    semilogy(iter,max(abs(dVx)) /max(abs(Vs)) , '+');
    semilogy(iter,max(abs(dT)) /max(abs(T)) , 'o');
    semilogy(iter,max(abs(dCSi)) /max(abs(CSit)) , 'v');drawnow
    set(gcf, 'position', [965.4000 352.6000 560 420])
end
if max(errs) < eiter && iter > 50
    break;
end
end
%%% Plot and save
if mod(it,nout_it) == 0 | it == 5
    display(['Time step: ',num2str(it),' of ',num2str(nt)])
    figure(2)
    hold off;
    sgtitle(['Time step = ',int2str(it),' Iterations per time step = ', ...
            int2str(iter)]);
    subplot(331),plot(phi_i,x,'k--',phi,x,'k-'); title('\phi'); grid on
    subplot(332),plot(Pf-Pt,x,'k-'); title('P_f-P_t'); grid on
    subplot(333),plot(Pf0,x,'k--',Pf,x,'r-',Pt,x,'k-'); title('P_f & P_t'); grid on
    subplot(334),hold off; plot(rhofg_i,x,'r--',rhofg,x,'r-', ...
        rhosg_i,x,'k--',rhosg,x,'k-'); title('\rho_m & \rho_s'); grid on
    subplot(335),plot(T_i,x,'r--',T,x,'r-'); title('T'); grid on
    subplot(336),plot(Vm(2:end),x,'r-'); title('V_{melt}'); grid on
    subplot(337),plot(CMgm_i,x,'r--',CMgm,x,'r-',CMgs_i,x,'k--',CMgs,x,'k-');
        title('CMg_m & CMg_s'); grid on
    subplot(338),plot(CSim_i,x,'r--',CSim,x,'r-',CSis_i,x,'k--', ...
        CSis,x,'k-',CSit_i,x,'b--',CSit,x,'b-');
        title('CSi_m, CSi_s & CSi_{tot}'); grid on
    subplot(339),plot(Vs(2:end),x,'b-'); title('V_{solid}'); grid on
    set(gcf, 'position', [43.8000 89 915.6000 682.8000])
    drawnow
    save(['THMC_S15_cond_',num2str(it,['%',num2str(3),'.',num2str(3),'d']),'.mat'])
end
end
function C=avx(C)
C = 0.5*(C(1:end-1)+C(2:end)); end
function C=expv(C)
C = [C(1) C C(end)]; end

```

